Lithium-Ion Battery Formation Modeling and Diagnostics

by

Andrew Weng

A dissertation submitted in partial fulfillment
of the requirements for the degree of
Doctor of Philosophy
(Mechanical Engineering)
in the University of Michigan
2024

Doctoral Committee:

Professor Anna Stefanopoulou, Chair
Associate Professor Neil Dasgupta
Professor Judy Jin
Associate Research Scientist Jason B. Siegel

Andrew Weng
asweng@umich.edu
ORCID iD: 0000-0002-3680-0195

DEDICATION

To my mom and dad.

ACKNOWLEDGEMENTS

I could not have undertaken this journey without the support of my professor and chair of my committee Anna Stefanopoulou. Despite my unconventional background, she accepted me into her research group with open arms. Throughout my years in graduate school, she showed constant support for my research ideas and was my biggest advocate. If it weren't for her, I would not have decided to return to school to pursue graduate studies.

I am also grateful to Dr. Jason Siegel for being the research scientist every research group wishes they had. As a new student joining a lab, we are often left picking up the pieces of work from recently-graduated students, an often time-consuming and frustrating experience. This doesn't happen in our lab because Jason is always there as a perpetual mentor and source of knowledge. His expertise and willingness to help form the backbone of so much of what we can accomplish in this group.

Many thanks to my committee members professor Neil Dasgupta and professor Judy Jin. You have brought fresh perspectives to my research and challenged me to make my work resonate with multiple academic communities. I believe that the best research can bridge gaps between scientific and engineering disciplines. Thank you for your guidance towards this challenging but worthwhile endeavor.

Special thanks to my former labmates Suhak Lee, Peyman Mohtat, Ting Cai, Tino Sulzer, for welcoming me to Ann Arbor and the Battery Control Group with open arms in the middle of a raging pandemic.

I am also thankful to my present labmates Vivian Tran, Clement Wong, Everardo Olide, Hamidreza Movahedi, Omar Ahmed, and Sravan Pannala, for being wonderful academic companions and friends throughout the years. I was glad to have Vivian as a study partner in a graduate-level course on model-predictive control. Seeing how she was not intimidated by the advanced math from the course made me believe that I could also survive the class. Vivian also helped keep my office plant alive during my frequent absences; the plant is now on track to outlast my tenure at the office. Clement brought joy with his presence and occasional shipments from Costco which included dried mangoes and matcha powder. Everardo was an indispensable intellectual partner throughout my work on the formation model. Everardo's intuition on how to think about battery physics is unparalleled. He

was the one who suggested representing the boosted SEI growth dynamics using first-order dynamics. He also frequently challenged my thinking, helping spark new ideas and different approaches.

I'd also like to recognize the folks at the Michigan Battery Lab: Greg Less, Joe Gallegos, William Hicks, Art Sinclair. Their willingness to help and their expertise were what enabled the work presented in this thesis. Every university should have a resource like the one we do with the battery lab.

Thanks also go to my colleague Peter M. Attia for helping me navigate my transition from industry back to academia. Peter was a key mentor during my first year as a graduate student who taught me how to read papers, how to "write good," and gave me the confidence to be ambitious. Peter's exceptional academic work has also helped me set the bar for quality in research and writing.

To our department staff and administrative professionals Adam Mael, Karen Brown, Andrea Fulton: you are so good at what you do. I am thankful for the speed and attention to detail you give to every email I've sent over the years, be they big or small. If batteries were as reliable as you then we would be all out of jobs.

Finally: to my mom, my model for boundless devotion; my dad, my model for boundless curiosity, and my partner, Rebecca, my life companion, my best friend, my source of courage, and my daily role model as a parent and as a professional.

TABLE OF CONTENTS

LIST OF FIGURES

FIGURE

LIST OF TABLES

TABLE

LIST OF APPENDICES

LIST OF ACRONYMS

ARC accelerated rate calorimetry

BMS battery management system

CAM cathode active material

CE coulombic efficiency

CC constant current

CMC carboxymethyl cellulose

CV constant voltage

DEC diethyl carbonate

DMC dimethyl carbonate

DVA differential voltage analysis

EC ethylene carbonate

EV electric vehicle

FCE first cycle efficiency

FEC fluoroethylene carbonate

HPPC hybrid pulse power characterization

ICA incremental capacity analysis

LAM loss of active material

LLI loss of lithium inventory

LFP lithium iron phosphate

NMC nickel manganese cobalt

NMP n-methylpyrrolidone

NPR negative to positive ratio

ODE ordinary differential equations

OCV open circuit voltage

PVDF polyvinylidene fluoride

RPT reference performance test

RUL remaining useful life

SBR sytrene butadiene rubber

SEI solid electrolyte interphase

SOC state of charge

SPM single particle model

SOH state of health

VC vinylene carbonate

ABSTRACT

The world needs to transition to sustainable energy as quickly as possible. A cornerstone of this transition is a fully electrified transportation sector which will require the production of automotive-grade lithium-ion batteries at a massive scale. Among the many challenges of battery production, the battery formation step, the last step in battery manufacturing, is both paramount and problematic. It is paramount since all batteries undergo the formation process to build a resilient solid electrolyte interphase (SEI) and to screen for defects. It is problematic because the formation process is expensive to operate, is a major source of factory energy demand, requires larger factory footprints, and takes an order of magnitude longer than nearly every other manufacturing step. Despite the centrality of the formation process in battery manufacturing, steps taken to optimize formation protocols remain ad hoc in the absence of fundamental design principles and physical models.

In this thesis, we develop models and methods to enable advances in battery formation protocol design, battery manufacturing process control, and battery lifetime prediction. The work begins by introducing a physics-based electrochemical model of the battery formation process which, for the first time, bridges the gap between the electrochemistry of SEI formation and full-cell performance metrics. We demonstrate that the model can predict emergent system properties such as SEI passivation and cell aging. Using the model, we also verified that faster formation protocols are achievable without compromising battery lifetime. Next, we take a data-driven approach to studying the battery formation process through the lens of scalable diagnostic features, or "electrochemical fingerprints." We show that these diagnostic features can be used to improve battery manufacturing process control and for predicting the impact of formation protocols on battery lifetime immediately after manufacturing. However, great care is needed to ensure reproducible data collection. Finally, the thesis ends by investigating the question of "how much variability is too much," i.e. how much process control is really in battery manufacturing? We demonstrate that, when dissimilar battery cells are cycled in a parallel configuration, the degradation trajectory of individual cells may converge, suggesting that some amount of variability in cell properties at the beginning of life may be tolerated.

CHAPTER 1

Introduction

1.1 Context

1.1.1 The Transition to Full Vehicle Electrification

The transition to electric vehicles (EV) is a cornerstone to achieving a net-zero emissions future. A core enabling technology is industrial-scale battery manufacturing which supplies the automotive-grade lithium-ion batteries at the heart of all EVs. Enabled by this steady supply of batteries, EVs accounted for more than 10% of new passenger vehicles sold globally in 2022, a number expected to rise to 20% by 2025 and 59% by 2035 [1].

The rapid shift towards EVs has required battery cell manufacturers to expand production capacity at an unprecedented rate. In 2022 alone, cell manufacturers expanded production capacity by more than 600 GWh globally – the equivalent to producing up to 91 million individual battery cells per day[1]. This trajectory will only increase through to 2030 as countries race to fully electrify their fleet, with global demand for lithium-ion batteries projected to exceed 3,000 GWh by 2030 [2] (Figure 1.1). Recent U.S. industrial policies such as the Inflation Reduction Act (IRA) have also spurred a race to "onshore" battery factories. In 2022 alone, U.S. companies collectively announced plans to open more than 17 battery "gigafactories" across multiple states including Michigan, North Carolina, Georgia, and Tennessee, with the promise to create over 50,000 domestic jobs as part of a new "battery belt" [1, 3].

1.1.2 Manufacturing Scale-Up Challenges

The journey to open and operate battery factories rapidly is fraught with challenges. The battery manufacturing process requires cleanliness levels rivaling the semiconductor industry, yet the battery manufacturing industry lacks a mature, systematic understanding of process

[1] Assumes production of 21700 form factor cylindrical cells with a nominal energy of 18 Wh.

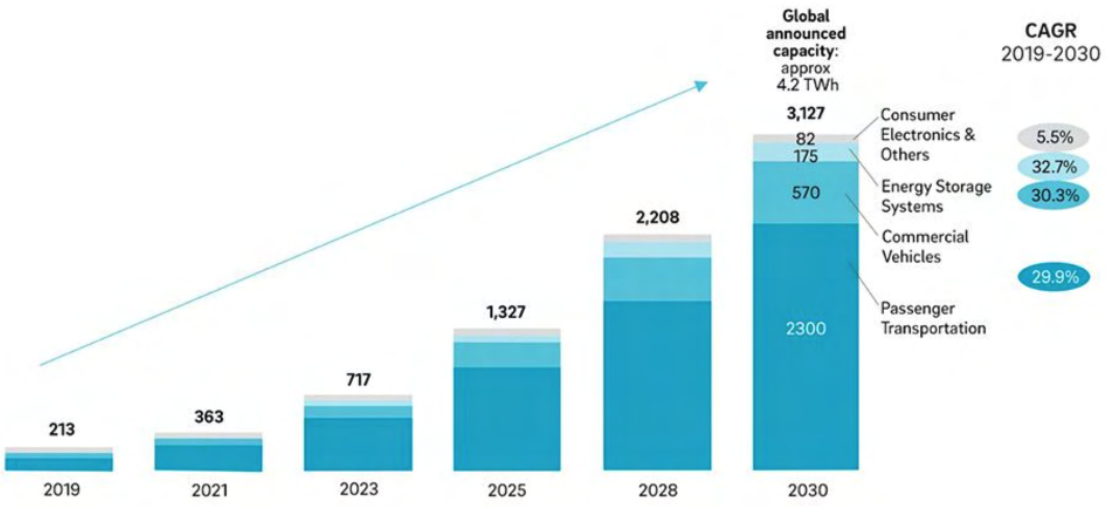

Figure 1.1: Global demand for lithium-ion batteries to quadruple by 2030 [2]. Passenger transportation accounts for the majority of demand. CAGR: compound annual growth rate. Sources: Avicenne, Fraunhofer, IHS Markit, interviews with market participants, Roland Berger.

control factors owing to the industry's nascency and the inherent complexity of lithium-ion battery electro-mechanochemistry. As a result, slow feedback cycles and insufficient in-line inspection systems cause new battery factories to experience scrap rates of 30% during line commissioning, a number that does not improve beyond 10% even under steady-state conditions [1].

Among the many steps in manufacturing a battery, the **battery formation process** is among the most challenging. As the very last step in battery manufacturing, the formation process plays an outsize role in determining the longevity of batteries. The formation process is also one of the most energy-intensive and operationally expensive steps in manufacturing. Finally, the formation process also introduces logistical challenges since the formation step is an order of magnitude slower than the next slowest manufacturing step. These difficulties motivate the development of improved tools and methods for developing better formation processes.

1.2 Thesis Outline

In this thesis, we develop physics-based data-driven models and diagnostic tools to enable advances in battery formation protocol design, manufacturing process control, and battery lifetime prediction. A visual guide to the organization of this thesis is shown in Figure 1.2.

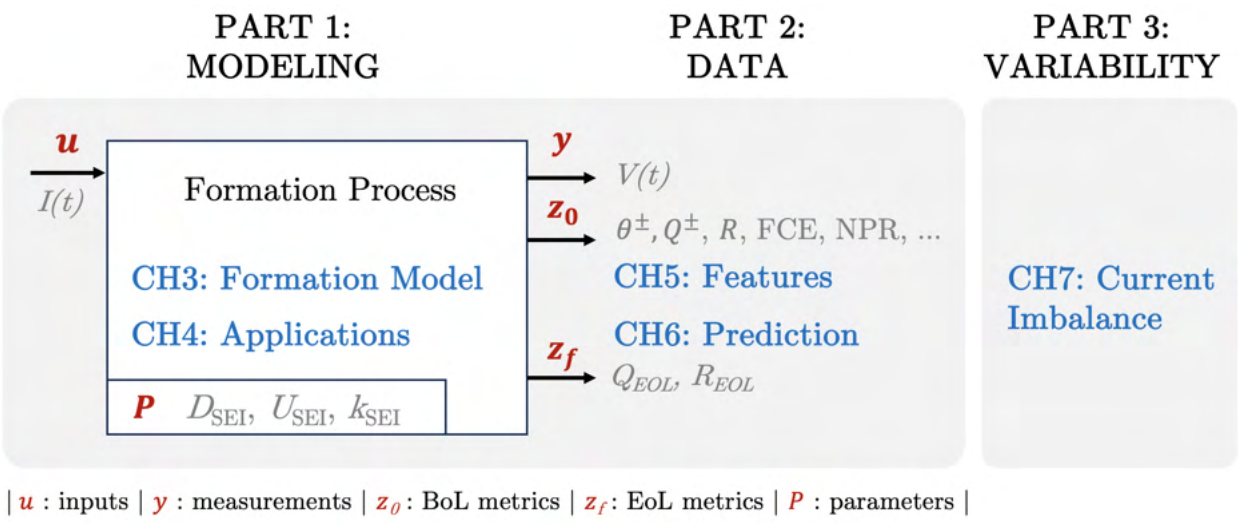

Figure 1.2: A visual outline of the main sections of this thesis.

Chapter 2 first provides an introduction to the core concepts that this thesis builds upon. Topics covered include the battery manufacturing process with an emphasis on the formation process, the electrochemistry of solid electrolyte interphase (SEI) formation, and the challenges and opportunities of extracting voltage-based diagnostic features at the end of the battery manufacturing line.

The rest of the thesis is divided into three parts. In **Part I: Modeling**, we focus on developing the mathematical foundations for simulating the behavior of battery formation. **Chapter 3** proposes a reduced-order model for the solid electrolyte interphase (SEI) growth process during the early stages of lithium-ion battery formation cycling and aging. This model enables dynamical simulations of the battery formation process in the context of a full cell, the first of its kind. **Chapter 4** then explores how the formation model can be applied to various future applications including simulating faster formation protocols, designing optimal formation protocols, simulating cycle life, degradation model parameter identification, and designing diagnostic features.

In **Part II: Data**, we take a data-driven approach to analyzing electrochemical data for applications in manufacturing process control and lifetime prediction. **Chapter 5** presents methods for collecting and analyzing full cell voltage data towards developing physically interpretable diagnostic features with applications for battery manufacturing process control and lifetime prediction. **Chapter 6** details the usage of one particular voltage-based feature collected immediately after battery formation, the low-SOC resistance, to predict the future lifetime trajectories of batteries. This chapter highlights the opportunity to use battery manufacturing data to enable lifetime prediction without needing cycle life test data.

In **Part III: Variability**, we propose analytical and simulation methods to understand the implications of cell manufacturing variability on the lifetime of battery systems. **Chapter 7** focuses on studying the collective dynamics of battery cells connected in parallel, a common configuration in battery packs. We show that, when battery cells with dissimilar capacities are connected and cycled in parallel, the capacities of the individual cell may sometimes converge.

Chapter 8 concludes the thesis by re-summarizing the main contributions and providing a roadmap for future research based on this work.

1.3 List of Contributions

This thesis represents research that was done in collaboration with many others. My contributions to the work in the thesis chapters, in order of appearance, are listed below. I will use the CRediT taxonomy [4] to detail these contributions.

The contents of **Chapter 3** have been adapted from the following works:

- [5] **Andrew Weng**, Everardo Olide, Iaroslav Kovalchuk, Jason B Siegel, and Anna Stefanopoulou. *Modeling battery formation: SEI growth boosting, multi-species reactions, and irreversible expansion.* Journal of the Electrochemical Society 170(9): 090523, 2023

Contributions: conceptualization, data curation, formal analysis, investigation, methodology, project administration, software, validation, visualization, writing - original draft, writing - review & editing.

The contents of **Chapter 4** have been adapted from the following works:

- **Andrew Weng**, Jason B. Siegel, Anna G. Stefanopoulou. *Modeling fast formation: capacity cross-over, additive consumption knees, and lifetime prediction.* (Manuscript in preparation)

- **Andrew Weng**, Hamidreza Movahedi, Jason B. Siegel, Anna Stefanopoulou. *Control-oriented model of SEI growth and expansion: towards optimal control of battery formation protocols.* American Control Conference 2024 (submitted)

Contributions: conceptualization, data curation, formal analysis, investigation, methodology, software, validation, visualization, writing - original draft.

The contents of **Chapter 5** have been adapted from the following works:

- [6] **Andrew Weng**, Jason B. Siegel, and Anna Stefanopoulou. *Differential voltage analysis for battery manufacturing process control.* Frontiers in Energy Research, 11, 2023

Contributions: conceptualization, data curation, formal analysis, investigation, methodology, project administration, software, validation, visualization, writing - original draft, writing - review & editing.

The contents of **Chapter 6** have been adapted from the following works:

- [7] **Andrew Weng**, Peyman Mohtat, Peter M Attia, Valentin Sulzer, Suhak Lee, Greg Less, and Anna G Stefanopoulou. *Predicting the impact of formation protocols on battery lifetime immediately after manufacturing.* Joule 5(11):2971-92, 2021

Contributions: conceptualization, data curation, formal analysis, investigation, methodology, project administration, software, validation, visualization, writing - original draft, writing - review & editing.

The contents of **Chapter 7** have been adapted from the following works:

- [8] **Andrew Weng**, Hamidreza Mohavedi, Jason B Siegel, and Anna G Stefanopoulou. *Current imbalance in dissimilar parallel-connected batteries and the fate of degradation variability.* Journal of Dynamic Systems, Measurement, and Control, November, 1-22, 2023

- [9] **Andrew Weng**, Sravan Pannala, Jason B Siegel, and Anna G Stefanopoulou. *Parallel-connected battery current imbalance dynamics.* IFAC-PapersOnLine, 55(37):37–43, 2022.

Contributions: conceptualization, data curation, formal analysis, investigation, methodology, project administration, software, validation, visualization, writing - original draft, writing - review & editing.

The contents from **Appendix A** this chapter have been adapted from the following works:

- [10] **Andrew Weng**, Eric Dufek, and Anna Stefanopoulou. *Battery passports for promoting electric vehicle resale and repurposing.* Joule, 7(5):837–842, May 2023

Contributions: formal analysis, investigation, methodology, software, visualization, writing - original draft, writing - review & editing.

The research I performed with the Stefanopoulou group extends beyond the work presented in this thesis. These additional contributions are listed below:

- **Andrew Weng**, Omar Y. Ahmed, Anna Stefanopoulou. *Early evidence of labor productivity shifts due to the electric vehicle transition in the U.S.* (Manuscript in preparation)
- Weihan Li, Billy Wu, Anna Stefanopoulou, Gregory J. Offer, Xuning Feng, Hamidreza Movahedi, **Andrew Weng**, Monica Marinescu, Minggao Ouyang, Christiane Rahe, Dirk Uwe Sauer. *How fast can you go: accelerated degradation testing to predict lithium-ion battery durability.* (Manuscript in preparation)
- [11] Sravan Pannala, **Andrew Weng**, Ian Fischer, Jason B. Siegel, and Anna Stefanopoulou. *Low-cost inductive sensor and fixture kit for measuring battery cell thickness under constant pressure.* IFAC-PapersOnLine, 55(37):712-717, January 2022
- [12] Omar Y. Ahmed, Robert J. Middleton, Vivian Tran, **Andrew Weng**, Anna G. Stefanopoulou, Kenneth S. Kim, and Chol-Bum M. Kweon. *Model predictive control of combustion phasing in compression ignition engines by coordinating fuel injection timing and ignition assist.* IFAC-PapersOnLine, 55(24):90-96, January 2022

CHAPTER 2

Background

2.1 Introduction

This chapter reviews the core concepts upon which this thesis is built. We set the stage by first reviewing the battery manufacturing process with an emphasis on manufacturing scale-up challenges. We then review the critical role that battery formation plays as the last step in manufacturing including recent efforts by the academic community to understand the limits of faster formation protocols. We end by reviewing the relevant literature on mathematical models and non-destructive methods to understand and diagnose battery health.

2.2 Battery Manufacturing and Formation

2.2.1 Of Battery Makers and Cookie Bakers

A pedagogical introduction to the lithium-ion battery manufacturing process might often evoke the process of baking a cookie (Figure 2.1. This analogy is in some ways appropriate since there are indeed many similarities between the steps involved with each process. Consider the language used to describe the electrode manufacturing steps: mixing, baking, coating, cutting, and so on. But here is where the similarities end.

The biggest difference between battery-making and cookie-baking is perhaps in the environmental and cleanliness requirements. Take, for example, the fact that cookies can be made under the ambient conditions of a kitchen. If a piece of hair gets into a batch of dough during mixing, the cookie will still be edible, albeit with a tinge of hair taste, and only if you were paying close attention. Comparatively, in battery manufacturing, the materials being handled, including the cathode active material (CAM) and the electrolyte, are usually highly moisture-sensitive, requiring material handlers to work in de-humidified rooms while dressing up in full-body "bunny suits" to prevent the transfer of moisture from their breaths

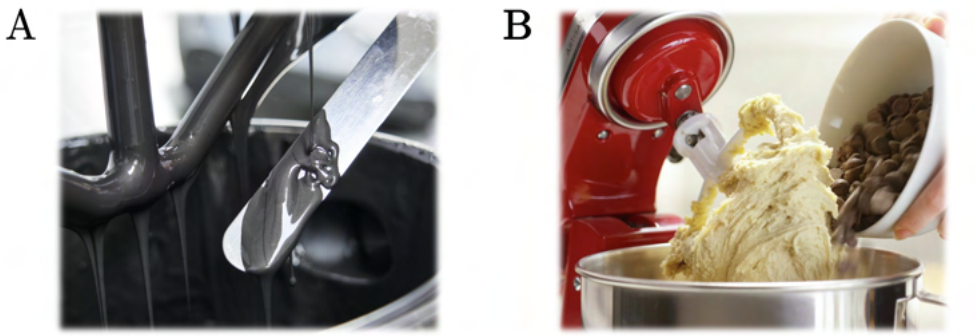

Figure 2.1: Of battery makers and cookie bakers. (A) An electrode slurry paste after being mixed using a planetary mixer. (B) Chocolate cookie dough being mixed using a KitchenAid® stand mixer.

onto the material. Cookie-bakers should be glad they don't have to wear bunny suits to make the cookies taste good. Also, in battery manufacturing, any bit of material impurities, including metal contamination, introduced at any stage of the battery manufacturing process could lead to eventual internal shorts and battery fires which pose a public safety hazard and represent an existential threat to the viability of those in the business of making and selling batteries and battery products.

Here is a final analogy to underscore the vast difference between making batteries and baking cookies: with cookies, you can perform quality control by sampling a cookie, i.e. by taking a bite of it. However, with batteries, not only is it inedible, but you may have great difficulties with taking the state of health (SOH) measured from a freshly-made battery and using it to predict the lifetime of a battery a decade later[1].

2.2.2 Manufacturing Steps

Details of the battery manufacturing steps have been previously reviewed by many [13, 14, 15, 16, 17]. Here, we review the key manufacturing steps which are conventionally organized into three steps: (1) electrode manufacturing, (2) cell assembly, and (3) cell finishing (see Figure 2.2A). A quick note on terminology: in battery manufacturing, it is common to use the words 'cathode' and 'anode' as shorthands for the positive and negative electrodes, respectively. This thesis will follow this convention for describing battery manufacturing processes. However, in later chapters that deal with electrochemical models, we revert to using the language of positive and negative electrodes to follow the convention of

[1]Electric vehicle battery powertrain warranties typically span 8 years and grid storage applications are typically operated for 20 years or longer.

the electrochemical community.

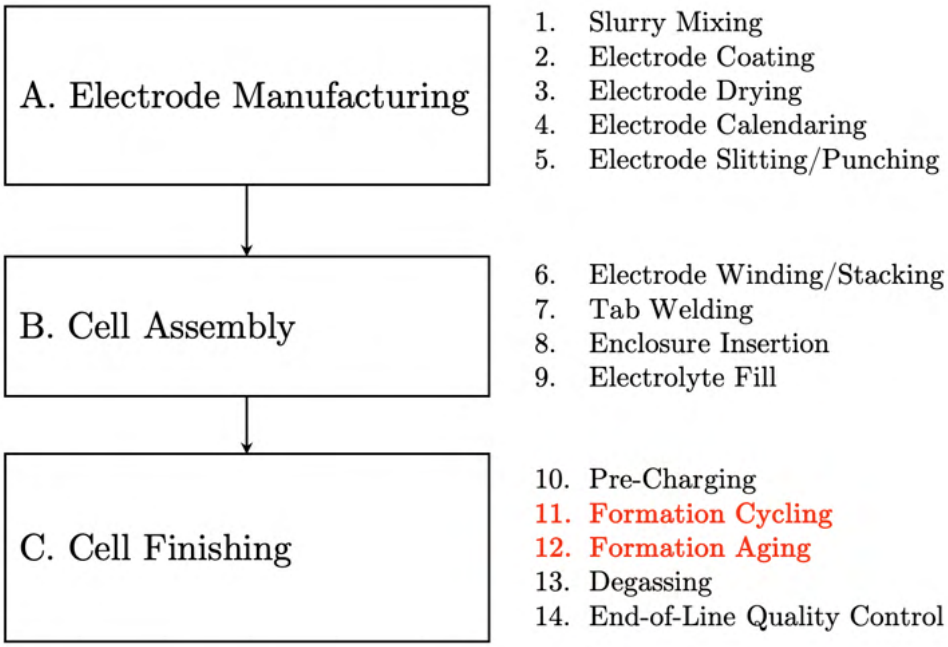

Figure 2.2: Battery manufacturing process overview.

2.2.2.1 Electrode Manufacturing

In electrode manufacturing, active material powders are first mixed in a solvent along with binder materials in a process called **electrode slurry mixing**. The solvent can either be an organic compound such as n-methylpyrrolidone (NMP) or be aqueous (water-based). The binder material is mixed in a small quantity, typically less than 5 wt%, to improve electronic conduction between the active particles and to achieve favorable mechanical properties for the subsequent manufacturing steps. In the cathode, polyvinylidene fluoride (PVDF) typically acts as the binder with NMP as the solvent. In the anode, sytrene butadiene rubber (SBR) and carboxymethyl cellulose (CMC) are popular aqueous binders. A well-mixed slurry achieves uniformity and dispersion of the active materials.

After slurry mixing, the active material slurry is coated onto the current collector substrate in a process called **electrode coating**. Aluminum serves as the current collector for the cathode while copper serves as the current collector for the anode. In electrode coating, the electrode slurry is poured into a slot die which continuously transfers the slurry onto a roll of current collector as the current collector is fed through. The process of transferring the

slurry onto the current collector is carefully controlled to achieve a target loading[2] while maximizing film uniformity.

Following electrode coating, the coated current collectors are fed through a series of ovens in a process called **electrode drying**. This step is essential for evaporating the solvents used to make the slurry. This step is noteworthy for its energy usage and factory footprint: large ovens, often operating at high temperatures, are necessary for electrode drying. The solvents may also be toxic, as is the case with NMP, which motivates the development of solvent recovery systems or, more recently, the usage of solve-free processes [18]. We also note that the electrode coating and drying process is sometimes repeated twice since the current collectors must be coated on both sides. To do this, the spool of single-side coated collector is fed back to the electrode coater to repeat the coating process for the non-coated side.

After the coated electrodes are dried, the next step of electrode manufacturing is **electrode calendaring** [19, 20][3], an essential step to ensuring the final cell achieves the desired energy density target. Calendaring involves applying high pressures to the electrode films to achieve the desired film thickness and porosity. The pressure must be applied uniformly and continuously to the coated electrode sheet, a challenging engineering problem. A typical calendaring process involves continuously feeding the coated electrodes through roll presses.

At this stage, the calendared electrodes are finished but need to be cut down to size in preparation for assembly. For high-volume battery manufacturing, this step is called **electrode slitting** and involves the usage of rotary blades to cut the electrode sheets down to the correct width. For lower-volume manufacturing, i.e. for stacked pouch cell designs, this step is sometimes called **electrode punching** which refers to the usage of punch presses to cut the electrode stock material down to the proper dimensions.

At the end of electrode slitting, the rolls of electrode material are ready to be brought into the assembly process where the materials are combined to build the battery cell. Note that most battery factories have two electrode manufacturing lines running in parallel: one for the anode and one for the cathode. These lines are kept separate from each other to avoid cross-contamination. The processing steps for each step may also differ. For example, graphite-based anode slurries are typically made using an aqueous solvent, while NMC-based cathode slurries typically require an organic solvent, i.e. NMP, which could require solvent recovery processes to be set up in the cathode line.

[2]Loading may be quantified by the grams of material per unit centimeter, for example.

[3]Not to be confused with battery "calendar aging" which is the process of storing finished cells at a preset state of charge (SOC) and temperature to age the cell.

2.2.2.2 Cell Assembly

The cell assembly process can look very different depending on the manufacturer, the cell form factor (e.g. cylindrical, pouch, prismatic, etc.), and the level of automation. In a typical cylindrical cell assembly process, rolls of cathode, anode, and separator material are loaded on a machine called the winding machine which rolls the material together [21, 22]. This process is often called **electrode winding**. While conceptually simple, the winding process in practice requires a high degree of precision to make defect-free battery cells. In high-volume production, process parameters that need to be controlled may include winding tension, geometric alignment of each layer, and the absence of defects. Failure to meet quality specifications set out by the manufacturer can cause the wound material to be rejected and discarded.

For stacked pouch cell designs, the counterpart to electrode winding is called **electrode stacking**. This process is analogous to electrode winding, but instead of winding the active material layers together, individual layers of electrodes are stacked together while the separator layer is fed and interleaved between each active layer. This configuration is sometimes referred to as a "z-fold stacked" design.

Another important step of cell assembly is **tab welding** which involves joining one or more tabs to the cathode and anode current collectors. These tabs form electrical pathways from the current collectors to the external-facing battery cell terminals. Proper placement and joining of the tabs are essential for ensuring low cell resistance. Popular welding techniques used include ultrasonic welding, resistance welding, and laser welding [23][4]. The tab welding process may occur as part of the winding/stacking process or afterward.

After tab welding, the roll/stack of active material layers needs to be inserted into an enclosure. We can refer to this process as **enclosure insertion** for short. For cylindrical cell formats, the enclosure is a cylindrical can typically made of stainless steel. For pouch cells, the enclosure may be a laminated polymer sheet. In this processing step, precise alignment of the components is essential to avoid internal shorts during cell operation.

At this stage, the active material layers are ready to be soaked with electrolyte in a step called **electrolyte filling**. Here, it is helpful to think of the active material layers as a porous sponge. The uncompressed separator, typically made of polypropylene, is usually 50% porous while the cathode and anode layers are usually 20%-30% porous. In the electrolyte filling step, a nozzle dispenses a pre-set quantity of electrolyte into the enclosure. The electrolyte usually consists of a salt, such as lithium hexafluorophosphate ($LiPF_6$) which is dissolved in

[4]Note that an analogous process happens in battery module and pack manufacturing in which the positive and negative terminals of individual battery cells are joined together in series and parallel. The material joining these battery cells together is also confusingly called current collectors.

an organic solvent that can comprise several different components, the most typical include ethylene carbonate (EC), dimethyl carbonate (DMC), and diethyl carbonate (DEC). Often, a small quantity of electrolyte additive such as fluoroethylene carbonate (FEC) or vinylene carbonate (VC) is added to improve the passivation of the thin film that is formed between the anode and the electrolyte which we will discuss later. The electrolyte is uptaken by the active material layers via a combination of capillary action and the application of vacuum suction.

The electrolyte is essential for enabling the conduction of lithium ions between the electrodes. All parts of the active layers, including the separators, must be fully wetted to ensure full electrochemical utilization of the active materials. The manufacturing challenge of electrolyte filling is thus to efficiently fill all of the pore space of the active layers. Surface properties of each active layer, such as the surface tension with the electrolyte, or "wettability," become essential design parameters for optimal wetting. Recent developments to improve the electrolyte filling process include applying external voltages to induce electric fields inside the active material layers which in turn boost wetting [24].

The last step of cell assembly is **enclosure sealing**. The now-wetted cell needs to be hermetically sealed to prevent the electrolyte and gaseous reaction byproducts during battery operation from escaping the battery cell. The seal also prevents moisture from the atmosphere from entering the cell which is a source of contamination that decreases cell lifetime. The specific steps to enclosure sealing vary by form factor.

2.2.2.3 Cell Finishing

At the end of the cell assembly process, the work of mechanically assembling the cell is complete. However, the cell is not yet ready to be used until a sequence of "finishing" steps, including formation cycling and aging, are completed. We'll briefly review these steps now.

After the electrode active layers come into contact with the electrolyte during the electrolyte filling step, the full cell voltage starts at ca. 0V and needs to be **pre-charge**d, or "tap charged." The goal of this step is to apply a small amount of charge to the cell to raise the voltage to above ca. 1.5V. This step is needed since the anode (negative electrode) is initially at sufficiently high potential vs. Li/Li^+ that the copper current collector may oxidize, releasing copper ions into the electrolyte [25]. Charging the cell above ca. 1.5V decreases the negative electrode potential vs Li/Li^+ below the oxidation potential of copper which mitigates potential issues with copper dissolution. Completion of the pre-charge step ensures that the cells can be stored for longer periods (e.g. days to weeks) to await the formation steps. Longer storage periods are sometimes necessitated due to factory logistics, e.g. if the formation process is bottle-necked, or are intentionally set to give time for the

electrolyte to fully wet the pores of the electrodes.

After pre-charge, cells undergo **formation cycling**. During formation cycling, the cell is externally charged for the very first time to create the SEI at the negative electrode-electrolyte interface [26, 27, 28, 29, 30, 31]. The formation cycling process consists of a sequence of charge and discharge events. A good formation protocol forms a passivating SEI layer which limits further SEI growth over the battery's life. Formation cycling protocols are often proprietary; no industry standards exist.

Formation cycling is followed by **formation aging**, during which the battery cells are stored at high temperatures and high SOCs for days to weeks to continue the SEI growth process and screen for quality defects [14]. The specific conditions for formation aging, including SOC, temperature, and duration, are also dependent on the manufacturer. Note that the term "formation aging" will be used exclusively to refer to the aging process occurring in battery manufacturing, not to be confused with "calendar aging" or "aging tests" which are usually conducted outside of the

At the end of formation aging, the finished cells undergo **end-of-line quality inspection**. The specific measurements performed at the end of the line vary by manufacturer but will often include measurements of open circuit voltage (OCV) and internal resistance [13].

Note that some variants of the cell finishing process may also include a degassing step in which gaseous reaction byproducts that are formed during formation cycling and formation aging steps are ejected out of the cells.

2.3 Formation Challenges

The formation process brings many challenges that make it more difficult to build and operate battery factories. First, the formation process is costly. The formation equipment, which consists of cell cyclers and automation equipment to load and unload cells from the cyclers, is costly to build and operate. Nelson et al. estimated the cost of formation and aging to be ca. 32% of total manufacturing costs, including equipment depreciation, cost of labor, and plant floor space [32]. Second, material handling for formation is difficult because of the long dwell time of cells in formation, which can take up to 1.5 to 3 weeks according to Heimes et al. [13]. While the cells are undergoing formation cycling and aging, more cells are continuously made in cell assembly. These cells must be retained in a buffer zone in the factory to wait for the cells undergoing formation cycling to complete. Lastly, the formation process is energy-intensive. The formation cyclers, of course, need energy to charge the cells. The formation aging process also requires bringing large rooms in the factory up to elevated temperatures and maintaining this temperature continuously. Altogether, the formation process accounts

for ca. 27% of factory energy consumption [33][5]. Battery manufacturing energy consumption has recently come to attention as another source of load on the electricity infrastructure and represents yet another source of greenhouse gas emissions. Degen et al. estimated that today's manufacturing technology consumes 20 to 40 kWh of energy for every 1 kWh of cell production, depending on the cathode material [33].

2.4 Formation Protocols

With conventional formation processes being so time, capital, and energy-intensive, battery manufacturers are motivated to develop faster formation protocols that can help lower manufacturing costs without compromising battery performance, lifetime, and safety.

Faster formation protocols have been demonstrated to be possible. In 2004, Lee et al. proposed a fast formation protocol on lithium cobalt oxide — graphite cells [34]. They demonstrated that formation cycle time can be halved without without affecting the cycle efficiency or cycle life of the batteries. In 2017, An et al. then introduced an "ultra-fast formation protocol" [30, 31] which decreased the formation time by a factor of three compared to a baseline protocol. These authors designed the fast formation protocol to prioritize spending time at higher SOCs which is believed to result in a denser, more passivating SEI [35]. When tested on multi-layer pouch cells, the fast formation protocol showed similar beginning-of-life and cycling characteristics compared to the baseline protocol. In 2019, Rago et al. then demonstrated that the same fast formation protocol was usable for cells containing Si-graphite composite anodes which also showed similar cycling performance compared to the control [36]. In 2021, Ryan et al. independently verified that formation charge rates as high as 2C were feasible without compromising long-term cycle life performance [37]. The cells that underwent 2C charging showed lower initial discharge capacity suggesting more lithium was consumed during the formation cycle. For these cells, the authors found visible lithium plating during a tear-down study following formation. Yet, despite the presence of lithium plating, the cells showed similar thermal abuse behavior as measured via accelerated rate calorimetry (ARC).

The existing literature on formation protocols has thus solidified the notion that formation protocols can be made faster without compromising battery lifetime and safety. A logical question follows: "What is the optimal formation protocol for a given cell system?" Answering this question requires a more principled understanding of the electrochemistry of SEI growth which is at the heart of the formation process.

[5]This number can be calculated using the raw data files from Degen et al. [33] assuming NMC811 chemistry

2.5 The Solid Electrolyte Interphase

2.5.1 Chemistry

The term "solid-electrolyte interphase" (SEI) was first coined by Peled in 1979 to describe a thin surface layer that spontaneously forms between alkali earth metals and an organic electrolyte [38][6]. The usage of the word "interphase" highlights that the interface is formed between a solid phase (the electrode) and a liquid phase (the electrolyte). The simplest analogy for an SEI could be the spontaneous surface reaction of aluminum with atmospheric oxygen to form aluminum oxide:

$$4\mathrm{Al} + 3\mathrm{O_2} \rightarrow \mathrm{Al_2O_3}. \tag{2.1}$$

This reaction creates a thin, insulating (or passivating) film on any aluminum metal exposed to air, explaining aluminum's favorable anti-corrosion properties[7]. Similarly, in a lithium-ion battery, a reaction also occurs at the negative electrode (anode) and electrolyte interphase. A simplified reaction scheme this reaction is given by:

$$\mathrm{S} + n\mathrm{e^-} + n\mathrm{Li^+} \rightarrow \mathrm{SEI} \downarrow + \mathrm{P} \uparrow, \tag{2.2}$$

where S stands in for some component of the battery liquid electrolyte, usually a solvent molecule, SEI is the reaction product, a solid, P is a reaction byproduct, often a gas, and n is the number of participating electrons.

Equation 2.2, though over-simplified, already underscores some key details of SEI formation. First, it depletes the inventory of lithium in the cell. In a full cell, this lithium originates in the positive electrode active material during synthesis and is conserved since the full cell is a closed system[8]. Second, any number of electrolyte components can participate in SEI-forming reactions, either in parallel, in series, or both, making reaction dynamics difficult to characterize and model [39, 28]. The complexity of the electrolyte blend, which includes a lithium salt (e.g. $\mathrm{LiPF_6}$), various solvent species (e.g. DMC, DEC, EC), and electrolyte additive species (e.g. VC, FEC), is necessitated by the fact that the electrolyte system needs to solve for several performance characteristics simultaneously: it must achieve

[6] Peled originally referred to these systems as "nonaqueous systems" but the battery community today would simply call this "electrolyte" for short with the understanding that most common liquid electrolyte batteries require an organic electrolyte.

[7] It is also why, when you are trying to use a multimeter to measure the resistance of aluminum, you have to "dig" a little with the probes to get past the insulating oxide later and get a good reading.

[8] Solvated lithium ions in the electrolyte are not considered to be part of the inventory of cyclable lithium since ions cannot be added to the pool of cyclable lithium without violating charge conservation.

good SEI passivation while maintaining favorable ionic conductivity at a wide range of operating temperatures, it must have favorable thermal runaway characteristics, and it must be affordable for mass-production [40, 41, 28, 42, 43].

Finally, the SEI film, being highly reactive, is also difficult to study experimentally. It was only within the last several years that advanced materials characterization methods have enabled researchers to glean into the SEI-forming process [44, 45, 46, 47].

2.5.2 Models

The complexity of the SEI formation process has not impeded attempts by researchers to model the SEI formation process using a number of methods (Figure 2.3). These methods include atomistic-scale simulations [48], continuum-based methods [49, 27, 50, 51, 52, 53, 54], multi-scale methods [39], equivalent-circuit models [55], and reduced-order methods [56, 57, 58, 59, 60, 61, 62]. All of these methods can be roughly understood as falling under the categories shown in Figure 2.3.

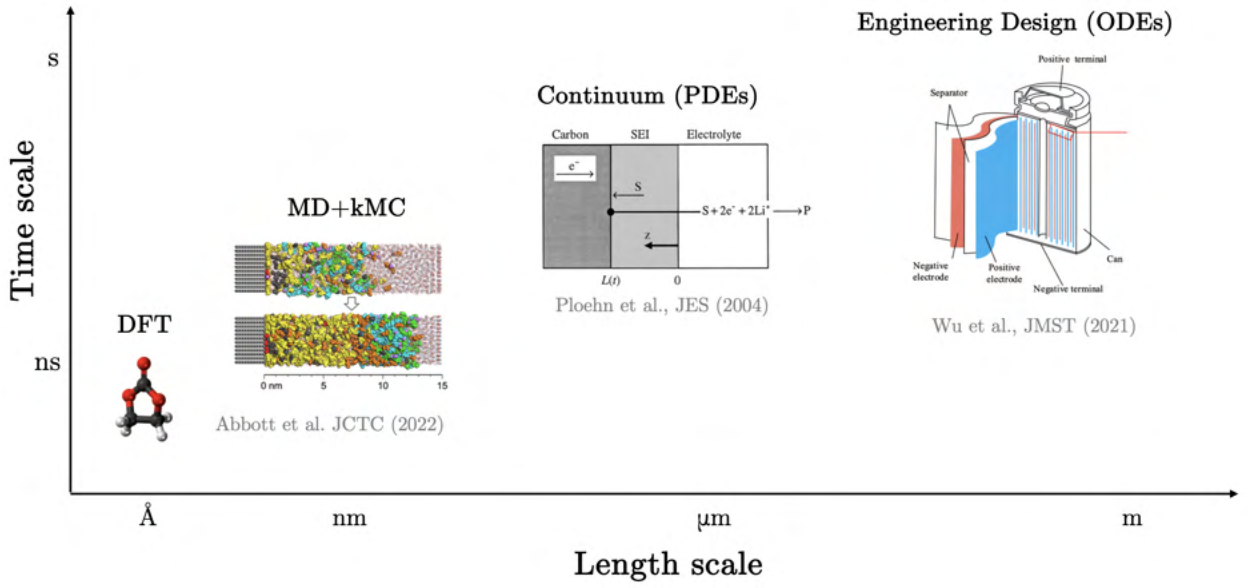

Figure 2.3: Comparison of different SEI modeling approaches, including atomistic approaches leveraging density functional theory (DFT), molecular dynamics (MD) and kinetic Monte Carlo (kMC) methods, continuum-level formulations (including reduced-order models), and models compatible with the engineering design of full cell systems. Images for the various plot elements have been adapted from Abbott et al. [63], Ploehn et al. [50] and Wu et al. [45].

We now pay particular attention to reduced-order continuum models from which the work from Chapter 3 is based. These reduced-order models typically represent the SEI with one

spatial dimension and describe the SEI formation process using "classical" electrochemical processes including the usage of Butler-Volmer kinetics to describe the charge transfer process and Fick's law for modeling solvent diffusion. In particular, Ramadass et al. [64] proposed a kinetically-controlled reaction scheme while Ploehn et al. [50] suggested that solvent diffusion through the existing SEI layer must be a rate-limiting step. Later, Safari et al. [57] combined the two limiting mechanisms in what was referred to as "mixed mode control." More recently, Yang et al. implemented SEI reaction dynamics in the context of a single particle model (SPM) and also included lithium metal deposition, or lithium plating, as a competing reaction pathway [65].

Figure 2.4, adapted from the work of Yang et al. [65] and Pinson et al. [27], summarizes the canonical reaction pathways that Chapter 3 will develop. The figure highlights the charging process in which neutral lithium de-inserts, or deintercalates, from the positive electrode, releasing an electron in the process to be collected by the current collector:

$$\mathrm{LiM} \rightarrow \mathrm{Li}_y\mathrm{M} + (1-y)\mathrm{Li}^+ + (1-y)\mathrm{e}^- \qquad (\mathrm{Positive, charging}) \tag{2.3}$$

where M stands in for a metal host structure and y is the lithium mole fraction, or stoichiometry, inside the host structure. This half-cell reaction occurring at the positive electrode must be balanced by a complimentary half-cell reaction at the negative electrode to preserve charge neutrality in the electrolyte. The desired reaction pathway, indicated by path 2, involves the insertion, or intercalation, of atomic lithium into the graphite host material:

$$x\mathrm{Li}^+ + x\mathrm{e}^- + \mathrm{C}_6 \rightarrow \mathrm{Li}_x\mathrm{C}_6 \qquad (\mathrm{Negative, charging}) \tag{2.4}$$

where C stands for carbon and x is the lithium stoichiometry in graphite. However, two other competing pathways can also occur: SEI growth (pathway 1) and lithium metal deposition (pathway 3). The dynamics of SEI growth forms the subject of Chapter 3. Lithium metal deposition is understood to occur when the negative electrode surface potential drops below 0V vs $\mathrm{Li/Li}^+$[9]. The lithium metal deposition process is included in this diagram for completeness but will not be further studied as part of this thesis.

Figure 2.4 was finally designed to highlight an element of SEI modeling that has thus far been missing from most literature, which is the treatment of the lithium-ion battery full cell as a closed system. Such a treatment is necessary to understand the dynamics of the full cell which makes up the battery formation process. In a full cell, the total inventory

[9]This common assumption has been recently challenged by compelling experimental results suggesting that lithium surface concentration, not surface potential, is the main thermodynamic driving factor for lithium metal deposition on the surface of graphite [66].

of cyclable lithium is finite and is determined by the capacity of lithium in the positive electrode. Modeling the exchange of cyclable lithium between the electrodes alongside the SEI reaction dynamics will thus enable a more complete perspective of the battery formation process as we will demonstrate in Chapter 3.

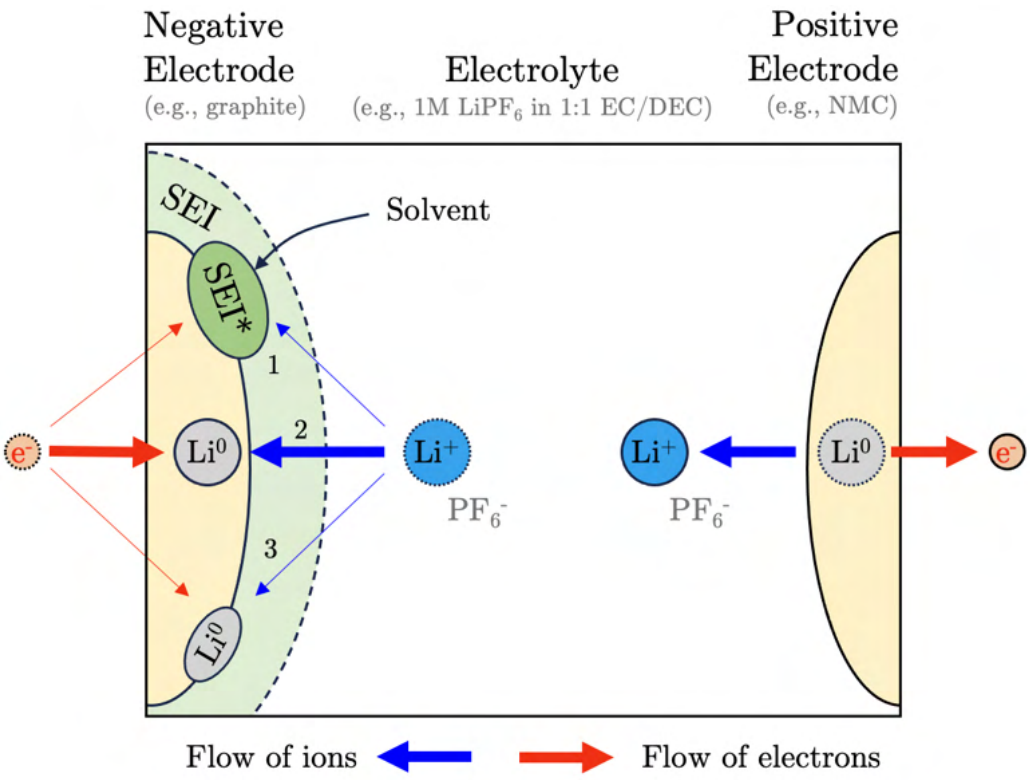

Figure 2.4: Principles of lithium-ion battery operation from the perspective of SEI formation during the first charge. Three reaction pathways are shown: (1) Lithium reacting with a solvent to form new SEI, (2) Lithium intercalating into the graphite electrode, and (3) Lithium metal deposition at the surface of the negative electrode.

2.6 Diagnostic Features

Voltage and current data from the battery formation process can be continuously and automatically collected, stored, and analyzed to develop smarter manufacturing process specifications or tolerances, ensuring that all cells leaving the factory have a guarantee on performance, lifetime, and safety [14]. Using voltage-based measurements is also appealing from a manufacturing standpoint since they can be measured using existing formation cyclers. This data may be directly collected as part of the formation protocol or immediately after the formation protocol completes but before the cells are taken off of the formation cyclers [7].

Thus, collecting voltage-based data bears no additional capital costs to a factory. Since the number of formation cyclers grows with the production volume, the voltage-based metrics will also naturally scale as factory throughput increases.

When full cell voltage data is carefully collected and analyzed, they can be used to derive physically-interpretable, electrochemical diagnostic features that provide insights into the thermodynamic and kinetic properties of the cell. A slow-rate (C/20) full-cell voltage curve can, for example, be analyzed using incremental capacity analysis (ICA) [67] or differential voltage (dV/dQ) analysis [68, 69] to understand thermodynamic quantities such as active material losses and lithium inventory losses. The data can be collected immediately after the formation cycles are complete. Unlike cell dissections and electrode harvesting, voltage-based analysis is non-destructive. The same cell that is analyzed in manufacturing can thus be tracked throughout its remaining life, either through accelerated cycle life testing in a lab or through fleet telemetry of real-world usage inside of an EV. The ability to establish an electrochemical "fingerprint" on the pristine cells immediately after manufacturing can help improve lifetime prediction models as we will demonstrate in Chapter 6.

Currently, battery factories may not be taking full advantage of voltage-based measurements at the end of line, partly owing to difficulties in data interpretation. Resolving the complex electrochemical details using full-cell voltage data alone is inherently challenging since these measurements reflect a combination of thermodynamic and kinetic factors originating from nearly every cell component and their interactions with each other. These inherent difficulties are compounded by a general lack of clear literature guidance on best practices for collecting and analyzing voltage data. As a result, commonly reported electrochemical metrics derived from voltage data, such as modeled electrode capacities from dV/dQ analysis often differ in both data collection and analysis methods, limiting their interpretability and reproducibility. Without careful data collection and interpretation, manufacturing tolerances may be set too tightly, increasing reject rates and lowering production throughput, or too loosely, which may increase production throughput in the short term but lead to lifetime and safety issues after years of usage in the field. The nuances of data collection and interpretation are further discussed as part of Chapter 5.

We note that voltage-based electrochemical features do not replace the need for more advanced end-of-line metrology methods in the factory, including X-ray [70, 71] and ultrasonic imaging [72, 73], which may be necessary for catching non-electrochemical related cell defects. Rather, the voltage-based features complement root-cause analyses by providing crucial measures of the system such as the as-manufactured electrode capacities, cyclable lithium inventory, and negative-to-positive ratio (NPR).

CHAPTER 3

Electrochemical Model of Battery Formation

3.1 Abstract

This chapter proposes a physics-based electrochemical model for the SEI growth process during the early stages of lithium-ion battery formation cycling and formation aging. By combining a full-cell model that tracks half-cell equilibrium potentials, a zero-dimensional model of SEI growth kinetics, and a semi-empirical description of cell thickness expansion, the resulting model replicated experimental trends measured on a 2.5 Ah pouch cell, including the calculated first-cycle efficiency, measured cell thickness changes, and electrolyte reduction peaks during the first charge dQ/dV signal. This chapter also introduces an SEI growth boosting formalism that enables a unified description of SEI growth during both cycling and aging. This feature can enable future applications for modeling path-dependent aging over a cell's life. The model further provides a homogenized representation of multiple SEI reactions enabling the study of both solvent and additive consumption during formation. This work bridges the gap between electrochemical descriptions of SEI growth and applications towards improving industrial battery manufacturing process control where battery formation is an essential but time-consuming final step. We envision that the formation model can be used to predict the impact of formation protocols and electrolyte systems on SEI passivation and resulting battery lifetime.

3.2 A Phenomenological Basis for Formation Modeling

Despite the microscopic complexities of SEI growth, the battery formation process for commercial-scale cells yields electrochemical signals that can be directly measured using standard equipment during formation cycling. Figure 3.1 shows example data collected on a 2.5 Ah pouch cell (Panel B) that underwent three formation charge-discharge cycles, followed by reference performance test (RPT)s, followed by formation aging (see Section 3.4.1

for more experimental details). This dataset can be directly used to calculate the coulombic efficiency (CE), according to:

$$\mathrm{CE}_i = \frac{Q_{\mathrm{d},i}}{Q_{\mathrm{c},i}}, \tag{3.1}$$

where $Q_{\mathrm{d},i}$ and $Q_{\mathrm{c},i}$ are the discharge and charge capacities of the ith cycle, calculated via current integration. The CE of the first cycle, also known as the first cycle efficiency (FCE), is characteristically lower than the CE for all subsequent cycles owing to the rapid consumption of lithium during the first charge cycle to form the SEI.

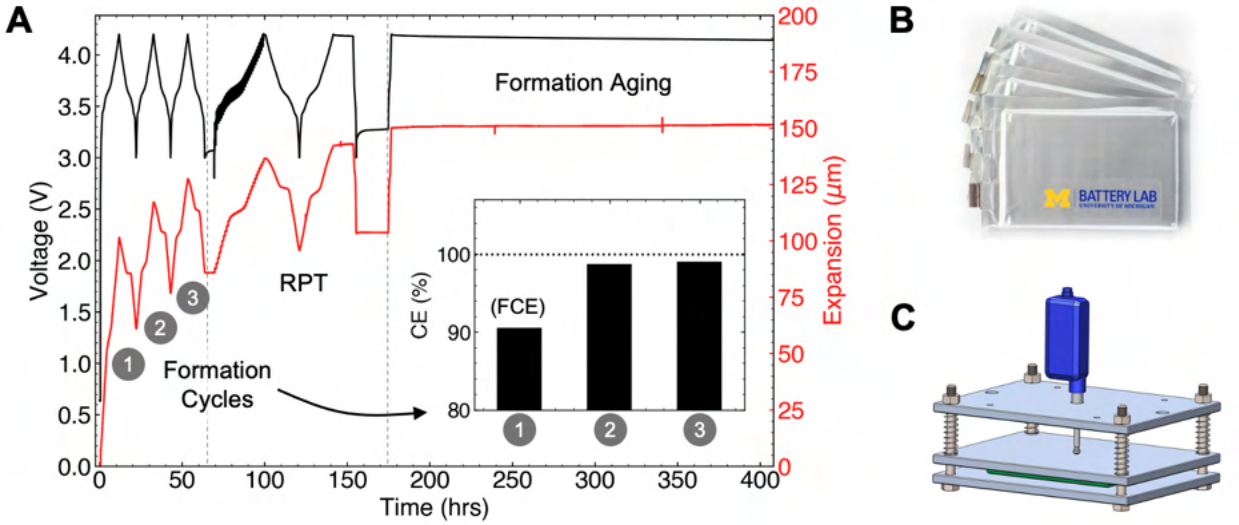

Figure 3.1: Experimentally-measurable signals from the battery formation and aging process. (A) Electrochemical (voltage and current) signal is shown in black. These signals are obtainable directly from the equipment used for battery formation cycling. Cell thickness expansion is shown in red. (B) Example image of the multi-layer stacked pouch cells similar to the one used for this work. (C) An expansion fixture instrumented with a linear displacement sensor enabling real-time cell thickness expansion during the formation process.

For pouch cell form factors, thickness expansion can also be directly measured using a sensor fixture shown in Figure 3.1C [74, 75, 11]. The measurements suggest that total cell expansion can be attributed to two distinct sources. The first source is due to changes in the lithium content (or stoichiometry) in the positive and negative electrode particles. During lithiation, the particles swell, and during delithiation, the particles contract. Since this process is reversible, we will refer to this source as "reversible expansion." The reversible expansion tracks closely to the measured cell voltage, or SOC, which determines the lithium content in either electrode. The second source of expansion can be noticed from the *minimum expansion* at the end of every discharge cycle. This expansion appears to always increase

over cycles. We will thus refer to this expansion source as "irreversible expansion" [43, 75]. The irreversible expansion is attributed to the growth of the SEI layer during formation and aging. Consistent with the CE data, the irreversible expansion is high during the first cycle, but then slows down over the next two cycles. During formation aging, the irreversible expansion rate appears to decrease, indicating a possibly slower SEI growth process compared to cycling.

3.3 Main Contributions

This work presents a semi-empirical modeling framework describing the SEI growth process during battery formation cycling and formation aging. The model builds on established electrochemical descriptions of SEI growth which uses Butler-Volmer kinetics to describe the SEI-forming solvent reduction process [64, 76, 57, 77] and linearized Fick's law to describe solvent diffusion [50, 78, 27, 58]. To model cell expansion, a semi-empirical approach is taken which draws from existing literature [79, 80, 74, 81, 82, 83], but separates the reversible and irreversible expansion contributions to the total expansion. Since we aim to develop a reduced-order description of SEI growth that can be deployed in a battery manufacturing context, our modeling approach does not explicitly consider spatial variations in the SEI layer [49, 84, 85, 86] or competing reaction pathways [39]. However, as will be demonstrated, a reduced-order, zero-dimensional model can accurately capture macroscopic, observed trends during both formation cycling and formation aging shown in Figure 3.1, including CE, expansion, and first cycle dQ/dV peaks indicating electrolyte reduction processes.

Our model introduces three extensions to the existing literature on zero-dimensional SEI growth models. First, we introduce a semi-empirical model of macroscopic thickness expansion of the battery, accounting for both the reversible expansion due to lithium intercalation reactions as well as the irreversible expansion due to SEI growth (see Section 3.5.6). Second, we introduce a mathematical formalism to describe "boosted SEI growth" during charging (see Section 3.5.7). This model extension unifies the description of SEI growth and cell expansion during cycling, which is fast, and during calendar aging, which is slow. Finally, we introduce a homogenized, multi-species representation of the SEI growth process, enabling the prediction of volume-averaged SEI film properties under multiple reacting species (see Section 3.5.8). This model extension enables a description of solvent consumption and additive consumption as two parallel and coupled processes which combine to create a composite SEI film with a volume-averaged film diffusivity.

The formation model we develop resolves the dynamics of lithium consumption and cell

expansion during formation cycling and formation aging. The same model can be applied to track lithium inventory loss over the remaining life of the cell, including during cyclic aging and calendar aging. By explicitly considering multiple electrolyte reduction reactions during the first cycle, the model also provides a pathway for future studies on how formation protocols influence SEI passivation properties [35] and their consequences on battery lifetime.

3.4 Experimental Methods

Figure 3.1 summarizes the experimental data collected for this work. This dataset defines a basic set of macroscopic observations that the formation model will seek to capture. The experiment consists of three parts: (1) formation cycling, (2) RPTs, and (3) formation aging at 100% SOC. The proceeding sections describe the cell build process in relation to the formation cycling and formation aging experiments shown in Figure 3.1A.

3.4.1 Cell Build

Experimental data was collected on a 2.5Ah, multi-layer stacked pouch cell (Figure 3.1B). The cell was built on a prototype cell manufacturing line using a process similar to the one outlined in Weng et al. [7]. The cell consisted of a single-crystal $Ni_{0.6}Mn_{0.2}Co_{0.2}$ (NMC622) positive electrode (Targray) and a graphite negative electrode (Superior SLC, 1520-T), based on the available stock. A standard electrolyte formulation was used (SoulBrain PuriEL R&D 326), which consisted of EC and ethyl methyl carbonate (EMC) in a 3:7 weight ratio, 1.0M $LiPF_6$ and 2 wt% VC additive. The cell stack consisted of 7 double-sided positive electrode layers and 8 double-sided negative electrode layers, resulting in 14 active unit cells along the pouch cell thickness direction. The positive electrode formulation consisted of NMC622:C65:PVDF (94:3:3), where C65 and PVDF are binder materials. The negative electrode consisted of graphite:CMC:SBR (97:1.5:1.5), where CMC and SBR are binder materials. Positive (negative) electrode single-sided loadings were 17.2 (9.7) mg/cm^2 and with porosity targets of 30% (20%). The negative-to-positive capacity ratio was targeted to be 1.1.

3.4.2 Electrolyte Filling and Cell Fixture

After electrolyte filling and enclosure sealing, cells were loaded in a custom-built pressure fixture shown in Figure 3.1C. The pressure fixture was developed based on work by Mohtat et al. [74]. The fixture applied 5 psi of compression via a spring-loaded plate. To minimize copper dissolution at high negative electrode potentials immediately after electrolyte filling

[87], the cell was tap-charged to 2.8V at a C/3 charge rate. The cell was subsequently left overnight to ensure the electrodes were completely wetted before formation charging.

3.4.3 Formation Cycling and Formation Aging

Formation cycling was conducted while the cell/fixture assembly was placed in a temperature-controlled oven set to 45°C. The fixture maintained a pressure of 5 psi throughout formation cycling and formation aging. For formation cycling, the cell was charged and discharged using an Arbin BT2000 system.

The formation protocol consisted of three back-to-back constant current (CC) charge-discharge cycles at a rate of C/10. Each charge terminated when the cell reached 4.2V, followed by a constant voltage (CV) hold step with a C/20 current cut-off. Each discharge terminated when the cell reached 3.0V without CV holding. No rest periods were included between each charge and discharge.

Formation cycling was followed by RPT, which included a pulse charge-discharge sequence for calculating cell resistances and C/20 charge-discharge voltage curves for dV/dQ analysis [7]. The details and contents of the RPT are not immediately relevant to this work, but the RPT data has been presented here to preserve data continuity with the subsequent experimental step.

After the RPT, the cell was charged to 100% SOC to undergo formation aging at 45°C. The goal of this step was to ensure SEI passivation and to screen for quality defects [14]. This aging step lasted for 14 days. After aging, the cell was finally discharged. Note that Figure 3.1A only shows the first 10 days of the 14-day aging protocol for brevity.

3.4.4 Expansion Measurements

Thickness expansion of the cell was measured using a linear displacement sensor (Keyence GT2 series) mounted to the fixture (Figure 3.1C). Expansion data was logged in real-time using a data acquisition system (LabVIEW) throughout the entire experiment. The expansion data was combined with the electrical signals during post-processing.

3.5 Model Derivation

3.5.1 Model Assumptions

Figure 3.2 shows the canonical reaction pathways for SEI formation [27, 88] assumed for this work. The general SEI reaction is represented by:

$$n\mathrm{Li}^+ + n\mathrm{e}^- + S \rightarrow \mathrm{SEI}\downarrow + P\uparrow, \tag{3.2}$$

where S represents a solvent molecule, n is the number of participating electrons, 'SEI' stands for the newly-formed solid reduction product, and P denotes some reaction byproduct, usually a gas [89]. Candidate solvent molecules include EC and DEC. Note that S can also represent electrolyte additives such as VC.

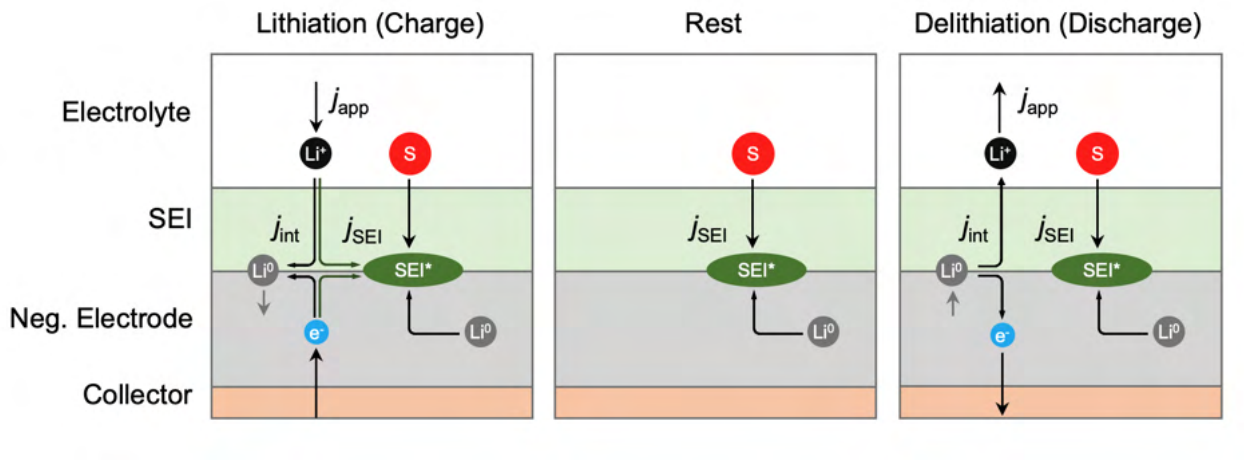

Figure 3.2: Consolidated SEI reaction pathways during charging, discharging, and rest. S: solvent molecule, e.g. ethylene carbonate (EC) or vinylene carbonate (VC). SEI*: newly SEI formed at the electrode-SEI interface. Li^+: solvated lithium ions from the electrolyte. Li^0: neutral lithium intercalated into the negative electrode.

To build a model of SEI growth during both formation cycling and formation aging, SEI reaction pathways occurring during full cell charging, discharging, and rest, need to be consolidated. Doing so enables the same modeling framework to simulate both cycling and calendar aging after formation completes. The reaction formulation we chose, summarized by Attia et al. [88], considers two distinct SEI reaction modes, termed 'electrochemical' SEI growth, which occurs in the presence of external current (i.e. during charge and discharge), and 'chemical' SEI growth, which always occurs. Both SEI growth mechanisms share the same general reaction scheme described by Eq. 3.2, but only differ by the source of lithium.

In 'electrochemical' SEI growth, the external current drives solvated lithium ions from the electrolyte towards the reaction interface. In 'chemical' SEI growth, intercalated lithium from the negative electrode migrates to the reaction interface. These reaction modes will be unified by the model formulation presented in Section 3.5.4.

Further general modeling assumptions are listed below:

- *Reaction interface.* The SEI-forming reaction takes place exclusively at the electrode-SEI interphase [27].
- *Rate-limiting mechanisms.* The SEI reaction rate is determined by two processes: (1) interfacial reaction kinetics according to Butler-Volmer kinetics, and (2) diffusion-limited solvent transport through a porous SEI. No other rate-limiting mechanisms such as electron conduction [84] are considered.
- *Idealized degradation.* SEI reaction at the negative electrode is the only source of full cell capacity loss. Considerations for other degradation modes, such as thermal SEI decomposition [88], lithium plating [37], active material degradation (e.g. cathode phase transformations [90], particle cracking [91], binder delamination [92]), and positive electrode side-reactions [93, 94], are left for future work.
- *Irreversibility.* SEI reactions are irreversible.
- *No gas formation.* Gas-forming reaction dynamics [89] are ignored and left for future work.
- *No cross-talk.* Cross-reactions between different electrolyte components are left as future model extensions.

3.5.2 Electrode Potentials and Lithium Stoichiometries

A reduced-order full-cell model was used as a starting point for this work, shown in Figure 3.3. In this model, the negative electrode equilibrium surface potential, U^-, provides the thermodynamic basis for SEI-forming reactions. However, U^- is not directly controllable or observable during the formation process in commercial devices. Rather, the terminal voltage, V_t, is observed and controlled. A practical model of battery formation therefore requires a description of V_t, written as:

$$V_\mathrm{t} = U^+(\theta^+) - U^-(\theta^-) + \eta^+ + \eta^-, \tag{3.3}$$

where U^+ is the positive electrode equilibrium surface potential, θ^+ and θ^- are the lithium stoichiometries at the electrode surfaces, and η^+ and η^- are electrode overpotentials. U^- and U^+ are described by empirical functions such as the ones shown in Figure 3.3B. The lithium stoichiometries are defined by:

$$\theta^+ = c^{\mathrm{s}}_{\mathrm{s,p}}/c^{\max}_{\mathrm{s,p}} \tag{3.4}$$

$$\theta^- = c^{\mathrm{s}}_{\mathrm{s,n}}/c^{\max}_{\mathrm{s,n}}, \tag{3.5}$$

where $c^{\mathrm{s}}_{\mathrm{s,p}}$ ($c^{\mathrm{s}}_{\mathrm{s,n}}$) is the lithium concentration at the surface of the positive (negative) electrode, and $c^{\max}_{\mathrm{s,p}}$ ($c^{\max}_{\mathrm{s,n}}$) is the maximum lithium concentration of the positive (negative) electrode. Finding the lithium surface concentrations will typically require solving the spherical diffusion equation [95]. Here, we simplify the representation by assuming that the current density is sufficiently low such that the solid-phase concentration gradient is approximately zero, hence $c^{\mathrm{s}}_{\mathrm{s,i}} \approx c^{\mathrm{avg}}_{\mathrm{s,i}}$. Hence, the lithium stoichiometries can be directly updated via Coulomb counting the intercalation current:

$$\frac{d\theta^+(t)}{dt} = -\frac{I_{\mathrm{app}}(t)}{Q^+} \tag{3.6}$$

$$\frac{d\theta^-(t)}{dt} = +\frac{I_{\mathrm{int}}(t)}{Q^-}, \tag{3.7}$$

where θ^+ and θ^- are the average lithium stoichiometries, Q^+ and Q^- are the total electrode capacities corresponding to $c^{\max}_{\mathrm{s,p}}$ and $c^{\max}_{\mathrm{s,n}}$, respectively, I_{app} is the applied current into the full cell, and I_{int} is the intercalation current at the negative electrode. We take the convention that $I_{\mathrm{app}} > 0$ when the cell is charged. Similarly, $I_{\mathrm{int}} > 0$ corresponds to lithium intercalation into the negative electrode. At the positive electrode, the intercalation current and the applied current are equal since our model assumed no side reactions at the positive electrode. At the negative electrode, the applied current is split between the intercalation current and the SEI reaction current, and only the intercalation current contributes to updating the lithium stoichiometry in the negative electrode. Overall, Eqs. 3.6 and 3.7 amount to a zero-dimensional, 'dual-tank' representation of lithium stoichiometries at each electrode, providing a basis for tracking reaction potentials and expansions at each electrode (Figure 3.3B).

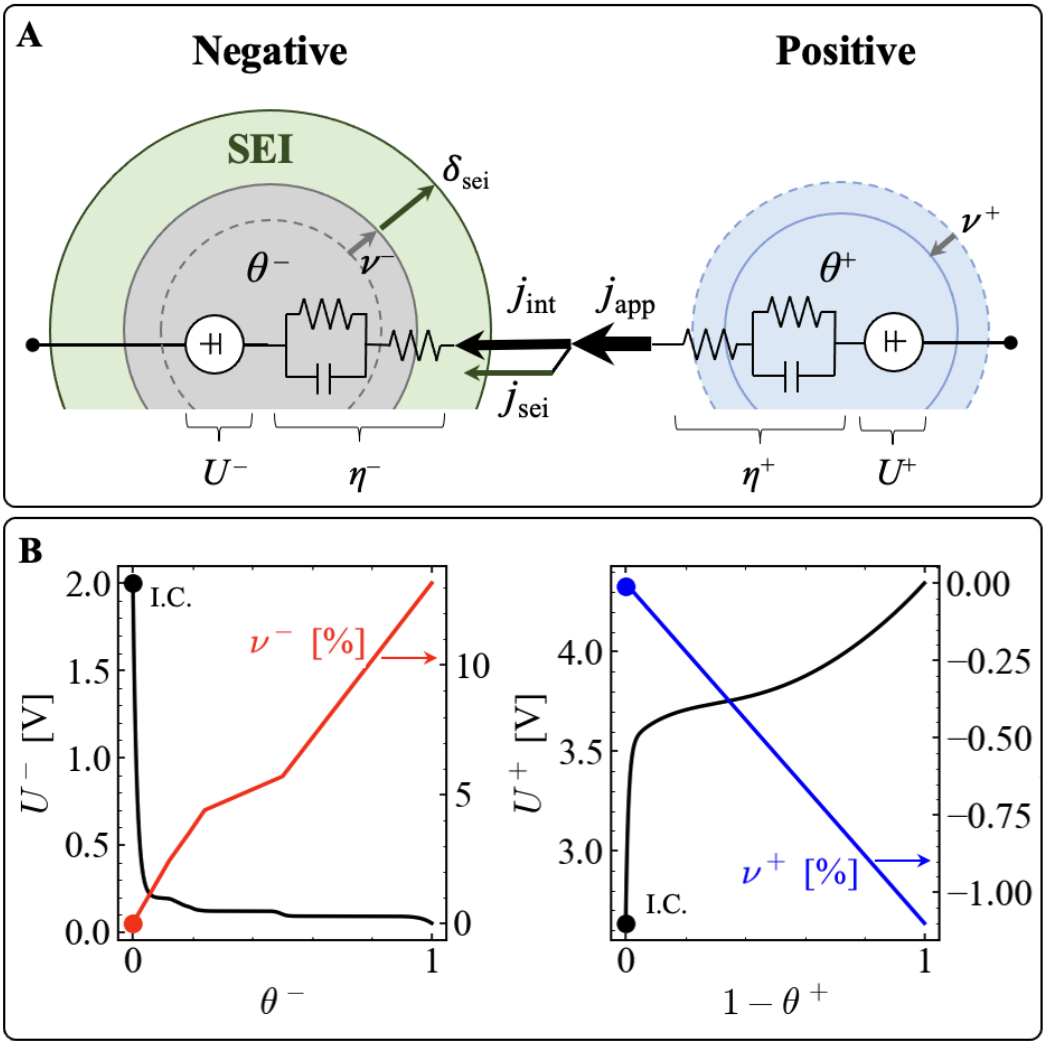

Figure 3.3: Zero-dimensional 'dual-tank' formation modeling framework. (A) Model components and key state variables. At each electrode $i = (+, -)$, the lithium stoichiometry $\theta^{\pm}$ is tracked and used to update the electrode equilibrium surface potentials $U^{\pm}$ and volumetric expansions $\nu^{\pm}$. Electrode surface overpotentials are represented by R-RC elements which capture both charge-transfer and solid-state diffusion dynamics. The total applied current density j_{app} passes through the positive electrode. However, at the negative electrode, the current is split between the intercalation current density j_{int} and the SEI current density j_{sei}. SEI build-up leads to SEI thickness growth, denoted by δ_{sei}. (B) Electrode equilibrium potential functions and volumetric expansion functions assumed for this work, adapted from Mohtat et al. [74]. The markers indicate the initial conditions (I.C.s) corresponding to the state of the cell before formation begins.

3.5.3 Electrode Overpotentials

The electrode surface overpotentials are governed by charge-transfer kinetics at the electrode-electrolyte interface and solid-state diffusion dynamics. Our work reduces the overpotential dynamics using a first-order representation as follows:

$$\eta^{\pm}(t) = R^{\pm}_{\text{ct}} I_{\text{app}}(t) + R^{\pm}_{\text{dif}} I^{\pm}_{\text{dif}}(t), \tag{3.8}$$

where the superscript indicates the positive (+) or negative (−) electrode, $\eta^{\pm}$ is the overpotential, $R^{\pm}_{\text{ct}}$ is a lumped resistance term that includes both series and charge-transfer resistance, $R^{\pm}_{\text{dif}}$ represents solid-state diffusion resistance, and $I^{\pm}_{\text{dif}}$ follows first-order dynamics given by [96]:

$$\frac{dI^{\pm}_{\text{dif}}(t)}{dt} = -\frac{1}{\tau^{\pm}_{\text{dif}}} I^{\pm}_{\text{dif}}(t) + \frac{1}{\tau^{\pm}_{\text{dif}}} I_{\text{app}}(t), \tag{3.9}$$

where $\tau^{\pm}_{\text{dif}}$ is the diffusion time constant. Note that Eqs. 3.8 and 3.9 are identical to the equations for an R-RC equivalent circuit model.

The negative electrode reaction potential, η^{-}, will play a role in determining the SEI reaction kinetics at the negative electrode-electrolyte interphase, which will be detailed in the next section.

3.5.4 SEI Reaction Kinetics

Since our experimental data uses EC as a solvent, we will describe our representation of SEI reaction kinetics in the context of EC reduction for convenience. However, it is to be understood that the formulation described here can apply to any SEI reaction that follows Eq. 3.2. A canonical EC reduction reaction pathway proceeds according to [97, 98]:

$$2\text{EC} + 2\text{e}^{-} + 2\text{Li}^{+} \rightarrow \text{LEDC} \downarrow + \text{C}_2\text{H}_4 \uparrow, \tag{3.10}$$

where LEDC is lithium ethylene dicarbonate, the solid reaction product considered to be the SEI [99], and C_2H_4 is ethylene gas. The SEI reaction current density is assumed to take a Tafel-like form [57]:

$$j_{\text{sei}} = nFk_{\text{sei}} c^{\text{s}}_{\text{EC}} \exp\left(-\frac{\alpha n F}{RT}\eta_{\text{sei}}\right), \tag{3.11}$$

where k_{sei} is the reaction rate constant, c^{s}_{EC} is the concentration of solvent molecules at the reaction surface, α is the symmetry factor, and η_{sei} is the SEI reaction overpotential. n is the number of electrons involved in the reaction. For the EC reaction, $n = 2$. In the

Doyle-Fuller-Newman model, η_{sei} is determined by [100, 56]:

$$\eta_{\text{sei}} = \phi_{\text{s,n}} - \phi_{\text{e}} - U_{\text{sei}} - j_{\text{app}} R_{\text{sei}} \delta_{\text{sei}}, \tag{3.12}$$

where $\phi_{\text{s,n}}$ is the electrode surface potential, ϕ_{e} is the electrolyte potential, U_{sei} is the SEI reaction potential, R_{sei} is the SEI resistivity, and δ_{sei} is the SEI thickness. Note that $\phi_{\text{s,n}}$ and ϕ_{e} do not explicitly appear in our formulation due to our simplified model representation. To then define η^- in our system, we notice that [100, 56]:

$$\eta^- = \phi_{\text{s,n}} - \phi_{\text{e}} - U^-(\theta^-) - j_{\text{app}} R_{\text{sei}} \delta_{\text{sei}}, \tag{3.13}$$

which can be substituted into Eq. 3.12 to yield:

$$\eta_{\text{sei}} = \eta^- + U^-(\theta^-) - U_{\text{sei}}. \tag{3.14}$$

Eq. 3.14 is now directly solvable, since η^- is provided for by Eq. 3.8. Note that this representation of η_{sei} does not explicitly represent the SEI resistivity R_{sei}. However, this is easily remedied by lumping R_{sei} into R_{ct}^- in Eq. 3.8.

Solvent transport limitations through the SEI is modeled using a linearized Fick's law which takes the form [101, 56]:

$$D_{\text{sei}} \frac{c_{\text{EC}}^{\text{s}} - c_{\text{EC}}^0}{\delta_{\text{sei}}} = \frac{j_{\text{sei}}}{nF}, \tag{3.15}$$

where D_{sei} is the effective diffusivity of the SEI and c_{EC}^0 is the concentration of solvent molecules in the bulk electrolyte phase. Reniers et al. combined Eqs. 3.11 and 3.15 into a more explicit representation of the reaction and diffusion-limited processes by eliminating c_{EC}^{s} from the equations, yielding [78, 102]:

$$j_{\text{sei}} = \frac{-c_{\text{EC}}^0}{1/(nFk_{\text{sei}} \exp(-\alpha nF\eta_{\text{sei}}/RT)) + \delta_{\text{sei}}/(D_{\text{sei}} nF)}. \tag{3.16}$$

We further rewrite Eq. 3.16 in terms of two limiting currents:

$$\frac{1}{j_{\text{sei}}} = \frac{1}{\tilde{j}_{\text{rxn}}} + \frac{1}{\tilde{j}_{\text{dif}}}, \tag{3.17}$$

with:

$$\tilde{j}_{\text{rxn}} \triangleq nFk_{\text{sei}}c^0_{\text{EC}} \exp\left(-\frac{\alpha nF}{RT}\eta_{\text{sei}}\right) \tag{3.18}$$

$$\tilde{j}_{\text{dif}} \triangleq \frac{nFD_{\text{sei}}c^0_{\text{EC}}}{\delta_{\text{sei}}}. \tag{3.19}$$

Eq. 3.18 represents the reaction-limited SEI current in the absence of diffusion limitations ($c^{\text{s}}_{\text{EC}} = c^0_{\text{EC}}$) while Eq. 3.19 represents the diffusion-limited SEI current in the absence of reaction limitations ($c^{\text{s}}_{\text{EC}} = 0$). Eq. 3.17 thus highlights that the SEI current is the harmonic mean of two limiting currents. The slower of the two processes limits the overall flow of SEI current.

The SEI current density can be converted to total SEI current by:

$$I_{\text{sei}} = a^- A^- L^- j_{\text{sei}}, \tag{3.20}$$

where a^- is the specific surface area (i.e. surface-to-area volume ratio) of the negative electrode, A^- is the geometric area of the negative electrode, and L^- is the geometric thickness of the negative electrode. The SEI current can then be directly integrated to yield the total capacity of lithium lost to SEI-forming reactions:

$$Q_{\text{sei}} = \int I_{\text{sei}}(t)\mathrm{d}t. \tag{3.21}$$

Current conservation can finally be used to solve for the total lithium intercalation current:

$$I_{\text{int}} = I_{\text{app}} - I_{\text{sei}}. \tag{3.22}$$

Eq 3.22 unifies the SEI reactions during charging, discharging, and resting, according to the reaction scheme proposed in Figure 3.2. During charging, I_{app} is positive and is split between I_{int} and I_{sei} which are both positive. During discharging, I_{app} and I_{int} are both negative, but I_{sei} remains positive since the SEI reaction is irreversible. During rest, $I_{\text{app}} = 0$ so $I_{\text{int}} = -I_{\text{sei}}$, consistent with the scheme that lithium deintercalation from the negative electrode drives the SEI reaction during rest. In all cases, Eqs. 3.17 and 3.22 provide a consistent framework for capture the SEI reaction dynamics.

3.5.5 Solvent Consumption

As SEI grows, solvent molecules are consumed according to Eq. 3.2, decreasing the bulk solvent concentration. The solvent consumption process can be described by:

$$\frac{dc_{\mathrm{EC}}^{0}}{dt} = \frac{a^{-} j_{\mathrm{sei}}}{nF}. \tag{3.23}$$

As solvent is consumed, j_{sei} is further decreased according to Eq. 3.16. The solvent depletion process is thus self-limiting.

3.5.6 Expansion Modeling

The goals of developing an expansion model are three-fold. First, an expansion model enables the prediction of macroscopic expansion trends during formation cycling and formation aging seen in Figure 3.1, which could then be extended to predict expansion over the remaining lifetime of the cell. Second, the predicted expansion dynamics can lead to deeper insights into the formation process since SEI growth and irreversible cell expansion are linked. Finally, an expansion model fit to experimental expansion data enables a richer dataset for model parameterization.

This work proposes a phenomenological representation of the total cell thickness expansion, Δ_{tot}, of the form:

$$\Delta_{\mathrm{tot}}(t) = \Delta_{\mathrm{sei}}(t) + \Delta_{\mathrm{rev}}(t). \tag{3.24}$$

The first term in Eq. 3.24 represents the irreversible cell thickness expansion due to SEI film growth and is given by:

$$\Delta_{\mathrm{sei}}(t) = \frac{N_{\mathrm{layers}} L^{-}}{R^{-}(1 + \nu^{-}(\theta^{-}(t))/3)} \delta_{\mathrm{sei}}(t), \tag{3.25}$$

where δ_{sei} is SEI film thickness at a negative electrode particle, L^{-} is the geometric length of the negative electrode, and N_{layers} is the number of active layers in the stacked configuration. R^{-} is the radius of a single negative electrode particle and ν^{-} is the reversible expansion function of the negative electrode (see Figure 3.3B). Eq. 3.25 is derived in Section 3.10.

The SEI film thickness, δ_{sei}, evolves due to the accumulation of SEI current according to Safari et al. [57]:

$$\frac{d\delta_{\mathrm{sei}}}{dt} = V_{\mathrm{sei}} \frac{j_{\mathrm{sei}}}{nF}. \tag{3.26}$$

V_{sei} is the SEI molar volume in $\mathrm{m}^3/\mathrm{mol}$, defined by $V_{\mathrm{sei}} \triangleq M_{\mathrm{s}}/\rho_{\mathrm{s}}$, where M_{s} is the SEI molecular weight and ρ_{s} is the SEI density.

The second term in Eq. 3.24 represents the reversible expansion of the positive and negative electrodes, given by:

$$\Delta_{\text{rev}}(t) = N_{\text{layers}} \cdot \left(\frac{L^+}{3} \nu^+(\theta^+(t)) + \frac{L^-}{3} \nu^-(\theta^-(t)) \right), \tag{3.27}$$

where ν^+ and ν^- are the volumetric expansion functions for each electrode, shown in Figure 3.3B. The reversible volumetric expansion functions are due to lithium intercalation-induced swelling of the electrodes. Graphite, for example, expands up to 12% volumetrically during lithiation [103]. Layered oxide materials also expand and contract, but the total expansion depends on the range of lithium stoichiometries reachable within the full cell voltage window [104]. The expansion functions ν^+ and ν^- are typically quantified by measuring unit cell lattice parameter changes during lithiation and delithiation via in-situ X-ray diffraction [103, 104]. The prefactor terms convert the microscopic volumetric expansions to macroscopic thickness expansions and are derived in Section 3.10.

Further expansion modeling assumptions and clarifications are given as follows:

- Expansion and compression of the inactive layers, including the separators, current collectors, and pouch cell enclosure, are ignored.
- Electrode particles are spherical.
- The expansion functions $\nu^+(\theta^+)$ and $\nu^-(\theta^-)$ remain invariant over the formation and aging process.
- Expansion and contraction in the electrode planar direction are ignored.

3.5.7 Boosted SEI Growth Rate During Charging

We next introduce a concept called "SEI growth boosting." The boosting refers to enhanced SEI growth rate during cell charging which has been previously explored in the context of degradation modeling [79, 80, 105]. This effect is especially important to consider during formation cycling, during which the electrodes are experiencing the largest change in lithium stoichiometry. This stoichiometry change creates more particle-level strains which expose new reaction surfaces, boosting the SEI growth rate [105, 80]. As we will later show in Section 3.7.3, this model extension was necessary for unifying the observed macroscopic formation trends during both formation cycling and formation aging as shown in Figure 3.1.

Figure 3.4 illustrates the boosted SEI growth mechanism. Panel A describes a graphite particle that starts at the fully delithiated state. As the full cell is charged, the graphite

lithiates and expands. Ideally, the SEI elastically deforms to accommodate the particle swelling. However, if the SEI film is brittle, then parts of the SEI film may fracture, exposing fresh electrode surfaces to new electrolyte [80], shown in Figure 3.4A. Reacting molecules near these newly-exposed electrode surfaces will see more facile reaction kinetics since no pre-existing SEI film is present to limit the diffusion of reacting molecules to the reaction surface. The overall SEI current density will thus be temporarily boosted.

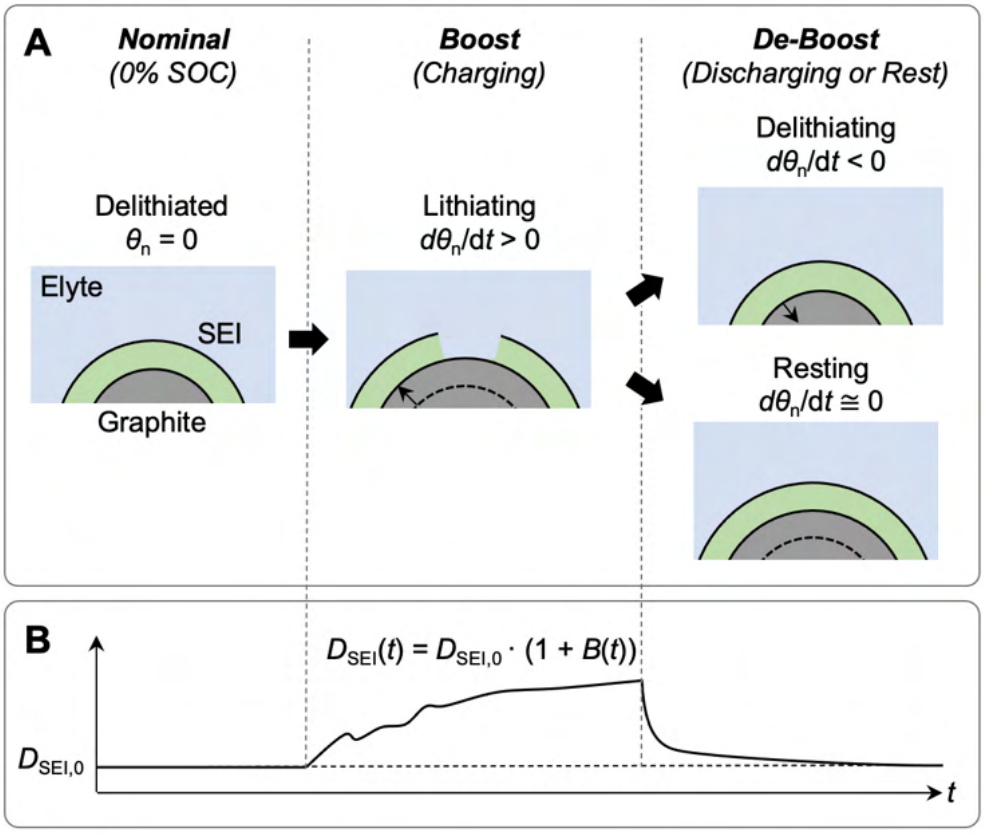

Figure 3.4: Schematic of the SEI growth boosting mechanism. (A) During lithiation (charging), SEI growth rate is boosted due to SEI fracture as the negative electrode particles expand. During resting and delithiation (discharging), the SEI growth rate is de-boosted to the nominal rate as the SEI film 'self-heals.' (B) Boosting dynamics is represented by $B(t)$ which modifies the effective SEI diffusivity D_{sei}. Elyte: electrolyte.

Next, we consider the case of delithiation and resting. During resting, new SEI is formed to fill in the fresh electrode surfaces. As the SEI thickness in these regions approaches the volume-averaged thickness, the overall SEI reaction rate is restored to the rate before boosting. During delithiation, the SEI is assumed to remain in contact with the graphite particles which are contracting, so no new electrode surfaces are exposed. Note that this assumption may be violated by systems having high volumetric expansions such as silicon

[106] which we leave for future work to explore. Overall, during resting and discharging, we assume that boosting no longer occurs and the SEI growth rate is gradually restored to the original rate before boosting.

This work interprets the SEI growth boosting process as a modification to the effective SEI diffusivity, D_{sei}. In this interpretation, newly exposed electrode surfaces are represented as increases in the local SEI porosity which in turn increas the volume-averaged SEI porosity ε. Changes in the volume-averaged porosity are represented by the effective diffusivity according to [107, 108]:

$$D_{\text{sei}}(t) = D_{\text{sei},0}\frac{\varepsilon(t)}{\tau}, \tag{3.28}$$

where D_{sei} is the effective diffusivity that we have been using for this work, $D_{\text{sei},0}$ is a reference diffusivity, ε is the volume-averaged SEI film porosity, and τ is the tortuosity. Note that this expression can be further simplified using the Bruggeman relation $\tau = \varepsilon^{-0.5}$ [100].

To describe the dynamics of the porosity evolution, we define an empirical "boost factor" $B(t)$ which modifies the effective SEI diffusivity according to:

$$D_{\text{sei,boosted}}(t) = D_{\text{sei},0}(1 + B(t)), \tag{3.29}$$

where $D_{\text{sei,boosted}}$ is the boosted SEI diffusivity. We assume that the dynamics of boosting is described by some unknown function $f(B(t))$ which is driven by the negative electrode expansion rate:

$$f(B(t)) = \gamma\frac{d\nu^-(\theta^-(t))}{dt}, \tag{3.30}$$

where ν^- is the negative electrode volume expansion function and γ is an input sensitivity parameter. A first-order Taylor expansion of $f(B(t))$ leads to our proposed state equation describing SEI growth boosting:

$$\tau\frac{dB(t)}{dt} + B(t) = \gamma\frac{d\nu^-(\theta^-(t))}{dt}. \tag{3.31}$$

In this equation, τ is the time constant for the first-order dynamics. This equation can be further separated for boosting during lithiation and "de-boosting" during delithiation and rest, with separate time constants describing each process:

$$\begin{cases} \tau_\uparrow\frac{dB(t)}{dt} + B(t) & = \gamma\frac{d\nu^-(\theta^-(t))}{dt} \quad I_{\text{app}} > 0 \quad \text{(Boost)} \\ \tau_\downarrow\frac{dB(t)}{dt} + B(t) & = 0 \qquad\qquad\qquad\quad I_{\text{app}} \leq 0 \quad \text{(De-boost).} \end{cases} \tag{3.32}$$

During charging, the boosting time constant $\tau_\uparrow$ describes how quickly the effective diffusivity increases in response to newly-created reaction surfaces for SEI growth. During discharging

and resting, the de-boosting time constant $\tau_{\downarrow}$ describes the rate of "self-healing" as the freshly-created surfaces fill up with new SEI and the effective diffusivity approaches its original value, $D_{\text{sei},0}$.

3.5.8 Homogenized Multi-Species SEI Reaction Model

So far, our description of SEI growth reaction kinetics applied to the case of a single reacting species to form a single-component SEI solid product. However, the SEI growth process in commercially-relevant systems involves the simultaneous reaction of multiple electrolyte components including solvent and additive components. We therefore extend our model to describe the case of multiple reacting species, using Figure 3.5 as a guide. This model extension enables a reduced-order representation of multiple, parallel SEI reactions. We will later demonstrate the usage of this model to represent the reaction of two electrolyte components, a solvent species (EC) as well as an additive species (VC), during the first formation charge cycle (see Section 3.7.1).

This model extension treats each SEI reaction as being governed by its own set of rate parameters (e.g. $U_{\text{sei}}, D_{\text{sei}}, k_{\text{sei}}, ...$). However, the reactions kinetics become coupled since all reacting species must diffuse through the same set of solid SEI products to reach the reaction interface. Moreover, at the reaction interface, the charge-transfer reaction kinetics also become coupled since the chemical state of the electrode is described by U^-, a singule value that evolves as a function of the total integrated SEI reaction current. A mathematical treatment is as follows.

Each SEI reaction proceeds according to Eq. 3.2 and is assumed to occur in parallel. The total SEI reaction current density thus takes the form:

$$j_{\text{sei}} = \sum_r j_{\text{sei},r} \tag{3.33}$$

$$= \sum_r \left(\frac{1}{\tilde{j}_{\text{rxn,r}}} + \frac{1}{\tilde{j}_{\text{dif,r}}} \right)^{-1}, \tag{3.34}$$

where $r = \{\text{EC}, \text{VC}, ...\}$ represents the different electrolyte species that are reduced to form their respective SEI solid products, and the expansion of the right-hand side is due to Eq. 3.17.

The reaction-limited current density for the rth species is:

$$\tilde{j}_{\text{rxn,r}} = n_r F k_r c_r^0 \exp\left(-\frac{\alpha_r n_r F}{RT} \left(\eta^- + U^-(\theta^-) - U_{\text{sei},r} \right) \right). \tag{3.35}$$

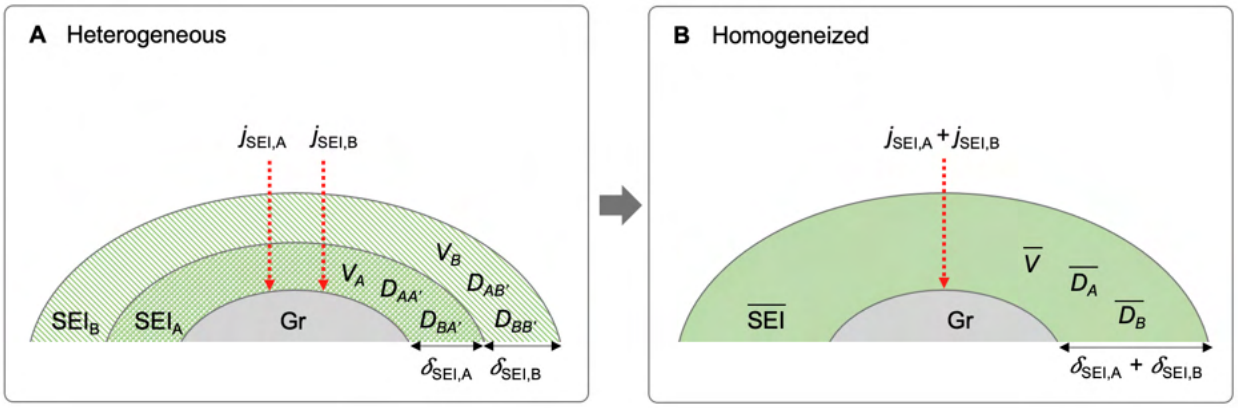

Figure 3.5: Homogenized representation of multi-species SEI reaction kinetics. (A) Heterogeneous representation. (B) Homogenized representation. Variables with bars indicate volume-averaged (homogenized) quantities. In the homogenized representation, SEI reactions occur in parallel but the reaction kinetics are coupled through a homogenized medium represented by homogenized diffusivities for each reacting species, r, $\bar{D}_{\text{sei},r}$, and the total SEI thickness. In the heterogeneous case, there are $(n_r \times n_r)$ diffusivities, where n_r is the number of reacting species. In the homogeneous case, the number of diffusivities is reduced to only n_r elements.

Each reaction is thus governed by independent rate parameters $\{k_r, c_r, U_{\text{sei},r}, n_r\}$. However, a coupling is introduced through $U^-(\theta^-)$ which changes as a function of the total SEI current.

To model the diffusion-limited current densities, the diffusion parameters in Eq. 3.15 require reinterpretation, since each reacting species r must now diffuse through a solid SEI layer consisting of multiple solid reaction products. Here, we update our interpretation of the effective diffusivity to consider both the reacting molecule and its environment:

$$D_{\text{sei},rl} : \text{reacting molecule } r \text{ through solid product } l. \tag{3.36}$$

With n_r reacting molecules and n_l resulting solid products, we assume that $n_r = n_l$ according to Eq. 3.2, and therefore, $D_{\text{SEI},rl}$ is a matrix of size $(n_r \times n_r)$. To simplify the model, we introduce the notion of average diffusivities for each reacting species, according to:

$$\frac{1}{\bar{D}_{\text{sei},r}} = \sum_l \frac{\mu_l}{D_{\text{sei},rl}}, \tag{3.37}$$

where $\bar{D}_{\text{sei},r}$ is the average diffusivity of reacting species r through a homogenized solid medium consisting of l solid products. $\mu_l = m_l / \sum_l m_l$ are weights based on the mass of each solid product m_l. In this representation, each reacting species r is assigned its own

diffusivity which describes the diffusivity of species r through a homogenized environment consisting of n_l solid products. The model thus carries only n_r number of $\bar{D}_{\text{sei},r}$. The diffusion-limited SEI current density can then be written as:

$$\tilde{j}_{\text{dif,r}} = \frac{\bar{D}_{\text{sei},r} c_r^0 n_r F}{\delta_{\text{sei}}}. \tag{3.38}$$

The thickness of each SEI layer grows independently according to:

$$\frac{d\delta_{\text{sei},r}}{dt} = V_{\text{sei},r} \frac{j_{\text{sei},r}}{n_r F}. \tag{3.39}$$

The total SEI thickness is taken to be the sum of each individual thickness:

$$\delta_{\text{sei}} = \sum_r \delta_{\text{sei},r}. \tag{3.40}$$

In this representation, the thickness of each SEI is defined in a volume-averaged sense without making a distinction on the spatial arrangement of the SEI layers. The model thus remains zero-dimensional.

In summary, the multi-species SEI reaction model treats the solid SEI product as a zero-dimensional, homogenized medium with volume-averaged properties. While each SEI reaction is described by independent sets of rate parameters, the reactions become coupled since each reacting molecule must diffuse through the same medium and react at the same electrode surface. The homogenization approach taken for this work enables the prediction of non-trivial SEI formation dynamics involving multiple electrolyte components, as will be detailed in Section 3.7.

3.6 Model Implementation

Equations from Table 3.1 were numerically integrated using a forward difference scheme. The simulation was run with a timestep of $\Delta t = 10$ seconds. Each charge and discharge cycle takes less than 1 second to complete execution on a 2.6 GHz 6-Core Intel Core i7 processor. All code was written in Python and is publicly available[1]. The code is written to be modular and extensible, drawing from the design of other battery simulation software suites [109, 110].

The simulation framework also supports constant voltage (i.e. potentiostatic) operation mode. During this charging mode, Eq. 4.11 is inverted to update the current for a given

[1] github.com/wengandrew/formation-modeling

target voltage. The reduced-order representation of cell overpotentials allows for a closed-form solution of the form:

$$I_{\mathrm{CV}} = \frac{V_{\mathrm{t}} - U^{+} + U^{-} - \sum_i R^{\pm}_{\mathrm{dif}} I^{\pm}_{\mathrm{dif}} \exp\left(-\frac{\Delta t}{\tau^{\pm}_{\mathrm{dif}}}\right)}{\sum_i \left(R^{\pm}_{\mathrm{ct}} + R^{\pm}_{\mathrm{dif}}(1 - \exp\left(-\frac{\Delta t}{\tau^{\pm}_{\mathrm{dif}}}\right))\right)}, \tag{3.41}$$

where $\tau^{\pm}_{\mathrm{dif}} \triangleq R^{\pm}_{\mathrm{dif}} C_{\mathrm{dif},i}$.

Parameterization. Model parameters used for this work are summarized in Tables 3.2 and 3.3. Model parameters were either calculated based on the cell build parameters, taken from literature, fit to the experimental data, or assumed. Since parameter identification was not a focus of this work, the parameters chosen for this work may not be optimal. A more detailed investigation of parameter identification and output sensitivity analysis will be left for future work.

SEI components. While the formation model supports simulating an arbitrary number of SEI-reacting species, we focus on studying a model system consisting of two SEI components: ethylene carbonate (EC) and vinylene carbonate (VC). These two components represent a subset of the experimentally-tested electrolyte (3:7 EC:DEC with 2 wt% VC, see Section 3.4.1). Both EC and VC are also well-studied in literature, with established reaction pathways and some known model parameters [111, 44, 112, 35]. VC, in particular, is present in a small quantity (2 wt%) as an electrolyte additive and is known to be consumed during the formation process to help stabilize the SEI film [113, 114, 115, 116]. VC, which reduces at ca. 1.35V [111], is also markedly higher than EC, which reduces at ca. 0.8V [44], and is thus expected to reduce first. VC thus provides a contrasting electrolyte component to understand both the capabilities and limitations of the model's ability to capture first-cycle reaction dynamics with multiple SEI components. EC and VC starting concentrations were calculated to match the experimental values. The EC reaction is given by Eq. 3.10. The VC reaction is given by [117]:

$$2\mathrm{VC} + 2\mathrm{e}^{-} + 2\mathrm{Li}^{+} \rightarrow \mathrm{LVDC} \downarrow + \mathrm{C_2H_4} \uparrow, \tag{3.42}$$

where LVDC is lithium vinylene dicarbonate, the VC-derived SEI layer. Like EC and other solvents, multiple reaction pathways are possible, and each reaction may occur in multiple stages [117]. However, for this work, we simplify the representation by considering only Eq. 3.42 as the VC reaction scheme.

Electrode capacities. Electrode capacities Q^{+} and Q^{-} were initialized using a differential voltage fitting procedure outlined in Weng et al. [6]. This method uses a C/20 charge voltage curve to extract information about electrode-specific capacities. The voltage curve used for

this analysis was taken at the end of the two-week formation aging step. This work assumes that the electrode capacities remain invariant throughout the formation process, i.e. no loss of active material. This assumption can be revisited as part of future work.

Initial conditions. Special attention was made to set the initial cell state prior to formation cycling. Before the formation cycles, we assumed that the negative electrode was fully delithiated ($\theta^- = 0$) and the positive electrode was fully lithiated ($\theta^+ = 1$). The measured cell terminal voltage before formation was then used to constrain the set of possible half-cell potentials, according to:

$$V_t|_{t=0} = U^+(\theta^- = 1)|_{t=0} - U^-(\theta^+ = 0)|_{t=0}. \tag{3.43}$$

For the cell under study, the full cell terminal voltage V_t was measured to be 635mV before formation charging began. To identify the initial potentials of the positive and negative electrodes before formation, half-cells with lithium metal counter-electrodes were built. Half-cell potentials were measured immediately after electrolyte fill and assembly. The negative electrode (graphite) half-cells were measured to have potentials of $\{2.939, 2.925, 0.770, 1.698\}$V vs Li/Li$^+$, and the positive electrode (NMC622) half-cells were measured to have potentials of $\{1.814, 2.813\}$V vs Li/Li$^+$. The wide range of measured potentials measured suggest that more work is necessary to verify the initial half-cell potentials which we leave as future work. For this work, we picked $U^-(\theta^- = 0) = 2.00V$ and $U^+(\theta^+ = 1) = 2.65V$, which satisfies Eq. 3.43.

Half-cell potentials. Half-cell near-equilibrium potential functions U^- and U^+ were adapted from Mohtat et al. [74]. These curves were linearly extrapolated to satisfy the boundary condition given in Eq. 3.43. These functions are plotted in Figure 3.3B.

Expansion functions. Volumetric expansion functions for the positive and negative electrodes were taken from Mohtat et al. [74] and shown in Figure 3.3B. For the simulations, a simplified version of Eq. 3.24 was implemented assuming constant and fitted prefactors, i.e.:

$$\Delta_{\text{tot}} = c_0\delta_{\text{sei}} + c_1\nu^+(\theta^+) + c_2\nu^-(\theta^-). \tag{3.44}$$

A future iteration of this work will implement Eq. 3.24 directly by tuning L^-, L^+, and R^-, creating additional constraints used for model parameter tuning.

Table 3.1: Summary of formation model equations

Electrodes	$\frac{d\theta^+(t)}{dt} = -\frac{I_{\text{app}}(t)}{Q^+} \qquad \frac{d\theta^-(t)}{dt} = +\frac{I_{\text{int}}(t)}{Q^-}$	(3.6, 3.7)
	$V_{\text{t}} = U^+(\theta^+) - U^-(\theta^-) + \eta^+ + \eta^-$	(3.3)
	$\eta^\pm(t) = R^\pm_{\text{ct}} I_{\text{app}}(t) + R^\pm_{\text{dif}} I^\pm_{\text{dif}}(t) \qquad i \in (\text{n}, \text{p})$	(3.8)
	$\frac{dI^\pm_{\text{dif}}(t)}{dt} = -\frac{1}{\tau^\pm_{\text{dif}}} I^\pm_{\text{dif}}(t) + \frac{1}{\tau^\pm_{\text{dif}}} I_{\text{app}}(t)$	(3.9)
SEI (EC only)	$I_{\text{int}} = I_{\text{app}} - a^- A^- L^- j_{\text{sei}}$	(3.20, 3.22)
	$j_{\text{sei}} = \left(\frac{1}{\tilde{\tilde{j}}_{\text{rxn}}} + \frac{1}{\tilde{\tilde{j}}_{\text{dif}}} \right)^{-1}$	(3.17)
	$\tilde{\tilde{j}}_{\text{rxn}} = nF k_{\text{sei}} c^0_{\text{EC}} \exp\left(-\frac{\alpha n F}{RT} \left(\eta^- + U^-(\theta^-) - U_{\text{sei}} \right) \right)$	(3.18)
	$\tilde{\tilde{j}}_{\text{dif}} = \frac{nF D_{\text{sei}} c^0_{\text{EC}}}{\delta_{\text{sei}}}$	(3.19)
Solvent	$\frac{dc^0_{\text{EC}}}{dt} = -\frac{a^- j_{\text{sei}}}{nF}$	(3.23)
Expansion	$\Delta_{\text{tot}} = c_0 \delta_{\text{sei}} + c_1 \nu^+(\theta^+) + c_2 \nu^-(\theta^-) \qquad \text{(simplified)}$	(3.44)
	$\frac{d\delta_{\text{sei}}}{dt} = V_{\text{sei}} \frac{j_{\text{sei}}}{nF}$	(3.26)
Boosting	$D_{\text{SEI,boosted}} = D_{\text{SEI},0}(1 + B)$	(3.29)
	$\tau_\uparrow \frac{dB}{dt} + B = \gamma \frac{d\nu^-}{dt} \qquad \text{Charging (boost)}$	(3.32)
	$\tau_\downarrow \frac{dB}{dt} + B = 0 \qquad \text{Discharging and rest (de-boost)}$	(3.32)
Multi-Species	$j_{\text{sei}} = \sum_r j_{\text{sei},r} = \sum_r \left(\frac{1}{\tilde{\tilde{j}}_{\text{rxn,r}}} + \frac{1}{\tilde{\tilde{j}}_{\text{dif,r}}} \right)^{-1}$	(3.33)
	$\tilde{\tilde{j}}_{\text{rxn,r}} = n_r F k_r c^0_r \exp\left(-\frac{\alpha_r n_r F}{RT} \left(\eta^- + U^-(\theta^-) - U_{\text{sei},r} \right) \right)$	(3.35)
	$\tilde{\tilde{j}}_{\text{dif,r}} = \frac{\bar{D}_{\text{sei},r} c^0_r n_r F}{\delta_{\text{sei}}}$	(3.38)
	$\bar{D}_{\text{sei},r} = \left(\sum_l \frac{\mu_l}{D_{\text{sei},rl}} \right)^{-1}$	(3.37)
	$\delta_{\text{sei}} = \sum_r \delta_{\text{sei},r}$	(3.40)

Table 3.2: Variables, parameters, and initial conditions, part 1. Asterisks (*) indicate values computed during simulation run-time. "I.C." indicates an initial condition. Double asteriks (**) indicate that values were modified from the literature values.

Symbol	Definition	Value 1	Value 2	Units	Ref.
	SEI Properties	A	B		
r	SEI reacting species	EC	VC	-	-
l	SEI solid product from species r	LEDC	LVDC	-	-
$U_{\text{sei},r}$	SEI reaction potential	0.8	1.35	V	Refs. [44, 111]
$j_{\text{sei},r}$	SEI reaction current density	*	*	A/m^2	Eq. 3.16
c_r^0	Bulk-phase concentration	4541	304.4	mol/m^3	Ref. [57] / Calculated
k_r	Reaction rate constant	3.0×10^{-17}	7.0×10^{-19}	m/s	Fitted
$D_{\text{s},rA'}$	Effective diffusivity of r in solid $l = A'$	4.2×10^{-20}	4.2×10^{-20}	m^2/s	Fitted
$D_{\text{s},rB'}$	Effective diffusivity of r in solid $l = B'$	6.6×10^{-18}	6.6×10^{-18}	m^2/s	Fitted
$Q_{\text{sei},r}$	SEI capacity of the rth species	*	*	A s	Eq. 3.21
$V_{\text{sei},r}$	SEI molar volume	9.585×10^{-5}	5.810×10^{-5}	m^3/mol	Ref. [57]
$\tau_\uparrow$	SEI growth boosting time constant	10	10	mins	Fitted
$\tau_\downarrow$	SEI growth de-boosting time constant	100	100	mins	Fitted
γ	SEI boosting input sensitivity factor	2.4×10^7	2.4×10^7	s/m	Fitted
	Electrode Potentials	*pos.*	*neg.*		
$U^\pm$	electrode potential vs Li/Li$^+$	2.635 (I.C.)	2.000 (I.C.)	V	Fitted
$\theta^\pm$	electrode lithium stoichiometry	1.0 (I.C.)	0.0 (I.C.)	-	Ref. [74]**
$Q^\pm$	electrode maximum capacity	2.95	3.14	Ah	Based on [6]

Table 3.3: Variables, parameters, and initial conditions, part 2. Asterisks (*) indicate values computed during simulation run-time. "I.C." indicates an initial condition. Double asteriks (**) indicate that values were modified from the literature values.

Symbol	Definition	Value 1	Value 2	Units	Ref.
	Electrode Overpotentials	*pos.*	*neg.*		
$\eta^{\pm}$	electrode over-potential vs Li/Li^+	*	*	V	Eq. 3.8
$I^{\pm}_{\text{dif}}$	electrode diffusion current (through $R^{\pm}_{\text{ct}}$)	*	*	A	Eq. 3.9
$R^{\pm}_{\text{ct}}$	electrode charge-transfer resistance	0.01	0.01	Ω	Assumed
$R^{\pm}_{\text{dif}}$	electrode diffusion resistance	0.001	0.001	Ω	Assumed
$C_{\text{dif},i}$	electrode diffusion capacitance	7.6×10^4	7.6×10^4	F	Assumed
$\tau^{\pm}_{\text{dif}}$	electrode diffusion time constant	*	*	s	Assumed
	Electrode Geometry and Expansion	*pos.*	*neg.*		
$a_{\text{s},i}$	electrode specific surface area ($3\varepsilon_i/R_i$)	-	1.05×10^5	1/m	Assumed
A_i	electrode geometric area	-	0.097566	m^2	Calculated
L_i	electrode geometric length	-	80	μm	Assumed
c_0	expansion fitting coefficient	-	127	-	Fitted
c_1	expansion fitting coefficient	-	0.00045	-	Fitted
c_2	expansion fitting coefficient	-	0.00045	-	Fitted
Δ_{tot}	macroscopic pouch cell thickness expansion	-	-	m	Eq. 3.24
ν_i	electrode particle volumetric expansion	*	*	%	Ref. [74]
δ_{sei}	SEI thickness expansion	-	5×10^{-9} (I.C.)	m	Eq. 3.26

3.7 Model Behavior

The formation model was simulated by inputting the current profile from Figure 3.1. The results highlight some of the key characteristics of a two-component SEI growth mechanism involving the sequential reduction of VC followed by EC. The observed results underscore the coupled nature of SEI formation dynamics, including the interplay between cell expansion and boosted SEI growth, as well as the interplay between reaction dynamics involving multiple SEI components. The same results introduced here will also set the stage for comparison against experimental data which will be discussed in Section 3.8.

3.7.1 SEI Growth Dynamics During First Charge

Figure 3.6 highlights key model outputs before and during the first formation charge. The simulation begins with the cell at rest before any external charge is applied. At this stage, the positive electrode is completely lithiated ($\theta^+ = 1$) and the negative electrode is completely delithiated ($\theta^- = 0$). Negligible SEI growth occurs during this stage since the negative electrode potential of 2.0V vs Li/Li^+ exceeds the reaction potentials of both VC and EC (Panel A, marker 1). After 30 minutes, an external current of C/10 (0.25A) is applied to begin the formation charge process (Panel B). Within minutes, the negative electrode potential drops below the VC reaction potential of 1.35V and VC begins to reduce (marker 2). This reaction current reaches a peak within minutes and falls back down. Next, as the negative electrode becomes more lithiated, the negative electrode potential falls below the EC reaction potential of 0.80V and EC begins reducing (marker 3). Similar to VC, the reaction current for VC also soon reaches a peak, but then gradually decreases.

The buildup of VC and EC-derived SEI products during the initial stages of formation contributes to the macroscopically-observed cell thickness expansion (Panel C). The predicted total expansion is a result of both the irreversible expansion due to SEI growth and the reversible expansion due to lithium intercalation/deintercalation in the electrodes. The model predicts that SEI growth plays a dominant role in determining the total cell expansion during the first cycle.

During the first charge cycle, the negative electrode expands, activating the SEI growth boosting mechanism which increases the effective SEI diffusivity (see Section 3.5.7). Since the negative electrode expansion increases monotonically during the charge cycle, boosting persists throughout the cycle. Note that, at mid-SOCs, the expansion rate for the lithiated graphite is lowered (marker 4) which decreases the boost magnitude according to Eq. 3.32. The EC reduction current decreases accordingly (marker 5). The boosting mechanism will be explored in more detail in Section 3.7.3.

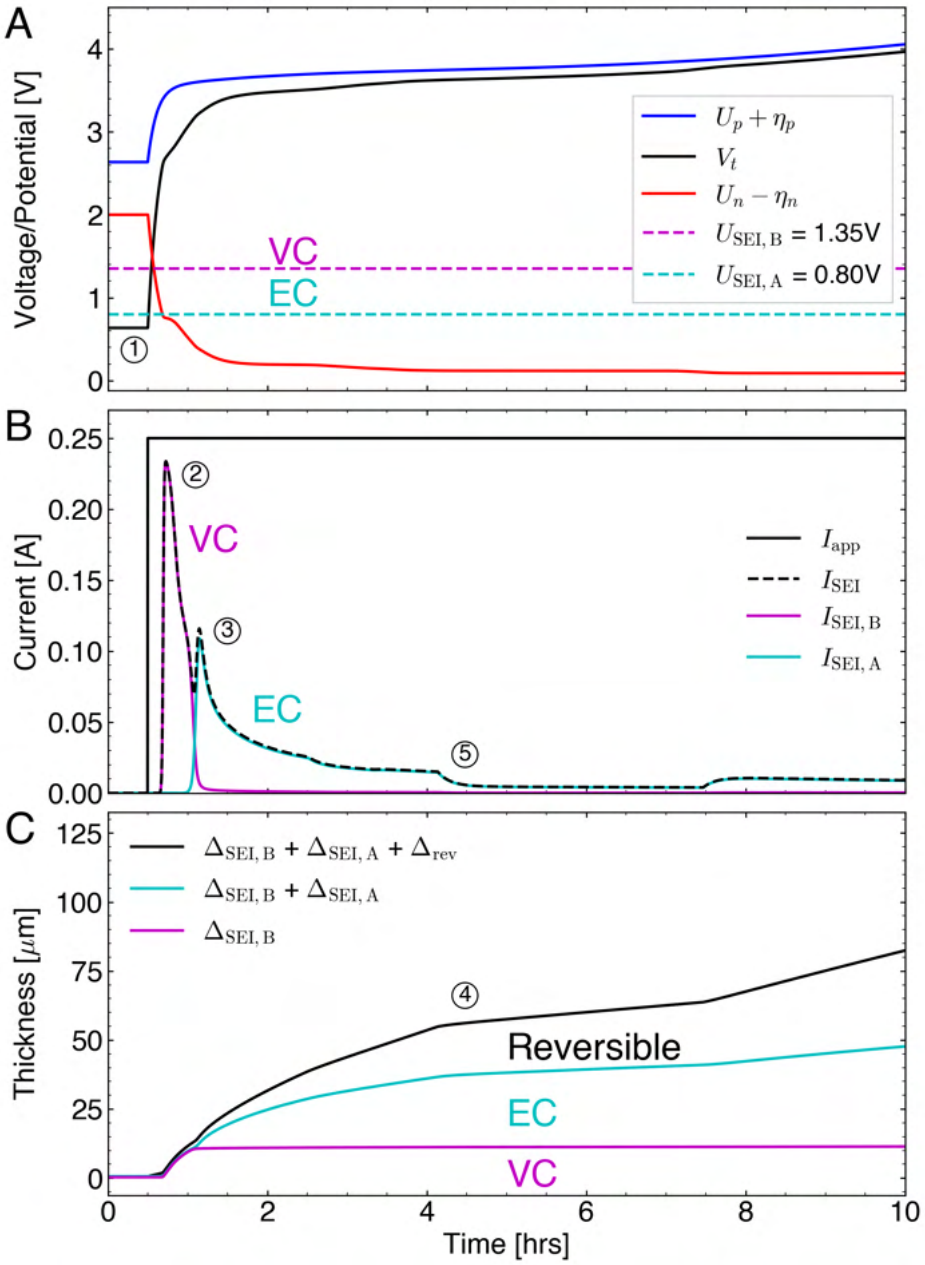

Figure 3.6: SEI reaction and full cell expansion dynamics during the first formation charge cycle. (A) Full cell voltage, electrode potentials, and SEI reaction potentials. (B) Applied current and SEI reaction currents. (C) Full cell thickness expansion, including both reversible expansion from electrode intercalation and irreversible expansion from SEI components. (1) Negligible SEI growth occurs before the first charge cycle due to reaction limitations. (2) VC reduces first, followed by (3) EC reduction. (4) Expansion rate of lithiated graphite slows down at mid-SOCs, causing a (5) decrease in the EC reduction current as a result of the SEI growth boosting/de-boosting mechanism.

3.7.2 Exploring the Limiting Current

Figure 3.7 explores the limiting SEI current during the initial stages of formation. Before any external current is applied, the SEI currents are reaction-limited since the negative electrode, at 2.0V vs Li/Li^+, is above the reaction potential for both VC (1.35V) and EC (0.8V) (marker 1 in both Figures 3.6 and 3.7), so Eq. 3.11 would predict very small current densities. However, after the external current is applied, the negative electrode potential decreases rapidly due to the steepness of the negative electrode equilibrium potential function U^-. This decreases the SEI reaction overpotential (Eq. 3.14) towards more negative values, increasing the overall SEI current (Eq. 3.11). This process explains why the initial surge in SEI current coincides with the rapid decrease in the negative electrode potential (marker 2 in both Figures 3.6 and 3.7). The reacting species with the higher reaction potential will tend to react first, as was the case with VC and EC in this model system.

3.7.2.1 Transition from Reaction-Limited to Diffusion-Limited SEI Growth

After the initial surge in SEI current, the SEI currents reach a peak and then begin to decrease. This can be observed for both the VC and EC reactions (marker 3 in Figure 3.7). We attribute this SEI current decay to the transition from a reaction-limited regime to a diffusion-limited regime. During this transition, the reaction-limited current continues to increase as the negative electrode potential continues to decrease. However, simultaneously, the diffusion-limited current decreases as the SEI film thickness increases according to Eq. 3.26. This film thickness increase limits the concentration of reacting molecules at the electrode surface. Eventually, the diffusion-limited current drops below the reaction-limited current. After this point, further increases in the reaction kinetics are no longer fully realized and the total reaction current begins to follow the diffusion-limited current (Eq. 3.19). The diffusion-limited current continues to decrease as the SEI film builds, limiting the overall SEI reaction rate.

3.7.2.2 Multi-Species Diffusive Coupling and Boosted SEI Growth

After 1.2 hours, the VC reaction current density experiences another drop (marker 4 in Figure 3.7). This drop is due to the coupling between the EC and VC diffusivities introduced by the multi-species reaction model (see Section 3.5.8). As EC begins to react, the EC-derived film begins to grow. For this simulation, the effective diffusivity of the EC-derived film was assumed to be two orders of magnitude lower than that of the VC-derived film (see Table 3.2). After the EC reaction begins, the effective diffusivity of VC through the SEI, which now consists of both the VC and EC-derived films, is pulled towards the lower diffusivity of

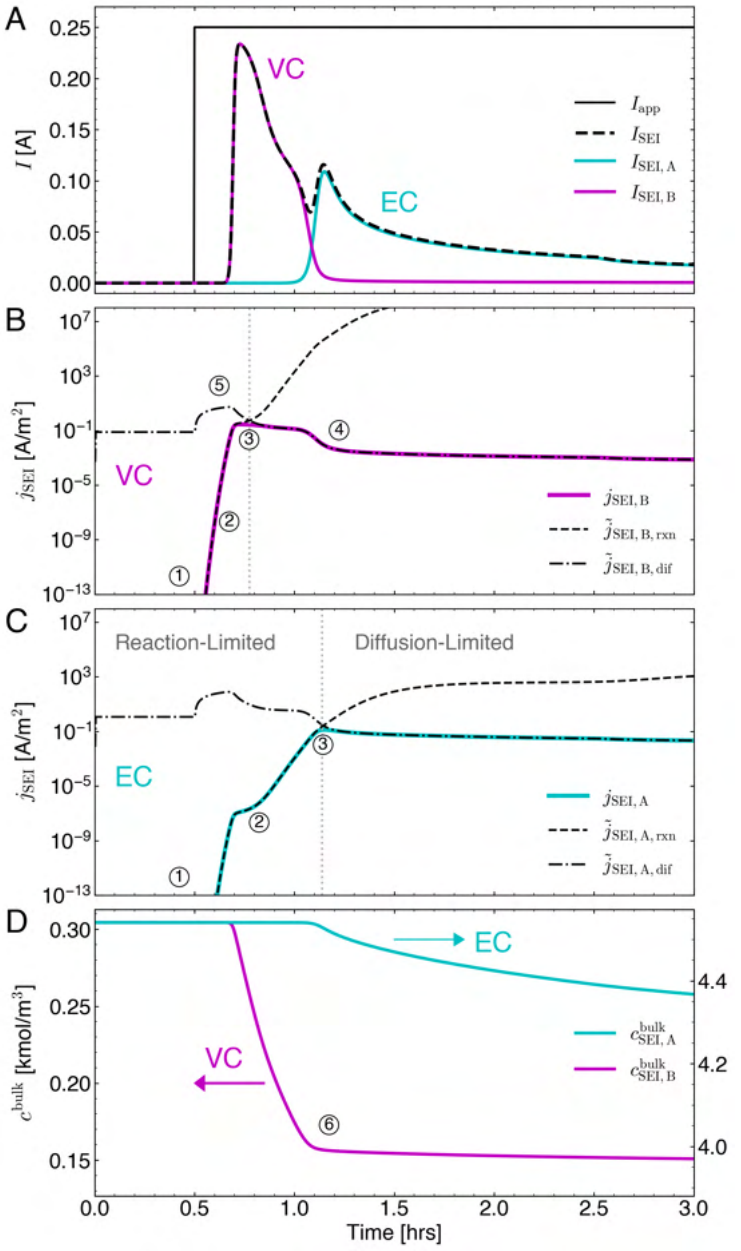

Figure 3.7: Reaction-diffusion and solvent consumption dynamics during the first formation charge cycle. (A) Applied current and SEI reaction currents. (B) Breakdown of limiting current for EC and (C) VC. (D) Bulk solvent concentration. (1) Negligible SEI growth occurs before the first charge due to reaction limitations. (2) The EC and VC reduction processes are both initially reaction-limited. (3) Transition from reaction-limited to diffusion-limited regimes. (4) Decrease in VC reaction current density due to the coupling between EC and VC diffusivities introduced by the multi-species reaction model. (5) Surge in diffusion-limited current due to the effect of boosted SEI growth. (6) VC consumption rate plateaus due to the decrease in VC reaction current density.

the EC-derived film, causing the VC reaction rate to be further slowed.

The effect of the boosted SEI growth mechanism is again observed in Figure 3.7B,C. The diffusion-limited currents here do not monotonically decrease as would be predicted by Fick's law. Rather, the diffusion-limit current initially surges when external current is applied (marker 5). This surge is explained by the negative electrode expansion which modifies the SEI diffusivity according to Eqs. 3.29 and 3.31. The diffusion-limited current decreases shortly thereafter as the SEI film thickness begins to increase. See Section 3.7.3 for a further discussion on SEI boosting.

3.7.2.3 Solvent Consumption

Figure 3.7D plots bulk concentrations for EC and VC. Solvent and additive consumption occur due to SEI growth according to Eq. 3.23. The initial concentration of VC is much lower than that of EC (304 mol/m^3 versus 4541 mol/m^3) since VC is an electrolyte additive. VC is consumed rapidly during the initial stages of the first charge cycle. However, VC consumption appears to plateau afterwards (marker 6). This plateau coincides with the start of EC reduction, which depresses the VC reduction rate due to the diffusive coupling as previously explained. Hence, the VC concentration does not drop completely to zero during formation charge due to diffusion limitations. The model thus predicts the presence of trace amounts of electrolyte additives after formation cycling is completed.

3.7.3 Understanding SEI Growth Boosting

Figure 3.8 highlights the impact of boosting on the SEI growth rate. For this simulation, the cell was first charged at C/10 to 100% SOC, rested for 40 hours, then discharged at C/10 (Panel A). This pattern was then repeated. During each charge and discharge cycle, the negative electrode expands and contracts (Panel B). The negative electrode volumetric expansion rate, $d\nu^-/dt$, provides a non-linear input which activates the boosted SEI mechanism (see Section 3.5.7).

Panel C plots $B(t)$ along with $\gamma(d\nu^-/dt)$. During charging, $B(t)$ and $\gamma(d\nu^-/dt)$ track closely with each other since we have assumed a small value for the boosting time constant, with $\tau_\uparrow = 10$ mins. The step transitions (marker 1) are due to the piecewise-linear construction of the negative electrode expansion function, ν^-, consisting of three regions: steep, shallow, and steep, corresponding to low, medium, and high lithium stoichiometries, respectively (see Figure 3.3B). The SEI thickness growth rate tracks these different regions accordingly, initially starting fast, then slowing down, and then becoming fast again (Panel D).

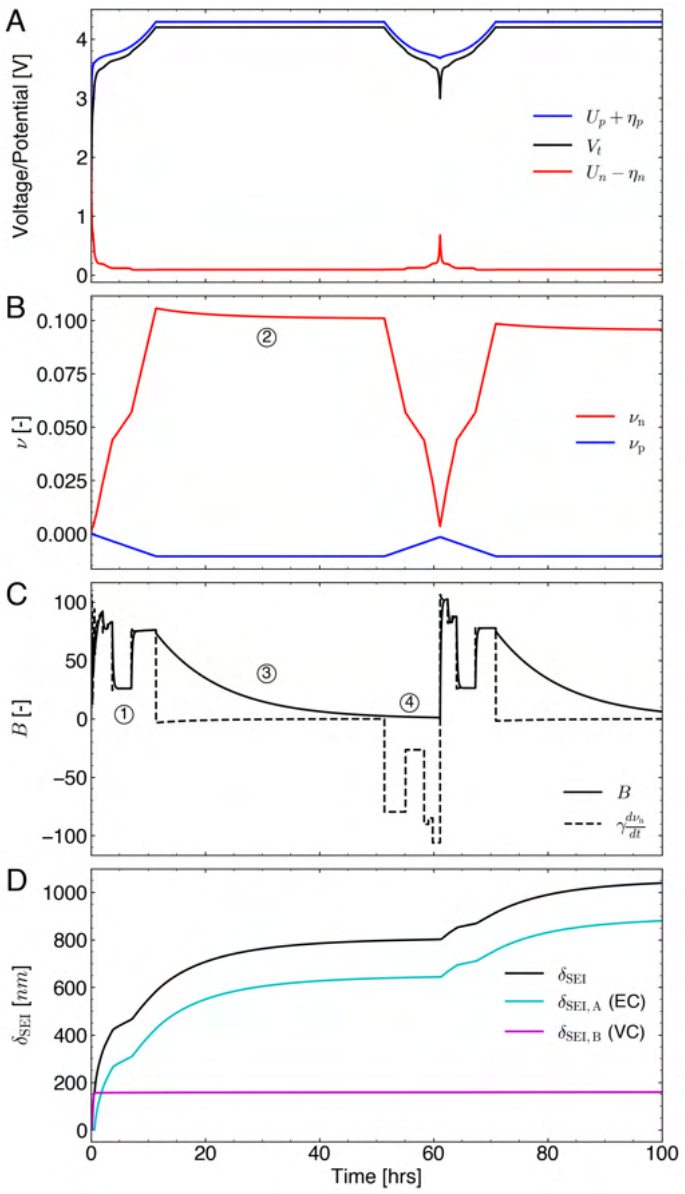

Figure 3.8: Demonstration of SEI growth rate boosting during charging and de-boosting during resting and discharging. (A) Full cell voltage and electrode potentials. (B) Positive and negative electrode volumetric expansion functions. (C) Boost function $B(t)$ plotted against the boosting input term $\gamma(d\nu^{-}/dt)$. (D) Comparison of SEI thickness growth rates on cycling versus calendar aging. (1) Step transitions in the boost function due to the piecewise-linear construction of the negative electrode expansion function. (2) Negative electrode contracts slightly during rest since lithium continues to deintercalate from the negative electrode to form the SEI. (3) The de-boosting process is assumed to be much slower than the boosting process for this work. (4) No boosting occurs during discharge due to the assumption that the SEI maintains physical contact with the negative electrode particles so no new reaction surfaces are exposed.

During rest, $\gamma(d\nu^-/dt)$ approaches zero, but it is not exactly zero, since lithium continues to deintercalate from the negative electrode to form SEI during rest, causing the negative electrode to contract slightly (marker 2). Overall, the magnitude of $d\nu^-/dt$ during resting remains small. $B(t)$, however, takes hours to decay from its boosted state since we assumed that the de-boosting process is much slower than the boosting process, with $\tau_{\downarrow} = 100$ mins (marker 3).

As the rest step transitions into a discharge step, $\gamma(d\nu^-/dt)$ inverts sign, but $B(t)$ continues to exponentially decay towards zero (marker 4). Physically, this behavior represents the assumption that, as the negative electrode particles contract, the SEI maintains physical contact with the particle and no new reaction surfaces are exposed. As the previously-exposed negative electrode surfaces rebuild SEI, the SEI effective diffusivities return to their nominal values prior to boosting.

Panel D highlights the effect of boosted SEI growth on SEI thickness expansion. During charging, the SEI build-up is accelerated. However, during resting and discharging, the SEI growth rate slows down, corresponding to a steady-state diffusion regime. During the subsequent charge, this steady-state regime is interrupted as the SEI growth rate is boosted again by the charging process.

3.8 Comparison to Experiment

A main goal of this work was to develop a model capable of capturing macroscopic trends observed in experimental formation data. Here, we demonstrate that our formation model achieves this goal for a range of metrics, including full cell voltages, cell thickness expansions, coulombic efficiencies, and first cycle dQ/dV.

3.8.1 Full Cell Voltage

Figure 3.9A compares the modeled versus measured full cell voltage during and after the formation cycles. Model-predicted positive and negative electrode potentials vs Li/Li^+ are also shown for reference. The simulation was run using the parameters described in Section 3.6 and with a current input that matches the experimental data. The result shows that the formation model outputs generally match the observed voltage trends over the course of the formation charge-discharge cycles and during the subsequent formation aging step.

However, despite the general agreement between model and experiment, several model mismatches can be observed. First, the cell voltage was under-predicted during the three formation discharge steps. This may be because the half-cell equilibrium potential functions

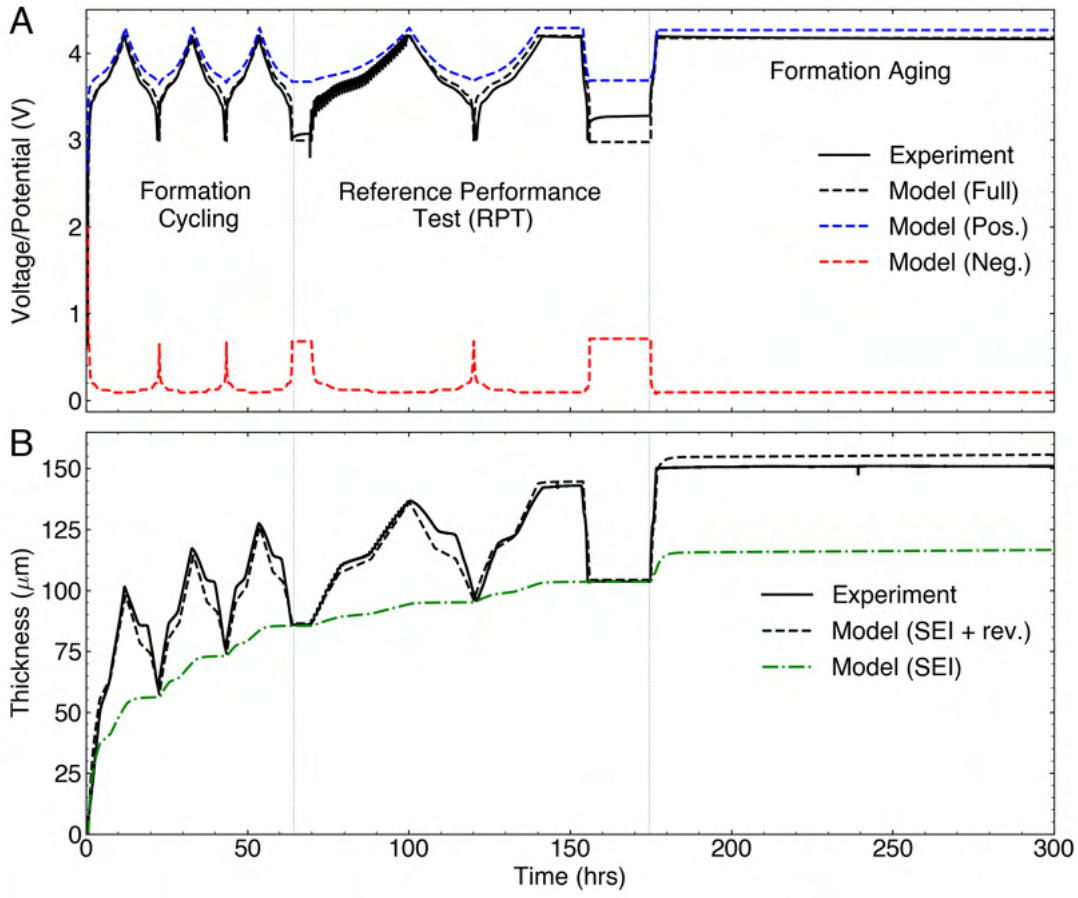

Figure 3.9: Model comparison against experimental data. The dataset consists of three formation charge-discharge cycles, a reference performance test (RPT) sequence, and formation aging at 100% SOC. (A) Full cell voltage. (B) Thickness expansion.

[74] were based on charge curves and thus do not account for hysteresis effects [118, 119, 120]. The half-cell equilibrium potential functions were also inherited from a previous work [74] which had similar but not identical positive and negative electrode compositions. Next, the voltage rebound at 0% SOC was not predicted by the model. This model mismatch is attributed to the fact that our overpotential model uses a cell resistance does not vary with SOC, yet it is well-known that cell resistance increases significantly at lower SOCs owing to kinetic limitations in the NMC positive electrode [7, 121, 122, 123].

3.8.2 Full Cell Expansion

Figure 3.9B compares the modeled versus measured full-cell thickness expansion during and after the formation cycles. The model-predicted irreversible expansion due to SEI growth is also shown as a green dashed line. The model captures macroscopic trends in both irreversible and reversible full-cell expansion, across formation cycles and subsequent formation calendar aging. Consistent with the experiment, the model correctly predicts that the irreversible expansion slows down during the formation aging step. This result was achieved by using the boosted SEI growth formulation which accelerates the SEI growth process during cycling (see Section 3.5.7).

As with the voltage data, some model mismatches persist. First, the model over-predicts the electrode contraction at mid-SOCs during discharging steps. The origin of this mismatch is unclear, but we hypothesize that the graphite expansion function may also be subject to charge-discharge asymmetry. In this work, the expansion functions were parameterized on charge, not discharge [74], so the model would not be able to capture this hysteresis effect. Another model mismatch occurs during the formation aging step. While the model correctly captures the slope of the expansion data, the model 'over-boosted' the SEI growth rate, and thus the total expansion, during the C/2 charge leading up to the formation aging step. This result suggests that the first-order representation of the boosting mechanism given by Eq. 3.32 may be insufficient to capture the dynamics of boosting at all C-rates. Thus, while the SEI growth boosting mechanism represented in this work remains a reasonable starting point to capture expansion differences between cycling and calendar aging, there remains room to improve the representation of higher-order dynamical effects such as the effect of cycling C-rates.

We finally note that active material loss mechanisms are not currently represented in the model, which could contribute to another source of model error. As the electrodes lose active material, e.g. due to loss of electronic conduction pathways, or due to material phase transformations, the lost active material will no longer participate in reversible expansion, decreasing the overall observed reversible expansion. Finally, similar to the equilibrium potential functions, the volumetric expansion functions ν^- and ν^+ are also inherited from literature [74] and may not be exact, contributing to yet another possible source for model error.

3.8.3 Formation Coulombic Efficiencies

Figure 3.10 compares the modeled versus measured FCE during the first formation cycle as well as the CE of the subsequent two cycles, defined by Eq. 3.1. The formation model

predicted the FCE within 1 percentage point of the measured result. However, the model underestimated the CE of the next two cycles. The model mismatches here are attributed to suboptimal parameter tuning which can be improved with further optimization.

Overall, the formation model not only predicted that the FCE is much lower than the CE of subsequent cycles, but the model also gave an intuitive explanation for why this is necessarily the case: the first charge cycle is the only cycle that sees reaction-limited SEI growth. After the first charge cycle, the SEI reaction becomes diffusion-limited, slowing down the SEI reaction rate for all subsequent cycles (see Section 3.7.2.1).

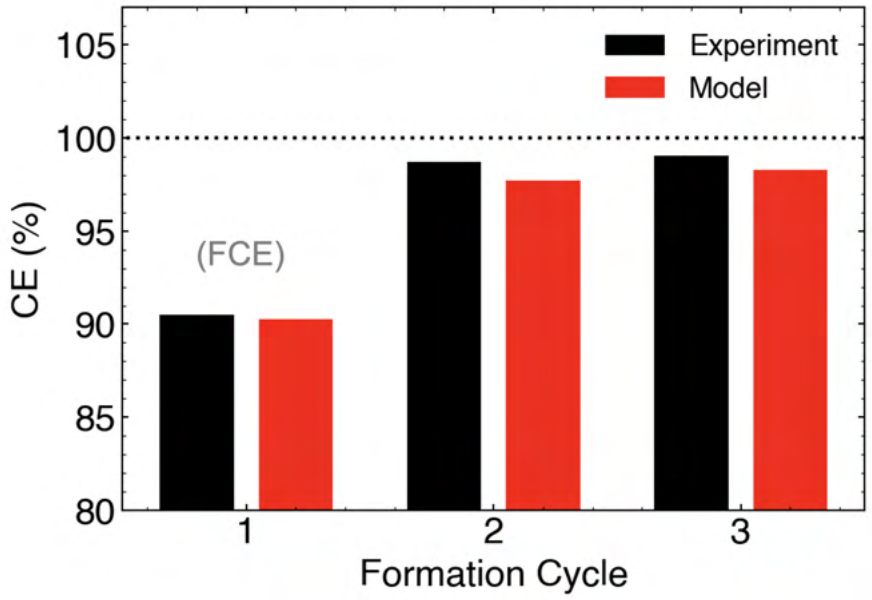

Figure 3.10: Modeled vs. measured Coulombic efficiency (CE). First cycle efficiency (FCE) is defined as the CE of the first formation charge cycle.

3.8.4 Formation Charge dQ/dV

Figure 3.11A compares the model vs. measured full cell dQ/dV curve during the first formation charge. The plot represents the incremental capacity accumulated by the cell at each increment of full cell voltage. This plot is experimentally observable, with the measured result plotted as a dashed line. This plot is commonly studied in electrolyte development studies since peaks in dQ/dV during the initial formation charge cycle can often be attributed to SEI-forming electrolyte reduction processes. However, care is usually needed in interpreting the data since the dQ/dV peaks can also be due to shifts in the solid-phase potentials as the positive electrode is delithiated and the negative electrode is

lithiated.

In the experimental data, a dQ/dV peak was observed at approx. 2.8V (marker 1). The formation model attributed this peak to the reduction of the VC additive. The model predicted the position of this reduction peak and also qualitatively captured the peak shape. The model additionally predicted a second, broad peak, corresponding to EC reduction (marker 2). However, the EC peak was not observed in the experimental data. This model mismatch may be due to differences in the electrolyte composition: the experimental data was obtained with an electrolyte comprising both EC and DEC, but the model only represented EC.

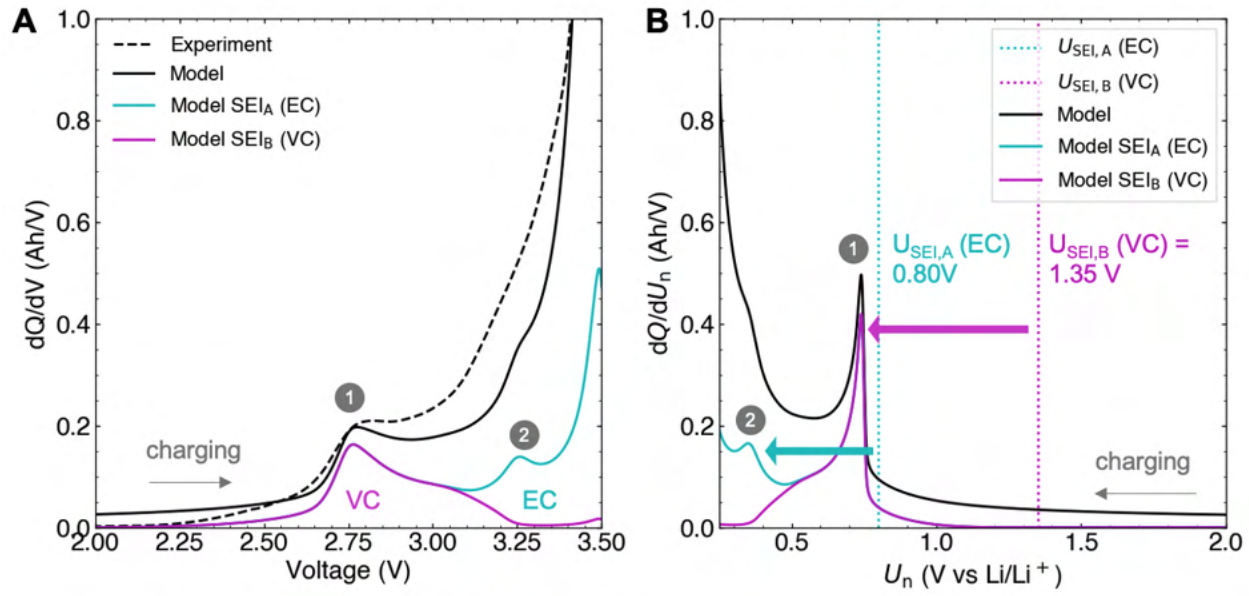

Figure 3.11: Modeled vs. experimental dQ/dV trace during the formation charge cycle. (A) dQ/dV vs V, where V is the full cell voltage. (B) dQ/dU^- vs U^-, where U^- is the negative electrode equilibrium potential.

3.9 Discussion: Mechanistic Insights

The formation model developed in this work provides a quantitative understanding of what makes the first formation charge process different from all subsequent cycles in lithium-ion battery systems. This understanding holds important practical implications as well as mechanistic insights, which we discuss in this section.

3.9.1 What is Special About the First Formation Charge?

Minimal SEI growth before formation charge. The formation model predicts that SEI growth does not begin until the cell is externally charged for the first time. Before the charge step, the SEI formation process is suppressed according to Eq. 3.11 since the negative electrode potential, at ca. 2.0V, is above the reaction potentials for the reacting molecules studied for this work (0.8V for EC and 1.35V for VC). This observation has some practical implications: since SEI formation only begins when the cell is charged, the duration elapsed between electrolyte filling and the first formation charge cycle may be discounted as a potential source of variability in SEI properties and subsequent cell performance. Note, however, that copper dissolution at high negative electrode potentials, which may occur during the time between electrolyte filling and formation charge [124, 125], creates a separate source of variability that warrants further study using the formation model.

Reaction-limited SEI growth occurs exclusively during formation charge. The first cycle efficiency (FCE) during formation is typically between 80% to 90% and can vary as a function of the electrolyte system [126], negative electrode type [126], and formation protocol [124]. The FCE is thus much lower than subsequent measures of CE which typically exceeds 99%. This result was experimentally replicated in our formation dataset and was also predicted by our formation model, see Figure 3.10. The formation model provides a simple explanation to why the FCE is low compared to the CE of subsequent cycles: the first formation charge is the only time the SEI growth process is reaction-limited. After the first charge cycle, SEI growth becomes diffusion-limited (see Figure 3.7). Intuitively, the SEI film is the thinnest during the first formation charge, making solvent diffusion facile. During the first formation charge, a sufficient amount of SEI is built up and the SEI reaction becomes self-limiting due to diffusion limitations. For the remaining life of the battery, the SEI reaction remains diffusion-limited. This result suggests that the effective SEI diffusivity, D_{sei}, is a key parameter describing the passivation of the SEI over a battery's life. A low effective SEI diffusivity is thus essential for creating a long-lasting battery. By contrast, the SEI kinetic rate parameter, k_{sei}, appears to only play a role in determining the SEI formation dynamics during the first charge cycle. The model predicts that k_{sei} becomes inconsequential to the SEI growth rate during later formation cycles and for the rest of the cell's life.

Extended lithium stoichiometric ranges and electrode surface potentials. Figure 3.12 shows how the lithium stoichiometries in each electrode evolve during and after the formation cycles (Panel A), along with their corresponding electrode potentials (Panel B). Before the first formation charge, the negative electrode is completely empty of lithium ($\theta^- = 0$) and the positive electrode is completely full of lithium ($\theta^+ = 1$), shown in red circles. After formation completes, neither electrode will be able to access these initial lithium stoichiometries

and their corresponding electrode potentials. Notably, the maximum accessible lithium stoichiometry in the positive electrode continues to decrease over the RPT and formation aging (Panel A inset) due to the irreversible consumption of lithium from the positive electrode to form the SEI. By the end of the formation aging step, the maximum positive electrode stoichiometry has decreased from 1.0 to ca. 0.8 (blue triangles). Meanwhile, the minimum negative electrode potential has also increased from 0.0 to ca. 0.018. In both electrodes, these permanent shifts in the accessible lithium stoichiometry range also restrict the range of electrode potentials observable after formation completes (Panel B). The negative electrode starts at 2.0V vs Li/Li^+ before formation, but by the time the first formation charge completes, the negative electrode will never see potentials above 0.7V vs Li/Li^+. These restrictions in electrode potentials may not bear much consequence to the overall SEI reaction rate over life, since the SEI reactions will be primarily driven by diffusion limitations as explained in Section 3.7.2.1. However, this result does explain why copper dissolution, which occurs at high negative electrode potentials, is a concern during the formation process but is less of a concern over the remainder of a battery's life.

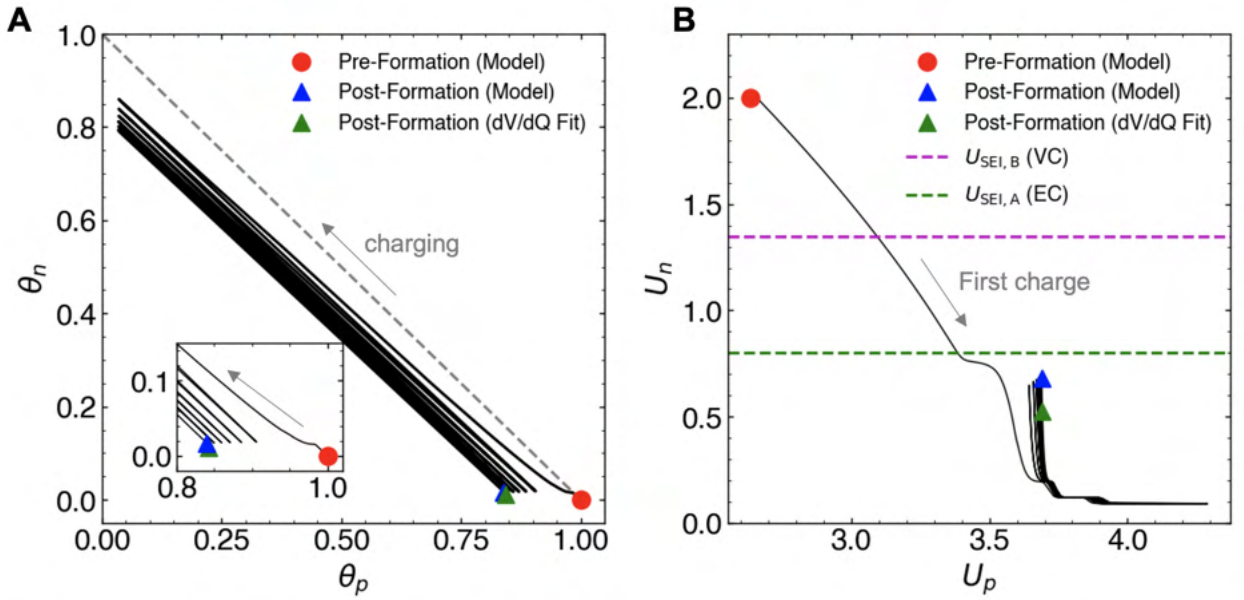

Figure 3.12: Lithium stoichiometry and electrode potential maps over formation cycling, RPT, and formation aging. (A) Positive and negative electrode lithium stoichiometries. Inset: expanded view of the lithium stoichiometries at the end of each discharge cycle. (B) Positive and negative electrode equilibrium potentials. Red circle: state of the system before formation. Triangles: state of the system after formation completes and the cell is discharged. Green triangle: prediction from dV/dQ fitting method on C/20 charge voltage data taken at the end of the formation process, adapted from Weng et al. [6].

3.9.2 Reinterpreting dQ/dV Peaks for SEI Reaction Studies

Returning to Figure 3.11, Panel B shows a dQ/dV plot where the differential capacity is plotted against the differential negative electrode equilibrium potential U^-. This result is discussed briefly now to gain further insight into the rate-limiting mechanisms during formation charge. A key observation here is that the position of the reduction peaks for both EC and VC do not indicate their respective reaction potentials, as is often assumed in previous literature studies. Rather, there is a delay between the reaction potentials and the respective reduction peaks. For example, the VC reaction potential is at 1.35V, yet the observed dQ/dV peak does not occur until the negative electrode has dropped below 0.8V. Similarly, the EC reaction potential is at 0.8V, but its corresponding dQ/dV peak occurs below 0.4V. This delay suggests that the dQ/dV peaks do not indicate the reaction potentials; rather, the peak indicates the transition from the reaction-limited to the diffusion-limited regime, which occurs sometime after the negative electrode potential falls below the reaction potential (see Figure 3.7. This result partly explains why literature reports of SEI reaction potentials, U_{sei}, can vary widely.

3.9.3 Analyzing Rate-Liming Regimes

The transition from reaction-limited SEI growth to diffusion-limited SEI growth appears to be a key characteristic of the first formation charge cycle. Due to its importance, we briefly discuss some analytical approaches to further characterizing this transition to promote future investigations in this area.

We define a dimensionless number, Bu, as:

$$\text{Bu} \triangleq \frac{\tilde{j}_{\text{rxn}}}{\tilde{j}_{\text{dif}}}, \tag{3.45}$$

Bu characterizes the ratio of SEI current carried by the reaction versus the diffusive process. When Bu $\ll 1$, the SEI current is reaction-limited, and when Bu $\gg 1$, the SEI current is diffusion-limited. Bu can be found by substituting Eqs. 3.18 and 3.19 into Eq. 3.45, yielding:

$$\text{Bu} = \frac{k_{\text{rxn}}}{k_{\text{dif}}}, \tag{3.46}$$

where:

$$k_{\text{rxn}} \triangleq k_{\text{sei}} \exp\left(-\frac{\alpha F}{RT}\eta_{\text{sei}}\right) \tag{3.47}$$

$$k_{\text{dif}} \triangleq \frac{D_{\text{sei}}}{\delta_{\text{sei}}}. \tag{3.48}$$

k_{rxn} is the apparent reaction-limited rate parameter which depends on both the pure rate constant k_{sei} as well as the reaction over-potential $\eta_{\text{sei}} = f(U^-, U_{\text{sei}})$. k_{dif} is the apparent diffusion-limited rate parameter which accounts for both the effective diffusivity as well as the film thickness. These rate parameters clarify that the rate-limiting process depends on both internal material properties, such as k_{sei} and D_{sei}, as well as external factors such as U^- and δ_{sei}.

3.9.4 Implications of SEI Growth Boosting

The boosted SEI growth mechanism and its mathematical representation were key developments enabling the model to capture experimental trends during both formation cycling and formation aging (see Sections 3.5.7, 3.7.3). Here, we further clarify the modeling assumptions and physical implications of the SEI boosting mechanism, highlighting its role in enabling the formation model to be extended toward general-purpose cycle life and calendar aging simulations.

Necessity. A key insight from this work was that a boosted SEI growth mechanism during charging was necessary to capture the macroscopic trends in capacity fade and cell expansion during formation cycling and formation aging. Without the boosted SEI mechanism, the model could only fit formation cycling and formation aging using separate parameter sets, but not both using the same parameter set. Specifically, without boosting, SEI diffusivities that explained the voltage and expansion data during formation cycling led to unrealistically high degradation rates during formation aging. Conversely, an SEI diffusivities that explained the voltage and expansion data during formation aging was too small to explain the cell expansion trend during formation cycling. When the boosted SEI growth mechanism was introduced, both formation cycling and formation aging were explained by the same set of SEI diffusivities (see Figure 3.9). Introducing the boosted SEI mechanism thus enabled a unified representation of SEI growth rates across cycling and storage.

Reaction rate asymmetry. The boosted SEI growth mechanism also introduces a source of reaction rate asymmetry: SEI growth is predicted to occur more quickly during charging (negative electrode lithiation) compared to discharging (negative electrode delithiation). This result is consistent with experimental results from Attia and Das [112, 54]. The boost-

ing mechanism frames the reaction rate asymmetry as a particle stress-driven phenomenon whereby reaction rates are boosted only when the SEI expansion but not when it shrinks. Boosting thus provides a unified description of the apparent SEI reaction rate asymmetry described in earlier works.

Capacity fade does not trend with the square root of time. Attia et al. [88] reported that experimental data on lithium-ion battery degradation often did not strictly follow a $\sqrt{t}$ relationship, as would be expected with diffusion-limited SEI growth. The boosted SEI growth mechanism provides a quantitative description of why the $\sqrt{t}$ relationship is violated, and more specifically, why the exponent is often more than 0.5. During charging, the boosting mechanism enhances the SEI reaction rate, taking the system out of the steady-state diffusion regime. The $\sqrt{t}$ dependence can thus be viewed as a limiting case where the boost factor γ is zero.

Model representation. In our model, the SEI growth boosting process was represented as a modification to the effective diffusivity D_{sei}. In reality, the effective reaction rate parameter k_{sei} could also be boosted since the reaction surface area could increase during SEI cracking. However, in the model, increasing k_{sei} will have little impact on the SEI growth rate beyond the initial formation charge cycle since the SEI growth process becomes diffusion-limited by the end of the first cycle (see Figure 3.7). Overall, our treatment of SEI growth boosting remains phenomenological: the model captures the macroscopic trends in voltage and expansion without elucidating the mechanistic details of the SEI boosting process. Such mechanistic details would be more appropriate to address using higher-fidelity models.

3.10 Conclusions

This chapter develops a reduced-order electrochemical model of the formation cycling and formation aging process for lithium-ion batteries. The model supports simulating an arbitrary number of electrolyte components that react at the negative electrode surface to form a composite SEI film with volume-averaged properties. The model also tracks electrode-level lithium stoichiometries and potentials, enabling the tracking of SEI current densities as a function of full-cell voltages. The model further couples an electrode expansion model which accounts for both reversible and irreversible expansion. We finally introduce an SEI growth boosting mechanism that enabled a unified description of SEI growth during both formation cycling and formation calendar aging. We demonstrated that the formation model qualitatively matched experimental formation data, including cell voltages, cell expansion, coulombic efficiencies (including first cycle efficiency, or FCE), and the dQ/dV curve during the first charge cycle which indicated the reduction of the VC electrolyte additive.

The formation model clarified why the first formation charge cycle is special. First, SEI growth does not begin until an external current is applied to the cell. Second, the SEI growth process is reaction-limited during the first formation charge but becomes diffusion-limited for the remaining life of the cell. Third, during the first formation charge, each electrode sees an extended range of lithium stoichiometries and electrode surface potentials which will never be accessed again for the remaining life of the cell.

We envision that the formation model can be leveraged to improve formation protocol design, electrolyte engineering, cell lifetime simulations, and physics model parameter identification. In a battery manufacturing context, our model could see potential applications as a physics-based digital twin of the formation process.

Overall, the proposed modeling framework enables practical pathways for bridging the electrochemistry of battery formation to macroscopic variables related to battery performance, safety and lifetime.

Chapter 3: Supplemental Sections

Reversible Expansion Derivation

The reversible expansion of a battery cell originates from lithium intercalation-induced electrode swelling. Here, we derive the scaling law to convert between the lattice expansion of the electrode host structures and the macroscopic expansion of a battery cell. Unit cell lattice parameters can be converted into a net volume change $\nu^{\pm}$ according to:

$$\nu^{\pm} = \frac{dV^{\pm}}{V^{\pm}}, \tag{3.49}$$

where $V^{\pm}$ is the volume of a unit cell in the positive or negative electrode. To relate the experimental data $\nu^{\pm}$ to the macroscopically observed cell thickness change, we first define the volume-averaged number of particles along the total length of the electrodes, $\bar{N}_p$, as:

$$\bar{N}_p \triangleq \frac{L^{\pm}}{R^{\pm}} \tag{3.50}$$

where $L^{\pm}$ is the total electrode thickness and $R^{\pm}$ is the radius of a single electrode particle which is assumed to be spherical. A key assumption we make is that $\bar{N}_p$ remains constant as the particles expand and contract, and hence:

$$\bar{N}_p = \frac{dL^{\pm}}{dR^{\pm}}, \tag{3.51}$$

where $dL^{\pm}$ is the incremental total thickness change of the electrodes and $dR^{\pm}$ is the corresponding electrode particle radius change. Combining Eqs 3.50 and 3.51 yields the scaling law to convert from microscopic expansion to macroscopic expansion.

$$dL^{\pm} = \frac{L^{\pm}}{R^{\pm}} dR^{\pm}. \tag{3.52}$$

The last step is to convert $\nu^{\pm}$ to radial expansion, $dR^{\pm}$, by assuming a spherical particle, in which case:

$$dR^{\pm} = \frac{R^{\pm}}{3}\nu^{\pm}, \tag{3.53}$$

where we have substituted the equation of a sphere for $V^{\pm}$ and its differential form $dV^{\pm} = 4\pi(R^{\pm})^2 dR^{\pm}$. We can now substitute Eq. 3.53 into Eq. 3.52 to arrive at:

$$dL^{\pm} \triangleq \Delta^{\pm} = \frac{L^{\pm}}{3}\nu^{\pm}. \tag{3.54}$$

Irreversible Expansion Equation Derivation

Irreversible expansion of battery cells is attributed primarily to growth of the SEI. We derive here the scaling law to convert from microscale SEI expansion to macroscale total cell thickness expansion. Assuming constant particle density, we have that:

$$\rho_{\mathrm{s}} = dm_{\mathrm{sei}}/dV_{\mathrm{sei}}, \tag{3.55}$$

where m_{sei} is the SEI mass accumulated in kg and ρ_{s} is the SEI density in kg/m^3, and V_{sei} is the SEI volume in m^3. SEI mass accumulation is proportional to total charge accumulated, Q_{sei}, according to:

$$dm_{\mathrm{sei}} = \frac{M_{\mathrm{s}}}{nF} dQ_{\mathrm{sei}}, \tag{3.56}$$

where M_{s} is the molar mass and $Q_{\mathrm{sei}} = \int I_{\mathrm{sei}} dt$ is the charge accumulated to form SEI. It follows that:

$$dV_{\mathrm{sei}} = V_{\mathrm{sei}} \frac{dQ_{\mathrm{sei}}}{nF}. \tag{3.57}$$

We can then use 3.56 and 3.57 to derive an expression for the SEI thickness on the negative electrode particles:

$$\delta_{\mathrm{sei}} = \frac{dV_{\mathrm{sei}}}{N^- \cdot 4\pi (R^-)^2} \tag{3.58}$$

$$= \frac{1}{N^- \cdot 4\pi (R^-)^2} V_{\mathrm{sei}} \frac{dQ_{\mathrm{sei}}}{nF} \tag{3.59}$$

where N^- is the number of negative electrode particles. Differentiating both sides and substituting $I_{\mathrm{sei}} = dQ_{\mathrm{sei}}/dt$ and $j_{\mathrm{sei}} = I_{\mathrm{sei}}/(N^- \cdot 4\pi (R^-)^2)$ yields:

$$\frac{d\delta_{\mathrm{sei}}}{dt} = V_{\mathrm{sei}} \frac{j_{\mathrm{sei}}}{nF}. \tag{3.60}$$

Eq. 3.52 can finally be used to convert the SEI thickness growth into a macroscopic expansion:

$$dL_{\mathrm{SEI}} \triangleq \Delta_{\mathrm{SEI}} = \frac{L^-}{R^- + dR^-} \delta_{\mathrm{sei}} \tag{3.61}$$

$$= \frac{L^-}{R^-(1 + \nu^-/3)} \delta_{\mathrm{sei}}, \tag{3.62}$$

where we have assumed that the SEI grows on the negative electrode particle with a radius $R^- + dR^-$.

CHAPTER 4

Formation Model Applications

4.1 Introduction

This chapter explores how the formation model introduced in Chapter 3 can be applied towards a variety of future applications in designing better formation protocols, improving battery factory process control capabilities, and improving battery lifetime prediction.

In the first application, we demonstrate that the formation model can be applied to predict the dynamics of a faster formation protocol. We show that the formation model can reproduce experimental data on the fast formation protocol, including voltage and cell thickness expansion, within reasonable accuracy. We then compare and contrast the first cycle charge dynamics between the fast formation protocol vs. a baseline control protocol, demonstrating that faster formation protocols can lead to higher lithium consumption during the formation cycles but ultimately lead to a more passivating SEI that may be better for cycle life.

In the second application, we extend the usage of the formation model to directly simulate cycle life. In doing so, we demonstrate that the formation model can serve as a general-purpose lifetime simulation tool, one which can support future understanding of how formation parameters can affect lifetime. By comparing the simulated cycle life of cells formed using both a fast formation protocol and a baseline formation protocol, we show that the fast formation protocol showed a marginally lower degradation rate owing to a lowered homogenized SEI diffusivity. The formation model finally predicted that fast formation may help delay the onset of electrolyte additive knees, a novel prediction arising from the multi-species reaction representation SEI growth afforded by the model.

In the third application, we pose the formation protocol optimization problem as an optimal control problem, highlighting the promise of using model-based control approaches that leverage formation as a potential tool for minimizing beginning-of-life cell variability. We first re-summarize the model equations in compact form. We next write down the optimal

control problem which treats the formation model and the model parameters as nonlinear constraints. We then develop a block diagram representation of the formation model to clarify the various interactions between the model sub-components. We finally develop a state-space realization of the model that further elucidates the mathematical structure of the system of equations.

In the fourth application, we view the formation model through the lens of parameter identification. We highlight that the formation model can lend itself towards improved identifiability of crucial cell degradation parameters such as D_{sei}. The formation model, when applied to experimental formation data, can potentially improve the accuracy of lifetime model parameterization without needing the typical parameter tuning process involving aged data. Toward this goal, we first provide a parameter sensitivity study to understand which model parameters have the greatest effect on the modeled outputs such as SEI thickness and SEI reaction current density.

In the fifth and final application, we utilize the formation model to rationalize physical connections between beginning-of-life diagnostic features. In doing so, we demonstrate that the formation model can help provide physical interpretations behind data-driven features. These diagnostic features are later used in Chapter 6 for applications in lifetime prediction. We present a case study here where the formation model is used to rationalize how the full cell resistance measured at low SOCs, or R_{LS}, is an indicator for the amount of lithium consumed during formation, or Q_{sei}. The physical connection we develop here will be further expanded upon in Chapter 6.

4.2 Application 1: Modeling Fast Formation

Here, we test the ability of the formation model developed in Chapter 3 to predict the system behavior of new formation protocols. We will focus on a particular case study of simulating a faster formation protocol proposed by An et al. [127]. This formation protocol will be later used as the basis for studying lifetime prediction applications in Chapter 6. For now, we focus on understanding whether the model can replicate experimental voltage and expansion data. We will also develop an understanding of the model-predicted first cycle dynamics as it relates to SEI passivation.

4.2.1 Methods

The formation model and model parameters used here are identical to those presented in Chapter 3. To review, the model was parameterized using a "baseline formation" protocol

which consisted of back-to-back C/10 charge/discharge cycles. The comparison of modeled vs. measured output for the baseline formation protocol was already presented in Chapter 3 and is reproduced in Figure 4.1(A,B) for convenience.

Experimental data on the fast formation protocol, which consisted of a rapid 1C charge to 3.9V followed by back-to-back shallow cycles at high SOCs (see Section 6.3.2), was collected on another pouch cell from the same batch of cells used in the work from Chapter 3. By choosing a cell from the same batch of cells as the baseline formation cell, cell design parameters including electrode capacities and electrolyte properties were kept constant across the experiments and the simulated result.

To simulate the fast formation protocol, the current input from the fast formation protocol was directly inputted into the formation model without modifying any of the model parameters. The simulation time spanned the formation cycles, the RPT following the formation cycle (to mirror the test protocol sequence of the baseline formation protocol), followed by a formation aging step which consisted of high-SOC storage for 2 weeks.

4.2.2 Results and Discussion

4.2.2.1 Model vs. Experiment

The model-predicted cell voltage and thickness expansion profiles are compared against the experimentally measured values in Figure 4.1(C,D). The modeled full cell voltage trace during formation qualitatively matched the experimentally measured values (Panel C). This result is perhaps surprising considering that the formation model was constructed using a 'dual-tank' representation which ignored solid-phase lithium concentration gradients that are bound to increase with increasing applied currents. Whereas the baseline formation protocol used a C/10 rate, the fast formation protocol used 1C. The model vs. experiment comparison suggests that, for the pouch cell design used for this study (see Table 6.1), the 1C rate does not induce high enough solid-phase lithium concentration gradients to render the full cell terminal voltage predictions inaccurate.

The modeled cell thickness expansion during formation also qualitatively matched the experimental trend within some error (Panel C). However, the model underestimated the thickness expansion during the very first charge by ca. 8% and overestimated the thickness expansion at the end of fast formation by ca. 6%. The presence of these errors suggests that further refinements to the expansion equations (see Section 3.5.6) may be necessary to accurately predict thickness expansion under high C-rates. These errors will become important to consider when relying on the model to predict SEI properties such as SEI density. Further model refinements to improve model accuracy are left as future work.

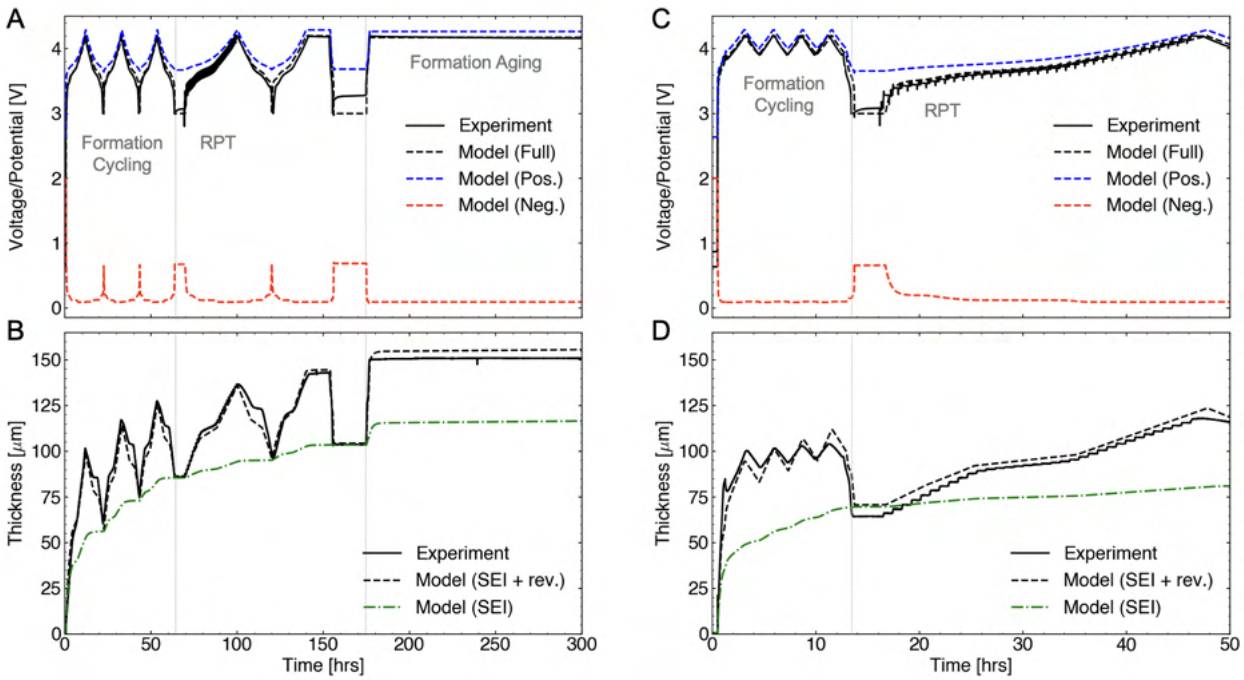

Figure 4.1: Model vs. experiment: comparison of different formation protocols. (A-B) Voltage and cell thickness expansion during the baseline formation protocol (from Figure 3.9). Formation cycling was followed by an RPT and formation aging. (C-D) Voltage and cell thickness expansion during the fast formation protocol. The model was tuned using data from the baseline formation protocol and ran directly on the fast formation current profile input without re-tuning.

4.2.2.2 First Cycle Charge Dynamics

We next turn to understanding the first cycle charge dynamics of fast formation. A central curiosity we focus on is the effect of the initial charge cycle on the passivation properties of the SEI. A pertinent question to ask here is: "how does the design of the initial formation charge cycle affect SEI passivation?"

The fast formation model supports the exploration of this question by enabling simulation of multiple lithium-consuming reactions to form the SEI (Section 3.5.8) which we briefly review here. The model treats each reaction as occurring in parallel, i.e.:

$$j_{\text{sei}} = \sum_{l} j_{\text{sei},l} \tag{4.1}$$

where j_{sei} is the total SEI reaction current and $j_{\text{sei},l}$ is the current from the SEI reaction

involving the lth electrolyte component according to the generalized reaction scheme:

$$\text{Elyte}_l + n\text{Li}^+ + n\text{e}^- \rightarrow \text{SEI}_l, \tag{4.2}$$

where n is the number of participating electrons. While each reaction occurs in parallel, the reactions remain coupled via a shared homogenized diffusivity term according to:

$$\bar{D}_{\text{sei}}(t) = \left(\frac{1}{Q_{\text{sei}}(t)} \sum_l \frac{Q_{\text{sei},l}(t)}{D_{\text{sei},l}} \right)^{-1} \tag{4.3}$$

where $D_{\text{sei},l}$ is the diffusivity of the lth SEI, $Q_{\text{sei},l}$ is the capacity of lithium lost to form the lth SEI, and $Q_{\text{sei}}(t) = \sum_l Q_{\text{sei},l}(t)$ is the total capacity of SEI formed. The diffusivity of each SEI component is thus weighted by the quantity of that SEI formed. Intuitively, each electrolyte component must pass through all formed SEI layers to react at the surface of the electrode/electrolyte interface, and thus the presence of each SEI layer affects the diffusion of all subsequent SEI-forming electrolyte species.

The formation model implemented two electrolyte components, $l = \{\text{EC}, \text{VC}\}$, where EC is the main electrolyte solvent and VC is an electrolyte additive. The relevant electrolyte and SEI properties of this system were given in Table 3.2 and re-summarized in Table 4.1. Of particular note is the difference in SEI diffusivities, D_{sei}: EC has a lower diffusivity compared to VC, implying that the more the composite SEI film is comprised on EC, the lower the homogenized diffusivity of the composite film will be. (The effect of homogenized diffusivity on cell lifetime will be further discussed in Section 4.3.)

Property	EC	VC	Unit	Source
n	2	2	-	Refs. [57], [41]
c^0	4541.0	304.4	mol/m^3	Calculated
U_{sei}	0.8	1.35	V vs Li/Li$^+$	Refs. [44], [111]
D_{sei}	4.2×10^{-20}	6.6×10^{-18}	m^2/s	Fitted

Table 4.1: Summary of electrolyte and SEI properties

We now follow the progression of the EC and VC reactions during the first charge cycle for both the baseline formation and the fast formation protocols, shown in Figure 4.2. In both simulations, the cell was rested for 30 mins and then began to charge. The baseline formation protocol used a C/10 charge while the fast formation used a 1C charge (Panel A). In both formation protocols, VC reacted first due to the higher reaction potential (Panel B). As the charge cycle proceeds, a transition occurs: as the negative electrode potential drops below the

EC reaction potential and EC begins to reduce. As EC begins to reduce, the homogenized SEI diffusivity is decreased since the EC-derived SEI product has a lower diffusivity compared to the VC-derived SEI product. The decrease in SEI diffusivity suppresses further reaction of VC. In the baseline formation protocol, this transition event occurred after ca. 40 minutes. However, in the fast formation, this transition occurs within 3 minutes of starting the charge owing to the ten-fold increase in charge C-rate. As a result, the fast formation protocol produced an SEI film that is compositionally more skewed towards EC (Panel C). Since EC has a lower SEI diffusivity than VC, the overall homogenized SEI diffusivity of the fast formation cell is thus lower compared to the baseline formation cell.

Finally, we note that the fast formation cell also produced a greater quantity of SEI during the first charge cycle: after 1.5 hours, the fast formation protocol produced 162 mAh of SEI capacity whereas the baseline formation protocol produced only 110 mAh. We attribute the increased production of SEI during fast formation to the higher C-rate used which plays a dual role. First, the higher C-rate increases the reaction overpotential at the negative electrode surface driving up the reaction rate during the reaction-limited regime of SEI formation (see Section 3.7.2.1). Second, the higher C-rate increases the effect of the SEI boosting mechanism driven by an increased rate of negative electrode expansion (3.5.7).

The effect of the formation protocol on the homogenized SEI diffusivity, $\bar{D}_{\text{sei}}$, is further illustrated in Figure 4.3, which plots $\bar{D}_{\text{sei}}$ as a function of the fractional composition of EC in the SEI according to Equation 4.3. During the first charge cycle, $\bar{D}_{\text{sei}}$ takes on the value of the VC diffusivity since VC reacts first. As the negative potential drops below the EC reaction potential, the SEI film becomes a mixture of both EC and VC reaction products. Since the diffusivity of EC is lower than that of VC, $\bar{D}_{\text{sei}}$ decreases as more of the EC reaction product is formed. After 1.5 hours, the fast formation protocol resulted in a lower $\bar{D}_{\text{sei}}$ (marker 2) compared to the baseline formation protocol (marker 1), indicating a more passivating SEI.

In summary, the formation model predicts that fast formation will result in a more passivating SEI, that is, an SEI that has a lower homogenized SEI diffusivity by the end of the formation protocol. The lowered SEI diffusivity implies that fast formation may result in a cell that has better cycle life compared to the baseline formation protocol. To test this theory, we turn to the next section where we apply the formation model for simulating cycle life.

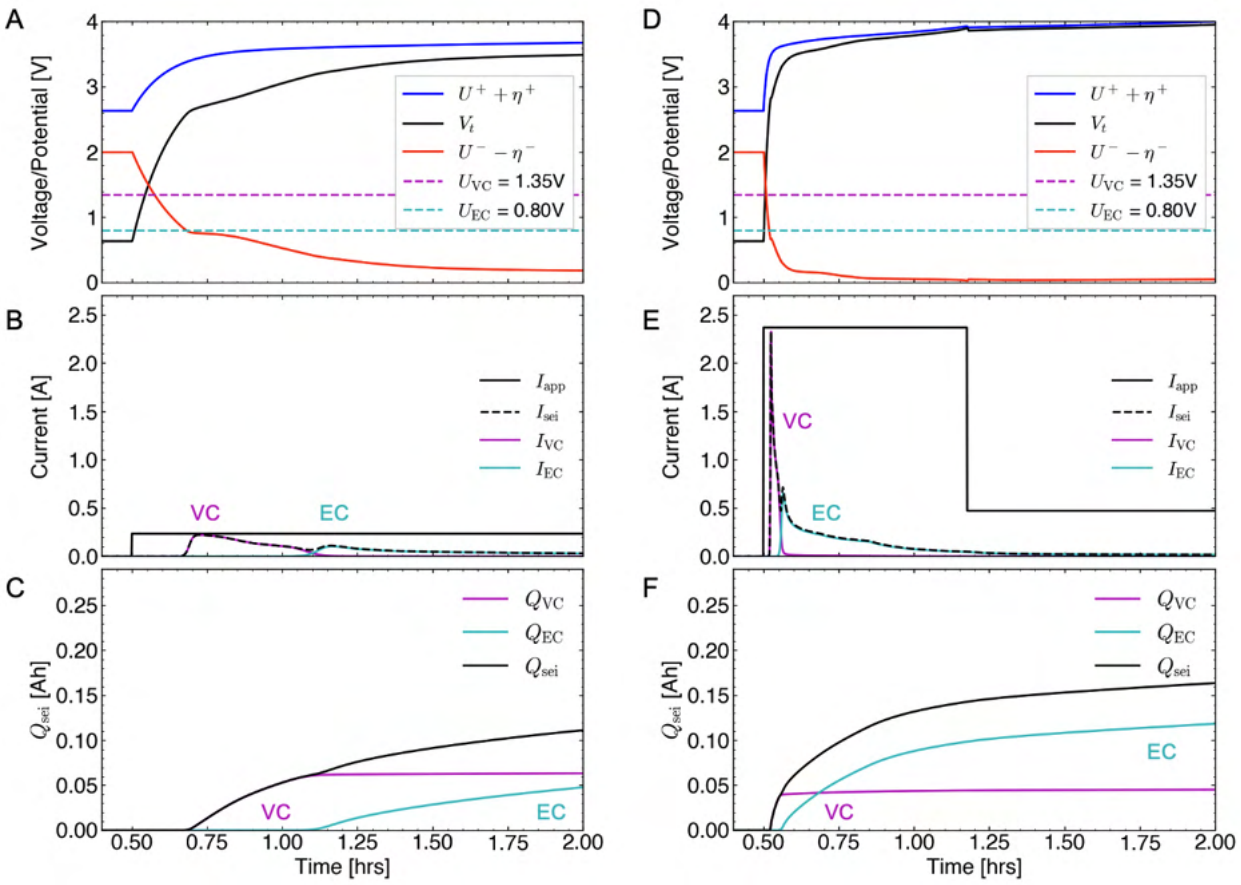

Figure 4.2: First cycle charge dynamics comparison between baseline formation (A-C) and fast formation (D-F). First row: full cell potentials and half-cell potentials. VC and EC reaction potentials are shown in dashed lines. Second row: applied currents plotted alongside SEI reaction currents. Third row: SEI capacity integrated from the SEI reaction currents.

4.3 Application 2: Lifetime Simulation

We next leverage the formation model to simulate cell cycle life. Using the formation model to directly simulate aging confers several advantages. First, the formation model provides a consistent representation of an essential degradation process, SEI growth, during the formation process and over the remainder of a cell's life. The resulting simulation therefore bridges the gap between a critical battery manufacturing process step (the formation process) and the resulting cell lifetime. Note that additional degradation mechanisms beyond SEI growth, such as active material losses, can be incorporated into the formation modeling framework, which we leave as future work. For this work, we stay focused on the SEI growth process which is generally understood to be the dominant degradation mechanism in many commercial lithium-ion systems and under typical use cases [128, 7].

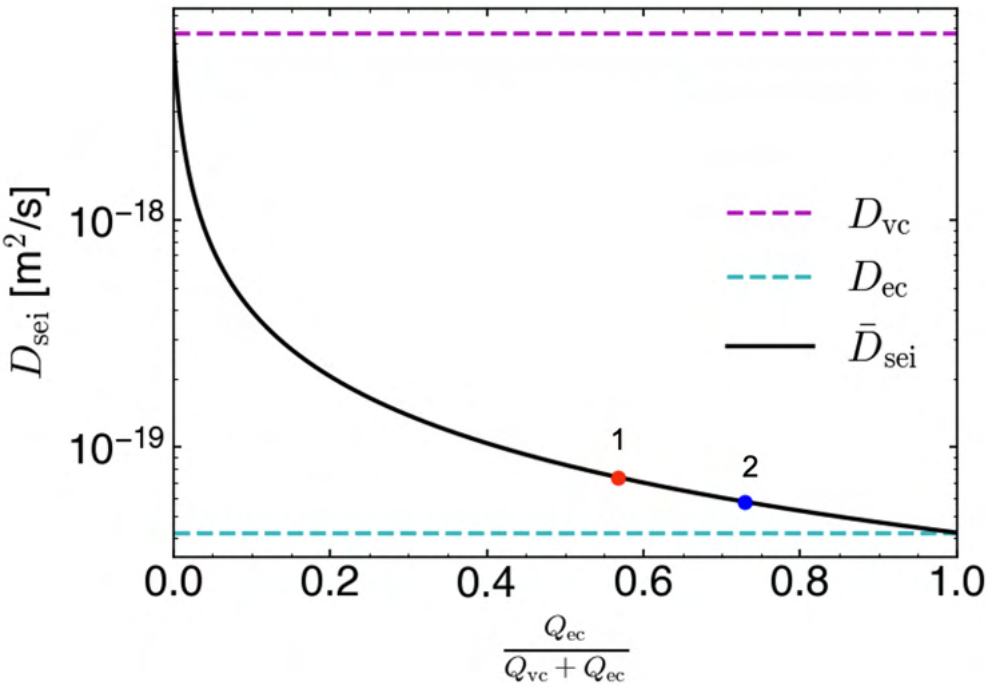

Figure 4.3: Effect of formation protocol on $\bar{D}_{\text{sei}}$. After 1.5 hrs of the first charge, fast formation has a lower $\bar{D}_{\text{sei}}$ (blue marker 2) compared to baseline formation (red marker 1), indicating a more passivating SEI.

Second, the formation model captures path-dependent aging by supporting simulations of arbitrary current profiles. The model also unifies the representation of cycling and calendar life aging via the boosted SEI growth mechanism. With this mechanism, the boost sensitivity factor, γ (Eq. 3.32), can be viewed as a 'cycling loss sensitivity' factor. As γ approaches zero, no SEI growth boosting occurs during cycling and the diffusion process remains under steady-state. Under this condition, the cell experiences only calendar aging losses. Such a scenario could describe 'power cells' having high electrode porosities and low energy densities. Meanwhile, as γ increases, the SEI growth process during cycling becomes boosted, so the cell becomes more sensitive to damage during cycling. Such a scenario could describe 'energy cells' having low electrode porosities and high energy densities. With the boosting mechanism, dynamical changes to the aging profile, including transitions between cycling and aging conditions, are naturally represented by the model.

Finally, the formation model, being a zero-dimensional model, is fast to run, making it suitable for lifetime simulations which often involve simulating hundreds to thousands of cycles. The existing implementation of the formation model, which uses a 5-second timestep and a simple forward Euler integration scheme, simulating 300 cycles is accomplished within

90 seconds of runtime. With further numerical optimizations, such as using built-in ordinary differential equations (ODE) solvers or using adaptive time steps [129], the simulation speed can be further decreased, enabling the possibility of on-board implementations in a battery management system (BMS) context.

4.3.1 Methods

Previously, our simulations spanned the formation cycling and formation aging steps only. The simulations were halted at the end of the formation aging step. Now, we will modify the simulations to include the simulation of additional cycles after the formation cycling steps are completed to represent an accelerated cycle life test protocol. Note that we have omitted the 2-week formation aging step in these simulations for brevity. Both the fast formation protocol and baseline formation protocol simulations are extended in this manner.

The cycling protocol we chose to simulate is a 1C/1C charge-discharge cycle, a protocol that will later be revisited experimentally as part of Chapter 6. For each cell simulated, a variable rest time was inserted as part of the RPT following formation so that both cells would begin the cycling test at the same time (Figure 4.4A). For the cycle life portion of the simulations, no modifications to the formation model or the model parameters were made. Note that the model parameters were tuned using formation cycling and formation aging data only. No cycle life data was involved in the parameter tuning process.

Since the only degradation mechanism represented in the model is lithium lost to form the SEI, the full cell discharge capacity fade rate can be simply understood as:

$$Q_{\mathrm{d}}(t) = Q_{\mathrm{d,0}} - Q_{\mathrm{sei}}(t) \tag{4.4}$$

where $Q_{\mathrm{d}}(t)$ is the full cell discharge capacity at time t, $Q_{\mathrm{d,0}}$ is the maximum possible capacity, and $Q_{\mathrm{sei}}(t)$ is the lithium lost to the SEI at time t. Notably, the domain of t now includes formation cycling, formation aging, and subsequent cycling. $Q_{\mathrm{d,0}}$ is identical for a given cell design, so the focus of the study is to understand differences in $Q_{\mathrm{sei}}(t)$ due to differences in formation protocols.

4.3.2 Results and Discussion

4.3.2.1 Lithium Consumption During Formation

Figure 4.4B compares the Q_{sei} trajectory between the two formation protocols. The cell that underwent fast formation lost more lithium to form the SEI during the initial formation cycle. By the time both formation protocols were completed, the cell that underwent

fast formation lost 342.2 mAh of capacity to form the SEI, whereas the cell that underwent baseline formation lost 330.8 mAh. Fast formation thus increased Q_{sei} by ca. 11 mAh according to the model. To preview a comparison against experimental results, the experiments reported in Chapter 6 suggested that fast formation increased Q_{sei} by 23 mAh. Thus, the model-predicted Q_{sei} agreed with the qualitative trend shown in the experimental data, though some numerical differences persist.

4.3.2.2 Q_{sei} Crossover

A key observation in the modeled Q_{sei} trend is highlighted by an asterisk (*) in Figure 4.1B which shows a crossover point in the Q_{sei} between the two cells. After this point, the Q_{sei} for the fast formation cell becomes lower than that of the baseline formation cell. A zoomed-in plot of this transition point, shown in Figure 4.10, shows this cross-over point clearly. After more than 300 cycles, the Q_{sei} for the fast formation cell continues to lag behind that of the baseline formation cell, shown in Figure 4.11.

To explain the presence of the Q_{sei} crossover point, we next study the trajectory of the homogenized SEI diffusivity $\bar{D}_{\text{sei}}$ which indicates SEI passivation as previously discussed in Section 4.2.2.2. Figure 4.4C verifies that the fast formation protocol yielded a lower $\bar{D}_{\text{sei}}$ throughout the formation steps. By plotting $\bar{D}_{\text{sei}}$ against Q_{sei} (inset), we verify that the fast formation protocol results in lowered $\bar{D}_{\text{sei}}$ for any given amount of lithium consumption; that is, the SEI formed by fast formation grows more slowly at any point along the degradation trajectory.

In summary, the formation model predicted that the fast formation protocol consumed more lithium during formation cycling compared to the baseline formation protocol. The increased lithium consumption resulted in a lower initial cell discharge capacity for the cell that underwent fast formation. However, the rate of growth of Q_{sei} for this cell was also comparatively lower, implying a slower degradation rate. As we will show later in Chapter 6, these results are consistent with the experimentally measured trends in battery, that fast formation protocol not only did not hurt lifetime, but it slightly improved it.

4.3.2.3 Electrolyte Additive Consumption and Knees

Revisiting Figure 4.4B, we notice that, while the fast formation protocol resulted in a numerically lower value of Q_{sei} compared to the baseline formation protocol after five cycles, this difference becomes marginal over extended cycles. This trend is explained by the fact that, for both formation protocols, the homogenized diffusivity $\bar{D}_{\text{sei}}$ (Panel C) converges towards the diffusivity of the EC-derived film as EC continues to reduce to create more SEI.

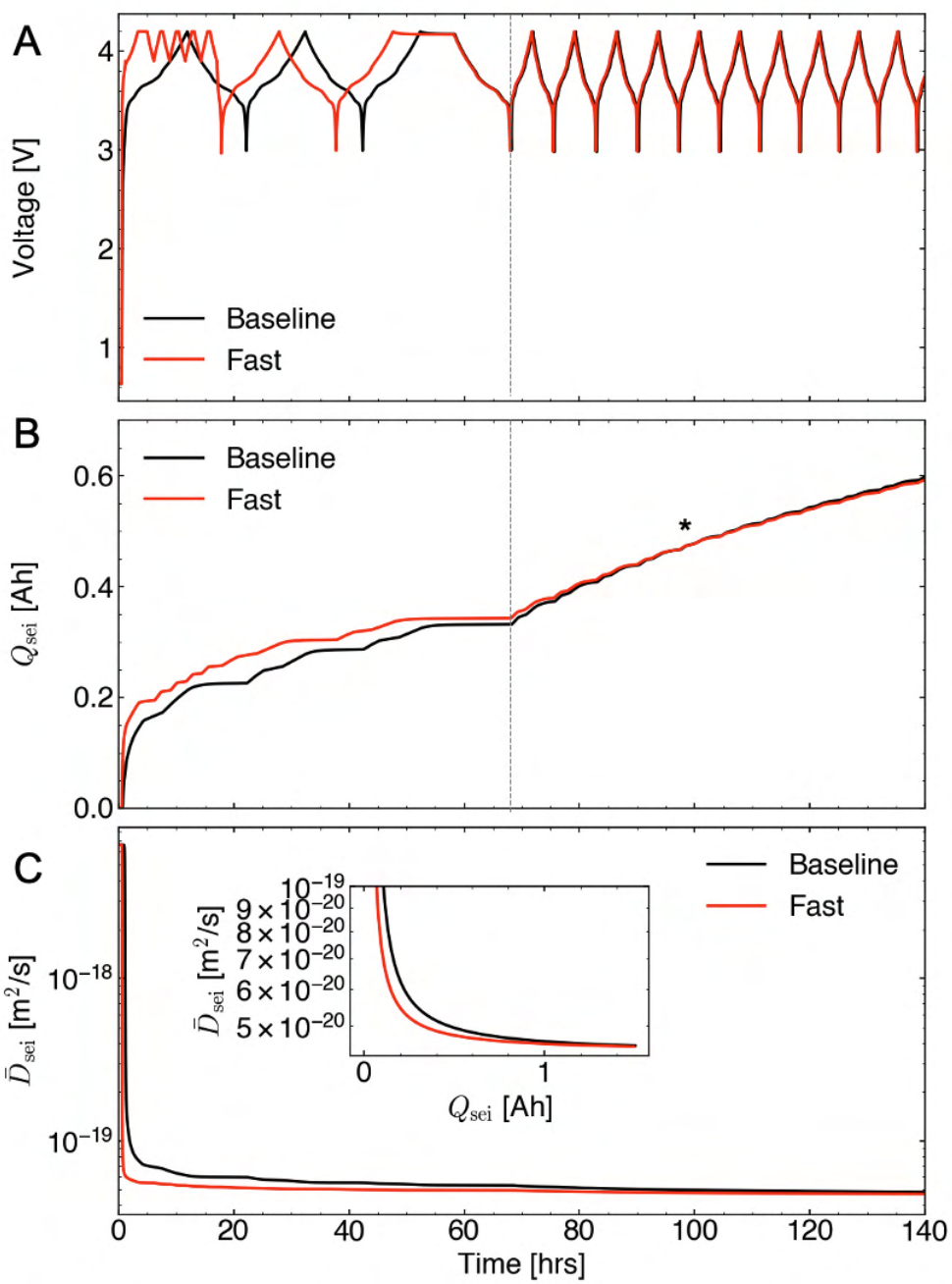

Figure 4.4: Combined formation and cycle life simulations: baseline formation (black) vs. fast formation (red). (A) Voltage traces during and after formation. (B) Capacity of lithium lost to form the SEI. Asterisk (*) shows the cross-over point in SEI capacity which occurs after the fifth cycle after formation completes. (C) Evolution of the homogenized SEI diffusivity $\bar{D}_{\text{SEI}}$. Inset: $\bar{D}_{\text{SEI}}$ plotted against Q_{sei}.

We extended the simulation to 300 cycles to confirm that the initial differences in Q_{sei} and $\bar{D}_{\text{sei}}$ get smaller throughout the cycles, see Figure 4.11. We further plotted the simulated

cycle-by-cycle discharge capacity, shown in Figure 4.5A, which confirms that the simulated discharge capacities between fast formation and baseline formation are trivial.

Thus, while fast formation decreased the rate of growth of Q_{sei} over the simulated cycles, this decrease is not likely to be large enough to explain the differences in cycle life reported in Chapter 6 where fast formation has been reported to improve cycle life by 25 to 50%. Another mechanism beyond differences in $\bar{D}_{\text{sei}}$ is thus needed to explain the experimentally observed phenomenon of fast formation improving cycle life.

Here, we re-examine the outputs of the formation model to propose an alternative explanation related to electrolyte additive depletion. Turning to Figure 4.4B, we observe that the fast formation cell had markedly higher VC concentration throughout the cycle life test, by about 25%. Meanwhile, the concentration of EC for both the fast formation and baseline formation cells stayed nearly the same (Panel C). Fast formation is thus predicted to suppress the consumption of VC during the initial formation cycle. The fast formation protocol achieves this by more quickly decreasing the negative electrode potential to begin the EC reaction. The EC reaction suppresses further reactions with VC by making a more passivating SEI, i.e. decreasing the value of $\bar{D}_{\text{sei},r}$. The baseline formation protocol spends a comparatively longer time cycling through the VC reaction regime and thus consumes more VC during formation.

Electrolyte additive depletion has been reported to have a disproportionate effect on lifetime considering their relatively low quantity compared to the solvent. Small quantities of electrolyte additives have been reported to delay the occurrence of the knee, see for example Ma et al. [130] and Li et al. [131]. It has also been experimentally demonstrated that the depletion of certain electrolyte additives, such as fluroethylene carbonate (FEC), can directly lead to a knee [132, 133, 134]. The formation model predicted that the additive in our system, VC, depleted more quickly from baseline formation than from fast formation. This model prediction could indicate that fast formation may be capable of delaying knee based on depletion of the VC additive. Note that the formation model does not yet account for the explicit dynamics of knee mechanisms, which we leave as future work.

In summary, a careful interrogation of the formation model outputs yielded a novel hypothesis explaining why fast formation can result in cells having longer cycle life: the fast formation cell suppressed the consumption of the VC additive during the formation cycle, leaving more VC remaining in the system during cycling which delayed the eventual additive consumption knee. This hypothesis will be further verified using experimental data from Chapter 6. We will see in the experimental data that the degradation rate of all cells are nearly identical until the occurrence of the knee, but cells that underwent fast formation had a delayed onset of the knee, suggesting that the main effect of the formation protocol is

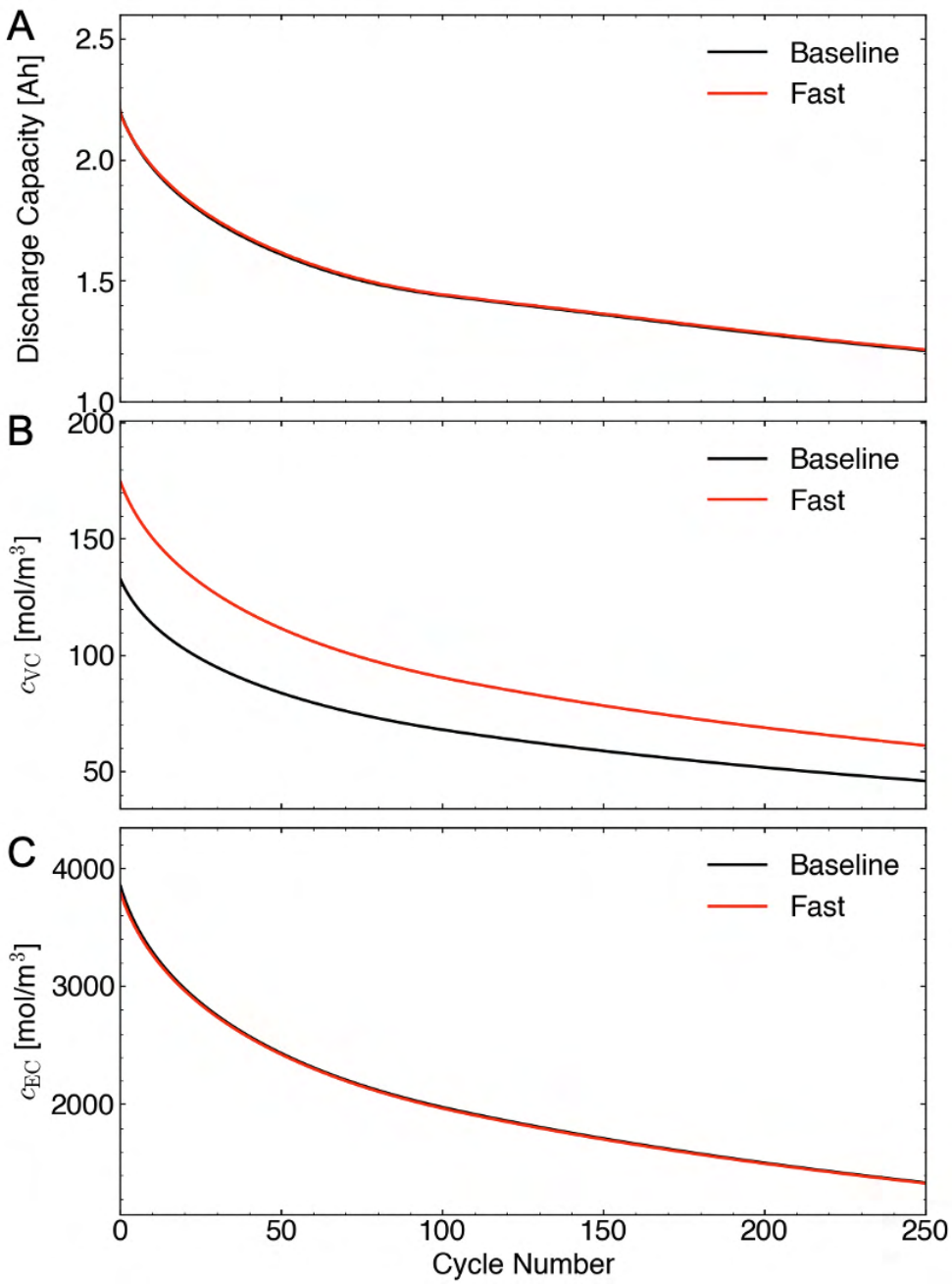

Figure 4.5: Model-predicted discharge capacity (A), VC additive concentration (B) and EC solvent concentration (C) over cycle number.

to influence the occurrence of the knee.

4.4 Application 3: Optimal Control

We now discuss how the formation model can be adapted towards future applications in optimal control of formation protocols. A control-oriented approach provides a rigorous framework for guaranteeing the optimality of a formation protocol given a design target, such as optimizing for formation time, cell lifetime, or both. A control-oriented approach also enables the design of controllers enabling real-time control of formation protocols that can adapt to changes in measured outputs. For example, a controller may be designed to adaptively change the formation protocol based on the measured output capacity. In doing so, the distribution of capacities may be further tightened. In another application, a controller can take upstream factory process parameters, such as electrode loadings, as an input, to adaptively change the formation protocol to maintain certain output targets such as cell energies.

While the bulk of the work in formation protocol optimal control remains to be done, we devote this section to setting up some mathematical preliminaries to encourage more future work in this direction.

4.4.1 Model Equations

We now re-summarize the main model equations from Chapter 3 for convenience. The formation model consists of four components: (1) electrode lithiation and overpotential dynamics, (2) multi-species SEI growth, (3) cell-level expansion, and (4) SEI growth boosting during charging. A representation of the model is shown in Fig. 3.3 which highlights the physical interpretation in Panel A and the non-linear input functions in Panel B. Symbols are defined in Tables 3.2 and 3.3. Here, we summarize the governing equations in compact form. For a complete derivation and discussion of the origin of these equations, see Ref. [135].

The *electrode lithiation dynamics* are represented by a "dual-tank" model which tracks average solid-phase lithium concentrations $\theta^{\pm}$ without considering concentration gradients (Eqs. 4.5, 4.6). This reduced order representation is reasonable for current rates typically used in battery formation which are less than C/5. At the positive electrode, the applied current I_{app} is used to update the lithium concentration. However, at the negative electrode, some of the applied current goes into SEI-forming reactions (Eq. 4.7) and only the intercalation current I_{int} contributes to increasing the solid-phase lithium concentration. Initial conditions for the system correspond to a fully lithiated positive electrode and a fully

delithiated negative electrode (Fig. 3.3B).

$$\frac{d\theta^+(t)}{dt} = -\frac{I_{\text{app}}}{Q^+} \qquad \text{I.C. :} \quad \theta^+|_{t=0} = 1 \tag{4.5}$$

$$\frac{d\theta^-(t)}{dt} = +\frac{I_{\text{int}}}{Q^-} \qquad \text{I.C. :} \quad \theta^-|_{t=0} = 0 \tag{4.6}$$

$$I_{\text{int}}(t) = I_{\text{app}}(t) - I_{\text{sei}}(t) \tag{4.7}$$

We take the convention that $I < 0$ represents charging.

The *electrode surface overpotential dynamics* are approximated using first-order dynamics (Eqs. 4.8,4.9) which is equivalent to an R-RC circuit model. Here, the series resistance $R^{\pm}_{\text{ct}}$ encapsulates charge-transfer reactions at the electrode-electrolyte interface while the resistance associated with the RC pair $R^{\pm}_{\text{dif}}$ approximates solid-state diffusion effects. As with the lithiation dynamics, the negative electrode overpotential dynamics reference I_{int} instead of I_{app}.

$$\eta^{\pm}(t) = R^{\pm}_{\text{ct}} I(t) + R^{\pm}_{\text{dif}} I^{\pm}_{\text{dif}}(t) \tag{4.8}$$

$$\frac{dI^{\pm}_{\text{dif}}(t)}{dt} = -\frac{1}{\tau^{\pm}_{\text{dif}}} I^{\pm}_{\text{dif}}(t) + \frac{1}{\tau^{\pm}_{\text{dif}}} I(t) \tag{4.9}$$

$$I(t) \triangleq \begin{cases} I_{\text{app}}(t) & \text{(Pos. electrode)} \\ I_{\text{int}}(t) & \text{(Neg. electrode)} \end{cases} \tag{4.10}$$

The measured cell terminal voltage V_t can then be calculated from the cell equilibrium (i.e. OCV) potentials $U^{\pm}$ and the cell overpotentials $\eta^{\pm}$ according to

$$V_{\text{t}}(t) = U^+(\theta^+(t)) - U^-(\theta^-(t)) + \eta^+(t) + \eta^-(t). \tag{4.11}$$

The *multi-species SEI growth* equations capture reaction-diffusion dynamics of multiple SEI reduction reactions occurring in parallel. The total cell SEI reaction current is obtained from the particle-level reaction current density using a geometric pre-factor (Eq. 4.12).

$$I_{\text{sei}}(t) = a^- A^- L^- j_{\text{sei}}(t) \tag{4.12}$$

The model represents each reacting molecule as participating in independent reactions according to the general reaction scheme:

$$\text{S} + n\text{e}^- + n\text{Li}^+ \rightarrow \text{SEI} \downarrow + \text{P} \uparrow \tag{4.13}$$

where n is the number of electrons participating in the reaction, S is the reacting molecule, SEI is the solid reduction product, and P is a reaction byproduct, usually a gas. In this representation, each reacting molecule must diffuse through a homogenized SEI medium with volume-averaged properties to arrive at the negative electrode surface where the reaction takes place [135]. The total SEI reaction current density j_{sei} is thus the sum of current densities of each individual reaction r (Eq. 4.14), given by:

$$j_{\text{sei}}(t) = \sum_r j_{\text{sei},r}(t) \tag{4.14}$$

The reaction dynamics for each reaction are described by two limiting currents (Eq. 4.15). The first limiting current corresponds to kinetic limitations which follow Tafel kinetics assuming the SEI reaction is irreversible (Eq. 4.16). The limiting current corresponds to diffusion limitations which are governed by Fick's law (Eq. 4.18) [136].

$$\frac{1}{j_{\text{sei},r}(t)} = \frac{1}{\tilde{j}_{\text{rxn,r}}(t)} + \frac{1}{\tilde{j}_{\text{dif,r}}(t)} \tag{4.15}$$

$$\tilde{j}_{\text{rxn,r}}(t) = n_r F c_r^0 k_r \exp\left(-\frac{\alpha_r n_r F}{RT}\eta_{\text{sei},r}(t)\right) \tag{4.16}$$

$$\eta_{\text{sei},r}(t) = \eta^-(t) + U^-(\theta^-(t)) - U_{\text{sei},r} \tag{4.17}$$

$$\tilde{j}_{\text{dif,r}}(t) = \frac{n_r F c_r^0 \bar{D}_{\text{sei},r}}{\delta_{\text{sei}}(t)} \tag{4.18}$$

The *cell-level thickness* equations convert particle-level expansion to electrode-level expansion via scaling laws [136, 135]. The model makes a distinction between cell thickness growth due to SEI growth (Eq. 3.25) versus reversible, intercalation-induced expansion of the electrodes (Eq. 4.23).

$$\frac{d\delta_{\text{sei},r}(t)}{dt} = V_{\text{sei},r}\frac{j_{\text{sei},r}(t)}{n_r F} \tag{4.19}$$

$$\delta_{\text{sei}}(t) = \sum_r \delta_{\text{sei},r}(t) \tag{4.20}$$

$$\Delta_{\text{tot}}(t) = \Delta_{\text{sei}}(t) + \Delta_{\text{rev}}(t) \tag{4.21}$$

$$\Delta_{\text{sei}}(t) = \frac{NL^-}{R^-(1+\nu^-(\theta^-(t))/3)}\delta_{\text{sei}}(t) \tag{4.22}$$

$$\Delta_{\text{rev}}(t) = N\left(\frac{L^+}{3}\nu^+(\theta^+(t)) + \frac{L^-}{3}\nu^-(\theta^-(t))\right) \tag{4.23}$$

Note that the SEI thickness $\delta_{\text{sei},r}$ can be re-expressed by substituting Eq. (3.35) into Eq.

(4.19) to yield:

$$\delta_{\text{sei},r}(t)\frac{d\delta_{\text{sei},r}(t)}{dt} + \frac{\bar{D}_{\text{sei},r}}{k_r\phi_r(t)}\frac{d\delta_{\text{sei},r}(t)}{dt} = \varphi\bar{D}_{\text{sei},r} \tag{4.24}$$

with

$$\phi_r \triangleq \exp\left(-\frac{\alpha_r n_r F\eta_{\text{sei},r}(t)}{RT}\right) \tag{4.25}$$

$$\varphi \triangleq \frac{V_{\text{sei},r}}{c_r^0 n^2 F^2}. \tag{4.26}$$

The *boosted SEI growth* mechanism models the fracturing of the SEI during charge which exposes fresh electrode surfaces and temporarily increases the SEI growth rate. Introducing this mechanism enables the model to predict SEI growth rates during both formation cycling and formation aging using a unified set of equations [135]. SEI growth boosting is captured by treating the SEI diffusivity $\bar{D}_{\text{sei},r}$ as a time-dependent quantity that increases (i.e. gets "boosted") during charging but is then restored to a baseline value during discharging and resting. A first-order representation of the boosting dynamics $B(t)$ is used, given by:

$$f_{\text{B}} = \begin{cases} \tau_\uparrow\frac{dB(t)}{dt} + B(t) & = \gamma\frac{d\nu^-(\theta^-(t))}{dt} \quad I_{\text{app}} < 0 \\ \tau_\downarrow\frac{dB(t)}{dt} + B(t) & = 0 \qquad\qquad\qquad\quad \text{(o.w.)} \end{cases} \tag{4.27}$$

This equation shows that the negative electrode expansion rate $\frac{d\nu^-}{dt}$ acts as the boosting input during charging. γ can be interpreted as a boost sensitivity factor: cells with high values of γ will be boosted more during charge. Notice the usage of asymmetric time constants on charge ($\tau_\uparrow$), representing SEI fracturing, versus discharge and rest ($\tau_\downarrow$), representing SEI healing [135]. The boosting dynamics is then used to modify the SEI effective diffusivity $\bar{D}_{\text{sei},r}$ from Eq. (4.18) according to:

$$\bar{D}_{\text{sei},r}^{\text{boosted}}(t) = \bar{D}_{\text{sei},r}(1 + B(t)). \tag{4.28}$$

4.4.2 The Optimal Control Problem

An optimal formation protocol will yield an SEI that minimizes both the amount of lithium consumed during formation and the SEI reaction rate at the end of the formation process. With more lithium consumed, less lithium is available for reversible cycling so the initial cell capacity is lowered, an undesirable result. For the SEI reaction current density, a lower reaction current at the end of the formation process indicates a well-passivated SEI which minimizes the rate of further side reactions over life.

With the formation model, we can represent the amount of lithium consumed during

formation by the SEI thickness δ_{sei} and the SEI reaction rate by the SEI reaction current density j_{sei}. The SEI thickness is a valid metric for lithium consumption since, in the model, the SEI thickness is proportional to the total quantity of lithium consumed during formation. We can thus define a vector of terminal states:

$$z = [\delta_{\text{sei},f}, j_{\text{sei},f}]^T \tag{4.29}$$

with:

$$\delta_{\text{sei},f} \triangleq \delta_{\text{sei}}(t = t_f) \tag{4.30}$$

$$j_{\text{sei},f} \triangleq j_{\text{sei}}(t = t_f, \theta^- = \theta_f, I_{\text{app}} = 0). \tag{4.31}$$

These states represent the SEI thickness and SEI reaction current density evaluated at the end of the formation process. θ_f is a reference stoichiometry chosen to evaluate j_{sei}. In designing formation protocols, we will seek to simultaneously minimize $\delta_{\text{sei},f}$ and $j_{\text{sei},f}$.

We will assume for now that we have an observer for z. We can then pose a constrained optimization problem that seeks to find an input current profile $u(t)$ that minimizes a cost function $\mathcal{J}$ according to:

$$\min_{u(t)} \quad \mathcal{J} = z^T S z \tag{4.32}$$

$$\text{s.t.} \quad \dot{x}(t) = h(x(t), u(t)) \qquad \text{for} \quad t \in [0, t_f] \tag{4.33}$$

$$x(0) = x_0 \tag{4.34}$$

$$x(t) \in \mathcal{X} \qquad \text{for} \quad t \in [0, t_f] \tag{4.35}$$

$$u(t) \in \mathcal{U} \qquad \text{for} \quad t \in [0, t_f] \tag{4.36}$$

In this system of equations, $S \in \mathbb{R}^{2\times 2}$ is a matrix of weights, Eq. (4.34) gives the initial conditions, and Eqs. (4.35,4.36) are physical constraints imposed on the states and input, where $\mathcal{X}$ and $\mathcal{U}$ represent the range of permissible states and inputs, respectively (for example, the lithium stoichiometries $\theta^{\pm}$ are restricted to the range $[0, 1]$). Note that the cost function only includes the terminal cost since our focus is to optimize the SEI quality at the end of formation.

Solving the optimal control problem posed in Eq. 4.32 will require further mathematical developments which we leave for future work. Specifically, the formation model as-is consists of a set of coupled, nonlinear ODEs. Further simplifications to the model may be necessary to find closed-form solutions to Eq. 4.32. Alternatively, nonlinear optimization methods may be considered. In either case, further mathematical analysis of the system is warranted.

Towards this end, we next present some perspectives on how the formation model can be adapted towards solving an optimal control problem.

4.4.3 Block Diagram Representation

The formation model exhibits a high degree of coupling between the various model sub-components. These interactions are clarified using a simplified block diagram shown in Fig. 4.6. In particular, the SEI current density j_{sei} modifies the electrode lithiation dynamics by decreasing the current used to update the negative electrode lithium stoichiometry (Eq. 4.6). j_{sei} is also the main input into the thickness expansion sub-model since j_{sei} is integrated to give the SEI thickness δ_{sei} (Eq. 4.19). The negative electrode volume expansion function ν^- creates another source of coupling. The negative electrode lithium stoichiometry θ^- updates ν^- which in turn updates both the reversible Δ_{rev} and irreversible Δ_{sei} thickness expansion (Eqs. 4.22,4.23) as well as the SEI growth boosting dynamics (Eqs. 4.28,3.32). Finally, j_{sei} and δ_{sei} also contribute to the growth of the negative electrode interfacial charge transfer resistance R_{ct}^- according to:

$$R_{\text{ct}}^-(t) = \frac{j_{\text{sei}}(t)\delta_{\text{sei}}(t)}{\kappa_{\text{sei}}} \tag{4.37}$$

where κ_{sei} is the SEI conductivity in units of $[\text{Sm}^{-1}]$. This dependency was omitted from the model formulation in this work to simplify the discussion.

4.4.4 State Space Realization

Optimal control applications benefit from a well-formulated state-space realization of the system dynamics. Here, we propose one such realization. For simplicity, we have assumed a single-component SEI reaction scheme. The system can be written as:

$$\dot{x} = \mathcal{A}x + \mathcal{F}f(x,u) + \mathcal{B}u \tag{4.38}$$

$$y = \mathcal{C}x + \mathcal{G}g(x,u) + \mathcal{D}u, \tag{4.39}$$

with

$$x = [\theta^+, \theta^-, \tau_{\text{dif}}^+, \tau_{\text{dif}}^-, \delta_{\text{sei}}, B]^\top \tag{4.40}$$

$$y = [V_{\text{t}}, \Delta_{\text{tot}}]^\top \tag{4.41}$$

$$u = I_{\text{app}} \tag{4.42}$$

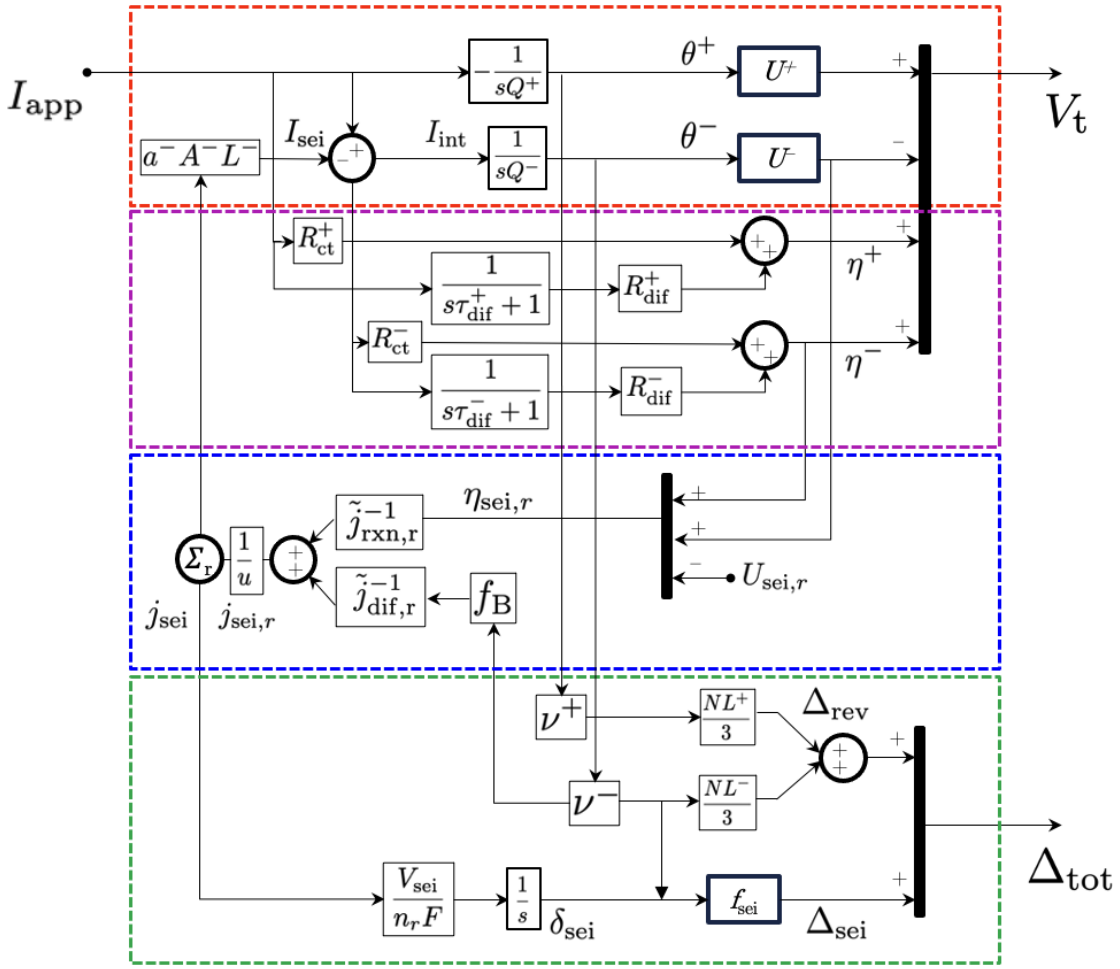

Figure 4.6: Simplified block diagram of the formation model. (A) Electrode lithiation dynamics via a "dual-tank" representation (B) Electrode overpotential dynamics. (C) Multi-species SEI reaction dynamics, including the SEI growth boosting mechanism. (D) Cell reversible and irreversible thickness expansion of the SEI growth and expansion model.

and

$$\mathcal{A} = \begin{bmatrix} 0 & 0 & 0 & 0 & 0 & 0 \\ 0 & 0 & 0 & 0 & 0 & 0 \\ 0 & 0 & -\frac{1}{\tau_{\text{dif}}^{+}} & 0 & 0 & 0 \\ 0 & 0 & 0 & -\frac{1}{\tau_{\text{dif}}^{-}} & 0 & 0 \\ 0 & 0 & 0 & 0 & 0 & 0 \\ 0 & 0 & 0 & 0 & 0 & 0 \end{bmatrix} \quad \mathcal{B} = \begin{bmatrix} -\frac{1}{Q^{+}} \\ \frac{1}{Q^{-}} \\ \frac{1}{\tau_{\text{dif}}^{+}} \\ \frac{1}{\tau_{\text{dif}}^{-}} \\ 0 \\ 0 \end{bmatrix} \tag{4.43}$$

$$\mathcal{C} = \begin{bmatrix} 0 & 0 & R_{\text{ct}}^{+} & R_{\text{ct}}^{-} & 0 & 0 \\ 0 & 0 & 0 & 0 & 0 & 0 \end{bmatrix} \quad \mathcal{D} = \begin{bmatrix} R_{\text{ct}}^{+} + R_{\text{ct}}^{-} \\ 0 \end{bmatrix} \tag{4.44}$$

$$\mathcal{F} = \text{diag}([0, -\frac{a^{-}A^{-}L^{-}}{Q^{-}}, 0, 0, \frac{V_{\text{sei}}}{n_r F}, 1]) \tag{4.45}$$

$$\mathcal{G} = \text{diag}([0, N]). \tag{4.46}$$

The functions $f(x,u)$ and $g(x,u)$ encode the non-linear components of the system dynamics and are given by:

$$f(x,u) = [0, f_2, 0, 0, f_2, f_6]^{\top} \tag{4.47}$$

$$g(x,u) = [g_1, g_2]^{\top} \tag{4.48}$$

where

$$f_2 \triangleq j_{\text{sei}} = \left[\frac{x_5}{\phi_1(1+x_6)} + \frac{1}{\phi_2 \exp(\phi_3[R_{\text{ct}}^{-}u + R_{\text{dif}}^{-}I_{\text{dif}}^{-} + U^{-}(x_2) - U_{\text{sei}}])} \right]^{-1} \tag{4.49}$$

$$f_6 = -\frac{x_6}{\bar{\tau}(u)} + \left[\frac{\gamma(u - \phi_4 f_2)}{\bar{\tau}(u) Q^{-}} \left. \frac{d\nu^{-}}{d\theta^{-}} \right|_{\theta^{-}} \frac{\text{sgn}(u) + 1}{2} \right] \tag{4.50}$$

$$\bar{\tau}(u) = \frac{\tau_{\uparrow} - \tau_{\downarrow}}{2} \cdot \text{sgn}(u) + \frac{\tau_{\uparrow} + \tau_{\downarrow}}{2} \tag{4.51}$$

$$\phi_1 = D_{\text{sei}} c^0 n F \tag{4.52}$$

$$\phi_2 = nFkc^0 \tag{4.53}$$

$$\phi_3 = -\frac{\alpha n F}{RT} \tag{4.54}$$

$$\phi_4 = a^{-}A^{-}L^{-} \tag{4.55}$$

and

$$g_1 = U^+(x_1) - U^-(x_2) \tag{4.56}$$

$$g_2 = \frac{L^-}{R^-(1+\nu^-(x_2))}x_5 + \frac{L^+}{3}\nu^+(x_1) + \frac{L^-}{3}\nu^-(x_2). \tag{4.57}$$

Note that $f_2 \triangleq j_{\text{sei}}$ and f_6 is derived from Eq. (3.32).

4.5 Application 4: Parameter Identification

Physics-based battery degradation models are typically calibrated against cycling and calendar aging data. See, for example, work by Reniers et al. [110]. These experimental datasets are collected on cells after formation has already been completed. Our work introduces an opportunity to leverage a new dataset, formation cycling and formation aging,to improve model parameter identification. The degradation parameters from the formation model (e.g. U_{sei}, D_{sei}, k_{sei}) may be directly transferable to other modeling contexts such as the Single Particle Model [137, 138] and the full Doyle-Fuller-Newman (or P2D) model [100, 139]. The experimental formation data provides additional, physically-relevant features, such as voltage traces during formation cycling and formation aging (Figure 3.3), the FCE (Figure 3.10) and the first charge dQ/dV (Figure 3.12), which all serve to constraint the set of possible degradation model parameters. Additionally, macroscopic expansion measurements can also be used to tune electrode parameters such as particle sizes and electrode dimensions (Eq. 3.24) as well as SEI properties such as SEI molar volume (Eq. 3.26).

We briefly introduce a parameter identification framework to motivate future work in this area. We define a vector of model parameters to identify as:

$$p = [D_{\text{sei}}, U_{\text{sei}}, k_{\text{sei}}, \gamma, ...]^T. \tag{4.58}$$

The parameter identification problem is then:

$$\begin{aligned} \underset{p}{\text{argmin}} &= \int_0^{t_f} \tilde{y}(\tau)^T Q \tilde{y}(\tau) d\tau \\ \text{s.t.} \quad & \text{Eqs.} \quad (4.33) - (4.36). \end{aligned} \tag{4.59}$$

where $y \triangleq [V_{\text{t}}, \Delta_{\text{tot}}]^T$, $\tilde{y} \triangleq y - \hat{y}$ represents the model output error, and $Q \in \mathbb{R}^{2\times 2}$ contains weights. Eq. (4.33) represents the system dynamics from Eqs. (4.5-4.27).

An expected obstacle for model parameter identification relates to the problem of pa-

rameter uniqueness, or parameter identifiability. Even with our reduced-order SEI growth representation, each electrolyte component is described by at least 4 intensive material properties: D_{sei}, U_{sei}, k_{sei}, and V_{sei}. While the presence of expansion measurements is expected to improve the identifiability of some parameters, it may still not be enough to identify all of the parameters. More ex-situ characterization may thus be generally needed to reduce the number of model parameters that need tuning. A suggested next step for this work is to first understand model parameter sensitivity, i.e. to answer the question of "which model parameters have the greatest impact on observed cell characteristics such as FCE, initial capacity, and degradation rates?" The next section thus introduces a simple parameter sensitivity study to highlight how this question could be answered.

4.5.1 Parameter Sensitivity

The formation model clarified how SEI passivation during formation depends on both electrolyte properties (e.g. electrolyte composition, additive amount, diffusivities, reaction potentials, rate constants) and the formation protocol (e.g. time spent at different negative electrode surface potentials, the negative electrode expansion rate). Identifying which of these parameters more strongly influence cell characteristics (e.g. FCE, initial cell capacity, long-term degradation rates) can help inform both electrolyte design and formation protocol design. One particular question that may be answered is: "how much influence does the formation protocol have on determining initial cell characteristics?"

We thus explore the sensitivity of the predicted SEI properties z (Eq. 4.29) on the model parameters p. We note that p consists of both material properties ($D_{\text{sei}}, U_{\text{sei}}, k_{\text{sei}}, \gamma$), which may be tunable through materials engineering, and a use case variable (C-rate) which can be controlled through the formation protocol. For each model parameter, we repeated the 'baseline formation' protocol simulation which consisted of three C/10 back-to-back charge and discharge cycles [135], each time varying the sensitivities about a nominal operating point given in Table 4.2. To simplify the analysis, we considered only a single-component SEI reaction. The range of values explored for each parameter represent physically-feasible ranges and are also given in Table 4.2.

The results of the sensitivity analysis, shown in Figure 4.7, highlight the fact that the SEI properties are relatively insensitive to choices of U_{sei}, k_{sei}, and C-rate. The insensitivity to C-rate is particularly relevant for manufacturing applications since it implies that faster formation protocols could be developed without affecting the quality of the SEI. The insensitivity to U_{sei} and k_{sei} is explained by the fact that these parameters only affect the SEI reaction process before the system transitions from a kinetically-limited to a diffusion-limited

Table 4.2: Index Used for Parameter Sensitivity Study

Variable	Units	Min -1	Nominal 0	Max $+1$
U_{sei}	V	0.5	1.8	3.1
D_{sei}	$\text{m}^2\ \text{s}^{-1}$	10^{-22}	10^{-21}	10^{-20}
k_{sei}	$\text{m}\ \text{s}^{-1}$	10^{-19}	10^{-17}	10^{-15}
γ	s	10^6	3.2×10^6	10^7
C-Rate	s^{-1}	C/20	C/8	C/5

regime (Figure 3.6B, markers 2 and 3); however, since the system becomes diffusion-limited within the first hour of the formation charge, the main driver for SEI reactions is not the kinetic parameters, but rather the ability for reacting molecules to diffuse to the surface of the negative electrode for reactions. Indeed, we see that the SEI properties are highly sensitive to the SEI diffusivity D_{sei}, with higher values leading to both a thicker film $\delta_{\text{sei},f}$ as well as a more rapid reaction rate at the end of formation $j_{\text{sei},f}$, both of which are associated with a poor-quality, non-passivating SEI. This result reinforces a recurring motif of this work: to form a well-passivated SEI, the electrolyte-electrode system should seek to minimize D_{sei}.

Finally, we see that increasing the boost sensitivity factor γ leads to an SEI film that is thicker but minimizes further SEI reactions. A system with a higher boost sensitivity factor corresponds to an SEI that more easily breaks apart due to the reversible expansion of the negative electrode. The model predicts that such a system would form a thicker SEI film due to the boosted SEI growth rate during charging. The thicker SEI film then suppresses further SEI reactions, leading to a lower SEI current density at the end of formation.

4.6 Application 5: Interpreting Diagnostic Features

In this last section of this chapter, we discuss how the formation model can be used to elucidate physical connections between beginning-of-life diagnostic features. These diagnostic features will be the basis for Part II of this thesis focusing on data-driven methods for battery formation diagnostics and lifetime prediction. We focus here on studying the connection between two metrics: the low-SOC resistance, or R_{LS}, and the quantity of lithium consumed during formation, or Q_{sei}. The low-SOC resistance will become central to a discussion around lifetime prediction in Chapter 6. As a preview of the in-depth discussion to come, we will leverage the formation model to demonstrate that R_{LS} can act as an indicator

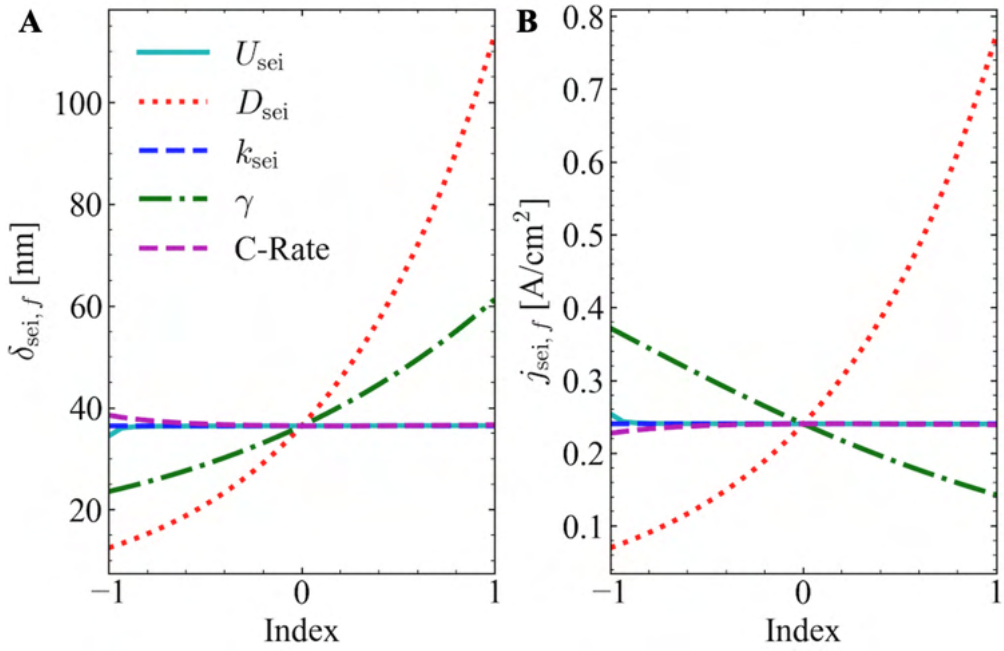

Figure 4.7: Parameter sensitivity analysis. (A) Sensitivity of the final SEI thickness $\delta_{\text{sei},f}$ on the input parameters. (B) Sensitivity of the final SEI reaction current density $j_{\text{sei},f}$ on the input parameters. The x-axis values are defined by Table 4.2.

for the quantity of lithium consumed during formation.

4.6.1 Methods

The formation model was initialized in the usual way, with $\theta^-|_{t=0} = 0$ and $\theta^+|_{t=0} = 1$ representing the lithiation state of each electrode before formation begins. We simulated the baseline formation protocol which consisted of three back-to-back charge-discharge cycles at the C/10 rate. The simulation outputs provided time-resolved trajectories of the internal states $\theta^-(t)$, $\theta^+(t)$, and $Q_{\text{sei}}(t)$. The lithiation states $\theta^-(t)$ and $\theta^+(t)$ are mapped to a shared capacity basis according to the following affine basis transformation:

$$q^+(t) = Q^+(1 - \theta^+(t)) \tag{4.60}$$

$$q^-(t) = Q^-\theta^-(t) + Q_{\text{sei}}(t) \tag{4.61}$$

where $q^\pm$ are the capacity of the electrodes in the shared capacity basis, $Q_{\text{sei}}(t)$ is the modeled capacity of lithium lost to form the SEI, and $Q^\pm$ are the electrode capacities. With the capacity basis resolved, the half-cell electrode potentials can be calculated at every point in q by starting with the functions $U^+(\theta^+)$ and $U^-(\theta^-)$ shown in Figure 3.3B and mapping

the stoichiometries to q according to Equation 4.60. The full cell potential V_{full} is finally computed as the difference between $U^{+}(q)$ and $U^{-}(q)$.

4.6.2 Results

The resulting calculations yield a plot of the alignment between positive and negative electrode voltage curves along a shared capacity basis (more on this in Chapter 5). Since the formation model provides time-resolved trajectories of the internal states, this voltage alignment plot can be updated at every discrete time interval throughout the simulation. Viewing the plots in succession provides an animation revealing the dynamics of half-cell potential curve shifts during the formation process. Figure 4.8 shows two snapshots from this animation towards the start (Panel A) and end (Panel B) of the baseline formation simulation. The asterisk (*) shows the growth in Q_{sei} throughout the formation protocol which creates the irreversible offset between the positive and negative electrode stoichiometries.

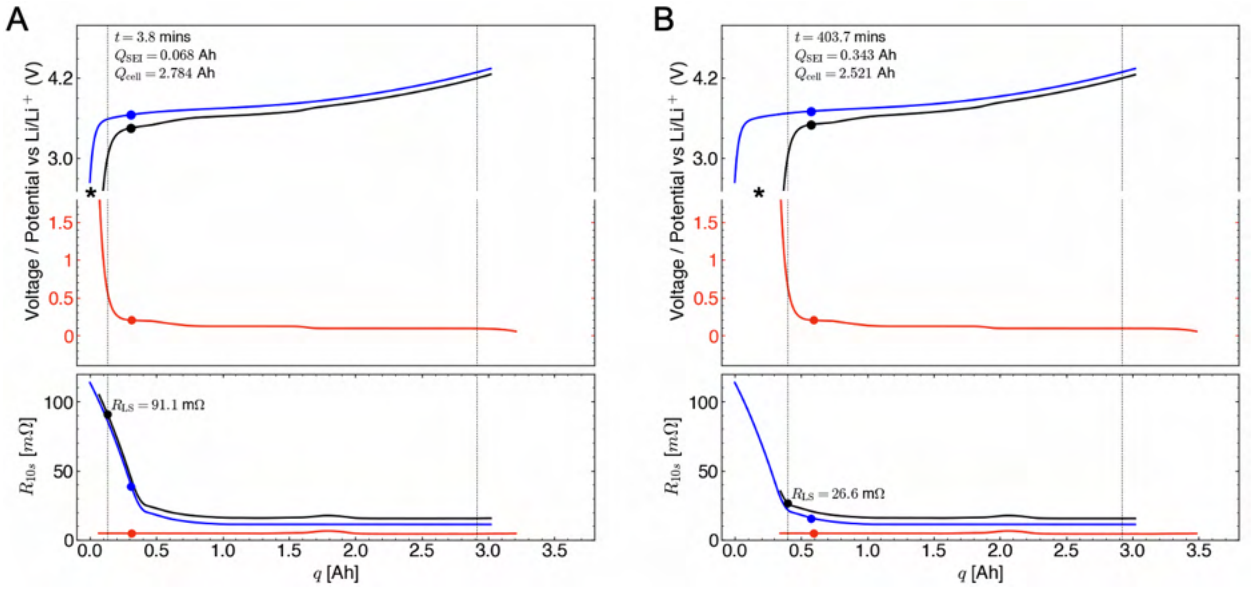

Figure 4.8: Verifying the connection between Q_{sei} and R_{LS} using the formation model. Snapshots of the formation model simulation near the beginning of formation (A) compared to the near the end of formation (B). Top row: full cell and half cell potential curves. Markers indicate the present state of the cell. Bottom row: corresponding full cell and half-cell resistance curves generated using the method from Section 6.3.6. R_{LS} indicates the low-SOC resistance, in this case measured at 0% SOC, which decreases from 91.1mΩ to 25.6mΩ.

The bottom row of Figure 4.8 shows the corresponding half-cell resistance curves for the graphite/nickel manganese cobalt (NMC) system. These curves were constructed based on

a method that will be later introduced as part of Chapter 6, Section 6.3.6. Briefly, at low-SOCs, the high measured full cell resistance is attributed to kinetic limitations in the positive electrode layered oxide material.

The simulations show that R_{LS} decreased from 91.1 mΩ to 25.6 mΩ between the two snapshots in time. The source of this decrease stems from the resistance "shoulder" in the positive electrode at low SOCs: comparing between the two frames, we see that, as Q_{sei} increases, the positive electrode curves shift towards the left relative to the negative electrode. The resulting measured resistance at 0% SOC from the perspective of the full cell is then decreased. The decrease in R_{LS} thus arises from the shifting electrode alignment due to lithium consumed to form the SEI. Put another way, as lithium is consumed to form the SEI, the positive electrode becomes less lithiated at 0% SOC since lithium was irreversibly consumed to form the SEI; as the positive electrode becomes less lithiated, the electrode is less kinetically limited; finally, this improvement in electrode kinetics is then reflected in the measured full cell resistance at 0% SOC. The decrease in R_{LS} is thus a reflection of changes in the maximum positive electrode lithiation due to the lithium consumed to form the SEI.

To emphasize this connection between R_{LS} and Q_{sei}, the model-predicted R_{LS} and Q_{sei} throughout the baseline formation cycle are plotted against each other in Figure 4.9. We have additionally simulated the fast formation protocol, which expectedly shows the same trend, since the relationship between R_{LS} and Q_{sei} is determined purely by the relative position of the equilibrium curves.

The mechanistic insight we describe here is consistent with the discussion to come in Chapter 6, Section 6.5.1.4. Through this example, we demonstrate how the formation model can be used to elucidate physical connections between different diagnostic features that can then lend themselves toward applications for lifetime prediction.

4.7 Conclusions

This chapter previewed five different applications of the formation model towards improving the design of formation protocols, improving factory process control, improving lifetime prediction, and understanding the mechanisms behind why fast formation could be better for battery lifetime. Ultimately, realizing any of these applications in practice will require further developments which is beyond the scope of this thesis. However, we hope that the contents of this chapter have provided a clear snapshot of the potential utility of the formation model towards these various applications, motivating future work in the relevant areas.

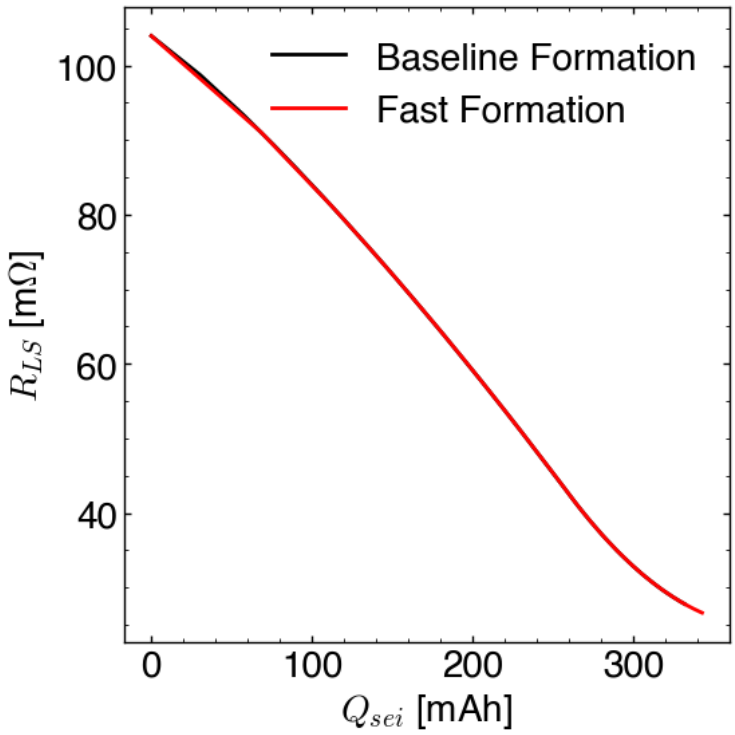

Figure 4.9: Model-predicted correlation between R_{LS} and Q_{sei}. The curve was generated by simulating the baseline formation and fast formation protocols. The correlation holds irrespective of the formation protocol.

Chapter 4: Supplemental Figures

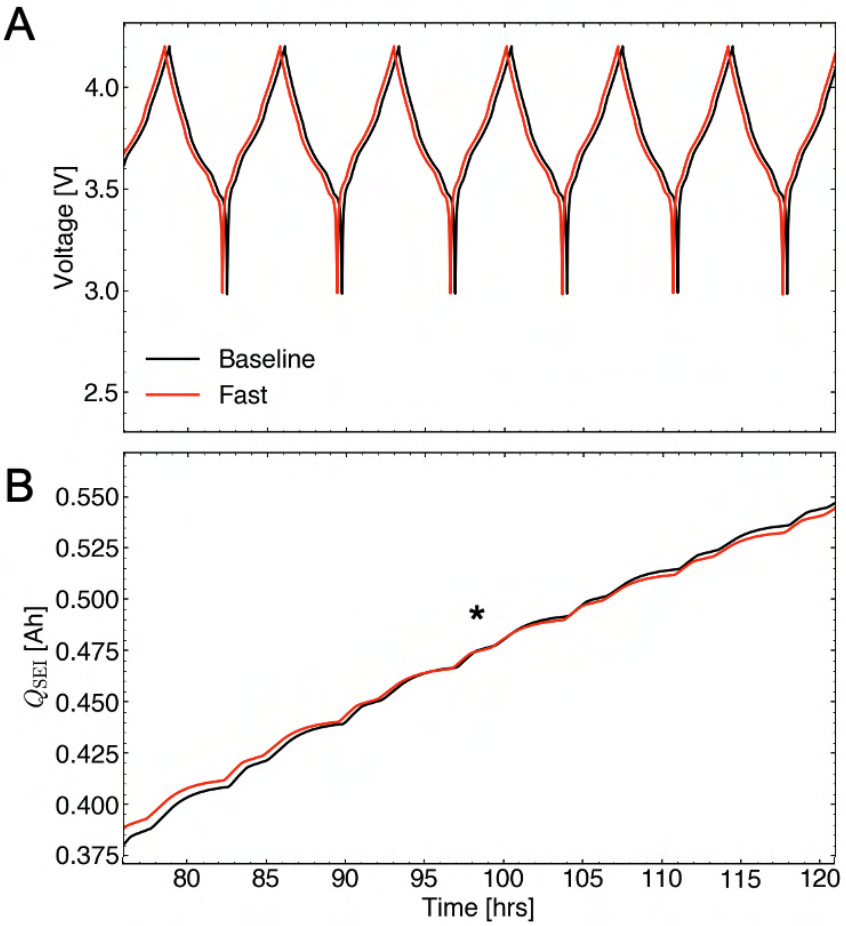

Figure 4.10: Combined formation and cycle life simulations: baseline formation (black) vs. fast formation (red), zoomed in. (A) Voltage traces during and after formation. (B) Capacity of lithium lost to form the SEI. Asterik (*) shows the cross-over point in SEI capacity which occurs after the 5th cycle after formation completes. (C) Evolution of the homogenized SEI diffusivity. (D) Evolution of EC and VC concentrations (secondary y-axis).

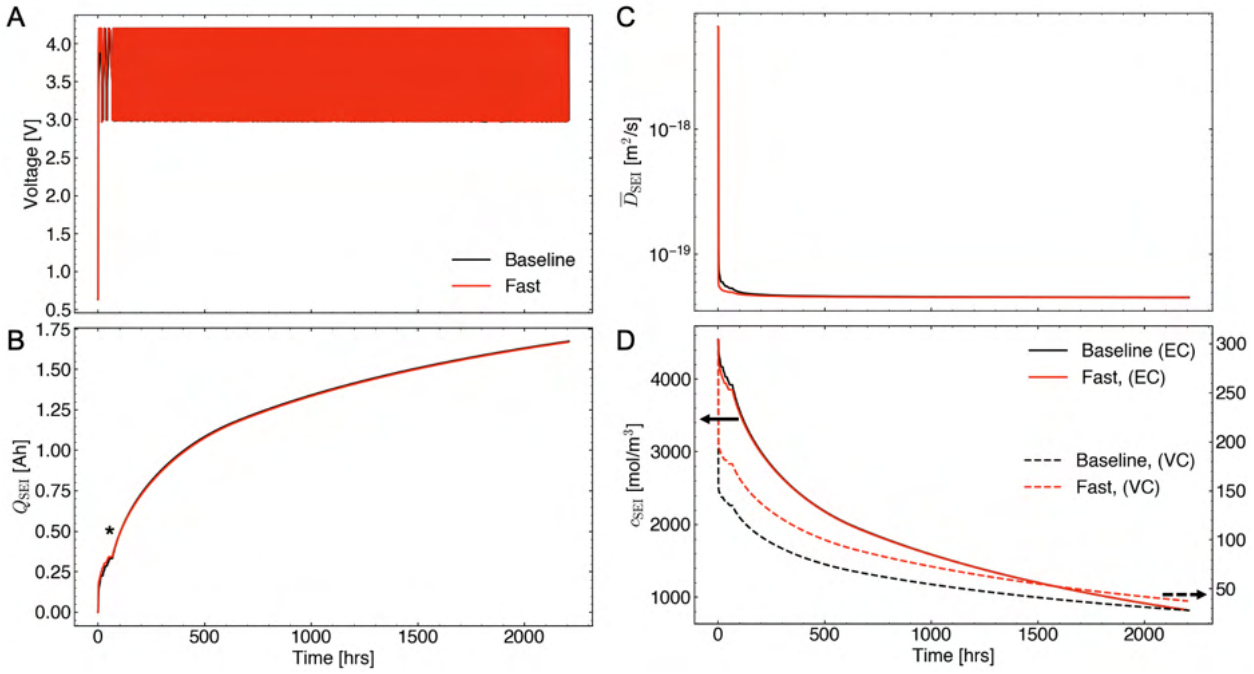

Figure 4.11: Combined formation and cycle life simulations: baseline formation (black) vs. fast formation (red), zoomed out. (A) Voltage traces during and after formation. (B) Capacity of lithium lost to form the SEI. Asterik (*) shows the cross-over point in SEI capacity which occurs after the 5th cycle after formation completes. (C) Evolution of the homogenized SEI diffusivity. (D) Evolution of EC and VC concentrations (secondary y-axis).

CHAPTER 5

Voltage-Based Diagnostic Features

5.1 Abstract

Voltage-based battery data are ubiquitous and essential in battery manufacturing diagnostics: they enable "electrochemical fingerprinting" of batteries at the end of line and are naturally scalable since the voltage data can be collected automatically as part of the battery formation process. Yet, despite their prevalence, interpretations of voltage-based signals are often ambiguous and require expert judgment. Difficulties stem from inconsistent guidelines for data collection and a lack of standardized methods for collecting and analyzing voltage-based data. In this work, we revisit methods for collecting and analyzing voltage-based features through the lens of method reproducibility and interpretability in a battery manufacturing context. The features we cover in this work include thermodynamic features derived from the DVA (or dV/dQ) method and resistance features derived from hybrid pulse power characterization (HPPC). We further extend the DVA method by clarifying the "inaccessible lithium problem" and propose new derived features directly relevant to setting manufacturing specifications including lithium consumed during formation and the practical N:P ratio. We summarize experimental and analysis considerations required to enable repeatable data reporting. We finally highlight a case study in which the DVA method is applied to quantify differences in internal cell states between two batches of cells built on the same manufacturing line. This work highlights both the opportunities and challenges of developing voltage-based diagnostic features in a battery manufacturing context.

5.2 Introduction

5.2.1 The Forecast for Tomorrow: More Battery Factory Data

The proliferation of battery factories worldwide is creating exponential growth in battery manufacturing data. To place the scale of this data in context, consider a battery factory

that supplies enough cells to produce one electric vehicle per minute, a production rate that has already been realized in industry [140]. Since the number of cells needed for each electric vehicle is on the order of hundreds for pouch cells and thousands for cylindrical cells, the cell production rate would need to exceed ca. 100 cells per minute for pouch cells and ca. 1,000 cells per minute for cylindrical cells. Every cell produced will generate voltage and current time-series data as part of the formation process, the last step of battery manufacturing.

5.2.2 Opportunities

Voltage and current data from the battery formation process can be continuously collected, stored, and analyzed to be used as process specifications (i.e. tolerances) with the goal of ensuring that all cells leaving the factory have a guarantee on battery performance, lifetime, and safety [14]. Using voltage-based measurements is appealing for manufacturing automation since they can be measured using existing formation hardware. Collecting voltage-based data thus bears no additional costs to a factory.

When voltage data is carefully collected and analyzed, they can be used to derive physically-interpretable, electrochemical features that provide insights into the thermodynamic and kinetic properties of the cell. For example, a slow-rate charge voltage curve can be analyzed using incremental capacity analysis (ICA) [67] or voltage fitting (dV/dQ) analysis [69] to understand thermodynamic cell properties such as active material losses and lithium inventory losses. The data can be collected and analysed within the time frame of a charge cycle (e.g. 20 hours) with shorter times being possible. Moreover, unlike cell dissections and electrode harvesting, the voltage-based analysis is non-destructive so the same cell that is analyzed can then go on to be used in consumer products. Another example of a voltage-based feature is resistance calculated from current data. Resistance can be used as a quality check on cells, where outliers could be used to used as a basis to reject cells suspected of defects. With careful data collection and analysis, resistance features can also lend insights into material properties at the cell component level.

5.2.3 Challenges

Caution is needed when setting manufacturing specifications based on voltage-based data. Without careful data collection and interpretation, manufacturing specifications may be set unnecessarily tightly, resulting in high cell reject rates, decreased production throughput, and increased factory waste. However, if the same specifications are set too loosely, variation in cell-to-cell properties, such as energies and resistances, may increase, which may lead to performance and reliability issues. Ultimately, manufacturing specifications must be set

based on an understanding of long-term consequences to performance, lifetime, safety, and reliability. The voltage-based features can afford the understanding of these long-term effects but only if they are carefully designed and interpreted.

Currently, factories are not taking full advantage of voltage-based features to set manufacturing specifications because they are difficult to interpret. All full-cell voltage measurements reflect a combination of thermodynamic factors originating from the two electrodes, as well as kinetic factors from nearly every cell component, including the electrodes, electrolyte, tabs, binders, current collectors, etc. Resolving the complex electrochemical details using full-cell voltage data alone is hence inherently challenging. The difficulties of data interpretation are compounded by a lack of clear literature guidance on best practices for collecting and analyzing voltage data. As a result, commonly reported features derived from voltage data, such as modeled electrode capacities (from dV/dQ or ICA) and resistances often differ in both data collection and data analysis methods, limiting their interpretability and reproducibility.

5.2.4 Main Contributions

The goal of this work is thus to guide experimental and modeling considerations needed to enable reproducible voltage-based battery manufacturing diagnostics. To accomplish this, we revisit two of the most popular voltage-based analysis techniques through the lens of battery manufacturing and reproducible data analysis. Section 5.3 discusses a method to analyze near-equilibrium full-cell voltage curves to obtain electrode-level parameters through DVA (or dV/dQ) analysis. Section 5.4 discusses a method to obtain direct current resistance at multiple states of charge, pulse durations, and temperatures through the HPPC method. For each of the presented methods, we detail the experimental and analysis considerations to improve data reproducibility and interpretability. Section 5.5 finally provides a case study in which the DVA method is leveraged to gain insight into differences between two batches of cells built in the same manufacturing line. This case study highlights the promise of using DVA to non-destructively quantify variability in cell internal states at the end of the manufacturing process.

The methods for defining diagnostic features outlined in this chapter set the foundation for future applications in manufacturing process control and battery lifetime prediction (Figure 5.1).

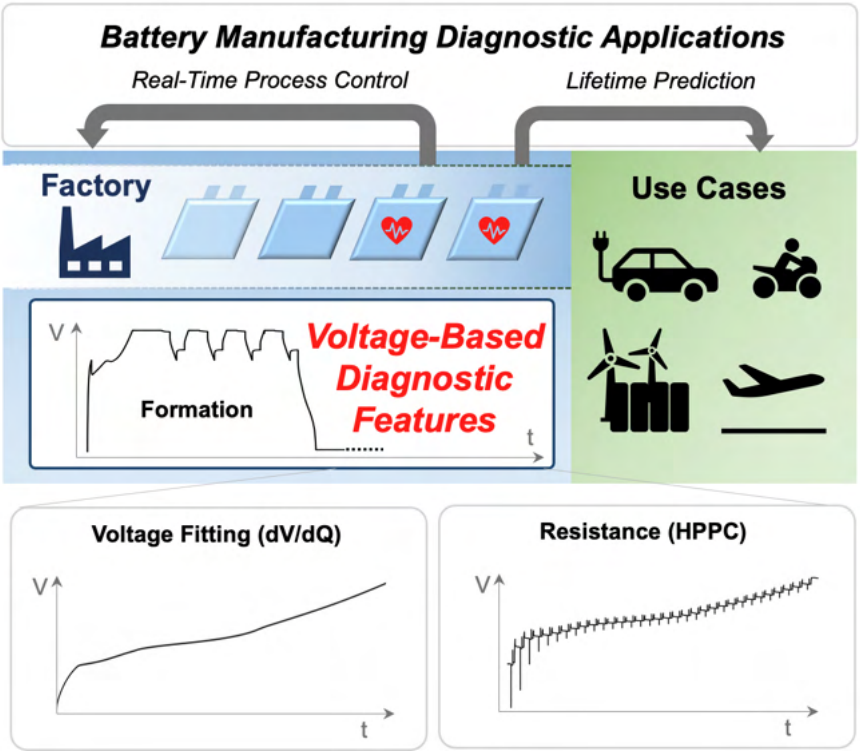

Figure 5.1: Voltage-based battery manufacturing diagnostic features can be measured automatically and immediately after cells complete formation cycling and before leaving the factory. The features can be used for closed-loop feedback for real-time process control and battery lifetime prediction. The main groups of voltage-based features we cover in this work are thermodynamic features from voltage fitting (dV/dQ) (Section 5.3) and kinetic (resistance) features from HPPC (Section 5.4).

5.3 Differential Voltage Analysis

Near-equilibrium (i.e. slow-rate) full cell voltage curves have been widely used to understand dominant cell degradation modes such as loss of active material (LAM) and loss of lithium inventory (LLI) [141, 142, 143, 144]. The appeal of these techniques is easy to appreciate: full cell data is easier and faster to collect than materials-level characterization data which often requires cell tear-down and electrode harvesting. Such types of analyses have been introduced under different names, including DVA, $\mathrm{d}V/\mathrm{d}Q$ analysis [141, 145], ICA [142, 146, 67], open-circuit voltage models [143, 147, 148], and voltage-fitting analysis [69]. While all of these methods rely on full cell voltage curve data, their data analysis approaches are different. In DVA, the voltage is differentiated with respect to capacity and plotted against capacity. The resulting data reveals peaks and troughs that can be attributed to either the positive or negative electrode. In ICA, the capacity is differentiated with respect to voltage and plotted

against voltage. The features observed from ICA are no longer linearly separable, but through careful data interpretation, distinct degradation modes can still be inferred [67]. Other variations of differential analysis have also been recently introduced which leverage signals such as expansion [149] and pressure [150], but since these methods require measurements beyond full voltage, they are omitted from present consideration.

In a battery manufacturing context, a quantitative and reproducible voltage-based analysis method is needed. The method must be quantitative to resolve minute differences in manufacturing process parameters which could have large, long-term consequences to battery performance, lifetime, and safety. The method must also be reproducible to scale. However, since current methods for extracting the electrode-level parameters vary from author to author, comparing results across different papers is complicated. Notably, some authors use full cell data alone, assigning features of interest and graphically inferring degradation metrics such as lithium inventory and electrode capacity losses [151], while others leverage half-cell "reference curves" [152] to build a model of the full cell voltage as a function of the electrode-level parameters [143, 147].

In this section, we develop an automated and scalable method for extracting electrochemical features from voltage curves. The method expands upon the mathematical foundations of DVA introduced by Lee et al. [69] by reformulating the model equations to account for the "inaccessible lithium problem," an essential step towards connecting the model outputs to electrode-level parameters such as active material loadings. We further provide formal definitions of novel cell design parameters, including the practical NP ratio and the lithium consumed to formation, which can be directly extracted from the modified method. We finally outline experimental considerations for collecting full cell and half cell data to enable the modified DVA method to be reproducibly automated at scale.

5.3.1 Base Model Formulation: A Review

The differential voltage model seeks to decompose the full cell near-equilibrium (i.e. open circuit) voltage curve into its constituent half-cell positive and negative potential curves vs Li/Li^+. The half-cell curves, also sometimes called "reference curves" [152], then provide information about the thermodynamic states of the cell, including positive and negative electrode capacities, positive and negative electrode lithium stoichiometries as a function of the full cell SOC, and the capacity of cyclable lithium inventory.

We now proceed with reviewing the quantitative treatment of DVA using Figure 5.2 as a visual guide. The derivation presented here is a summary of work from Lee et al. [69].

The fundamental state equation of the model is an assertion of voltage conservation

between the half-cell near-equilibrium potentials and the full-cell near-equilibrium potential given by:

$$V_{\text{full}}(q) = U^+(y) - U^-(x), \tag{5.1}$$

where V_{full} is the full cell near-equilibrium (i.e. open-circuit) voltage and U^+ and U^- are the positive and negative electrode near-equilibrium potential curves versus Li/Li^+, respectively. q is a vector of capacities in the full cell domain and is related to the cell SOC, $z \in [0, 1]$, by the relation:

$$z = \frac{q}{Q_{\text{full}}}, \tag{5.2}$$

where Q_{full} is the measured capacity of the full cell. $x \in [0, 1]$ and $y \in [0, 1]$ are vectors of lithium stoichiometries in the negative and positive electrodes, respectively. Note that x and y are identical to the variables θ^- and θ^+ in Chapter 3, but have been renamed in this chapter for notational convenience. The lithium stoichiometries are governed by the half-cell reactions:

$$x\text{Li}^+ + x\text{e}^- + \text{C}_6 \rightarrow \text{Li}_x\text{C}_6 \qquad \text{(Negative, charging)} \tag{5.3}$$

$$\text{LiM} \rightarrow \text{Li}_y\text{M} + (1-y)\text{Li}^+ + (1-y)\text{e}^- \qquad \text{(Positive, charging)}, \tag{5.4}$$

where the first reaction represents the intercalation of lithium into graphite, and the second reaction describes the release of lithium from any intercalation positive electrode such as (NMC), nickel cobalt aluminum (NCA), iron phosphate, etc.

Equation 5.1 assumes that both electrodes are at near-equilibrium, meaning that the current densities used to acquire the curves are sufficiently small so that over-potential contributions can be neglected. Note that while some authors attempt to use V_{full} to extract kinetic information such as resistance increase [142], we focus our analysis on extracting only thermodynamic quantities to limit the number of modeled output parameters and improve solution uniqueness. To ensure negligible kinetic effects, $V_{\text{full}}(q)$ must be collected at a sufficiently slow rate (see Section 5.3.4.1). The reference half-cell curves $U^+(y)$ and $U^-(x)$ may be obtained experimentally, e.g. via coin cell testing (see Section 5.3.4.2).

The terms in Equation 5.1 can be mapped to a common, full capacity basis q. Charge conservation requires that this mapping be affine (linear plus an offset). We can therefore define the following basis transformation equations:

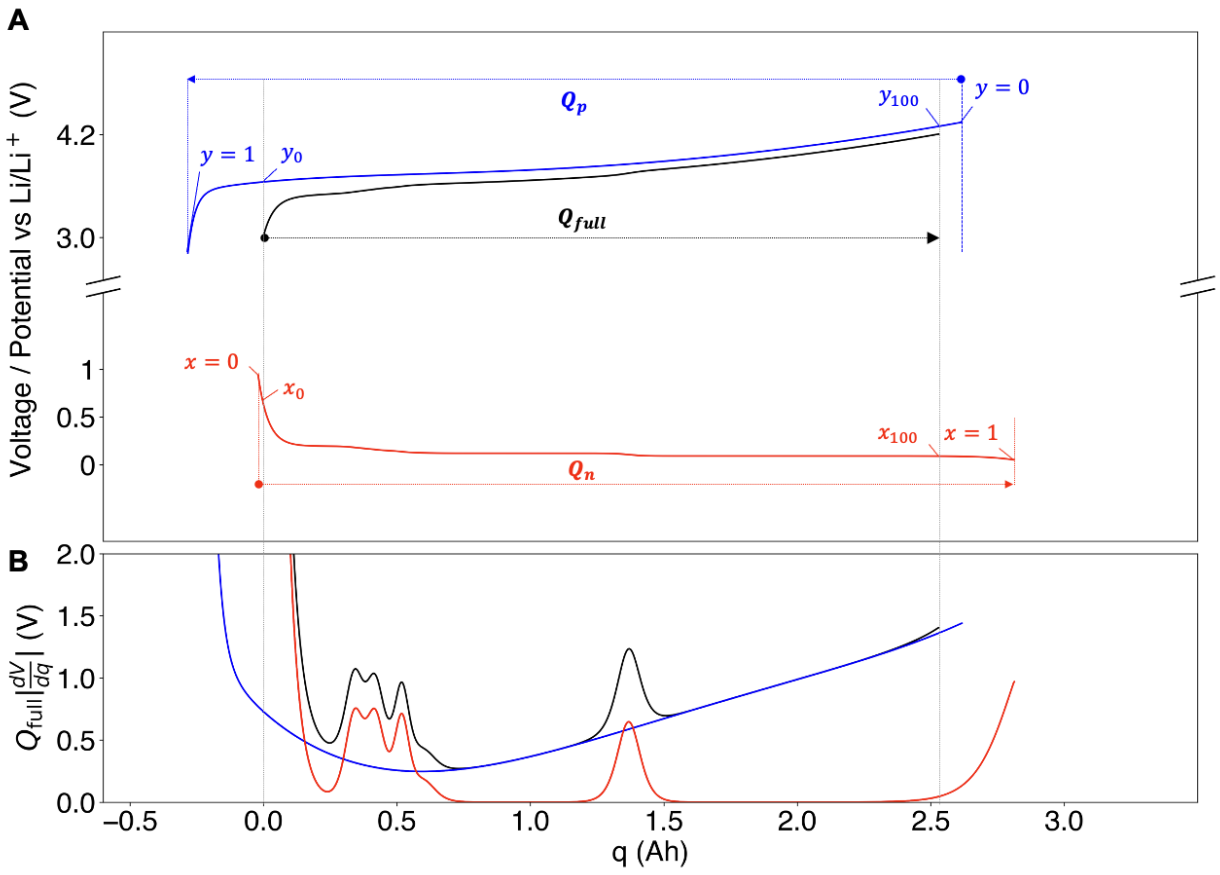

Figure 5.2: Concept illustration of the canonical DVA method. (A) The full cell near-equilibrium ('open circuit') voltage curve V_{full} (black) plotted alongside the corresponding positive electrode (blue) and negative electrode (red) near-equilibrium potential curves U^+ and U^-. (B) The corresponding differential voltage ($\mathrm{d}V/\mathrm{d}Q$) curves which illustrate how full cell $\mathrm{d}V\mathrm{d}/Q$ peaks can be attributed to features from the positive and negative electrodes.

$$x(q) = x_0 + \frac{q}{Q_n} \tag{5.5}$$

$$y(q) = y_0 - \frac{q}{Q_p}, \tag{5.6}$$

where Q_n and Q_p are the total negative and positive electrode capacities, respectively, and (x_0, y_0) are the negative and positive electrode stoichiometries in the fully discharged state. These equations are derived under the boundary condition that $q = 0$ corresponds to the fully discharged state, with $(x, y) = (x_0, y_0)$. Equations (5.5, 5.6) can be inverted to

obtain:

$$q(x) = Q_n(x - x_0) \tag{5.7}$$

$$q(y) = Q_p(y_0 - y), \tag{5.8}$$

which can be used to map lithium stoichiometries to the shared capacity basis. Note that, under this construction, q is allowed to take on negative values. For example, when $x = 0$, $q = -Q_n x_0 < 0$, according to Equation 5.7. Negative q values can be interpreted as "virtual capacities," that is, capacity present in the electrodes but is inaccessible from the perspective of the full cell due to the full cell minimum voltage constraint.

We can also define a complementary set of variables describing the lithium stoichiometries in the fully-charged state, (x_{100}, y_{100}), which can be written as:

$$x_{100} = x_0 + \frac{Q_{\text{full}}}{Q_n} \tag{5.9}$$

$$y_{100} = y_0 - \frac{Q_{\text{full}}}{Q_p}. \tag{5.10}$$

Q_{full} is a known quantity from the full cell data and is not considered to be a modeled parameter. Hence, (x_{100}, y_{100}) are not independent model parameters.

In summary, knowledge of four parameters:

$$\theta = \{Q_n, Q_p, x_0, y_0\} \tag{5.11}$$

provides a complete description of the model from Equation (5.1). These parameters bear physical meaning, since (Q_n, Q_p) are related to the total electrode capacities and (x_0, y_0) predict lithium stoichiometry-dependent electrode potentials. These model parameters can then be used to derive additional electrochemical features relevant to battery manufacturing diagnostics, as will be described in Section 5.3.3.

Note that the choice of model parameters are not unique. For example $\{Q_n, Q_p, x_{100}, y_{100}\}$ is an equally valid set of parameters. For the remainder of this work, we will continue to use the $\{Q_n, Q_p, x_0, y_0\}$ basis with the recognition that the model can always be reformulated using another set of four basis states using Equations (5.9,5.10).

The goal of the model is then to identify a unique combination of model parameters θ that provides the best fit against the measured voltage data. The optimization problem can

be solved by implementing an error function:

$$\mathrm{E(q}:\theta = \underbrace{U^{+}\left(y_0 - \frac{q(y)}{Q_p}\right) - U^{-}\left(x_0 + \frac{q(x)}{Q_n}\right)}_{\mathrm{V_{full}(q)}} - V_{\mathrm{meas}}(q), \tag{5.12}$$

where $V_{\mathrm{meas}}(q)$ is the experimentally-measured full cell voltage curve and the domain of q is now restricted to the full-cell domain spanning $(0, Q_{\mathrm{full}})$. The model returns an optimal parameter-set which minimizes an error function of the form:

$$\theta_{\mathrm{opt}} = \underset{\Theta}{\mathrm{argmin}} \sum_{q} \left(\lambda |\mathrm{E}(q:\theta)|^2 + (1-\lambda) \left| \frac{d\mathrm{E}(q:\theta)}{dq} \right|^2 \right). \tag{5.13}$$

The first term inside the summation is the voltage error and the second term represents the differential voltage error. $\lambda \in [0, 1]$ is a weight parameter, i.e. when $\lambda = 1$, the contribution from the differential voltage signal is ignored. The optimization problem can be solved using standard non-linear least-squares solvers which are available in most scientific programming languages such as Python or Matlab. Note that, in Figure 5.2, plotted full cell voltage data corresponds to the modeled data and the measured voltage data was omitted for graphical clarity. A real-world comparison of measured versus modeled full-cell voltages is later presented in Figure 5.10.

Variations of the optimization method exist in the literature. For example, Lee et al. [69] set $\lambda = 1$ and implemented additional constraints based on full cell voltage limits, i.e. $V_{\mathrm{max}} = U^{+}(y_{100}) - U^{-}(x_{100})$ and $V_{\mathrm{min}} = U^{+}(y_0) - U^{-}(x_0)$. With this approach, the model-predicted full cell capacity is guaranteed to match the measured value. However, solution convergence becomes more challenging in the presence of these additional constraints which could make the solution space ill-conditioned. Dahn et al. [153] included the differential voltage (dV/dQ) curves in the error function to assign preferential weight to the phase transition features (Figure 5.2B) and to negate the effects of impedance mismatch between the full cell and coin cell form factors. However, these dV/dQ methods reported previously are generally not fully automated, often requiring manually adjusting model parameters through graphical user interfaces [153] and evaluating goodness-of-fit by visually inspecting peak alignments. Overall, a "one-size-fits-all" optimization scheme is not known to exist yet. The specific details of the optimization may therefore need to be tuned to perform optimally for a given system.

5.3.2 The Inaccessible Lithium Problem

So far, we have laid the groundwork for the DVA method. We next outline a fundamental challenge with interpreting and reproducing model outputs known as the "inaccessible lithium problem." This issue was alluded to by Truchot et al. [154] and recently expanded upon by Lu et al. [155]. We will first describe how this issue affects the interpretation of the model outputs in a manufacturing context. We then propose corrections to the DVA model equations which clarify the interpretation of the model outputs.

The inaccessible lithium problem is summarized as follows. The model state equation assumes that U^+ and U^- are defined for the entire range of lithium stoichiometries spanning $y \in [0, 1]$ and $x \in [0, 1]$, respectively. Yet, half-cell potential curves are generally experimentally unattainable over the entire range of stoichiometries. For example, for layered oxide positive electrode systems such as NMC, full delithiation would render the host material thermodynamically unstable, impacting the reversibility of lithium intercalation reaction. Full lithiation of the layered oxide particles is also experimentally challenging due to massive kinetic limitations towards the fully lithiated state [156]. These kinetic limitations explain why it is so difficult to "fully discharge" a positive electrode half cell; even when discharging at small C-rates, the potential tends to rebound above 3V vs Li/Li^+ after resting.

Near-equilibrium potential data on layered-oxide positive electrodes can only be feasibly obtained within a restricted stoichiometry window, which is determined by the voltage limits of coin cell data collection. Defining $y_{\min}$ and $y_{\max}$ as the minimum and maximum observable lithium stoichiometry in the positive electrode, it must be the case that $y_{\min} > 0$ and $y_{\max} < 1$. An analogous situation applies to the graphite negative electrode, with $x_{\min} > 0$ and $x_{\max} < 1$, though the resulting errors from assuming $x_{\min} \approx 0$ and $x_{\max} \approx 1$ are generally understood to be more benign since lithium transport in graphite is generally more facile.

To proceed with the analysis, practitioners must either implicitly or explicitly assume that the tested range of potentials (e.g. 3.0V to 4.3V for layered oxide positive electrodes) correspond to the full range of lithium stoichiometries, i.e.:

$$(x_{\min}, x_{\max}, y_{\min}, y_{\max}) \approx (0, 1, 0, 1), \tag{5.14}$$

and proceed with the analysis method as described in Section 5.3. However, this simplification will lead to errors in the model outputs.

5.3.2.1 Error Analysis: A Case Study

To demonstrate the magnitude of model estimation errors caused by the inaccessible lithium problem, we study two cell batches made on the same manufacturing line and made using the

same active materials ($Ni_{0.33}Mn_{0.33}Co_{0.33}$ positive electrode and graphite negative electrode), but were made two years apart and differed in cell design parameters, including electrode loading targets and number of layers. Cells from the first batch, from Mohtat et al. [157], had nominal capacities of 5.0 Ah and were built in 2018 ($n = 21$). Cells from the second batch, from Weng et al. [7], had nominal capacities of 2.37 Ah and were built in 2020 ($n = 40$). For these cells, we restricted the cell population to those having full cell data collected at room temperature (RT) ($n = 20$) to match the measurement conditions from Mohtat et al. [157]. A table comparing relevant design parameters is given in Table 5.1. We will refer to these two datasets as Mohtat2021 and Weng2021, respectively.

With these two datasets, we can compare the positive and negative electrode capacities calculated using DVA to the true electrode capacities, which can be calculated by combining the theoretical capacities with the cell design parameters, according to:

$$Q = m \cdot f \cdot n_{\text{faces}} \cdot A \cdot Q_{\text{theor}}, \tag{5.15}$$

where Q is the electrode capacity in Ah, m is the electrode areal loading target in g/cm^2, f is the mass fraction of active material in the electrode, n_{faces} is the number of active electrode faces, A is the electrode area per face, excluding overhanging regions, in cm^2, and Q_{theor} is the theoretical capacity of the material in Ah/g.

The resulting calculations, summarized in Table 5.1, show that the estimated positive electrode capacity is only 54% to 55% of the true positive electrode capacity, while the estimated negative electrode capacity is 87% to 89% of the true negative electrode capacity. This result was demonstrated on both the Mohtat2021 and Weng2021 datasets, suggesting some level of generality. The gross underestimation of positive electrode capacity can be primarily attributed to the fact that the layered oxide $Ni_{0.33}Mn_{0.33}Co_{0.33}$ positive electrode material used in these works retains significant lithium inventory even above the coin cell upper cut-off potential of 4.3V vs Li/Li$^+$, and consequently, $y_{\text{min}} \gg 0$.

This case study suggests that ignoring the inaccessible lithium problem (Equation 5.14) will likely lead to inaccurate reporting of true electrode capacities and stoichiometries, especially for layered oxide positive electrode materials such as NMC. As a result, the model-predicted electrode capacities may not be directly usable for calculating electrode loadings using Equation 5.15. Unfortunately, the inaccessible lithium problem is a fundamental limitation of the coin cell data collection process used to initialize V_{pos} and V_{neg} in the model.

	Positive Electrode		Negative Electrode	
Source	Mohtat2021	Weng2021	Mohtat2021	Weng2021
Material	NMC111	NMC111	Graphite	Graphite
Number of active faces	28	14	28	14
Area per face (cm^2)	79.20	79.20	79.56	79.56
Loading, single-side (mg cm^{-2})	18.50	17.23	8.55	7.85
Theoretical capacity (mAh g^{-1})	279.5	279.5	372	372
Active material fraction	0.94	0.94	0.95	0.97
Total capacity (Ah)	10.78	5.02	6.73	3.16
(A) Q (mAh cm^{-2})	4.86	4.53	3.02	2.83
(B) $\tilde{Q}$ (mAh cm^{-2})	2.66	2.46	2.70	2.46
% of Q observed ($\tilde{Q}/Q$)	55%	54%	89%	87%

Table 5.1: Cell design comparison between the cells from Mohtat et al. [157] and Weng et al. [7], including a comparison of electrode theoretical areal capacities (A) versus practical areal capacities derived from DVA (B). The capacities predicted by the differential voltage analysis are lower than the theoretical values due to the 'inaccessible lithium problem' [155].

5.3.2.2 Model Revision: Enter the 'Tilde' Variables

Knowing that the inaccessible lithium problem can lead to large errors in the model outputs (x, y, Q_n, Q_p), we reformulate the model by defining 'tilde' variables ($\tilde{x}$, $\tilde{y}$, $\tilde{Q}_n$, $\tilde{Q}_p$), to represent estimated parameters. The state equation can then be re-written as:

$$V_{\text{full}}(q) = U^+(\tilde{y}) - U^-(\tilde{x}), \tag{5.16}$$

where:

$$\tilde{x}(q) = \tilde{x}_0 + \frac{q}{\tilde{Q}_n} \tag{5.17}$$

$$\tilde{y}(q) = \tilde{y}_0 - \frac{q}{\tilde{Q}_p}. \tag{5.18}$$

This modified system is identical to the original system but recognizes the fact that the modeled lithium stoichiometries and electrode capacities may, in general, be different from the true values which are not observable due to the limitations in coin cell data collection for U^+ and U^-.

The estimated parameters can then be related to the true parameters by the following

relations:

$$\tilde{Q}_p = Q_p(y_{\max} - y_{\min}) \tag{5.19}$$

$$\tilde{Q}_n = Q_n(x_{\max} - x_{\min}) \tag{5.20}$$

$$\tilde{y}_0 - \tilde{y}_{100} = \frac{y_0 - y_{100}}{y_{\max} - y_{\min}} \tag{5.21}$$

$$\tilde{x}_0 - \tilde{x}_{100} = \frac{x_0 - x_{100}}{x_{\max} - x_{\min}}. \tag{5.22}$$

This system of equations has more unknowns than equations, highlighting the difficulty in recovering the true parameters from the model alone. Ideally, the true lithium stoichiometries may be experimentally measured, e.g. via inductively coupled plasma optical emission spectroscopy (ICP-OES) [158]. True capacities may also be calculated using information about the electrode design (Equation 5.15). Without more measurements, further assumptions are needed to fully resolve the estimated model parameters, e.g. $\tilde{x}_{100} \approx x_{100}$ and $\tilde{y}_0 \approx y_0$.

Despite the data interpretation challenges introduced by the inaccessible lithium problem, we highlight several applications of the model outputs that remain unaffected by this problem. First, calculations of differences in electrode capacities are not affected. This is because the error terms in Equations 5.19 and 5.20 cancel when taking ratios of capacities. This fact explains why literature reports of losses of active material (LAM) and our analysis of electrode capacity loading differences from Section 5.5.0.1 are still valid even though the inaccessible lithium problem may render absolute values of Q_n and Q_p inaccurate. Second, the inaccessible lithium problem also does not impact the process of searching for an optimal set of model parameters (Equation 5.12) since the domain for optimization is strictly only within the full cell capacity window, i.e. $q \in (0, Q_{\text{full}})$. Missing data beyond the limits of the observable full cell voltage data is therefore inconsequential to the optimization.

In summary, the inaccessible lithium problem effectively introduces an optional post-processing step in which the model output parameters may be converted into true parameters using Equations 5.19, 5.20, 5.21 and 5.22. This final step would require additional input not provided for by the differential voltage model. Yet, even without knowing the true model parameters, the estimated model outputs remain useful for estimating differences in parameters such as electrode capacities. The main contribution of the model extension, including the introduction of the tilde variables, is thus to clarify that the model outputs must be interpreted as estimates of the true values due to the limitations in constructing U^+ and U^- from data.

5.3.3 Derived Electrochemical Features

We are now ready to introduce several additional electrochemical features relevant to battery manufacturing process control: the lithium consumed during formation ($\tilde{Q}_{\text{SEI}}$) the practical negative-to-positive ratio ($\text{NPR}_{\text{practical}}$) and the total cyclable lithium inventory (Q_{Li}). These features can be calculated directly from the optimized parameters of the modified model $\tilde{\theta}_{\text{opt}} = \{\tilde{Q}_n, \tilde{Q}_p, \tilde{x}_0, \tilde{y}_0\}$. In light of the previous discussion on the "inaccessible lithium problem", we make a distinction between estimated model parameters, denoted with tildes, and true model parameters. To aid understanding, expressions in the following sections will be given for both true values and estimated values, where appropriate. Figure 5.3 summarizes the revised parameters as defined by the augmented DVA model.

5.3.3.1 Lithium Consumed During Formation

The capacity of lithium consumed during formation, $\tilde{Q}_{\text{SEI}}$, is analogous to the first cycle Coulombic efficiency metric [124], defined as ratio of discharge and charge capacity during formation. However, unlike Coulombic efficiency, which requires slow-rate charge-discharge cycles to calculate, $\tilde{Q}_{\text{SEI}}$ provides a consistent measure of lithium consumption even when the formation protocol consists of complex charge-discharge cycles involving multiple C-rates and partial SOC windows, as is the case with modern formation protocols [30, 31]. Conveniently, since $\tilde{Q}_{\text{SEI}}$ can be obtained through the analysis of voltage data after formation completes, this metric enables the recovery of information about lithium consumed during formation even if formation data is missing.

We define the estimated capacity of lost lithium inventory due to formation, $\tilde{Q}_{\text{SEI}}$, as:

$$\tilde{Q}_{\text{SEI}} = q(x_{\min}) - q(y_{\max}) \tag{5.23}$$

$$= q(\tilde{x} = 1) - q(\tilde{y} = 0) \tag{5.24}$$

This formula can be understood by considering that, before formation, the positive electrode stoichiometry is at its highest value, $y_{\max}$, since all of the cyclable lithium has not yet left the positive electrode. For the same reason, the negative electrode stoichiometry is at its lowest value, $x_{\min}$. After formation completes, the lithium lost to the SEI will not return to the positive electrode during discharge, causing the highest possible stoichiometry value in the positive electrode to decrease by $q(x_{\min}) - q(y_{\max})$. Equation 5.23 can alternatively be interpreted as the capacity of unoccupied lithium sites in the positive electrode when the negative electrode is fully delithiated.

We note that the calculation assumes that the positive electrode voltage curve and ca-

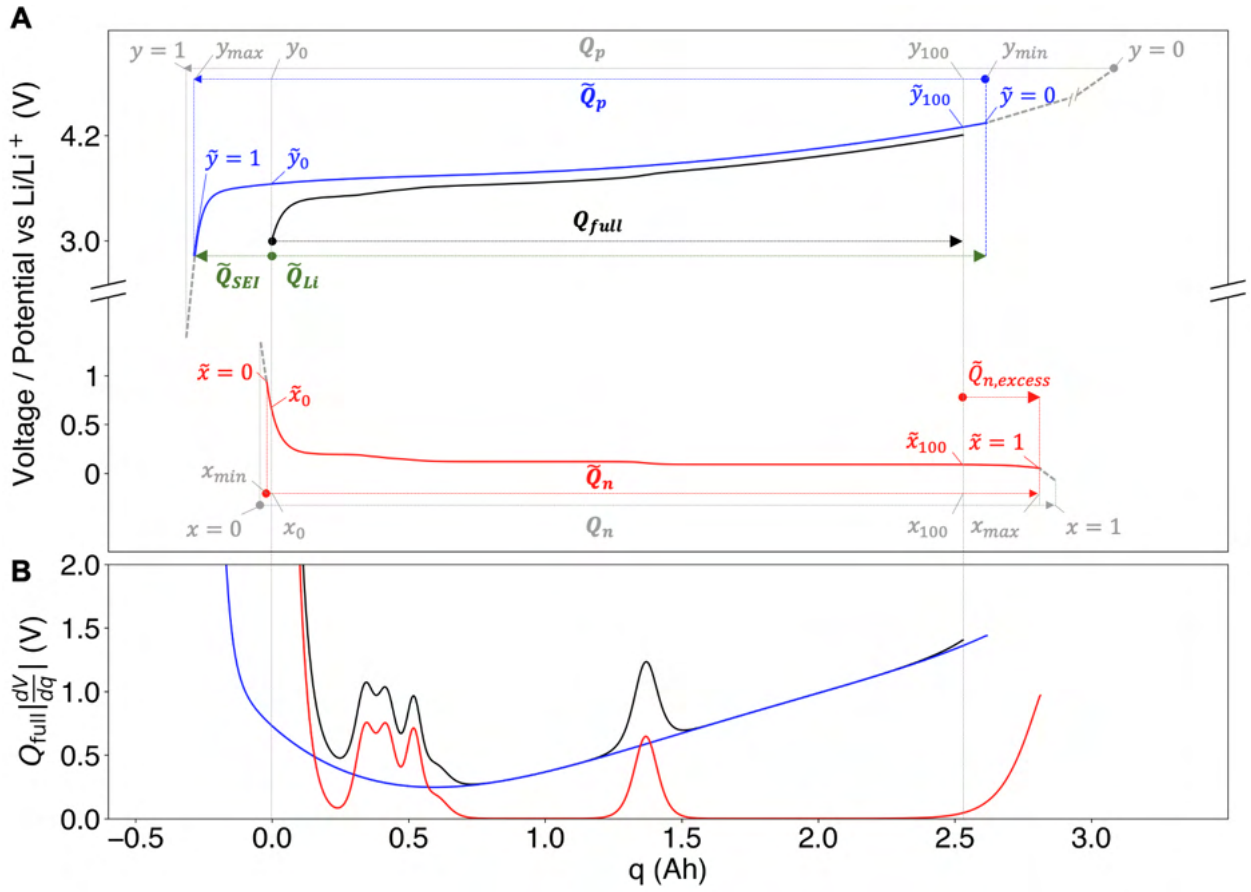

Figure 5.3: Augmented DVA for manufacturing process control applications, accounting for the "inaccessible lithium problem." (A) The full cell near-equilibrium ('open circuit') voltage curve V_{full} (black) plotted alongside the corresponding positive electrode (blue) and negative electrode (red) near-equilibrium potential curves U^+ and U^-. Parameters with tildes indicate estimated model parameters due to the inaccessible lithium problem (Section 5.3.2). Gray lines and variables indicate true model parameters that cannot be ascertained using the native model. (B) The corresponding differential voltage ($\mathrm{d}V/\mathrm{d}Q$) curves which illustrate how full cell $\mathrm{d}V\mathrm{d}/Q$ peaks can be attributed to features from the positive and negative electrodes.

pacity are unchanged during formation. Previous studies have shown that this assumption may not be true [90], which would introduce another error contribution to this calculation which warrants further studies. From a manufacturing standpoint, if the positive electrode system is known to be the same from batch-to-batch, then $\tilde{Q}_{\text{SEI}}$ may still be used to detect differences in the SEI formation process.

5.3.3.2 Re-Interpreting the Negative to Positive Ratio

The negative to positive ratio (NPR) is a common term used in battery design and generally refers to the ratio of negative to positive electrode capacities. The optimization of NPR is sometimes referred to as 'capacity balancing' [159], not to be confused with the process of balancing series-connected cells. Conventional wisdom suggests that the NPR must be greater than one to prevent over-lithiation of the negative electrode during charging. Increasing NPR also implies less utilization of the negative electrode, which could be advantageous in silicon-containing systems where volume expansion is a major contributor to cycle life degradation [160]. However, increasing the NPR requires putting more negative electrode active material into the cell without increasing usable energy content which decreases the cell energy density. Adding more negative electrode loading could also increase the surface area for SEI reactions which could be detrimental to calendar life. The NPR is therefore a critical cell design metric that should be optimized and tracked during manufacturing.

In this section, we first review the most commonly-held definition of the NPR and identify some conceptual gaps preventing a clear interpretation of this metric. We then propose a revised, more practical definition of the NPR which enables a more physically-grounded assessment of the lithium plating risk.

Issues With Conventional Definitions of NPR. To begin, consider a common definition of the NPR based on areal loadings and theoretical electrode capacities:

$$\mathrm{NPR}_{\mathrm{theor}} = \frac{m_n Q_{n,\mathrm{theor}}}{m_p Q_{p,\mathrm{theor}}}. \tag{5.25}$$

In this equation, m_n and m_p are the electrode active material mass loadings in grams, and $Q_{n,\mathrm{theor}}$ and $Q_{p,\mathrm{theor}}$ are the theoretical capacities in units of mAh/g. Applying this formula to the example $Ni_{0.33}Mn_{0.33}Co_{0.33}$|graphite systems from Mohtat2021 [157] and Weng2021 [7] yields calculated NPR values of 0.62 and 0.63, respectively (Table 5.1). This result would suggest that these cell designs have undersized negative electrode capacities and are at risk for lithium plating. However, this calculation assumes that all of the theoretical capacity of the $Ni_{0.33}Mn_{0.33}Co_{0.33}$ positive electrode (279.5mAh/g) can be utilized, which is false due to the inaccessible lithium problem (Section 5.3.2). This definition of NPR, while theoretically valid, is therefore not practically useful in a manufacturing context.

Repeating the calculation but using the estimated values $\tilde{Q}_n$ and $\tilde{Q}_p$ to define:

$$\mathrm{NPR}_{\mathrm{conventional}} = \frac{\tilde{Q}_n}{\tilde{Q}_p} \tag{5.26}$$

leads to yet another definition of NPR found in literature. This definition partly excludes the inaccessible lithium in the positive electrode since $\tilde{Q}_p$ and $\tilde{Q}_n$ are bounded by observable potentials in the coin cell data used to construct U^+ and U^-, respectively. However, this definition remains ambiguous because the calculated value of NPR will change based on the choice of potential ranges chosen for the half-cell reference potential curves which can vary across different datasets. NPR definitions based on $(\tilde{Q}_n, \tilde{Q}_p)$ therefore do not guarantee reproducibility across different authors and datasets.

Definition of Practical NPR. Here, we develop a practically relevant and consistent definition of the NPR, which we call the "Practical NPR." We first return to the original motivation of comparing relative loadings of positive and negative electrode capacities from a cell design perspective, which is to determine whether the negative electrode will become over-lithiated when the cell is fully charged to 100% SOC. A sensible boundary condition is to set the NPR equal to unity if the negative electrode is completely lithiated when the full cell is at 100% SOC (i.e. $x_{100} = 1$). An NPR greater than 1 would then indicate that there exists some excess negative electrode capacity at 100% SOC, which can serve as a margin to protect against lithium plating during charge.

Under this construction, we realize that a practical NPR definition must then be dependent on two factors: the voltage at which 100% SOC is defined, and how much lithium was consumed during formation. The voltage at which 100% SOC is defined becomes relevant since higher voltages require more utilization of both the positive and the negative electrodes, thereby decreasing the excess negative electrode capacity. How much lithium was consumed during formation becomes relevant because more lithium consumed during formation decreases the negative electrode lithium stoichiometry in the fully charged state, x_{100}, which effectively increases the negative electrode excess capacity. Since SEI formation continues over the life of the cell, x_{100} will continue to decrease, which will effectively increase the negative electrode excess capacity over life. Loss of negative active material, on the other hand, could have the opposite effect by shrinking the negative electrode curve [142].

Overall, a practical NPR definition cannot be a static metric, but one that changes after formation and over the life of a cell based on the competition between different degradation modes such as lithium inventory loss and active material loss.

Given the above realizations, we now formally define the Practical NPR as:

$$\mathrm{NPR}_{\mathrm{practical}} = 1 + \frac{\tilde{Q}_{n,\mathrm{excess}}}{Q_{\mathrm{full}}}, \tag{5.27}$$

where

$$\tilde{Q}_{n,\text{excess}} = q(x_{\max}) - q(x_{100}) \tag{5.28}$$

$$= q(\tilde{x} = 1) - q(\tilde{x}_{100}) \tag{5.29}$$

represents the measured excess capacity in the negative electrode when the cell is fully charged. The Practical NPR correctly accounts for the sensitivity to the full cell upper cutoff voltage window, where increasing voltage windows lead to decreasing NPRs (i.e. less protection against lithium plating). The definition is also sensitive to changes in the electrode stoichiometries (x_{100}) over life, and is therefore able to account for the increase in the Practical NPR over life as lithium loss shifts x_{100} to lower values over life.

Applying the Practical NPR definition to the dataset from Weng2021 and Mohtat2021 yields values of 1.14 and 1.24. This calculation shows that, after formation, the Mohtat2021 cells have more negative electrode excess capacity than the Weng2021 cells. The difference between the calculated practical NPRs can be attributed to more lithium consumed during formation for the Mohtat2021 cells (Section 5.5.1) which increased the negative excess capacity (Section 5.5.2). By contrast, none of the other definitions of NPR could distinguish this fact since those definitions did not consider the lithium lost during formation.

A summary comparison of different NPR calculation methodologies is provided in Table 5.2.

Definition	$\text{NPR}_{\text{theor}}$	$\text{NPR}_{\text{conventional}}$	NPR_{prac}
Equation	$\frac{m_n Q_{n,\text{theor}}}{m_p Q_{p,\text{theor}}}$	$\frac{\tilde{Q}_n}{\tilde{Q}_p}$	$1 + \frac{\tilde{Q}_{n,\text{excess}}}{Q_{\text{full}}}$
Ref.	Eq. 5.25	Eq. 5.26	Eq. 5.27
Excludes inaccessible lithium?	N	Y	Y
Considers effect of lithium lost to SEI?	N	N	Y
Mohtat et al. [157]	0.62	1.02 ± 0.009	1.14 ± 0.009
Weng et al. [7]	0.63	1.00 ± 0.014	1.24 ± 0.013

Table 5.2: **Comparison of various definitions of negative to positive ratio (NPR).** Numerical values show mean ± standard deviation. Values were calculated based on differential voltage analysis results performed on the datasets from Mohtat et al. [157] and Weng et al. [7].

5.3.3.3 Total Cyclable Lithium Inventory

The total cyclable lithium inventory in the system is imperative to track over life, since lithium inventory depletion is a primary reason for capacity loss in standard lithium-ion batteries [143, 67]. Lee et al. [69] proposed that the total cyclable lithium inventory can be accounted for from the equation:

$$\tilde{Q}_{\mathrm{Li}} = \tilde{x}_0 \tilde{Q}_n + \tilde{y}_0 \tilde{Q}_p, \tag{5.30}$$

where the first term captures the lithium trapped in the negative electrode due to the full cell minimum voltage constraint. Meanwhile, the second term includes both the cyclable lithium within the full cell operating voltage window and the inventory of lithium above the full cell maximum voltage. To gain a deeper intuition into Equation (5.30), we can rewrite the same equation on the basis of the shared capacity vector q as:

$$\begin{aligned} \tilde{Q}_{\mathrm{Li}} &= \underbrace{[q(y_{\min}) - q(y_{100})]}_{V>V_{\max}} + \underbrace{[q(y_{100}) - q(y_0)]}_{\text{Cyclable}} + \underbrace{[q(y_0) - q(x_{\min})]}_{V<V_{\min}} \qquad (5.31) \\ &= q(y_{\min}) - q(x_{\min}). \qquad (5.32) \end{aligned}$$

Equation 5.31 shows that the total lithium inventory consists of three components: the lithium available in the positive electrode above the full cell upper cut-off voltage (first term), the lithium available within the full cell voltage window (second term), and the lithium available in the negative electrode below the full cell lower cut-off voltage (third term). Note that if $x_{\min} \approx 0$ is assumed, then the third term drops out and Q_{Li} becomes simply a statement of the total lithium inventory remaining in the positive electrode after discounting for lithium lost to the SEI. By combining Equations (5.23) and (5.32), it can be verified that

$$\tilde{Q}_p = \tilde{Q}_{\mathrm{Li}} + \tilde{Q}_{\mathrm{SEI}}, \tag{5.33}$$

which clarifies the fact that all of the lithium inventory in the system originates from the positive electrode.

5.3.3.4 From Absolute Capacities to Capacity Losses

The DVA method may be repeated on full cell voltage datasets collected over the course of a cycle life or calendar aging test for the aged cell system. Taking $\{\tilde{Q}'_n, \tilde{Q}'_p, \tilde{Q}'_{\mathrm{Li}}\}$ to be model outputs from the aged cell, the following familiar quantities can be defined [161]:

$$\mathrm{LAM_{NE}} = 1 - \frac{\tilde{Q}'_n}{\tilde{Q}_n} \tag{5.34}$$

$$\mathrm{LAM_{PE}} = 1 - \frac{\tilde{Q}'_p}{\tilde{Q}_p} \tag{5.35}$$

$$\mathrm{LLI} = 1 - \frac{\tilde{Q}'_{\mathrm{Li}}}{\tilde{Q}_{\mathrm{Li}}}, \tag{5.36}$$

where $\mathrm{LAM_{PE}}$ is the loss of active material in the positive electrode, $\mathrm{LAM_{NE}}$ is the loss of active material in the negative electrode, and LLI is the loss of lithium inventory. Conveniently, these equations are equally valid for both true model parameters (e.g. Q) and observed model parameters (e.g. $\tilde{Q}$), and therefore, the 'inaccessible lithium problem' introduced in Section 5.3.2 does not affect the numerical outcome of the study of capacity losses over the lifetime of a cell.

Finally, we note that the definition of lithium inventory loss given by Equation 5.36 does not provide any information on where the lithium is physically lost. It is generally understood that a primary pathway for lithium loss is through electrolyte reactions at the negative electrode to form the SEI. However, lithium can also be irreversibly trapped in the negative and positive electrodes due to electrical isolation of particles, which could occur either due to physical fracturing of active material particles [162, 163, 164] or islanding of entire particles due to loss of adhesion to the binder material [165]. A more general expression for the loss of lithium inventory can be expressed as the sum of lithium trapped in each component:

$$\mathrm{LLI} = \mathrm{LLI_{pos}} + \mathrm{LLI_{neg}} + \mathrm{LLI_{SEI}} + \mathrm{LLI_{plating}}. \tag{5.37}$$

In this equation, the first two terms represent lithium trapped inside lithiated but electrically-isolated positive and negative electrode particles, the third term represents the lithium trapped in the negative electrode SEI [161], and the last term represents dead lithium lost to lithium plating [65]. It is important to recognize that differential voltage analysis cannot be used to decompose Q_{Li} or LLI into their constituent parts. Differential voltage analysis thus only reveals the quantity of lithium lost without providing information about where the lithium was lost. This limitation is fundamental to the technique, since different breakdowns of Q_{Li} yield identical voltage features [143]. More advanced, materials-level characterization, will be needed to fully understand the sources of lithium loss.

5.3.4 Data Collection Considerations

Collecting high-quality lab data is a starting point for ensuring that the differential voltage analysis results are reproducible. We therefore dedicate this section to discussing basic experimental considerations to enable reproducible differential voltage analysis for a given cell chemistry, using Figures 5.4 and 5.5 as guides.

5.3.4.1 Obtaining Full-Cell Near-Equilibrium Potential Curves

Differential voltage analysis requires the cell voltage curves to be collected at near-equilibrium conditions so that kinetic effects may be ignored. Without an assumption of near-equilibrium, Equation 5.1 would require additional terms to capture overpotential effects, complicating the analysis. A natural question that follows is "at what C-rate does the voltage data needed to be collected at to constitute near-equilibrium conditions?" This question is especially salient in battery manufacturing contexts, where the speed of diagnostic tests need to be as fast as possible.

In work by previous authors, C-rates ranging between C/20 and C/30 are most commonly used to obtain voltage curves at near-equilibrium conditions. For example, Dubarry et al. [166] used C/25 curves for both differential voltage analysis and incremental capacity analysis, Lu et al. [155] used C/30 curves, and Keil et al. [167] used a fixed current value which translated into C-rates ranging between ∼C/10 and ∼C/30, depending on the cell type.

Using our own datasets, we studied the effect of C-rate on the shape of the voltage and differential voltage curves in Figure 5.4. Panel A shows an example charge dataset collected on an $Ni_{0.6}Mn_{0.2}Co_{0.2}$|graphite system, with C-rates ranging between 1C and C/100. The result shows that the C/20 charge rate achieves a capacity of 2.50Ah, which is within 1% of the capacity of 2.52Ah measured at C/100. The corresponding differential voltage curves, shown in Panel C, shows that the C/20 rate provides peak features that are closely aligned with the near-equilibrium limit at C/100. (Note that, in this panel, each line is offset by an arbitrary constant α for clarity.) Therefore, in our dataset, C/20 appeared to be a reasonable C-rate to capture a near-equilibrium condition.

While C-rates ranging between C/20 and C/30 appear to provide viable input datasets for past work, this result may not always be true for all cell types in manufacturing. Notably, cells having higher energy densities may experience more kinetic limitations, and cells having larger form factors could experience more electrode-level lithium concentration heterogeneities. In both cases, even slower C-rates may be required to resolve the features in the differential voltage plots. Work by Mohtat et al. [74] further suggested that the performance

of voltage fitting methods deteriorates at higher C-rates due to peak smearing. Overall, more work is needed to quantify the effect of C-rate on the analysis outputs as well as the generalizability of C-rate setpoints across different cell chemistries and cell designs.

The directionality of charge must also be considered. Figure 5.4(B,D) show that the voltage and dV/dQ features on discharge are, similar, but not identical, to those on charge. At C/100, the low-SOC peaks, which correspond to graphite features, appear to have sharper peaks on discharge. An additional peak also appears in the discharge data, which can be attributed to the graphite 2L staging reaction (see Figure 5.5C). Practically speaking, the presence of the charge-discharge asymmetry suggests that the differential analysis outputs may be different depending on whether the charge or discharge curves are used. The extent of these differences should be further studied, which we leave as future work.

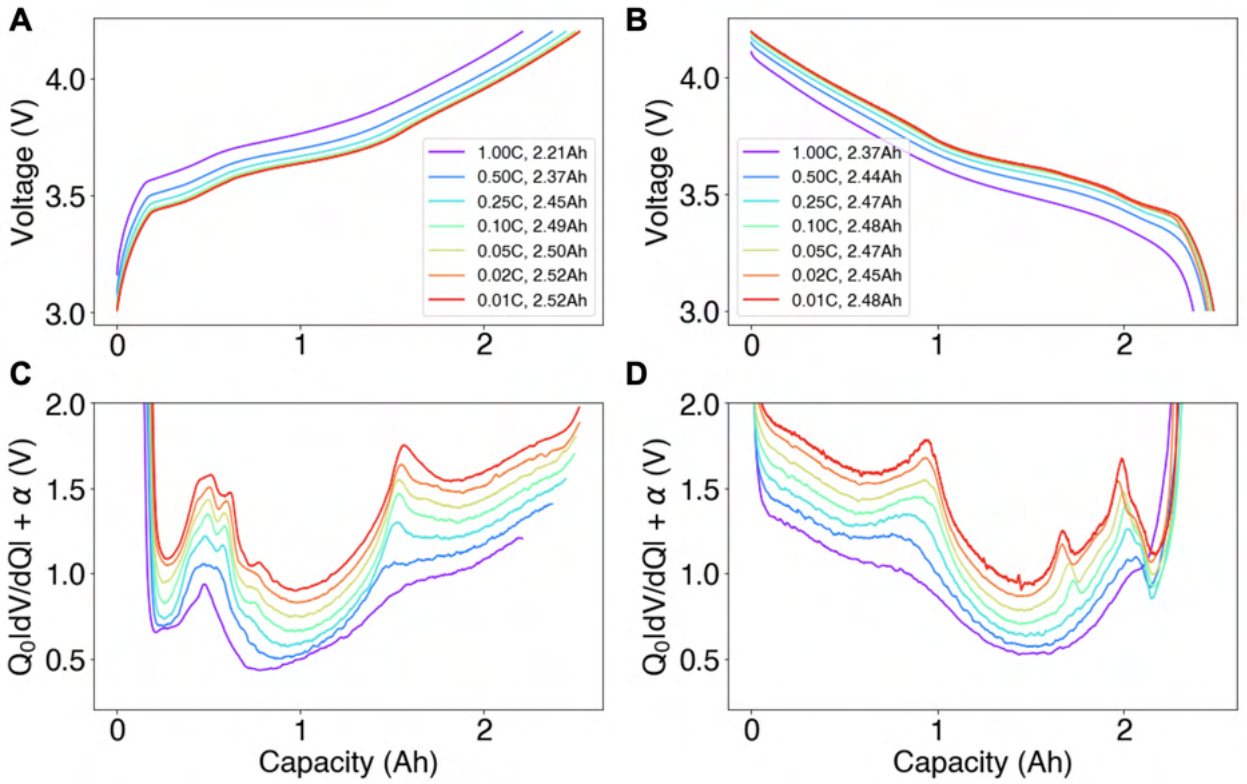

Figure 5.4: Full cell data collection example for DVA. (A, C) Full-cell constant-current charge curves collected at C-rates ranging between 1C and C/100 and their corresponding differential voltage curves. (B, D) The same curves, but collected on discharge. Q_0 is the nominal cell capacity (2.5 Ah). An arbitrary offset α has been added to each dV/dQ curve for clarity.

5.3.4.2 Obtaining Half-Cell Near-Equilibrium Potential Curves

Electrode near-equilibrium potential curves can either be obtained experimentally from scratch using coin cell testing [168, 169] or downloaded from open-access databases such as LiionDB [170]. In either case, due caution is necessary for several reasons.

First, the majority of datasets report half-cell potentials versus lithium stoichiometries, but since there is no common voltage range setting, different half-cell datasets will lead to different modeled outputs for electrode capacities and stoichiometries (see Section 5.3.2).

Second, the experimental procedures used to obtain the curves may differ, with some authors using continuous currents, while other authors obtaining 'quasi-static', or 'pseudo-OCV' curves, by combining data collected after some voltage period at each SOC, similar to the galvanostatic intermittent titration (GITT) technique [171]. While the latter method could theoretically provide a more accurate near-equilibrium potential curve, fewer data points are typically collected to ensure the test finishes within a reasonable time. As a result, some characteristic features related to phase transitions in the negative electrode (Figure 5.4C) may be lost [172].

A third reason for exercising caution when using half-cell data obtained from literature is that the current direction is sometimes not reported, yet current direction materially impacts the features seen in the voltage curves. Figure 5.5 shows that the current direction influences the voltage (and differential voltage) features for both a graphite negative electrode (Panels A,C) and an $Ni_{0.33}Mn_{0.33}Co_{0.33}$ positive electrode (Panels B,D). At the negative electrode, a hysteresis gap between the lithiation and the delithiation curves exists, which persists across consecutive charge-discharge cycles. The characteristic differential voltage feature occurring at $\sim$2.3 Ah, corresponding to the stage 2 transition, is sharper and higher in magnitude in the lithiation direction. The staging reactions 2 through 4 are also distinctly different. In particular, the staging reaction 2L appears sharper on lithiation and the stage 4L reaction appears sharper on delithiation [172].

At the positive electrode, a large kinetic limitation is observed at the end of the lithiation curve, causing the lithiation capacity to be measurably lower than the delithiation curve across multiple cycles. The observation of poor kinetics during lithiation of the positive electrode has been experimentally confirmed by Kasnatscheew et al. [158] and thoroughly discussed in Phattarasupakun et al. [156]. Overall, charge-discharge asymmetry exists at the material level for both the positive and the negative electrodes. For high-fidelity differential voltage analysis, the current direction used to obtain the electrode potential curves should be aligned against what is used for the full cell. Doing so will improve the model's ability to fully describe the full cell voltage curve using the electrode potential curves.

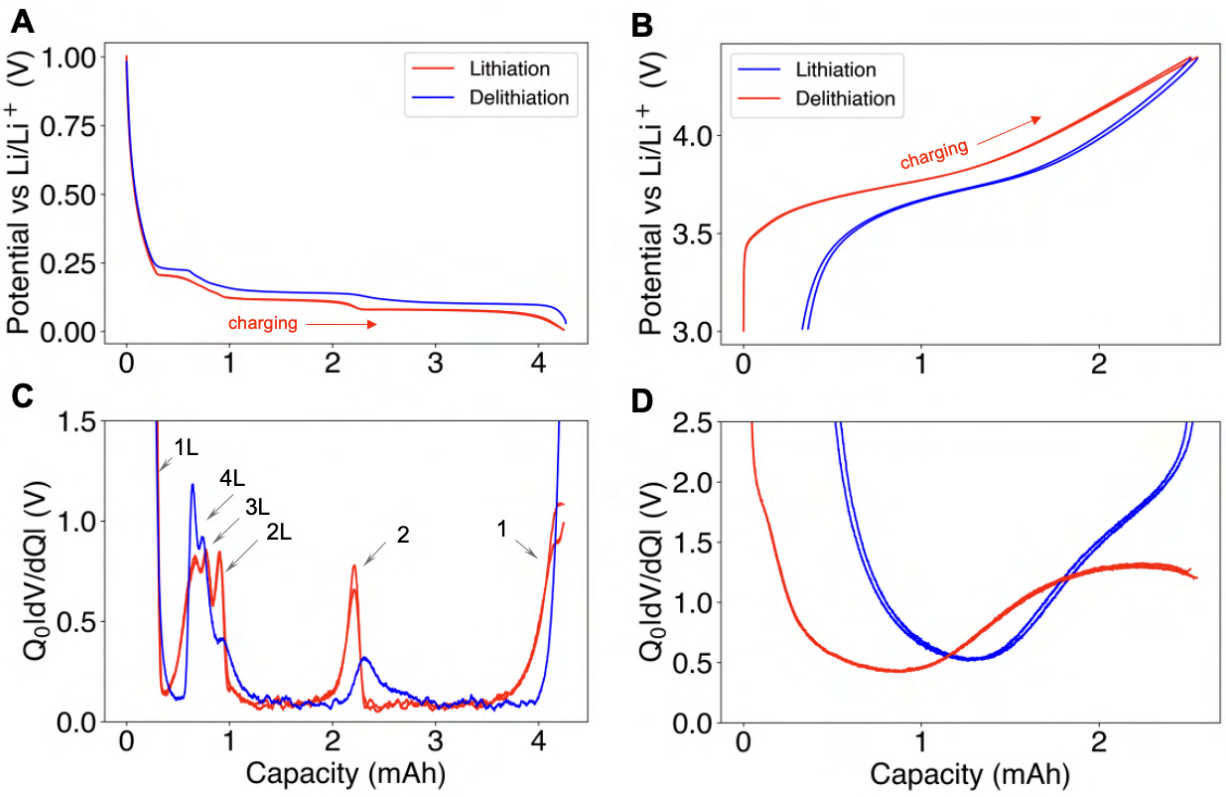

Figure 5.5: Half-cell data collection example for DVA. (A,C) Graphite|lithium half-cell lithiation and delithiation curves and their corresponding different voltage curves. (B,D) $Ni_{0.33}Mn_{0.33}Co_{0.33}$|lithium half-cell lithiation and delithiation curves and their corresponding differential voltage curves. All data is measured at C/50. To indicate reproducibility, data from two consecutive charge-discharge curves have been provided (except for the graphite delithiation curve). The direction corresponding to full cell charging is indicated by a red arrow.

5.3.4.3 Data Logging Frequency and Data Smoothing

The data logging rate and filtering method will affect the smoothness of the collected voltage curves and its derivatives. It is generally recommended to over-sample than under-sample to minimize data loss. Noise in the over-sampled data can be overcome by post-processing the data using filtering methods. A common approach is to use a Savitzky-Golay filter [173] which is included as part of most scientific programming languages. Note, however, that the process of selecting filtering parameters, such as window size and polynomial order, may introduce distortions in the data, decreasing the reproducibility of modeled results [174, 155, 175]. To improve model reproducibility, more studies are needed to understand the degree to which data filtering strategies impact model outputs, which we leave as future

work.

5.3.5 Comments on Factory Deployment

Here, we summarize how a battery manufacturer might deploy the differential voltage analysis method in the battery factory for online process control and quality control applications. We also highlight the remaining knowledge gaps that may prevent deployment today which warrant further research.

Enabling the differential voltage analysis in manufacturing requires both half-cell and full-cell data collection. The half-cell data only needs to be collected once. The data, once vetted, can be stored as part of the model input parameters and be re-used to analyze all full cell data belonging to the same family of positive and negative electrode material sets, e.g. across multiple cell batches and production lines.

The largest barrier to method deployment is then in the acquisition of the full cell near-equilibrium data. As discussed previously, current methods for differential voltage analysis generally require around 20 hours in order to collect the full cell voltage trace. If the measurement method is to be deployed on every cell coming out of formation, then the production throughput will decrease. Considering that the industry trend is to decrease formation times [31], any additional process that will make the total time on test longer may be untenable.

To improve the adoption of the method, we propose several pathways. First, rather than collecting the full cell voltage data after formation, the voltage data during the formation process itself may be processed for differential voltage analysis. To our knowledge, this method has yet been reported in academic literature, and is the subject of future work.

Second, a study should be conducted to understand the influence of higher C-rates on the modeled parameters. Historically, some of the challenges with differential voltage analysis arose in the analysis of aged cells, where the effective current density increases as the cell capacity decreases. For example, at 50% capacity retention, a "C/20" charge step would only take approximately 10 hours to complete since the C-rate is defined with respect to the nominal (pristine) cell capacity. In battery manufacturing, we are only concerned with studying the electrochemical state of the pristine cells without consideration for aging. Hence, the C-rates traditionally thought to be necessary to enable differential voltage analysis may be too conservative in a manufacturing context. A future study of the influence of C-rate on the modeled electrochemical parameters will provide some necessary guidance in this direction.

Finally, not every cell may need to be fingerprinted. For example, retaining and measuring several dozen cells (out of hundreds of thousands built per day) could provide enough

statistical information to track day-to-day changes in electrochemical process parameters. These measurements can still be made on formation equipment, and would only require a small, dedicated number of formation cyclers to be withheld for this purpose. This partitioning method can also encourage the adoption of more advanced characterization methods such as computed tomography (CT) [176, 177, 178], ultrasound imaging [72, 73], and strain measurements [149]. Measuring all of these parameters on the same cell could enable a more complete perspective on the cell's electrochemical and mechanical state, enabling deeper insights.

5.4 Resistance Measurement with HPPC

Battery resistance, also sometimes referred to as internal resistance or impedance, plays a vital role in battery manufacturing quality control since resistance differences can be attributed to intrinsic cell variability [179], tab weld quality [23], electrolyte wetting [180], internal short circuits [181], and battery lifetime [7]. Unlike measurements of capacity and energy, resistance measurements can be measured 'locally' at some fixed SOC reference point. The measurements are also fast, with measurement times ranging between 1 millisecond to 1 minute. Finally, the measurement can be obtained using resistance probes which are more portable and less expensive than full battery testers.

Many popular methods for measuring cell resistance exists. Perhaps the most lightweight method involves measuring an alternating current internal resistance (ACR) using a fixed-frequency sinusoidal current input, typically set to 1kHz [182]. Another popular method, known as the Hybrid Pulse Power Characterization (HPPC) method [183], involves applying one or more constant-current pulse charges or discharges, each lasting on the order of seconds, and computing the direct current resistance (DCR) using Ohm's law. Yet another popular method for measuring cell resistances is through electrochemical impedance spectroscopy (EIS), which enables the separation of different kinetic processes based on their time-scales [184]. Note that, while the EIS method provides a rich dataset for exploration, data acquisition times and equipment costs are both typically higher than direct current methods, making them less readily deployed in mass production settings. Overall, the multiplicity of available measurement methods makes cell resistance a particularly difficult metric to reproduce and compare across different authors and datasets. In general, conditions for measuring resistance are fixed within a single study, but vary greatly across different studies.

This section illustrates the issue of resistance measurement reproducibility by comparing the resistance measured using the HPPC method and at different testing conditions. The data is collected using an expanded HPPC test protocol which includes multiple pulse def-

initions. As we will demonstrate, the numerical value of resistance is highly dependent on experimental factors including SOC, temperature, and pulse conditions, highlighting that care is needed to the reporting of the resistance value reproducible. We end this section by recommending considerations for test design and data reporting to improve the reproducibility of reports of resistance.

5.4.1 Experimental

Figure 5.6 shows an extended version of an HPPC test that was run to probe the sensitivity of calculated resistance values across a range of experimental conditions. The test was run on a 2.5 Ah $Ni_{0.6}Mn_{0.2}Co_{0.2}$//graphite cell under a 5 psi load and at a temperature setpoint of 45°C. The voltage and current trace of the entire test protocol is shown in Panels A and D. The test began by resetting the SOC to 0% by discharging to 3.0V and performing a CV hold until C/50. The pulse sequence pattern shown in Panels B and E was then repeated across multiple SOCs. Each pulse sequence is preceded by a C/4 charge to increment the SOC by 2.5% (indicated by * in Panels B and E). The pulse sequence consists of 30-second pulses, each followed by a rest period. The pulse sequence is {+C/20, -C/20, +C/5, -C/5, +C/2, -C/2, +1C, -1C, +2C, -2C}, where negative C-rates indicate discharges, and positive C-rates indicate charges. The rest duration between each pulse was set to 2 hours for SOCs below 10%, and 30 minutes for the remaining SOCs. During each pulse, the voltage window was expanded to the range (2.0 V and 4.22 V). If the voltage during any pulse exceeds the voltage bounds, then the schedule advances to the next step. The test terminates when 4.2V is reached during an SOC-incrementing step.

The instantaneous resistance for any particular pulse is then given by Ohm's law (Panels C and F):

$$R_{[z]\mathrm{SOC},[t]\mathrm{sec}} = \frac{V_{[z]\mathrm{SOC}} - V_{[t]\mathrm{sec}}}{I}, \tag{5.38}$$

where $V_{[t]\mathrm{sec}}$ is the instantaneous measured voltage after t seconds, I is the constant-current input, and $V_{[z]\mathrm{SOC}}$ is the rest voltage corresponding to z SOC before the pulse begins. The SOC for every pulse within a pulse sequence (Panel B) is calculated by integrating the current from all of the preceding SOC-incrementing steps divided by the total capacity from all of the SOC-incrementing steps. Every pulse within a pulse sequence is assigned the same SOC value.

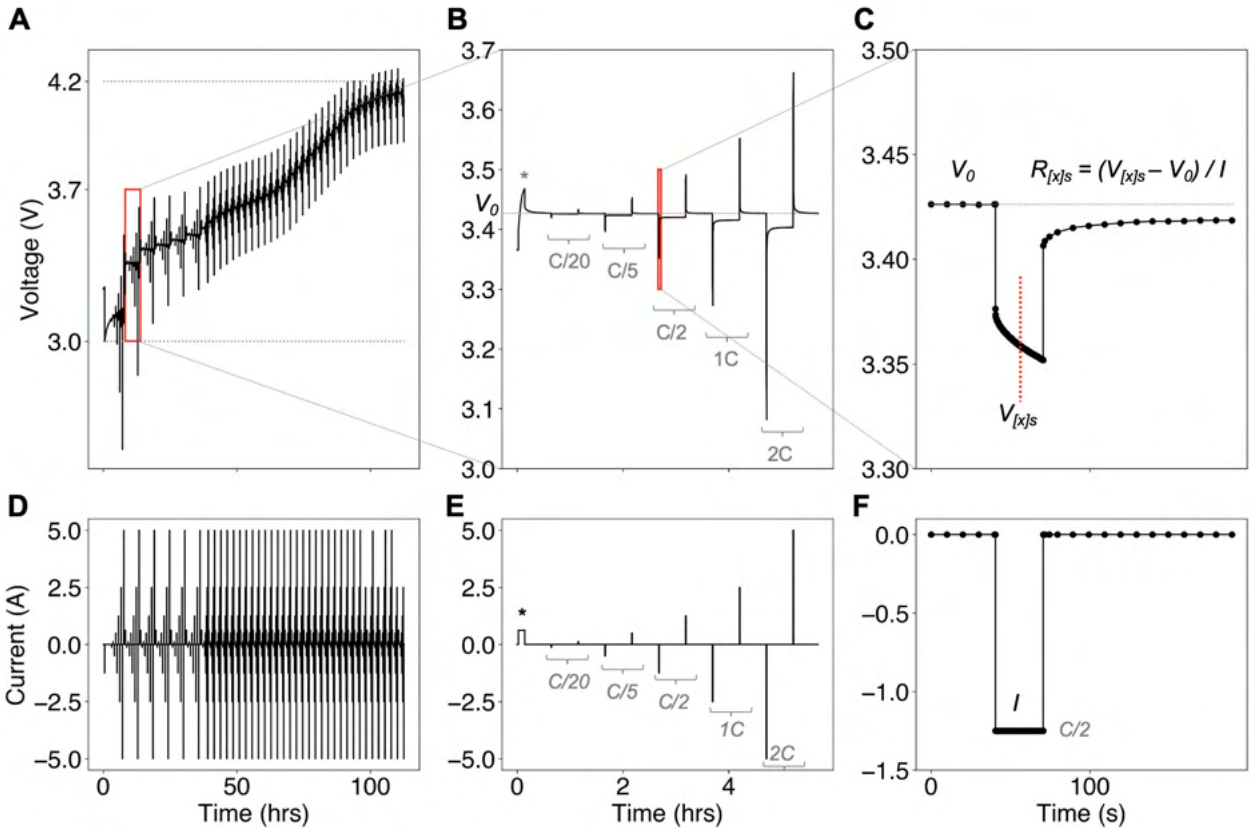

Figure 5.6: Resistance features computed from HPPC. (A) Voltage versus time of the entire HPPC test. (B) Magnification of one pulse sequence, which begins with a charge step to increment the SOC (*), followed by a pulse sequence. (C) Magnification of a single pulse, which starts at near-equilibrium conditions and ends with a rest. (D-F) Corresponding current profiles.

5.4.2 Test Conditions that Affect Measured Resistance

Equation 5.38 highlights the fact that resistance, while simple to calculate, is a function of many factors. Fundamentally, the measured resistance is a macroscopic representation of multiple, concurrent electrical and electrochemical phenomena, spanning multiple materials, interfaces, and timescales. These different phenomena can be better understood by treating the numerator of Equation 5.38 as an overpotential η which can be further broken down as [185]:

$$\eta = \eta_{\text{Ohmic}} + \eta_{\text{diffusion}} + \eta_{\text{charge-transfer}} + \eta_{\text{non-cell}}. \tag{5.39}$$

The Ohmic overpotential is due to the ionic conductivity of the electrolyte, the electronic conductivity of the active materials, and the electronic conductivity of the current collectors. Contact resistances due to internal interfaces (i.e. between the current collectors and the

active materials) and external interfaces (i.e. due to tab welding [23] can also be lumped into the Ohmic overpotential term. The diffusion overpotential is due to the solid-phase diffusion of lithium inside each electrode. The charge-transfer overpotential is due to the activation energy of exchanging electrons and ions at the electrolyte-electrode interface. Finally, the non-cell overpotential is due to contact resistances and cable resistances between the cell tabs and the measurement equipment. Note that the non-cell overpotential is also a form of Ohmic overpotential, but we separate this term in the equation since the physical origin is different.

Equation 5.39 can be used as a starting point to rationalize why resistances measured from HPPC depend on so many factors, including SOC (Section 5.4.2.1), temperature (Section 5.4.2.5), pulse current magnitude (Section 5.4.2.4), pulse current duration (Section 5.4.2.3), and pulse current direction (Section 5.4.2.2). The following sections discuss each factor in detail, referring to Figure 5.7 as a guide.

5.4.2.1 SOC Dependence

Figure 5.7(A,B) shows that the measured resistance can vary by more than 100% depending on the measurement SOC. For this particular system, the sharp rise in resistance at SOCs below 10% is attributed to kinetic limitations in the layered oxide cathode [163]. Resistances at mid-range SOCs can also have inflection points. In these cells, a resistance peak appears at ca. 50% SOC, which becomes more prominent with increasing pulse current duration. This resistance peak is due to the Stage 2 solid-solution regime of the graphite negative electrode [186].

The SOC-dependence of resistance has traditionally been attributed to some combination of the charge-transfer and diffusion processes occurring at either electrode. Indeed, Butler-Volmer kinetics, which describes the charge-transfer process, incorporates a dependence on the lithium concentration as part of the exchange current density prefactor [187]:

$$j = k_0 c_e^{1-\alpha} (c_{s,\max} - c_{s,e})^{1-\alpha} c_{s,e}^{\alpha} \left(\exp\left(\frac{(1-\alpha)F}{RT} \eta \right) - \exp\left(-\frac{\alpha F}{RT} \eta \right) \right), \tag{5.40}$$

where j is the reaction flux, the terms inside the exponentials describe the overpotential-dependence of the forward and backward reactions, and the exponential prefactor terms together describe the exchange current density. $c_{s,\max}$ is the theoretical maximum allowable lithium concentration in the solid phase, $c_{s,e}$ is the surface concentration of lithium, and k_0 is the reaction rate constant.

Solid-phase diffusion coefficients have also been experimentally confirmed to be dependent on lithium concentration [170]. Notably, Verma et al. [188] measured lithium diffusion

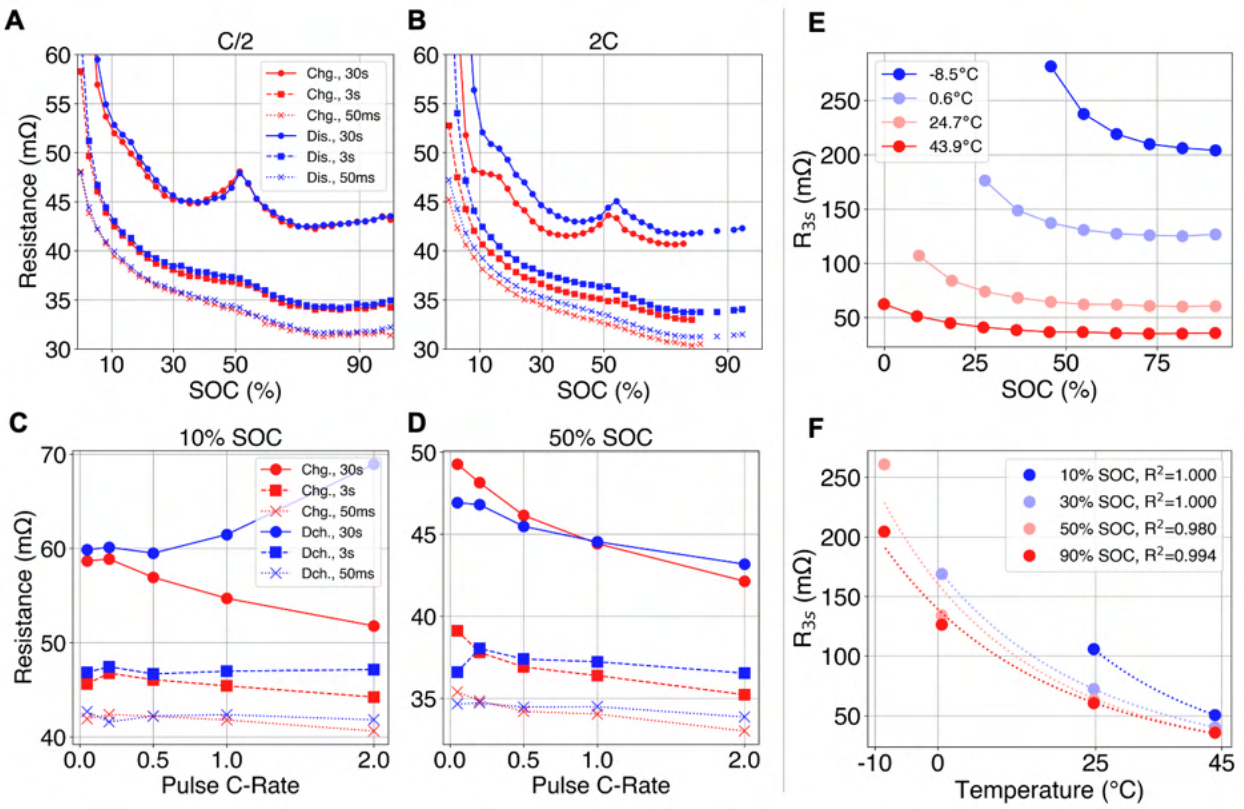

Figure 5.7: HPPC sensitivity studies for an example $Ni_{0.6}Mn_{0.2}Co_{0.2}$|graphite pouch cell. Panels A-D show resistances calculated at 30 seconds, 3 seconds, and 50 milliseconds, and for both charge (red) and discharge (blue) pulses. (A,B) Impact of pulse current magnitude on calculated resistance values. (C-D) Cross-section of the same dataset taken at at 10% and 50% SOC. (E-F) Impact of temperature on resistances calculated on 3-second, C/3 discharge pulses. Dotted lines in Panel F show Arrhenius fits to the measured data.

coefficients that are one order of magnitude lower as the lithium stoichiometry approached unity.

Ohmic and contact resistances are typically considered to be independent of SOC since the materials giving rise to these resistances (e.g. current collectors, tabs, binder, electrolyte) are assumed to be invariant to changes in solid-phase lithium concentrations which determine SOC. However, this assertion may not be completely true considering that lithation-induced strains in the electrodes could increase the contact pressure, thereby decreasing the contact resistances. For NMC—graphite systems, the total volumetric expansion is maximal at high SOCs [157], suggesting that the contact resistance could be lowest at highest SOCs. Such a result would be consistent with the findings reported in Figure 5.7, but it is impossible to deconvolute the effect of charge-transfer and diffusion from the effect of contact resistance

from this dataset alone.

The functional form of the SOC-dependence of resistance cannot be easily generalized across different cathode/anode systems, even within the same class of materials. For example, systems comprising an $Ni_{0.33}Mn_{0.33}Co_{0.33}$ cathode appear to have a flatter resistance profile at intermediate SOCs [7]. Lithium iron phosphate (LFP) systems also typically see an abrupt resistance rise towards 100% SOC, which is attributed to the appearance of the $FePO_4$ phase as the material becomes fully delithiated [189]. In contrast, sharp resistance rises at high SOCs are usually not observed in NMC systems which have excess lithium inventory in the positive electrode in the fully-charged state.

A more complete and physical description of the SOC-dependence of resistance would require resolving the full cell SOC in terms of positive and negative electrode stoichiometries. This can be accomplished using the voltage fitting framework introduced in Section 5.3, and in particular, using the basis transformations defined by Equations 5.5 and 5.6, where $q = zQ_{\text{full}}$. Exploring the full cell resistance through the lens of electrode-specific stoichiometries marks a new pathway to identify electrode-specific contributions to full cell resistance. Due caution will be needed to develop proper baseline resistance curves for the positive and negative electrodes, which we leave for future work.

5.4.2.2 Resistance Gap: Charge-Discharge Resistance Asymmetry

Resistances measured from HPPC may differ depending on whether the resistances are calculated from charge versus discharge pulses, leading to a 'resistance gap', as shown in Panels C and D. Panel C shows that, at 5% SOC, resistances calculated during a discharge pulse are higher than that calculated on a charge pulse. The resistance gap increases as the pulse current magnitude increases. The gap persists at higher SOCs and for C-rates greater than C/2 (Panels B and D). At C-rates below C/2, the gap is within the measurement noise and is no longer observable.

The presence of the resistance gap has been observed by previous authors [190, 182] and raises some fundamental questions about the nature of resistance measurement using the HPPC method. Does the resistance gap have a physical origin, or is it some artefact of the HPPC test design? Even more broadly, how can voltage polarization dynamics be accurately modeled if resistances vary on charge and discharge? While fully addressing these questions is beyond the scope of this present work, we will provide a brief discussion to prompt further investigations in this area.

In our design of the HPPC pulse sequence, every discharge pulse was designed to start at the same nominal initial voltage V_0 as shown in Figure 5.6B. This result was achieved since the capacity moved during the discharge pulse is recovered exactly by the subsequent charge

pulse. However, in this design, each charge pulse must necessarily start at a lower V_0, and hence a lower SOC, compared to the discharge pulses. The decrease in SOC is calculated by:

$$\Delta z_{\text{error}} = C_{\text{rate}} \times t_{\text{pulse}}, \tag{5.41}$$

where the C-rate is given in units of hrs^{-1} and t_{pulse} is the pulse duration in units of hours. For example, applying this formula to the 2C, 30-second charge pulses would yield an SOC decrement of 1.67% from the target value. Surprisingly, applying this SOC correction factor to the results from Figure 5.7 would widen the resistance gap between charge and discharge, not close it. Therefore, the SOC misalignment due to the test design cannot explain the presence of the observed charge-discharge asymmetry.

We note two distinct, physical sources of charge-discharge asymmetry: 'thermodynamic' voltage hysteresis and asymmetric charge-transfer kinetics. 'Thermodynamic' voltage hysteresis refers to the presence of a 'zero-current gap' between the charge and discharge OCV curve, which suggests that the same measured equilibrium potential corresponds to two different chemical states [119]. Asymmetric charge-transfer kinetics generally refers to reaction mechanisms with differing rate constants depending on the direction of the reaction. Explanations for this charge-transfer asymmetry have been ascribed to lithium-ion solvation and desolvation kinetics at the electrode-electrolyte interface [191]. We hypothesize that both thermodynamic and kinetic factors could be contributing to the observed charge-discharge resistance asymmetry.

5.4.2.3 Pulse Durations: How Long is Too Long?

The extended HPPC test design shown in Figure 5.6 used 30-second pulses at all of the tested C-rates. At this time-scale, Ohmic and charge-transfer processes are easily captured since both processes occur at timescales less than one second [191]. Extending the pulse duration further to 30 seconds enables the measured resistance to capture diffusion-related processes occurring at lower frequencies. A 30-second pulse is reasonable for capturing all of the different kinetic phenomena as outlined in Equation 5.39. Note that resistances at intermediate pulse durations can always be recovered by re-processing the data. For example, Figure 5.7 illustrates the resistances calculated at 50 milliseconds and 3 seconds from the same dataset.

A natural question to ask in designing an HPPC test is: how long should each pulse be? We discuss here both the advantages and disadvantages of longer pulse durations. First, we note that pulse durations longer than 3 seconds appear to be necessary for capturing certain kinetic phenomena. For example, Figure 5.7(A,B) show that resistances calculated from a

3-second pulse cannot capture the graphite staging peak at 50% SOC, suggesting that this resistance contribution from the graphite could be related to a slow diffusion process rather than a charge-transfer limitation.

Since the goal of the HPPC test is to provide resistance values localized to a fixed SOC set-point, we suggest that an upper limit be set on the maximum pulse duration so that the cell SOC does not change appreciably throughout the pulse, according to Equation 5.41. For example, if we desire no more than 1% SOC movement during a 1C pulse, then the maximum allowable pulse duration is 36 seconds. Exceeding this pulse duration will complicate the interpretation of the measured resistance since the underlying cell state cannot be assumed to be static throughout the pulse duration.

5.4.2.4 Pulse Current Magnitude Affects Measured Resistance

Smaller resistances are measured at higher current magnitudes under most pulse conditions. For example, Figure 5.7(A,B) shows that, at 30% SOC, a C/2 charge pulse yields a resistance of 46.5mΩ, but the same resistance measured on a 2C discharge pulse is 5% lower, at 44.1mΩ. Similar trends hold across most other pulse durations and SOCs. This phenomenon is attributable to the fact that, at higher current densities, the charge-transfer activation overpotential increases more slowly according to Butler-Volmer Kinetics [192].

Two exceptions break the general trend of lower measured resistances at higher current magnitudes: at low SOCs and for pulse currents lower than C/2. At low SOCs, resistances calculated from charge pulses continue to decrease as the C-rate is increased, but the trend is reversed on discharge, with higher pulse C-rates resulting in higher measured resistances. We attribute this to the fact that, at low SOCs, small increases in the cathode lithium concentration due to the pulse discharges will lead to significant decreases in the lithium diffusion coefficients [188]. At lower C-rates, the measured resistance values are noisier (see Figure S2), and measured resistance differences in this regime are within the signal-to-noise.

5.4.2.5 Temperature Dependence

Temperature sensitivity of battery parameters is perhaps the most often overlooked sensitivity in battery literature. Lack of temperature control is especially concerning for resistance measurements since resistances are highly temperature-dependent [193]. Nearly every lithium transport process in cells exhibits a non-trivial temperature dependence, including the electrode-electrolyte charge-transfer process [194, 195], bulk-phase lithium diffusion kinetics [65], and lithium transport through the electrolyte [196].

Figure 5.7(E,F) shows that, for our cells under study, the resistance at all measured

SOCs increase five-fold from 45°C to -10°C. In Panel F, we fit an Arrhenius law to the data according to:

$$R(T) = A \exp\left(-\frac{E_a}{RT}\right), \tag{5.42}$$

where A and E_a are fitting parameters, R is the universal gas constant, and T is the measured temperature in Kelvin. The fits show good agreement with the data, with $R^2 > 0.98$ in all cases. An Arrhenius plot is provided in Figure S3 for reference. The Arrhenius plot suggests that, if the data points at -10°C are further excluded, then the R^2 values improve to 1.000 at all measured SOCs, which suggests that a single activation energy is sufficient for describing the temperature-dependence between 0°C and 45°C. For temperatures lower than 0°C, another activation energy may be needed to capture additional temperature-dependent factors.

A practical consideration for experimental design is: "how much temperature variation is allowable?" An answer can be provided by calculating the local slope of the temperature sensitivity around the target operating temperature T_{ref}:

$$\left.\frac{dR}{dT}\right|_{T=T_{\text{ref}}} = \frac{AE_a}{RT_{\text{ref}}^2} \exp\left(-\frac{E_a}{RT_{\text{ref}}}\right). \tag{5.43}$$

For example, for a target operating temperature of $T_{\text{ref}} = 25$°C and at 90% SOC, the temperature sensitivity is -2.3mΩ/°C, or equivalently, every 1°C of temperature error will result in 2.3mΩ of resistance error.

5.4.2.6 Data Logging Frequency

From a manufacturing diagnostic perspective, it is highly desirable to separate the non-electrochemical (i.e. Ohmic) from the electrochemical (i.e. charge-transfer and diffusion) contributions to the total measured cell resistance. Separating the resistance contributions can help identify the origin of resistance differences. For example, manufacturing defects due to mechanical issues such as poor tab welding could be caught by studying differences in the Ohmic resistance, which is measured at high frequencies. Meanwhile, differences in the electrode material processing may affect the charge-transfer or diffusion process, which could show up in the longer time-scale resistances.

To accurately ascertain the Ohmic resistance from the HPPC data, the data acquisition frequency should be as high as possible so that the instantaneous voltage drop can be separated from the charge-transfer process. Since the charge-transfer process occurs on a timescale ranging between 1Hz and 1kHz [184], a measurement of true Ohmic resistance should be collected at frequencies higher than 1kHz. In our HPPC measurements presented

in Figure 5.7, 20 Hz (50 ms) was the highest measurement frequency practically achievable on a conventional Arbin BT-2000 battery testing system. Above this frequency, data could not be logged consistently.

5.4.3 Towards More Reproducible Resistance Measurements

The preceding section illustrated that a simple, point measurement of resistance cannot be precisely reproduced unless at least five factors are known: the state of charge before the pulse, whether the pulse was taken on charge or discharge, the magnitude of the pulse, the duration at which resistance was calculated, and the temperature of the pulse. For measurements of Ohmic resistance, the sample logging frequency also becomes imperative. All of these sensitivities (with the exception of data logging frequency) reflect physical realities of lithium transport dynamics across multiple materials and multiple interfaces; these sensitivities cannot be suppressed through experimental design. A comparison of the relative importance of each sensitivity is provided in Table 5.3. We note that the sensitivities reported here are applicable to the cells we studied, which are $Ni_{0.6}Mn_{0.2}Co_{0.2}$|graphite cells. Other cell chemistries, with different electrode choices or electrolyte formulations, may show different trends.

Ref.	Sensitivity	Condition	From	To	ΔR (mΩ)	ΔR (%)
5.4.2.1	State of charge	1	30% SOC	90% SOC	37.9 $\rightarrow$ 34.2	+9.8%
5.4.2.2	Current direction	1	discharge	charge	37.9 $\rightarrow$ 38.4	+1.3%
5.4.2.3	Pulse duration	1	3 sec.	30 sec.	37.9 $\rightarrow$ 45.0	+18.7%
5.4.2.4	Current magnitude	1	0.5 C	2.0 C	37.9 $\rightarrow$ 36.5	-3.7%
5.4.2.5	Temperature	2	25°C	30°C	72.2 $\rightarrow$ 60.8	-15.7%
Condition 1: 30% SOC, discharge, 0.5C, 3 second, 45°C: 37.9mΩ						
Condition 2: 30% SOC, discharge, 0.33C, 3 second, 25°C: 72.2mΩ						

Table 5.3: Experimental factors affecting measured resistance from HPPC. Results show measurements taken on $Ni_{0.6}Mn_{0.2}Co_{0.2}$|graphite pouch cells. For each sensitivity, the resistance difference is reported for a reference pulse condition.

Given that measured resistance values depend on so many different experimental factors, the battery manufacturer will need to take precautions to enable reproducible resistance measurements. A first step is to standardize the resistance measurement method itself. An explicit, step-by-step protocol is needed to specify the pre-conditioning steps to arrive at a target SOC. Next, pulse parameters, including pulse direction, magnitude, duration, need to be fully specified and recorded. Finally, the temperature must be measured.

With all of these metadata recorded and databased, manufacturers are better positioned to determine whether measured resistance differences reflect physical differences in the manufacturing process or cell lifetimes, or are due to differences in the measurement method. The availability of the metadata can also enable manufacturers to implement error-compensation models. For example, if temperature data is collected, then it can be used to calculate a temperature correction factor based on a pre-determined Arrhenius-based temperature calibration curve, much like the one presented in Figure 5.7F.

5.5 A Manufacturing Case Study

Here, we showcase an example of how the DVA method can be used for continuous monitoring of cell electrochemical features at the end of the manufacturing process. We highlight the various electrochemical metrics, or features, that can be extracted using the method and their significance for manufacturing process control.

Figure 5.8 shows the general analysis workflow and lists the electrochemical features extracted by the model. In this example, full cell voltage data (V_{full}) was collected on every manufactured cell after the formation cycling was completed (Section 5.3.4.1). Each dataset was analyzed using the differential voltage analysis model (Section 5.3). The model consisted of two pre-computed functions, U^+ and U^-, representing the positive and negative electrode near-equilibrium reference potential curves, respectively (Section 5.3.4.2). The same functions were used to analyze data from both Mohtat2021 and Weng2021, since the batches shared the same positive and negative electrode chemistries.

Returning to the Weng2021 and Mohtat2021 datasets introduced in Section 5.3.2.1, we apply the differential voltage model to extract positive and negative electrode capacities ($\tilde{Q}_p$, $\tilde{Q}_n$), the capacity of lithium available for cycling ($\tilde{Q}_{\text{Li}}$), the capacity of lithium lost to the SEI ($\tilde{Q}_{\text{SEI}}$), electrode lithium stoichiometries when the full cell is discharged ($\tilde{x}_0$, $\tilde{y}_0$), and cell design information including the practical negative-to-positive capacity ratio ($\text{NPR}_{\text{practical}}$) and the excess negative electrode capacity ($\tilde{Q}_{n,\text{excess}}$). The 'tildes' on each variable name indicate that they are estimates which may be different from the true parameters as described in 5.3.2. These extracted features can then be analyzed to determine whether machine parameter adjustments are needed in upstream manufacturing processes such as those in electrode coating or in electrolyte fill (E-fill).

Figure 5.9 show an example data visualization of the analysis outputs. Panel A uses box-and-whisker plots to compare compares several example metrics derived from the differential voltage analysis, including $\tilde{Q}_p, \tilde{Q}_n$, $\tilde{Q}_{\text{SEI}}$, and $\text{NPR}_{\text{practical}}$. The full-cell C/20 discharge capacity, Q_{full}, is also provided for reference. Since the Mohtat2021 and Weng2021 cells used

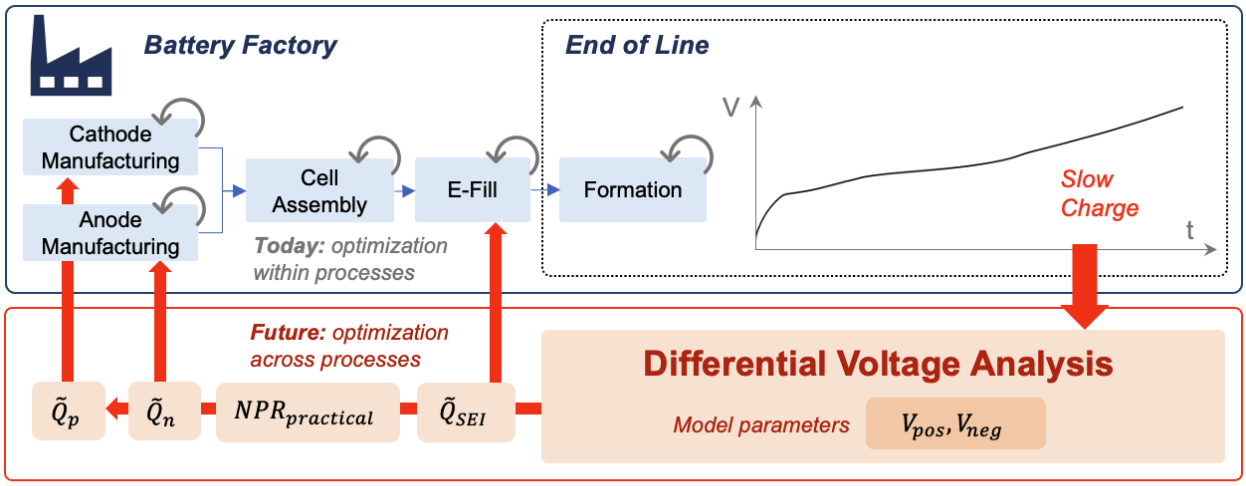

Symbol	Electrochemical Feature	Applications	Design Considerations
$\tilde{Q}_p$	Positive electrode (cathode) capacity	**Electrode manufacturing process control**	**Full Cell and Half-Cell Data** C-Rate Charge or discharge Temperature Voltage window Data acquisition rate Curve smoothing method **Optimizer** Objective function Solver settings Parameter identifiability
$\tilde{Q}_n$	Negative electrode (anode) capacity		
$\tilde{Q}_{SEI}$	Lithium consumed during formation	**Formation process control and electrolyte optimization**	
$\tilde{Q}_{Li}$	Cyclable lithium inventory capacity		
$\tilde{x}_0$	Negative electrode (anode) lithium stoichiometry at 0% SOC		
$\tilde{y}_0$	Positive electrode (cathode) lithium stoichiometry at 0% SOC		
$NPR_{practical}$	Practical N:P capacity ratio	**Lithium plating risk assessment**	
$\tilde{Q}_{n,excess}$	Excess negative electrode capacity		

Figure 5.8: Summary of how differential voltage analysis can enable coordinated battery manufacturing process control via end-of-line testing. The provided table describes the voltage-based electrochemical features derived from the method, including applications in manufacturing and test design considerations.

different numbers of electrode sheets, all of the capacity values reported here have been normalized to the respective electrode areas, enabling a head-to-head comparison. An example model fitting result is also provided in 5.10.

The following sections discusse how to interpret each group of features in the context of manufacturing process control.

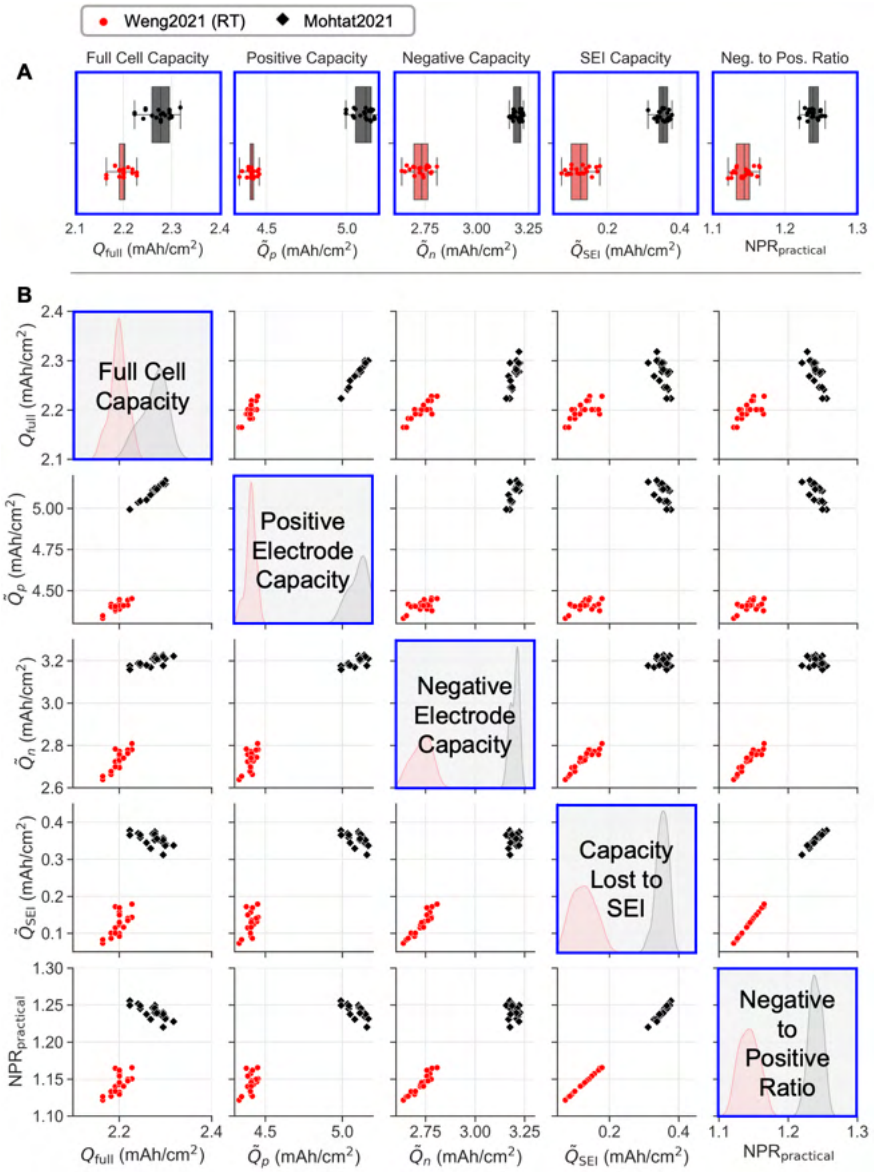

Figure 5.9: Leveraging DVA to non-destructively identify electrochemical differences between two cell batches at the end of the manufacturing line. Data spans two separate datasets from Weng2021 [7] ($n = 20$) and Mohtat2021 [157] ($n = 21$). Cells from both datasets share the same chemistry ($Ni_{0.33}Mn_{0.33}Co_{0.33}$|graphite), but were made in two separate batches and vary in cell design parameters. (A) Box-and-whisker plots comparing data from the two batches, where each marker shows modeled outputs on each individual cell. (B) correlation plots of the metrics, where diagonal elements show histograms comparing individual metrics across the two different batches.

5.5.0.1 Monitoring Electrode Capacities and Loadings

Figure 5.9A shows extracted values of positive and negative electrode capacities, $\tilde{Q}_n$, and $\tilde{Q}_p$, for every cell in this study. In a manufacturing context, the availability of data on $\tilde{Q}_n$ and $\tilde{Q}_p$ on every batch of cells in production, without needing cell dissections, can help to identify deviations from electrode loading set-points, e.g. due to electrode processing variations. These electrode-level variations would be difficult to detect by relying on full cell capacity check data alone, since capacity variability at the electrode level may not manifest in full cell capacity checks (Section 5.5.3).

We also found that the Mohtat2021 cells had, on average, 16% higher positive electrode areal capacity and 17% higher negative electrode areal capacity compared to the Weng2021 cells. However, according to the cell design parameters (Table 5.1), Mohtat2021 cells should have only 7% higher positive electrode areal capacity and 9% higher negative electrode areal capacity based on differences in the active material loading targets. The gap between the targeted and modeled capacities suggests that the as-built cells did not match their target loadings, and that electrode coating process parameters may need to be adjusted.

5.5.1 Monitoring Lithium Consumed During Formation

Figure 5.9A also compares the amount of lithium consumed during formation, $\tilde{Q}_{\text{SEI}}$, for all cells in this study. For the Mohtat2021 cells, the mean value was measured to be 0.35 mAh/cm^2, while the Weng2021 cells measured 0.12 mAh/cm^2. Mohtat2021 cells thus lost nearly three times more lithium during formation than compared to the Weng2021 cells. This result can be verified graphically by inspecting the voltage curve alignments from the fitting results which shows that the positive electrode is less lithiated at 0% SOC, reflecting the fact that extra lithium was irreversibly consumed to form the SEI and cannot return to the positive electrode on discharge. The increase in lithium consumption rate during the formation of the Mohtat2021 cells suggests a poorer quality of electrolyte or a less passivating negative electrode formulation. Note that both cell builds shared the same formation protocol, so differences in lithium consumption cannot be attributed to differences in the formation protocol. This example highlights a scenario in which the electrolyte filling process parameters may need to be inspected, or the quality of the electrolyte itself may need to be verified.

The increased lithium consumption in the Mohtat2021 cells also helps to explain why, although the Mohtat2021 cells had 16% higher positive electrode areal mass loading than the Weng2021 cells, the full cell capacities of the Mohtat2021 cells were only 3% higher on average. Thus, although the Mohtat2021 cells were designed with higher areal capacities

than the Weng2021 cells, most of the benefits to full cell capacity were lost due the increased lithium consumption rate during formation.

5.5.2 Measuring Margin to Lithium Plating Using the Practical NP Ratio

Since the Mohtat2021 cells had consumed more lithium during formation compared to the Weng2021 cells, the Mohtat2021 negative electrodes will also be less lithiated when the full cell is charged to 100% SOC. The Mohtat2021 cells will therefore have a wider margin of negative electrode capacity before the negative electrode is fully lithiated and lithium plating begins to occur, a result that can be visually seen in Figure 5.10. Thus, Mohtat2021 cells are expected to be less prone to lithium plating compared to the Weng2021 cells.

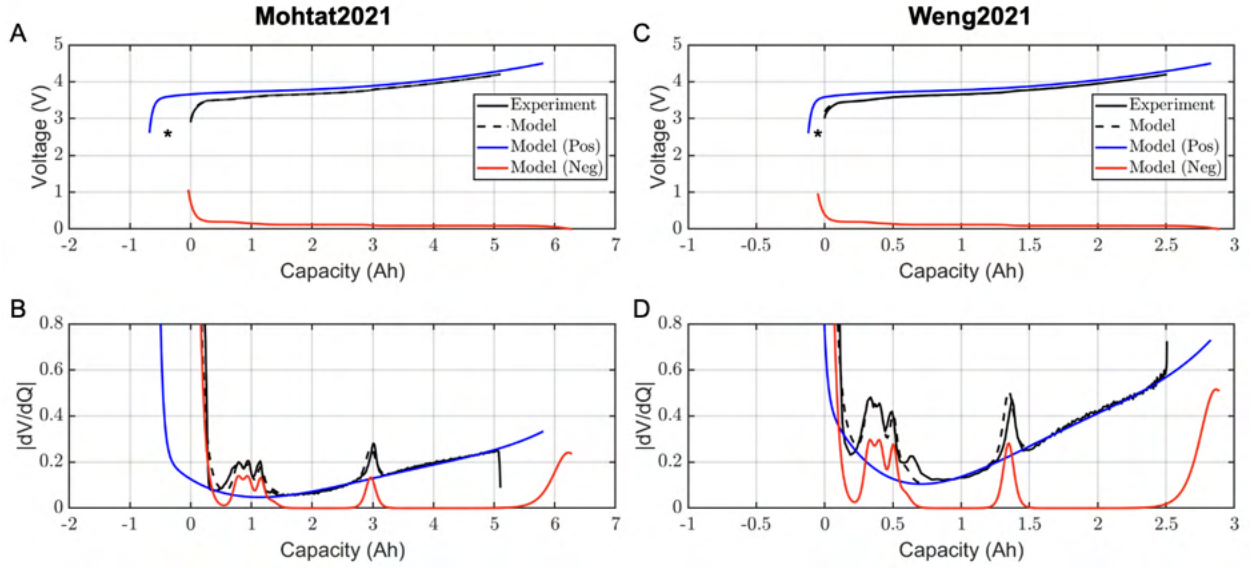

Figure 5.10: Comparison of DVA output between the Mohtat2021 and Weng2021 datasets. (A,B) voltage and differential voltage curves from Weng2021. (C,D) Voltage and differential voltage curves from Mohtat21. The asterik (*) highlights that the Mohtat2021 cell consumed more lithium during formation compared to the Weng2021 cells.

A metric that quantifies the capacity margin before lithium plating occurs is the negative to positive ratio (NPR). The differential voltage analysis provides such a metric, known as the practical NPR, or $\text{NPR}_{\text{practical}}$, which we developed in Section 5.3.3.2. The $\text{NPR}_{\text{practical}}$ for Mohtat2021 cells was measured to be 1.24, compared to 1.14 for the Weng2021 cells, confirming that the Mohtat2021 cells have a higher negative electrode capacity margin to protect against lithium plating. For the Weng2021 cells to achieve the same $\text{NPR}_{\text{practical}}$ as

the Mohtat2021 cells, either the positive electrode loading target would need to decrease, or the negative electrode loading target would need to increase.

5.5.3 Electrode Manufacturing Variability

Turning to Figure 5.9B, we next show how the differential voltage analysis outputs can be used to identify differences in electrode manufacturing variability from batch to batch. We immediately see that Mohtat2021 cells showed higher variability in the full cell capacity. The histograms of $\tilde{Q}_n$ and $\tilde{Q}_p$ reveal that the origin of the higher full cell capacity variability stems from the positive electrode loading, not the negative electrode loading. In fact, the negative electrode loading for Weng2021 cells had higher variability compared to the Mohtat2021 cells, yet this increased variability did not manifest in the full cell capacity. This result is expected considering the fact that the practical NP ratio of all cells are greater than 1, and hence, variations in the negative electrode capacities will mainly manifest in the excess negative electrode capacity rather than the full cell capacity. Thus, to decrease the full cell capacity variability in the Mohtat2021 cells, the manufacturer should focus on tightening the variability in the cathode manufacturing process, not the anode manufacturing process.

5.5.4 Parameter Correlations

Figure 5.9B finally presents correlation plots between every individual output variable of the differential voltage analysis model. One application of studying correlations is to understand which electrode-level parameters correlate to full cell capacity and hence directly impacts measurable cell performance. The correlation matrix reveals that, within each batch of cells, the positive electrode capacity correlates to full cell capacity. However, the correlation breaks when comparing across different batches of cells since the Mohtat2021 consumed more lithium during formation (Section 5.5.1). This result highlights the reality that multiple cell manufacturing factors, including electrode loadings, lithium consumption during formation, and the negative electrode excess capacity, all play a role in determining the full cell capacity. Achieving a certain full cell capacity outcome therefore requires coordinated control across multiple manufacturing processes.

In summary, this section highlighted the utility of applying the differential voltage analysis method to extract electrochemical metrics at the end of the cell manufacturing line. These metrics can then be directly used to adjust process upstream manufacturing process parameters such as those in electrolyte manufacturing or electrolyte filling. All of the data presented in this section were directly outputted from the differential voltage method without needing any electrode-level degradation analysis. Since the method can run on data

collected during battery formation, no additional work is necessary to extend the analysis to new cells coming off the manufacturing line, making the method highly scalable.

5.6 Conclusion

This chapter clarified how differential voltage analysis (DVA) can be used to extract cell thermodynamic diagnostic signals from slow-rate voltage curves. We also highlighted how the hybrid pulse power characterization (HPPC) method can be used to extract resistance signatures on a full cell.

For DVA, we highlighted opportunities for method automation towards applications in battery manufacturing process control. With this method, key electrochemical parameters, such as positive and negative electrode capacities, lithium lost to form the SEI, and negative to positive ratios, can be quantified non-destructively. We further applied the method to a battery manufacturing dataset to gain insight into the sources and consequences of manufacturing variability. In our example, we found that the source of variability in full cell capacity for one batch of cells is due to variations in positive electrode loadings. We also detected a three-fold difference in the amount of lithium consumed to form the SEI between two different cell batches, a conclusion we were able to make without observing any data from the formation cycles or using any destructive analytical methods.

To facilitate the adoption of the DVA method in manufacturing, we detailed the mathematical formalism required to implement the method as well as the input data requirements. We extended the base model formulation to explicitly account for model parameter errors due to the inaccessible lithium problem. Using the reformulated model, we defined an expanded set of electrochemical features which included the lithium consumed during formation, the practical NP ratio, the excess negative electrode capacity, and the total cyclable lithium. When combined, these features provide a "fingerprint" of the electrochemical state of the pristine cell which can then be used to adjust parameters in various manufacturing steps including electrode manufacturing and the formation process.

Besides clarifying the methods for diagnostic feature extraction, this work also recognized the importance of obtaining high-quality experimental data, including both full cell and half-cell data, to enable reproducible results. We identified several basic data collection considerations, including the C-rate, current direction (charge versus discharge), and data smoothing method, as being potential factors affecting model output reproducibility.

With improved awareness of the nuances involved with model construction, model output interpretation, and data collection, the battery community can be better positioned to deploy the DVA and HPPC methods in factories, driving continuous improvement to the battery

manufacturing process.

CHAPTER 6

Predicting the Impact of Formation Protocols on Battery Lifetime

6.1 Abstract

Increasing the speed of battery formation can significantly lower lithium-ion battery manufacturing costs. However, adopting faster formation protocols in practical manufacturing settings is challenging due to a lack of inexpensive, rapid diagnostic signals that can inform possible impacts on long-term battery lifetime. In this chapter, we identify the cell resistance measured at low states of charge as an early-life diagnostic feature for screening new formation protocols. We show that this signal correlates to cycle life and improves the accuracy of data-driven battery lifetime prediction models. The signal is obtainable at the end of the manufacturing line, takes seconds to acquire, and does not require specialized test equipment. We explore a physical connection between this resistance signal and the quantity of lithium consumed during formation, suggesting that the signal may be broadly applicable for evaluating any manufacturing process change that could impact the total lithium consumed during formation.

6.2 Introduction

With the increasing demand for electric vehicles, global lithium-ion battery manufacturing capacity is quickly approaching the terawatt-hour scale [197, 198, 199]. A key step in battery manufacturing is formation/aging, which has been estimated to account for up to 30% of total manufacturing costs [200, 201, 202, 17, 203]. The formation/aging process involves charging and discharging hundreds of thousands of cells in environmentally controlled chambers, an expensive process that takes days to weeks to complete but is necessary to improve battery performance and lifetime [204, 205, 206, 207, 208, 209].

Given the high cost burden, manufacturers are incentivized to develop new formation processes that decrease the total time consumed by formation/aging. A variety of fast formation strategies have been studied in academic literature, which employ some combination of rapid charge-discharge cycles, restricted voltage windows, and optimized temperature [205, 30, 210, 211, 212, 213, 214, 215, 37, 216, 217, 218, 34]. Recent studies have shown that formation time can be decreased while preserving battery lifetime [210, 218, 37], although conclusions remain tenuous due to the limited sample sizes typically used.

In real manufacturing settings, a 'one size fits all' formation protocol is unlikely to exist since cell designs with different electrolytes, electrodes, and active materials influence important formation factors such as charging capability, electrode wettability, and SEI reaction pathways. However, cycle life testing often takes months or years to complete, posing a significant barrier to the adoption of new, potentially cost-saving formation protocols. While characterization techniques such as volume change detection [219, 220, 221], impedance spectroscopy [222, 30], acoustic spectroscopy [223, 224, 225, 73] and X-ray tomography [226, 227] have been proposed for use in manufacturing settings, these methods can be costly to implement since the metrology will need to be deployed at scale in the battery factory. Diagnostic features that rely only on current-voltage signals that can be obtained using already available cycling equipment [228] and are thus highly attractive.

In this work, we show that the cell resistance at low states of charge can be used to screen new formation protocols and predict battery lifetime. Our work shows that this signal, measured at the beginning of life, is a stronger predictor of battery lifetime than conventional signals such as Coulombic efficiency. This metric can be measured within seconds and can be integrated directly into the battery manufacturing process with no additional capital costs. This low-SOC resistance metric can thus be deployed in practical manufacturing settings to accelerate the evaluation of new formation protocols. We further demonstrate that the low-SOC resistance decreases as the quantity of lithium lost to the SEI during formation increases. With this physical insight, we propose that this metric, in principle, also be used to diagnose the impact of any manufacturing process that alters the total lithium consumed during formation.

6.3 Methods

In this section, we outline the build process for the cells used in this study, the formation protocols used, the cycle life test protocols, and the analysis methods used to extract beginning-of-life and end-of-life diagnostic features as well as perform statistical analysis.

Forty NMC/graphite pouch cells with a nominal capacity of 2.36Ah were built for this

study (Table 6.1). Half of the cells underwent a fast formation protocol, and the remaining cells underwent a baseline formation protocol (see Section 6.3.2. Cells were further subdivided into 'room temperature' and '45°C' aging groups for cycle life testing. The cycling profile was identical for all cells: 1C charge to 4.2V with a CV hold to 10 mA and 1C discharge to 3.0V. Periodic RPTs [229] were inserted throughout the cycle life test, which includes slow (C/20) charge and discharge curves as well as a HPPC sequence [183] used to extract the cell internal resistance as a function of SOC.

	Dimensions	72 mm x 110 mm
	Stack (pos/neg)	7/8
Positive	Chemistry	NMC111
	Composition	NMC111 : C65 : PVDF
	Ratio	94 : 3 : 3
	Loading (double-sided)	34.45 mg/cm^2
	Collector thickness	12 um
Negative	Chemistry	Graphite
	Composition	MAG-E3 : CMC : SBR
	Ratio	97 : 1.5 : 1.5
	Loading (double-sided)	15.7 mg/cm^2
	Collector thickness	10 um
Electrolyte	Salt	1.0 M $LiPF_6$
	Solvent	EC : EMC
		(3 : 7)
	Additive	2 wt% VC, 4g/Ah
	Mass	10.55 g
Separator	Supplier	Entek
	Thickness	12 um

Table 6.1: Cell design parameters

Our experimental design (Figure 6.1a) used larger sample sizes ($n = 10$ per group) compared with those typically reported in the literature which often uses three cells or fewer per group. The increased sample size enables a more statistically rigorous analysis of the impact of different formation protocols on cell characteristics at the beginning and the end of life.

6.3.1 Cell Build Process

The pouch cell architecture is summarized in Figure 6.2.

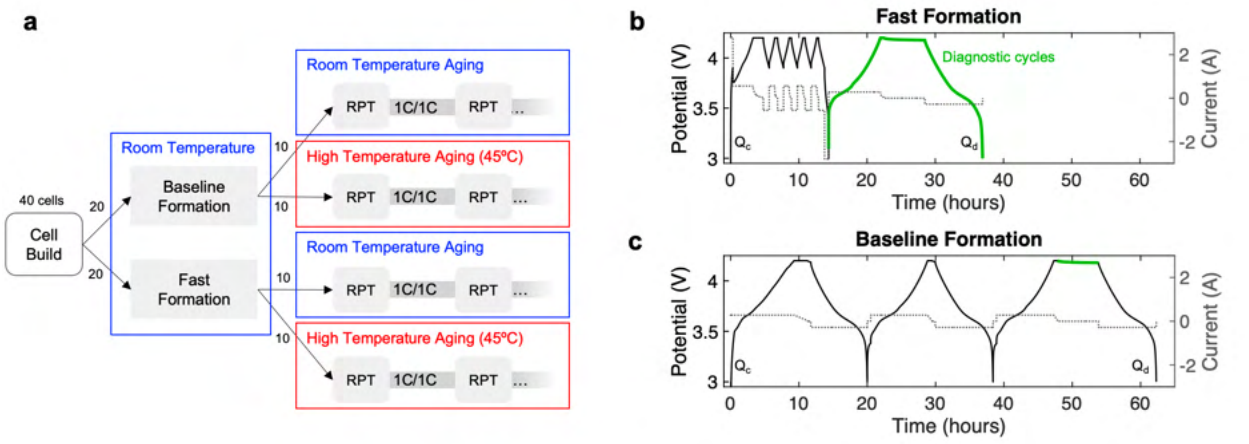

Figure 6.1: Experimental design. (a) Distribution of cells across two formation protocols and two aging temperatures. The aging test consists of 1C charge/discharge cycles between 3.0V and 4.2V, with RPTs inserted periodically into the test. (b, c) Voltage and current versus time profiles for (b) fast formation and (c) baseline formation. Green lines show diagnostic steps inserted into the formation protocols for this study only. The diagnostic cycles are not considered to be part of the formation protocol. Ignoring the diagnostic cycles, the fast formation protocol lasts 14 hours and the baseline formation protocol lasts 56 hours.

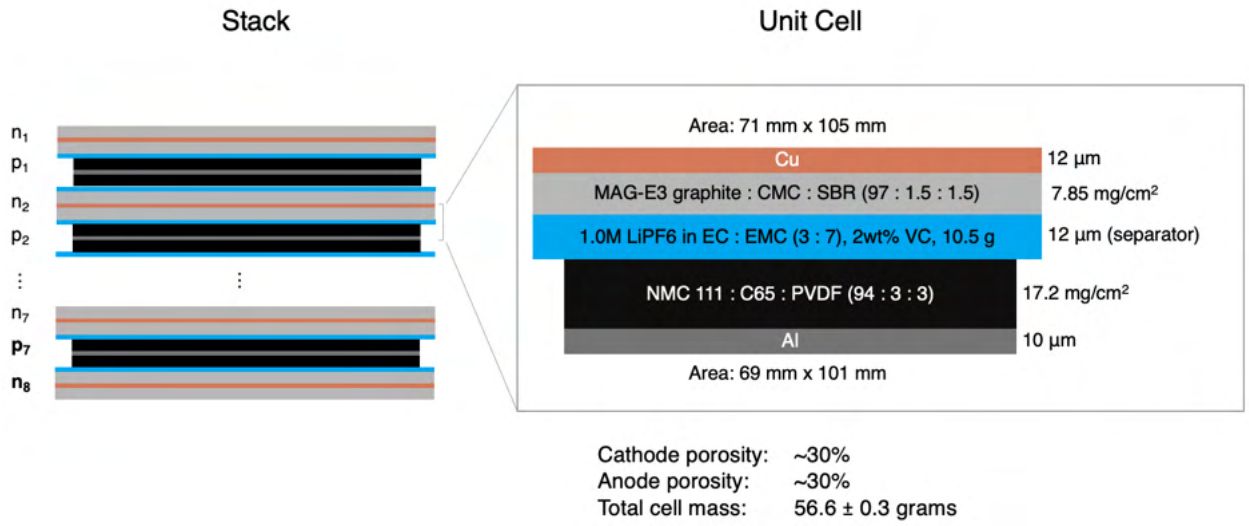

Figure 6.2: Pouch cell architecture. Left: cell stack definition. Right: unit cell definition. The same cell architecture is used for all cells in this study.

The cathode was comprised of 94:3:3 NMC 111 (TODA North America), C65 conductive additive (Timcal), and PVDF (Kureha 7208). The slurry was mixed in a step-wise manner, starting with a dry solids homogenization, wetting with NMP, and then the addition of the PVDF resin. The slurry was allowed to mix overnight under static vacuum with agitation

from both the double helix blades (30 rpm) and the high-speed disperser blade (1600 rpm). The final slurry was gravity-filtered through a 125 μm paint filter before being coated on a roll-to-roll coating machine (Creative & Innovative Systems). The electrode was coated using the reverse comma method at 2 m/min. The final double-sided loading was 34.45 mg/cm^2.

The anode was comprised of 97:0:(1.5/1.5) graphite (Hitachi MAG-E3), no conductive additive, and equal parts CMC (proprietary) and SBR (Zeon BM-451B). The graphite and pre-dispersed CMC were mixed before further let-down with de-ionized water and overnight dispersion under static vacuum and double helix blade agitation (40 rpm). Before coating, the SBR was added and mixed in with helical blade agitation for 15 minutes under active vacuum. The final slurry was gravity-filtered through a 125 μm paint filter before being coated on a roll-to-roll coating machine (Creative & Innovative Systems). The electrode was coated using the reverse comma technique at 1.5 m/min. The final double-sided loading was 15.7 mg/cm^2.

Both anode and cathode were calendared at room temperature to approximately 30% porosity before being transferred to a -40°C dew point dry room for final cell assembly and electrolyte filling. The cells, comprising 7 cathodes and 8 anodes, were z-fold stacked, ultrasonically welded, and sealed into formed pouch material (mPlus). The assembled cells were placed in a vacuum oven at 50°C overnight to fully dry prior to electrolyte addition. Approximately 10.5 g of electrolyte (1.0M $LiPF_6$ in 3:7 EC:EMC v/v + 2wt% VC from Soulbrain) was manually added to each cell before the initial vacuum seal (50 Torr, 5 sec). The total mass of all components of the battery is 56.6 $\pm$ 0.3g.

The now-wetted cells were each placed under compression between fiberglass plates held in place using spring-loaded bolts. The compression fixtures are designed to allow the gas pouch to protrude and freely expand in the event of gas generation during formation. All cells were allowed to wet for 24 hours before beginning the formation process.

After formation, the cells were removed from the pressure fixtures, returned to the -40°C dew point dry room, and degassed. The degassing process was completed in an "mPlus" degassing machine, automatically piercing the gas pouch, drawing out any generated gas during the final vacuum seal (50 Torr, 5 sec), and then placing the final seal on the cell. Cells are manually trimmed to their final dimensions before being returned to their pressure fixtures.

6.3.2 Formation Protocols

Two formation protocols were implemented: a fast formation protocol previously reported by Wood et al. [210, 30] which completes within 14 hours (Figure 6.1b) and a baseline formation protocol (Figure 6.1c) which completes in 56 hours.

The fast formation protocol maximizes the time spent at low negative electrode potentials to promote the creation of a more passivating SEI [30, 230, 231, 232]. In this protocol, the cell is brought to 3.9V using a 1C (2.36Ah) charge, followed by five consecutive charge-discharge cycles between 3.9V and 4.2V at C/5, and finally ending on a 1C discharge to 2.5V. Each charge step terminates on a CV hold until the current falls below C/100. A C/10 charge-discharge cycle was appended at the end of the test to measure the post-formation cell discharge capacity. A 6-hour step was included in between the C/10 charge-discharge steps to monitor the voltage decay. The formation sequence takes 14 hours to complete after excluding time taken for diagnostic steps.

A baseline formation protocol was also implemented which serves as the control for comparing against the performance of fast formation. This protocol consists of three consecutive C/10 charge-discharge cycles between 3.0V and 4.2V. A 6-hour rest was also added between the final C/10 charge-discharge step to monitor the voltage decay signal. The total formation time was 56 hours after excluding the diagnostic steps. Formation was conducted at room temperature for all cells and across both formation protocols.

All formation cycling was conducted on a Maccor Series 4000 cycler (0-5V, 30μA - 1A, auto-ranging). Following formation, one cell (#9) was excluded from this study due to tab weld issues. Consequently, the sample count for the 'baseline formation, 45°C' cycling group was decreased to 9. The remaining groups had sample counts of 10.

The mean cell energy measured at a 1C discharge rate from 4.2V to 3.0V at room temperature is 8.13 Wh. Full cell level volumetric stack energy density is estimated to be 365 Wh/L based on a volume of 69mm x 101mm x 71 mm x 3.2 mm, and the gravimetric stack energy density is estimated to be 144 Wh/kg based on a total cell mass of 56.6g.

6.3.3 Cycle Life Testing

Following the completion of formation cycling, cells were placed in spring-loaded compression fixtures to maintain a uniform stack pressure. Half of the cells from each formation protocol were placed in a thermal chamber (Espec) with a measured temperature of 44.2 ± 0.1°C. The remaining cells were left at room temperature and were exposed to varying temperatures throughout the day (24.5 ± 0.6°C). Long-term cycle life testing was conducted on a Maccor Series 4000 cycler (0-5V, 10A, auto-ranging). The cycle life test protocol was identical

for all cells and consisted of 1C (2.37A), CC charge to 4.2V with a CV hold to 10mA and 1C discharges to 3.0V. At every 50 to 100 cycles, the test was interrupted so that a Reference Performance Test (RPT) could be performed [229]. The RPT consists of a C/3 charge-discharge cycle, a C/20 charge-discharge cycle, followed by the Hybrid Pulse Power Characterization (HPPC) protocol [183]. The HPPC test is used to extract 10-second discharge resistance (R_{10s}) as a function of SOC (Figure B.6). Every cell was cycled until the discharge capacity was less than 1.18 Ah, corresponding to less than 50% capacity remaining. The total test time varied between 3 to 4 months and the total cycles achieved ranged between 400 and 600 cycles. Cycle test metrics are shown in Figures B.1, B.2, B.3, B.4.

6.3.4 Statistical Significance Testing

The standard Student's t-test for two samples was used throughout this study to check if differences in measured outcomes between the two different formation protocols were statistically significant. The p-value was used to quantify the level of marginal significance within the statistical hypothesis test and represents the probability that the null hypothesis is true. A p-value less than 0.05 was used to reject the null hypothesis that the population means are equal. All measured outcomes were assumed to be normally distributed. Box-and-whisker plots are also used throughout the paper to summarize distributions of outcomes. Boxes denote the inter-quartile range (IQR) and whiskers show the minimum and maximum values in the set. No outlier detection methods are employed here due to the small sample sizes ($n < 10$). Finally, the Pearson correlation coefficient, $-1 \leq \rho \leq 1$, was used to determine the significance of correlations between initial state variables and lifetime output variables. $|\rho| > 0.5$ is taken to indicate a statistically meaningful correlation.

6.3.5 Predictive Lifetime Model

Due to the small number of data points available, the model prediction results are sensitive to which cells are chosen for validation. Therefore, we used nested cross-validation [233] to evaluate the regularized linear regression model on all the data without over-fitting. The nested cross-validation algorithm is as follows: first, we separated the data into 20% 'validation' and 80% 'train/test'. Then, we performed four-fold cross-validation on the 'train/test' data to find the optimal regularization strength for Ridge regression, α^*, using grid search. Finally, we trained the Ridge regression algorithm with regularization strength α^*, using all of the train/test data, and evaluated the error on the validation data. We repeated this process for 1000 random train-test/validation splits and reported the mean and standard deviation of the mean percent error for each run,

$$\text{MPE}[\%] = \frac{1}{N}\sum_{k=1}^{N}\frac{y_k^{\text{pred}} - y_k^{\text{true}}}{y_k^{\text{true}}}. \tag{6.1}$$

Each run can select a different optimal regularization strength α^*.

6.3.6 Electrode Stoichiometry Model

To construct the stoichiometry model shown in Figure 6.8a, a full cell near-equilibrium potential curve was first extracted using the C/20 charge cycle from the RPT. A randomly-selected cell from the 45°C cycling group was selected for this data extraction. Positive and negative electrode near-equilibrium potential curves were adapted from Mohtat et al. [221]. The electrode-specific utilization windows are determined by fitting the positive and negative electrode potential curves to match the full cell curve by solving a least squares optimization problem as outlined in Lee et al. [69]. The resulting positive and negative electrode alignment minimized the squared error of the modeled versus the measured full cell voltage. The fast formation curve equilibrium potential curve was constructed by shifting the positive electrode curve horizontally and re-computing the full cell voltage curve.

The full cell resistance curves in Figure 6.8(c) sourced data from the HPPC sequence as part of the same RPT used to obtain the equilibrium potential curve shown in Figure 6.8(a). A cubic spline fit was used to create smooth resistance curves. (A model generated using a linear fit instead is provided in Figure B.20). To break down the resistance contribution into 'positive resistance' and 'negative + other resistances', a baseline reference resistance R_{ref} was first defined as the minimum measured full cell resistance below 1Ah. The 'negative + other resistances' was then assigned a value of $(1 - f_{\text{pos}}) \cdot R_{\text{ref}}$. The remaining resistance was then assigned to the positive electrode. f_{pos} was set to 0.7 to model a generic NMC/graphite system [234, 30, 235].

6.3.7 Voltage Fitting Algorithm

Methods for estimating electrode-specific state-of-health metrics using half-cell reference curves have been previously reported [141, 236, 142]. Here, we applied an automated voltage fitting approach based on work by Lee et al. [69] to extract electrode capacity losses LAM_{PE} and LAM_{NE}, as well as lithium inventory loss (LLI) for both fresh and aged cells. The input data consisted of C/20 charge curves measured at each RPT. An example set of C/20 charge curves over age is shown in Figure B.14.

The method to extract electrode-specific state of health indicators LLI, LAM_{PE} and LAM_{NE} is adapted from [69]. Positive and negative near-equilibrium potential curves were

adapted from Mohtat et al. [221]. The positive and negative electrode potential curves are obtained during delithiation and lithiation, respectively, which correspond to charging in the full cell. The curves were obtained at the C/20 rate and serve as proxies for the true equilibrium potential curves. The same equilibrium potential curves were used to model data at both test temperatures.

To prevent over-fitting, the positive electrode stoichiometry at 100% SOC (y_{100}) was fixed to 0.03 at every instance for this analysis. Fixing this value yielded smoother and more physical degradation trajectories over cycle life. Figure B.15 shows an example of voltage fitting results for a single cell. The degradation metrics, including LLI and LAM were computed in the usual manner (see Lee et al. [69] for more details).

6.3.8 Hybrid Power Pulse Characterization of Half Cells

Coin cell half cells were built with lithium iron phosphate (LFP), NMC111, and graphite as the working electrode and lithium metal as the counter electrode. The NMC material used was identical to that used in the pouch cells for the formation experiments (TODA North America). The graphite material used differed from the ones used in the pouch cells. The coin cell construction consisted of 2032 form factor components including a wavespring and spacer. The electrolyte used was 1M $LiPF_6$ with EC/EMC. The lithium counter electrode was 16 mm in diameter, the separator was 19 mm in diameter, and the working electrodes were 14mm in diameter. Working electrodes were measured to be approximately 60 μm thick and the lithium counter-electrodes were approximately 750 μm thick. Working electrodes were single-side coated. Calculated theoretical capacities for the NMC111, LFP, and graphite cells were 2.0 mAh, 2.9 mAh, and 4.6 mAh, respectively.

The Hybrid Pulse Power Characterization (HPPC) protocol was adapted for the coin cells. Potential ranges were modified depending on the working electrode. The currents used in the pulses were also scaled down to 0.4 mA for all cells (Figure B.17). The measured resistance drop includes a large Ohmic contribution due to the presence of the lithium metal counter electrode. However, since this counter electrode was present in all cells, differences in measured, SOC-dependent resistances between the different cells remain meaningful. All coin cells were pre-conditioned using at least three slow charge-discharge cycles before starting the HPPC sequence.

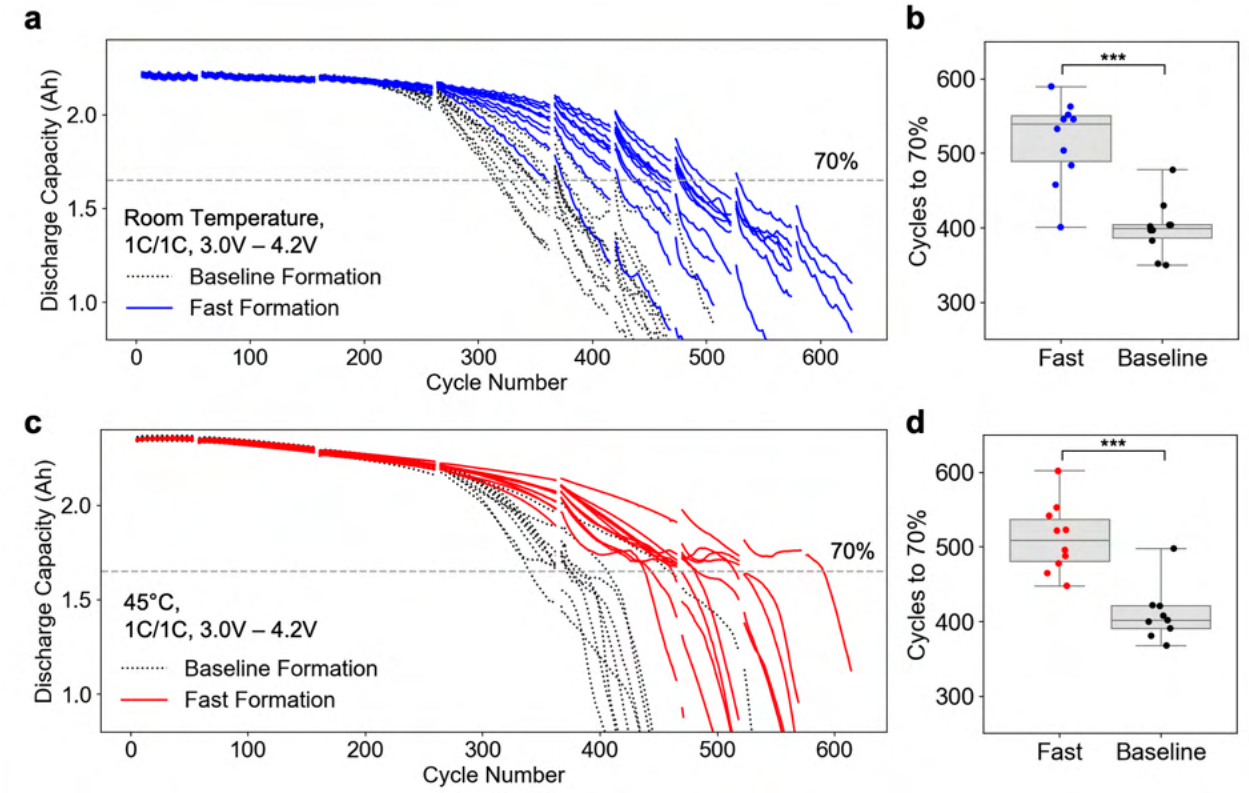

Figure 6.3: Cycle life test results. (a,c) Discharge capacity for individual cells measured during the 1C/1C aging test at (a) room temperature and (c) 45°C. Gaps in the curves correspond to the embedded RPT cycles. (b,d) End-of-life capacity retention distributions, defined as when the cell discharge capacity reaches 70% of initial capacity. '***' - statistically significant with p-value < 0.001.

6.4 Results

6.4.1 Fast Formation Cells Had Longer Cycle Life

Fast formation cells had higher average lifetimes than the baseline formation cells under the cycle life test, as shown in Figure 6.3. The degradation rate of fast formation cells initially track the baseline formation cells closely under both temperatures tested (Panels a, c). However, after 250 cycles, all cells begin to lose capacity rapidly. The fast formation cells sustained over 100 cycles longer before reaching the end of life, defined as when cells reach 70% of their initial measured capacity (Panels b, d). This result is highly statistically significant (p-value < 0.001). The general result that fast formation improved lifetime performance holds across multiple performance metrics, including Coulombic efficiency (Figure B.2) and voltage efficiency (Figure B.3), as well as when plotted against equivalent cycles (Figure B.5). Together, these results support the growing body of evidence that well-designed fast

formation protocols can improve cycle life [30, 37, 237].

6.4.2 Finding Diagnostic Signals at the Beginning of Life

Given the demonstrated impact of formation protocol on battery cycle life, we turn to investigating methods to quantify the impact of fast formation on the initial cell state. Differences in the initial cell state (e.g. lithium consumed during formation) may offer clues as to how fast formation could have improved cycle life. We focused our work on studying signals directly obtainable from full cell current-voltage data, which offer the lowest barrier-to-entry for deployment in real manufacturing settings.

6.4.2.1 Conventional Metrics of Formation Efficiency

Figures 6.4(a-c) show standard measures of formation efficiency extracted from the formation cycling data. The discharge capacity, Q_{d}, was measured at the end of each formation protocol during a C/10 discharge step from 4.2V to 3.0V. Q_{d} corresponds to the capacity of cyclable lithium excluding the contribution from lithium irreversibly lost to the SEI during formation. Fast formation decreased Q_{d} by 0.3%, a small but statistically significant difference ($p = 0.01$). The charge capacity, Q_{c}, was taken during the initial charge cycle, and includes both the capacity of cyclable lithium as well as the capacity of lithium lost irreversibly to the SEI. The quantity of lithium inventory lost to the SEI can be calculated as $Q_{\mathrm{SEI}} = Q_{\mathrm{c}} - Q_{\mathrm{d}}$ (Panel b). Note that while the two formation protocols differed in the initial charging rate, Q_{c} remains a fair comparison metric since both charge protocols ended on a potentiostatic hold at 4.2V until the current dropped below C/100. Fast formation increased Q_{SEI} by 23 mAh ($p = 0.03$). Finally, we also included another common evaluation metric, the formation Coulombic efficiency, defined as $\mathrm{CE_f} = Q_{\mathrm{d}}/Q_{\mathrm{c}}$ (panel c), which shows that fast formation decreased $\mathrm{CE_f}$ by 0.8% ($p = 0.02$). Measured values are summarized in Table 6.2. Together, the results show that fast formation marginally increased the amount of lithium consumed during formation. A p-value of less than 0.05 in all cases indicate that the measured differences, while small, are statistically significant to a least a 95% confidence level.

6.4.2.2 Low-SOC Resistance

Following formation, the cell internal resistance was measured using the Hybrid Power Pulse Characterization (HPPC) technique [183] prior to the start of the cycle life test. During this test, a series of 10-second, 1C discharge pulses were applied to the cell at varying SOCs, and the resistance is calculated using Ohm's law (Figure B.6). The 10-second resistance,

R_{10s}, was plotted against SOC for all cells cycled at 45°C (Figure 6.4d). R_{10s} generally remained flat at mid-to high SOCs. The peak at 55% SOC corresponds to the stage 2 solid-solution regime of the graphite negative electrode [186]. R_{10s} rose sharply below 10% SOC. Focusing on the low-SOC region (Figure 6.4e), we observed that R_{10s} measured at 4% and 8% SOC were lower for fast formation cells compared to that of baseline formation cells. This result was highly statistically significant, with a p-value less than 0.001 (Figure 6.4f). A similar result held when R_{10s} was measured at room temperature (Figure B.7). At mid to high SOCs, differences in R_{10s} between fast formation and baseline formation cells were generally not statistically significant (Figure B.7). Thus, differences in resistance between the two formation protocols appeared uniquely at low SOCs. All initial cell state metrics are summarized as part of Table 6.2.

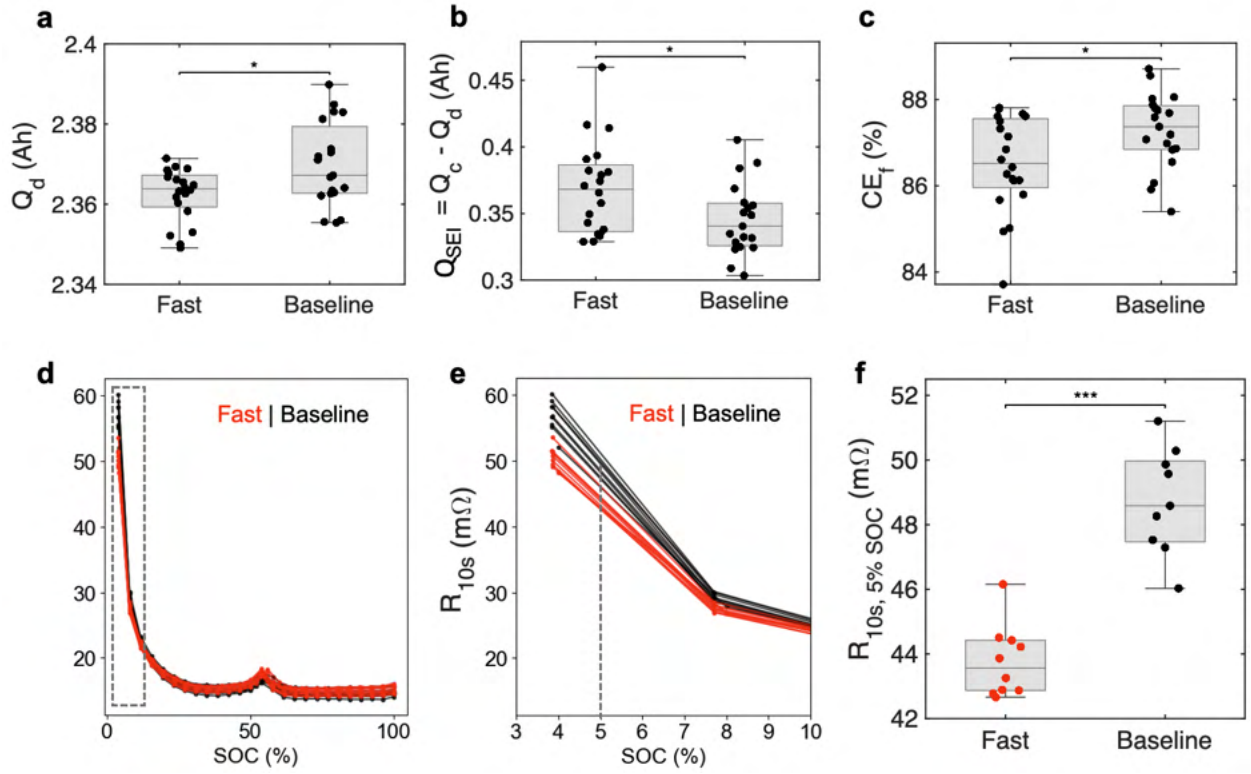

Figure 6.4: Diagnostic signals for differences in the initial cell state. (a) Final discharge capacity, (b) capacity of lithium inventory lost during formation, and (c) formation Coulombic efficiency, measured from the formation protocol. (d) 10-second resistance obtained from the Hybrid Pulse Power Characterization test prior to the start of the cycle life test. (e) Magnification of the 10-second resistance at low SOCs. (f) Distribution of 10-second resistance at 5% SOC comparing between the two formation protocols. (d-f) are sourced from the initial reference performance test from the 45°C cycle life test (see Figure B.7 for the results at room temperature cycle life test). '*' - statistically significant with p-value < 0.05. '***' - statistically significant with p-value < 0.001.

Metric	Unit	Temp.	Baseline Formation	Fast Formation	Δ (abs)	Δ (%)	p-value
Q_{d}	mAh	Room	2370 (11)	2362 (7)	-8	-0.3%	0.01
Q_{SEI} ($Q_{\mathrm{c}} - Q_{\mathrm{d}}$)	mAh	Room	346 (27)	369 (35)	+23	+6.6%	0.03
$\mathrm{CE_f}$	%	Room	87.3 (0.9)	86.5 (1.1)	-0.8	-0.9%	0.02
$R_{\mathrm{10s,5\%SOC}}$ ($\mathrm{R_{LS}}$)	mΩ	Room	139.7 (2.9)	130.0 (2.3)	-9.7	-6.9%	<0.001
$R_{\mathrm{10s,5\%SOC}}$ ($\mathrm{R_{LS}}$)	mΩ	45°C	48.7 (1.6)	43.8 (1.1)	-4.9	-10.0%	<0.001
$R_{\mathrm{10s,90\%SOC}}$	mΩ	Room	23.6 (0.1)	23.9 (1.0)	+0.3	+1.3%	0.28
$R_{\mathrm{10s,90\%SOC}}$	mΩ	45°C	14.5 (0.4)	14.9 (0.5)	+0.4	+2.8%	0.10

Table 6.2: Comparison of initial cell state metrics. Values are reported as mean (standard deviation). Q_{d}, Q_{SEI}, and $\mathrm{CE_f}$ are extracted directly from the formation test protocol. $\mathrm{R_{10s}}$ metrics are extracted from the initial reference performance test at the beginning of the cycle life test profile.

To study the robustness of the low-SOC resistance signal, we varied the SOC set-point between 4% and 10% and also computed the resistance under 1-second and 5-second pulse durations. In all cases, the resistance metric provided a high degree of contrast between the two different formation protocols (Figures B.8 and B.9). The lowest SOC measured in our dataset was 4% SOC.

The remainder of the paper will focus on the resistance measured at 5% SOC and with a 10-second pulse duration. From hereon, this metric will be referred to as the 'low-SOC resistance', $\mathrm{R_{LS}}$.

6.4.3 $\mathrm{R_{LS}}$ as a Diagnostic Signal: A Data-Driven Perspective

6.4.3.1 $\mathrm{R_{LS}}$ Correlates to Cycle Life

To evaluate the merit of low-SOC resistance ($\mathrm{R_{LS}}$) as a diagnostic feature, we explored the correlations between the initial cell metrics (Figure 6.4) and the cycle life, defined as cycles to 70% of the initial capacity. The results are shown in Figure 6.5. Out of all metrics studied, $\mathrm{R_{LS}}$ was the only signal with a meaningful correlation to cycle life, with a correlation coefficient of $\rho = -0.84$. Other metrics such as Q_{d} and $\mathrm{CE_f}$ were poorly correlated to cycle life ($|\rho| < 0.5$). We attribute the weakness of these correlations to the poor signal-to-noise inherent in cell capacity measurements in the absence of high-precision cycling [145, 238], a topic we explore in detail later. The resistance measured at high SOCs also did not correlate to cycle life. From these results, we observe that the low-SOC signal uniquely holds information related to cycle life. These results have been reproduced for different end-

of-life definitions ranging between 50% and 80% (Figures B.11, B.12), as well as for charge pulses (Figure B.13).

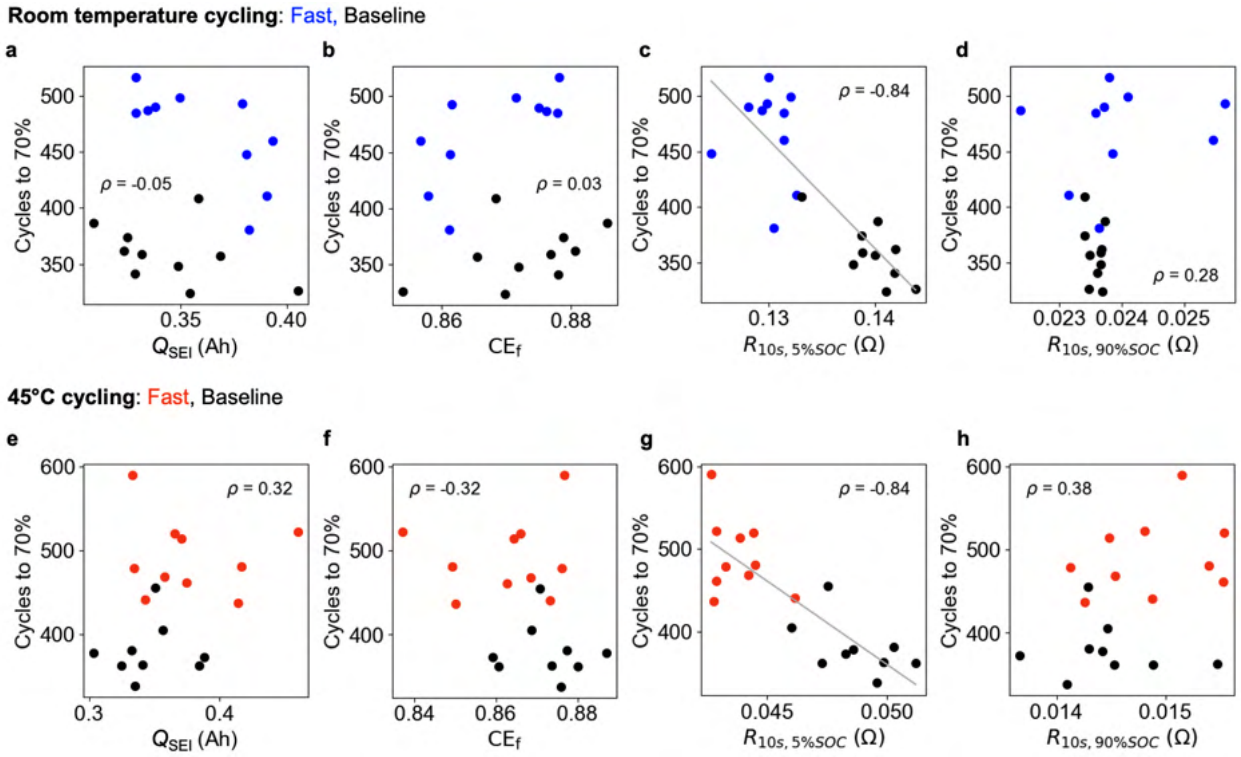

Figure 6.5: Correlation between early-life diagnostic signals and cycle life. (a-d) Correlations under room temperature cycling. (e-h) correlations under 45°C cycling. Cycle life is defined as cycles to 70% of initial capacity. Q_{SEI} and $\mathrm{CE_f}$ are taken directly from the formation test. $\mathrm{R_{10s,5\%SOC}}$ ($\mathrm{R_{LS}}$) and $\mathrm{R_{10s,90\%SOC}}$ are measured at the beginning of the cycle life test and thus share the same temperature as the cycle life test.

6.4.3.2 $\mathrm{R_{LS}}$ Predicts Cycle Life

To understand if $\mathrm{R_{LS}}$ can be used to improve battery lifetime prediction, we trained univariate prediction models with regularized linear regression models inspired by Severson et al. [239]. The performance of the predictive models are summarized in Table 6.3. A dummy regressor, which predicts the mean of the training set and requires no cycling data, was included as a benchmark. For room temperature cycling, the model trained using $\mathrm{R_{LS}}$ achieved the lowest test error of 6.9% compared to 13.3% for the dummy regressor. A similar result held under 45°C cycling. To compare, we also included the $\mathrm{Var}(\Delta Q_{100-10}(V))$ metric introduced by Severson et al. [239], defined as the variance in the discharge capacity versus voltage curve between cycle 10 and cycle 100. When applied to our dataset, this metric did not

yield a significant improvement over the dummy regressor. This result suggests that R_{LS} is a stronger predictor of battery lifetime than $\mathrm{Var}(\Delta Q_{100-10}(V))$.

We repeated this study with multivariate regularized linear regressions: one using the three capacity-based features from formation (Q_{SEI}, CE_f, and Q_d) and another using the previous three formation features plus R_{LS}. Using only the features from formation, no improvement over the dummy regressor was achieved. By including R_{LS} in the feature set, however, the test error was improved. Yet, the test error achieved did not exceed the test error of the univariate model using R_{LS} alone. This result suggests that the chosen set of formation features does not provide useful information about cycle life beyond what is provided by R_{LS}. This result is counter-intuitive considering the important role that lithium consumption plays in determining battery lifetime [204, 205, 206, 207, 208, 209], which should be reflected in the formation features such as Q_{SEI} and CE_f. We hypothesize that the reason for the poor model performance using formation signals is not because these formation signals lack physical meaning. Rather, due to the absence of high-precision cycling and temperature control, the useful information within these signals may be masked by the noise in the data (e.g. due to current integration errors, temperature variations over the course of 10+ hours of formation, etc.) R_{LS} appears to be able to overcome these limitations. We explore the connection between R_{LS} and the other formation metrics in detail later.

Model	Data needed	Room temp		45°C	
		Train	Test	Train	Test
Dummy regressor	none	13.3 (1.0)	14.4 (4.0)	14.0 (0.9)	15.1 (3.6)
R_{LS}	3 cycles	6.9 (0.5)	8.0 (2.8)	6.5 (0.6)	7.4 (2.9)
Q_{SEI}	formation	12.2 (1.2)	14.0 (4.6)	14.1 (0.8)	15.2 (4.4)
CE_f	formation	12.2 (1.2)	13.8 (4.5)	14.1 (0.7)	15.1 (4.3)
Q_d	formation	12.0 (1.2)	13.6 (5.0)	13.5 (0.8)	15.0 (4.0)
$\mathrm{Var}(\Delta Q_{100-10}(V))$	100 cycles	11.6 (1.7)	14.4 (5.2)	10.3 (1.1)	11.5 (4.7)
Q_{SEI} + CE_f + Q_d	formation	12.8 (1.3)	14.5 (5.1)	13.4 (1.1)	14.1 (4.0)
Q_{SEI} + CE_f + Q_d + R_{LS}	3 cycles	7.2 (1.1)	9.4 (4.0)	6.5 (1.0)	7.4 (2.9)

Table 6.3: Training and testing errors for different lifetime prediction models. Values represent means (standard deviations). The dummy regressor model uses no features and simply returns the mean of the training set, and hence is the baseline against which to judge the performance of other features. All remaining models use a Ridge regression with nested cross-validation to determine the optimal regularization strength (see Experimental Procedures).

As defined in this work, the model trained using R_{LS} required just three cycles of lifetime testing, i.e., one diagnostic cycle. (The two preceding cycles consisted of slow-rate charge-

discharge cycles as part of the reference performance test inserted at the beginning of the cycle life test.) By comparison, $\mathrm{Var}(\Delta Q_{100-10}(V))$ requires 100 cycles of lifetime testing. For future implementations, R_{LS} can be incorporated directly into the formation protocol, further decreasing the required measurement time. The total amount of data required to exercise each predictive model is summarized in Table 6.3.

Overall, the correlation and prediction results suggest that R_{LS} may be useful for advancing broad-scale efforts to improve cycle life prediction using small and readily-obtainable datasets at the beginning of life. While the results are promising, they are also limited, since only two types of formation protocols have been studied here. To understand the extent to which R_{LS} can generalize to other applications (e.g. chemistries, use cases, cell designs) and to understand the relation between R_{LS} and the other formation signals, the rest of the paper will focus on providing a physical interpretation of R_{LS}. A mechanistic understanding of R_{LS} will provide the necessary context required to evaluate the general scope of applicability and limitations of the method.

6.5 Discussion

6.5.1 R_{LS} as a Diagnostic Signal: A Mechanistic Perspective

Understanding the physical interpretation of diagnostic signals can help assess whether prediction frameworks leveraging such signals can generalize to new systems. In principle, different formation protocols, manufacturing process changes, and cell design changes could all lead to changes in lithium consumption and active material losses during formation. Towards this end, we will first review the commonly accepted theory of SEI passivation and showed how our observations of Q_{SEI} and CE_f support this theory. Next, we will show that our observations of R_{LS} are consistent with this theory but provide a stronger and more easily measurable signal compared to conventional measures.

6.5.1.1 Benefits of Fast Formation on Cycle Life

Lithium intercalation at negative electrode potentials higher than 0.25V-0.5V vs Li/Li^+ is generally associated with the formation of a porous, poorly-passivated SEI film [207, 232, 240, 241, 209]. Conversely, lithium intercalation at negative electrode potentials below 0.25V-0.5V has been found to promote the formation of a more conductive and passivating SEI film [237, 232]. Attia et al. [237] showed that the reduction of ethylene carbonate (EC) at negative electrode potentials above 0.5V vs Li/Li^+ is non-passivating. This negative electrode potential corresponds to a full cell voltage of below 3.5V, neglecting overpotential

contributions. Hence, an ideal formation protocol would minimize the time spent charging below 3.5V while maximizing the time spent above 3.5V. The fast formation protocol we tested [30] achieves this objective by rapidly charging the cell to above 3.9V at a 1C rate and subsequently cycling the cell between 3.9V and 4.2V, thus decreasing the time associated with the non-passivating EC reduction reaction. Focusing on the initial charge cycle, fast formation cells spent only 2 minutes below 3.5V and 12.9 hours above 3.5V, while baseline formation cells spent 30 minutes below 3.5V and 9.4 hours above 3.5V. Fast formation decreased the time spent below 3.5V by 28 minutes. Fast formation resulted in a net increase in total lithium consumed during formation, ΔQ_{SEI}, by 23 mAh (Table 6.2). This increase is attributed to the additional lithium consumed to form the passivating SEI.

While fast formation cells consumed more lithium during formation and thus exhibited lower $\mathrm{CE_f}$ (or, equivalently, higher Q_{SEI}), these cells lasted longer on the cycle life test. While a lower initial coulombic efficiency is conventionally associated with poor cycle life performance [145, 242], the opposite was true in our study since the additional lithium consumed during fast formation was associated with the creation of a more passivating SEI. A more passivating SEI can, for example, lower the rate of electrolyte reduction reactions associated with the formation of solid products that decrease the negative electrode porosity which could subsequently increase the propensity for lithium plating during charge [243, 56]. A more passivating SEI could therefore play a role in delaying the 'knee-point' observed in the cycle test data. Our result reinforces the notion that passivation of the SEI during the first cycle plays an important role in determining battery cycle life.

6.5.1.2 Lithium Loss Dominates Overall Cell Capacity Loss Over Cycling

We performed a voltage fitting analysis [141, 145, 142, 236, 69] to confirm that the main failure mode in our cells is the loss of lithium inventory (LLI) over cycle life (Figures 6.6, 6.7). We found that LLI can fully account for the thermodynamic (i.e. C/20) cell capacity loss over life. The knee-point in LLI over cycle life coincides with the knee-point in the capacity loss. All cells also experienced an increase in the loss of active material in the negative electrode ($\mathrm{LAM_{NE}}$) after the knee-point, which could indicate the occurrence of porosity decrease and/or electrolyte depletion as a result of a less passivating SEI, as discussed previously. The increased $\mathrm{LAM_{NE}}$ after the knee-point was less prominent in the fast formation cells, suggesting that the more passivating SEI generated from fast formation could be playing a role in delaying the knee-point to improve lifetime. Finally, all cells experienced a knee-point in the capacity fade rate irrespective of whether the discharge capacity is measured at higher (C/3) or lower (C/20) C-rates (Figure B.16), indicating that kinetic limitations cannot fully account for the observed knee-point in the cycle life data. The origin of the capacity loss

therefore has a strong thermodynamic component which can be attributed to the loss of lithium inventory. This analysis further supports the theory that consuming more lithium at low negative electrode potentials during formation can create a passivating SEI that is beneficial to cycle life [237].

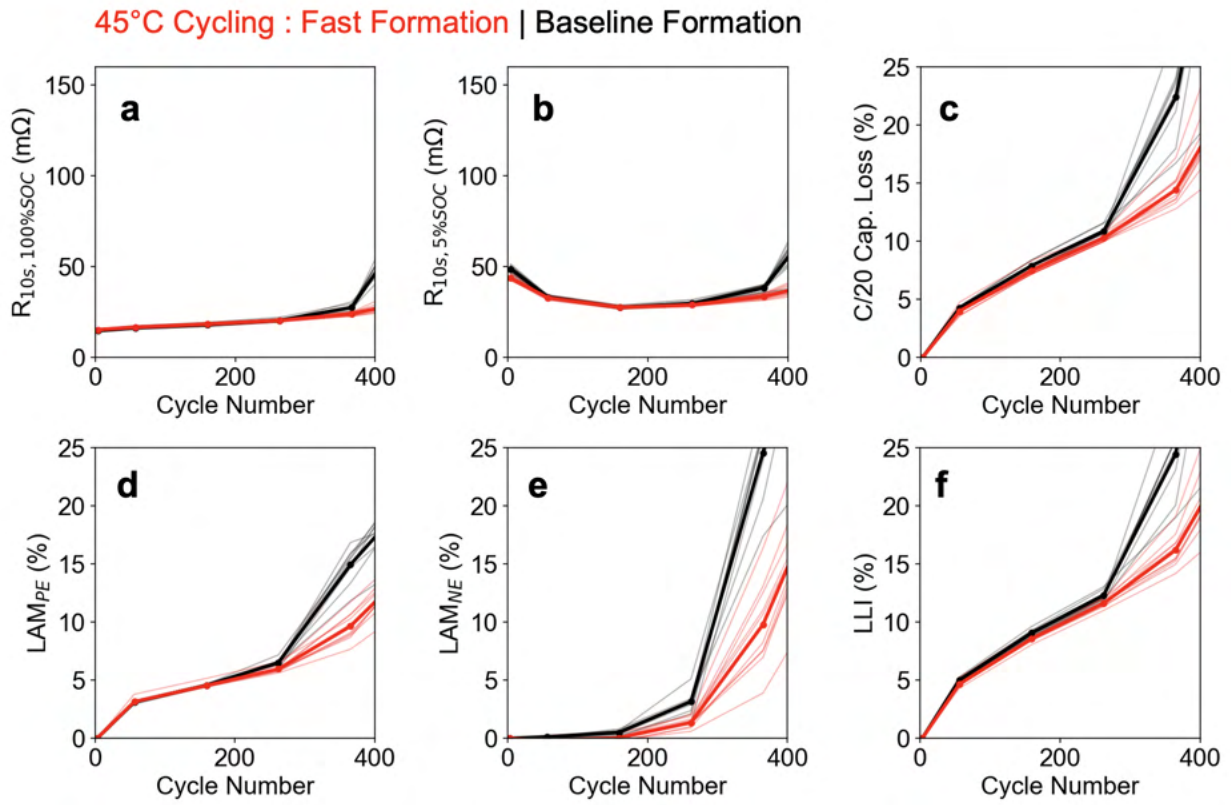

Figure 6.6: Evolution of diagnostic signals throughout the 45°C cycle life test. All metrics shown are calculated using data collected from the Reference Performance Tests (RPTs) run throughout the cycle life test. Metrics include (a) 10-second resistance calculated at 4% SOC, (b) 10-second resistance calculated at 100% SOC, (c) C/20 discharge capacity loss, (d) loss of active material in the positive electrode, (e) loss of active material in the negative electrode, and (f) loss of lithium inventory. Loss of active material and loss of lithium inventory are calculated using the voltage fitting techniques reported by Lee et al. [69] (e.g. Figure B.15). Thick lines show mean values averaged from each group of baseline and fast formation cells. Thin lines show results from individual cells.

6.5.1.3 R_{LS} is Attributed to Kinetic Limitations in the Positive Electrode

To explore possible physical connections between R_{LS} and the impact of fast formation on cycle life, we first develop a physical interpretation of the low-SOC resistance. We focus our discussion on the resistance contributions from the positive and negative electrode. While

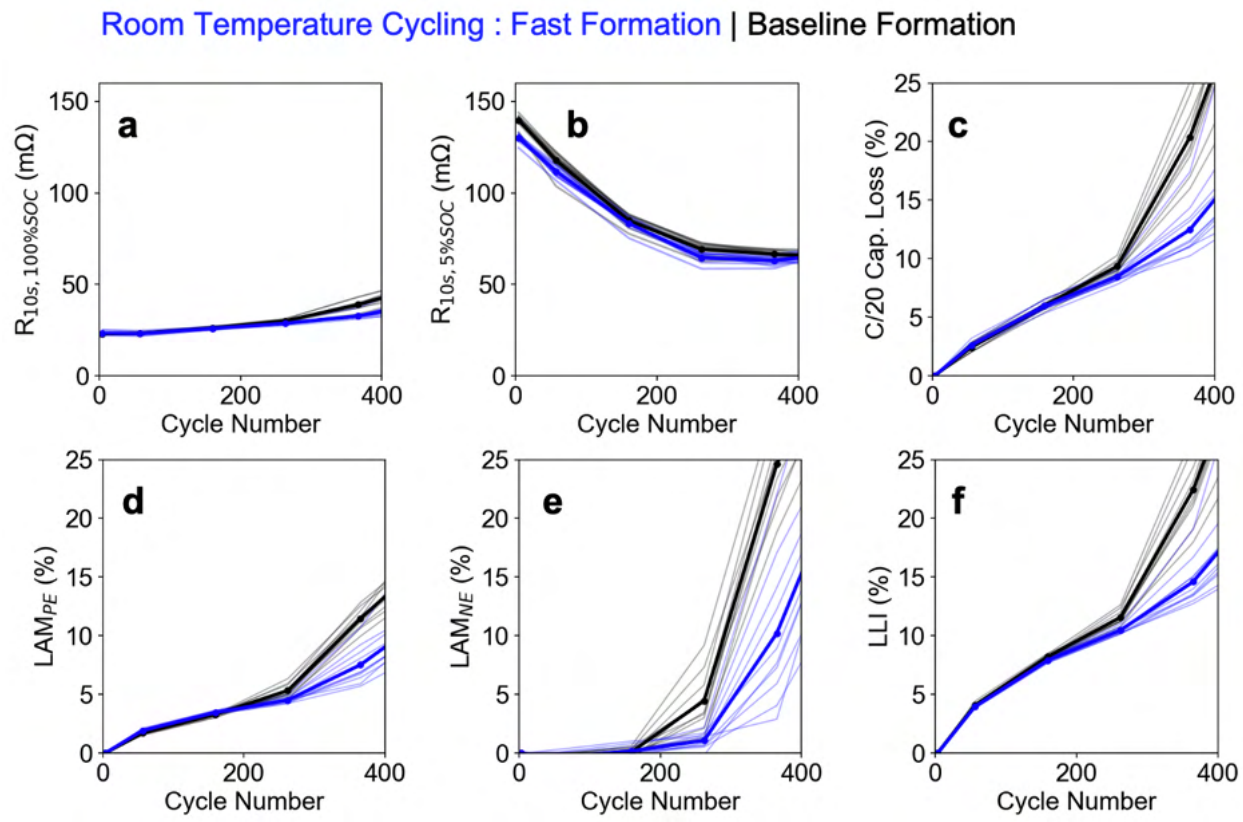

Figure 6.7: Evolution of diagnostic signals throughout the room temperature cycle life test. All metrics shown are calculated using data collected from the Reference Performance Tests (RPTs) run throughout the cycle life test. Metrics include (a) 10-second resistance calculated at 4% SOC, (b) 10-second resistance calculated at 100% SOC, (c) C/20 discharge capacity loss, (d) loss of active material in the positive electrode, (e) loss of active material in the negative electrode, and (f) loss of lithium inventory. Loss of active material and loss of lithium inventory are calculated using the voltage fitting techniques reported by Lee et al. [69] (e.g. Figure B.15). Thick lines show mean values averaged from each group of baseline and fast formation cells. Thin lines show results from individual cells.

other cell components (e.g. current collectors, tabs, and electrolyte) also contribute to the total cell resistance, they are not known to depend on SOC and hence cannot explain the rising resistance measured at low SOCs.

Positive electrode diffusion limitations generally play a significant role in the low-SOC cell resistance in NMC/graphite systems. The solid-state diffusion coefficient in NMC materials has been measured to decrease by more than one order of magnitude at high states of lithiation [162], a phenomenon attributed to the depletion of divacancies needed to support diffusion as the electrode becomes fully lithiated [163, 164]. Using half-cell HPPC measurements, we experimentally verified that the positive electrode dominates the low-SOC

resistance. In the coin cell form factor, the 10-second resistance of graphite/Li stayed below 100mΩ as the graphite approached full delithiation, while the 10-second resistance of NMC/Li exceeded 1000mΩ as the NMC approached full lithiation (Figure B.18). This finding is consistent with previous empirical studies on NMC/graphite systems [244, 235, 234]. In particular, An et al. [244] used a three-electrode pouch cell configuration to show that, for an NMC/graphite system, the positive electrode accounts for nearly all of the measured full cell resistance at all SOCs.

Charge transfer kinetics at either electrode could also play a role at determining total cell resistance. The charge transfer process at either electrode can be modeled using the Butler-Volmer equation [245]:

$$j = k_0 c_e^{1-\alpha}(c_{s,\max} - c_{s,e})^{1-\alpha} c_{s,e}^{\alpha}\Big(\exp\Big(\frac{(1-\alpha)F}{RT}\eta\Big) - \exp\Big(-\frac{\alpha F}{RT}\eta\Big)\Big). \tag{6.2}$$

In this equation, j is the reaction flux, the exponential terms describe the overpotential dependence of the forward and backward reactions, and the exponential prefactor terms together describe the exchange current density. $c_{s,\max}$ is the theoretical maximum allowable lithium concentration in the solid phase, $c_{s,e}$ is the surface concentration of lithium, and k_0 is the reaction rate constant. The exchange current density approaches zero as the electrode becomes either fully lithiated or fully delithiated. Indeed, our coin cell data shows that as the graphite negative electrode approaches full delithiation, the measured resistance rises steeply (B.18i). However, the magnitude of this charge transfer effect remains small compared to the contribution from the diffusion-limited NMC positive electrode (B.18h) at high states of lithiation.

In summary, we attribute the low-SOC resistance to kinetic limitations in the positive electrode. This result was experimentally verified using coin cell measurements of electrode resistances and is consistent with literature findings [244, 235, 234]. The kinetic limitation arises from a combination of diffusion and charge transfer limitations in the positive electrode. For NMC/graphite systems, diffusion limitations (i.e. 'kinetic hindrance' [164]) is a major component of the rapid rise in measured resistance at low SOCs.

6.5.1.4 Lithium Consumption Leads to an Apparent Decrease in R_{LS}

Fast formation decreased the measured low-SOC resistance (R_{LS}). From our previous analysis, fast formation also increased the lithium consumed during formation (Q_{SEI}) to create a more passivating SEI. To explain the connection between these two quantities, we employ a simple electrode stoichiometry model which describes both the thermodynamic potentials and kinetic limitations of both electrodes. Figure 6.8a shows the relative alignment of the

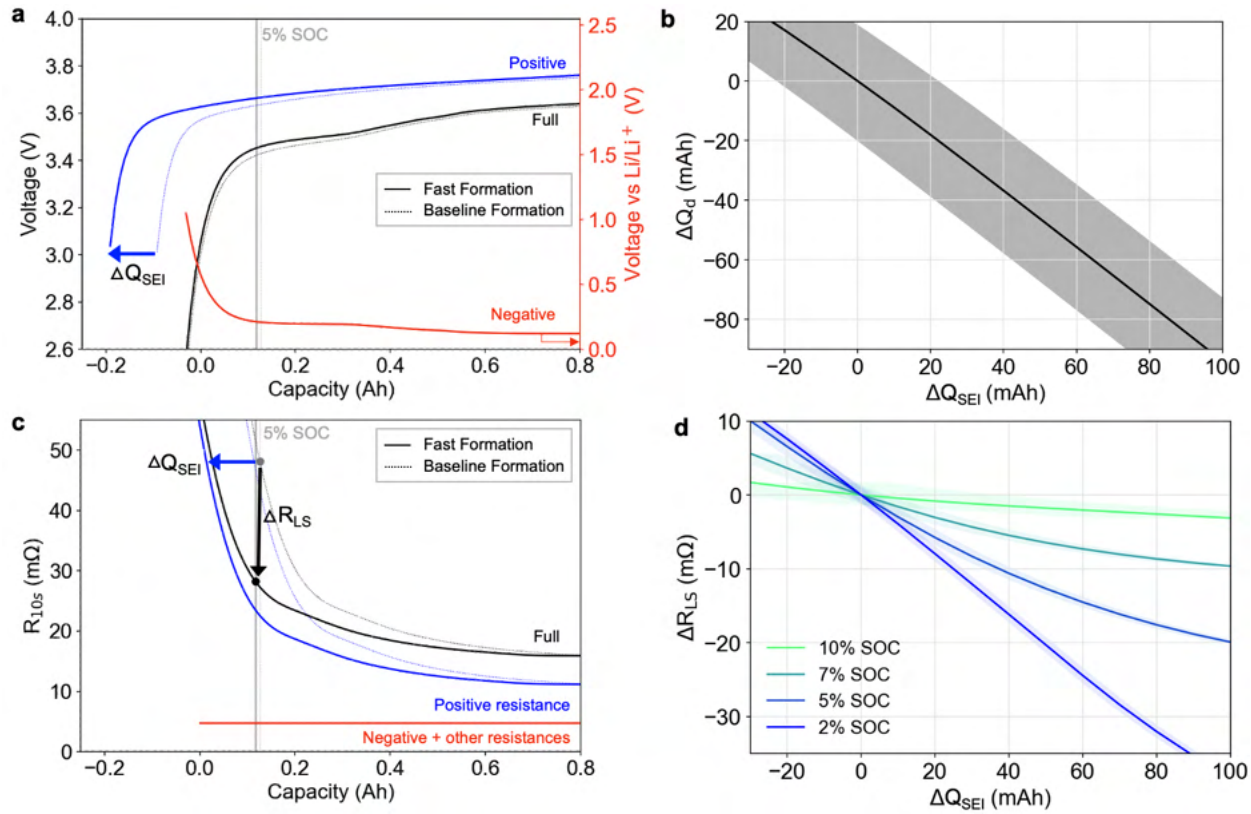

Figure 6.8: Electrode stoichiometry model illustrating the impact of lithium consumption on low-SOC resistance. (a) Relative alignment of the positive and negative equilibrium potential curves after baseline formation and fast formation. (b) Effect of increasing lithium consumption (ΔQ_{SEI}) on the measured discharge capacity. (c) The corresponding cell resistance curves, where the measured full cell resistance (black lines) have been broken down into positive electrode charge resistance (blue) and all other resistances (red). (d) The effect of increasing ΔQ_{SEI} on the measured low-SOC resistance for varying SOC set-points. Bands in (b,d) indicate estimates of the measurement error bound using conventional battery cycling equipment, clarifying R_{LS}'s improved accuracy in representing changes in Q_{LLI} when compared to Q_d (see Supplementary Materials).

positive and negative equilibrium potential curves after baseline formation and fast formation. The origin of the capacity axis corresponds to 0% SOC (3.0V) after baseline formation. The gap between the positive and negative potential curve endpoints is attributed to the lithium lost to the SEI during formation, or Q_{SEI} [142, 145]. By comparison, the curves prior to formation do not have a gap, corresponding to $Q_{\text{SEI}} = 0$ (Figure B.19). We shift the positive electrode curve to the left by some amount ΔQ_{SEI} to emulate the impact of additional lithium consumed during fast formation. Here, ΔQ_{SEI} has been set to an exaggerated value of 100mAh for graphical clarity. An alternative graphic is provided in Figure B.20, which sets $\Delta Q_{\text{SEI}} = 23$mAh to coincide with the measured difference between baseline formation

and fast formation.

Figure 6.8c shows the corresponding full cell 10-second resistance measured from the HPPC test. The full cell resistance is partitioned to model a scenario in which the positive electrode dominates the low-SOC resistance, consistent with previous findings. The resistance curve of the positive electrode must also translate to the left by the same amount ΔQ_{SEI} due to the increased lithium consumed during fast formation. From the reference frame of the full cell, the measured low-SOC resistance will decrease by $\Delta \mathrm{R_{LS}}$. In this manner, $\mathrm{R_{LS}}$ can decrease without any real change in positive electrode kinetic properties. The decrease in $\mathrm{R_{LS}}$ reflects the shifting of the positive electrode stoichiometry window as lithium is consumed.

Two additional observations support the connection between ΔQ_{SEI} and $\Delta \mathrm{R_{LS}}$. First, $\mathrm{R_{LS}}$ appears to be positively correlated to $\mathrm{CE_f}$ and negatively correlated to Q_{SEI} (Figure B.10), a result which is consistent with theory and predicted by the electrode stoichiometry model. The strengths of the correlations are generally weak, with correlation coefficients, $|\rho|$, ranging between 0.2 and 0.5. We attribute the weakness of the correlations to the poor signal-to-noise of the capacity measurements using typical battery cycling equipment, which may compound at room temperature where the temperature is not strictly controlled (Figure B.21). Second, we note that the resistance around 90% SOC is insensitive to small changes in SOC, so changes in resistance at 90% SOC provides a measure of true resistance changes rather than apparent changes due to electrode stoichiometry shifts (Figure 6.4d). Fast formation did not significantly increase the resistance at 90% SOC (Figure B.7), so the changes in $\mathrm{R_{LS}}$ is not likely to be due to material changes in the cell resistance (e.g. due to resistive surface films). This observation further supports the hypothesis that changes in $\mathrm{R_{LS}}$ are due to electrode stoichiometry window shifts in the presence of lithium consumption.

6.5.1.5 $\mathrm{R_{LS}}$ Improves the Observability of Lithium Loss During Formation

Figure 6.8b shows that the sensitivity of the measured cell discharge capacity (ΔQ_{d}) to the lithium consumed (ΔQ_{SEI}) is 0.9 mAh/mAh. The error in measuring Q_{d} is 20 mAh due to current integration inaccuracies using ordinary cycling equipment. Hence, using Q_{d} to estimate Q_{SEI} leads to a measurement error of 22 mAh. Since the total difference in lithium consumed between fast formation and baseline formation is 23mAh, measurement noise may prevent ΔQ_{d} from effectively resolving this difference. In our experiments, we relied on large sample sizes ($n = 10$ per group) to resolve the small difference in lithium consumption between the two formation protocols.

Figure 6.8d shows that the sensitivity of the low-SOC resistance ($\Delta \mathrm{R_{LS}}$) to ΔQ_{SEI} is 0.22 mΩ / mAh when measured at 5% SOC. The error in measuring $\mathrm{R_{LS}}$ is 0.88 mΩ due to

the voltage and current precision for calculating resistance using Ohm's law using ordinary cycling equipment. Hence, using R_{LS} measured at 5% SOC to estimate Q_{SEI} leads to a measurement error of 4 mAh, a five-fold improvement over using Q_d. Figure 6.8d further shows that the sensitivity of R_{LS} is improved at lower SOCs. For example, R_{LS} measured at 2% SOC leads to a measurement error of 2.5 mAh. Any SOC set-point lower than 7% SOC makes R_{LS} a more precise measure of Q_{SEI} compared to Q_d. See Supplementary Materials for a detailed derivation of the measurement errors.

6.5.2 Generalizability

So far, we have explored the sensitivity of R_{LS} to lithium lost during formation for an NMC/graphite system. By understanding the benefits of fast formation [237], we rationalized why R_{LS} is predictive of cycle life for our system. Here, we discuss the application of R_{LS} towards understanding other degradation modes, chemistries, and use cases. This discussion sets the stage for understanding how R_{LS} may be incorporated into generalizable lifetime prediction and diagnostic frameworks.

6.5.2.1 R_{LS} Can Detect Active Material Losses

In principle, some small quantity of positive and negative active material could be lost during formation, i.e. due to expansion and contraction of the electrodes during initial lithiation and delithiation. In the positive electrode, lithiation-induced stresses can induce particle fracturing in the metal oxide particles [246, 247, 248], leading to capacity loss. In the negative electrode, while graphite cracking is unlikely to occur under most applications [249], insufficient binder adhesion or electrolyte wetting [250] could create local islands of isolated graphite particles, leading to active material loss.

We develop a simple mechanistic electrode stoichiometry model to examine the influence of active material losses in both the positive and negative electrodes. Our model differentiates between loss of active material in the lithiated phase versus the delithiated phase [142]. For the positive electrode, loss of active material in the delithiated phase is represented by shrinking the positive electrode equilibrium potential curve with the point of minimum stoichiometry fixed (i.e. shrinking from the bottom, Figure B.22a), while loss of active material in the lithiated phase is represented by shrinking the positive electrode equilibrium potential curve with the point of maximum stoichiometry fixed (i.e. shrinking from the top, Figure B.22d). R_{LS} was found to increase with loss of positive active material, but only in the delithiated phase (Figures B.22b). By contrast, active material lost in the lithiated phase bears a negligible effect on R_{LS} (Figures B.22d,e). This result can be understood

graphically by considering the influence of the positive curve shifts on the positive electrode stoichiometry at low SOCs. In the case of loss of active material in the lithiated phase, the positive electrode stoichiometry at low SOCs does not significantly change, whereas in the delithiated case, the maximum positive electrode stoichiometry increases, causing R_{LS} to increase. Note that Q_d has the opposite sensitivity: Q_d is sensitive to loss of active material in the lithiated state only. Hence, R_{LS} and Q_d complement each other in the study of positive electrode active material loss mechanisms. A similar analysis can be done on the negative electrode (Figure B.23).

Figure B.24 compares the sensitivity of R_{LS} and Q_d to the four different modeled cases of active material losses. The results highlight that the measured value of R_{LS} is determined by multiple degradation factors, including both lithium inventory loss and active active material losses. It would therefore be impractical to use R_{LS} to identify any dominant degradation mode without some *a priori* understanding of the system through additional characterization and analysis. For diagnostic purposes, we recommend that R_{LS} be used within the context of a broader set of non-destructive techniques to enrich the understanding of degradation mechanisms. From a data-driven prediction perspective, however, the sensitivity of R_{LS} to active material losses in addition to lithium inventory loss may make it a more robust indicator for multiple degradation modes. In general, R_{LS} may need to be coupled with other signals to improve the observability of distinct degradation modes.

6.5.2.2 When is R_{LS} Sensitive to Lithium Loss?

We have so far focused on an NMC111/graphite system where kinetic limitations in the positive electrode dominates R_{LS}, a result which holds for nickel-rich cathode chemistries such as nickel cobalt aluminum (NCA) and higher nickel content NMC materials [164, 163]. In general, electrode design factors such as particle size [251] and surface modifications [252] could impact the relative contribution of each electrode to R_{LS}. To study how such changes could modify the sensitivity of R_{LS} to changes in Q_{SEI}, we performed a sensitivity study using our electrode stoichiometry model by varying the proportion of the total cell resistance attributed to the positive electrode. The results (Figures 6.9, B.25) show that R_{LS} becomes ineffective at quantifying Q_{SEI} if the positive electrode contributes to less than 50% of the total cell resistance at low SOCs. This result suggests that the utility of R_{LS} as a diagnostic signal for Q_{SEI} diminishes for systems where the positive electrode is not the main contributor to R_{LS}.

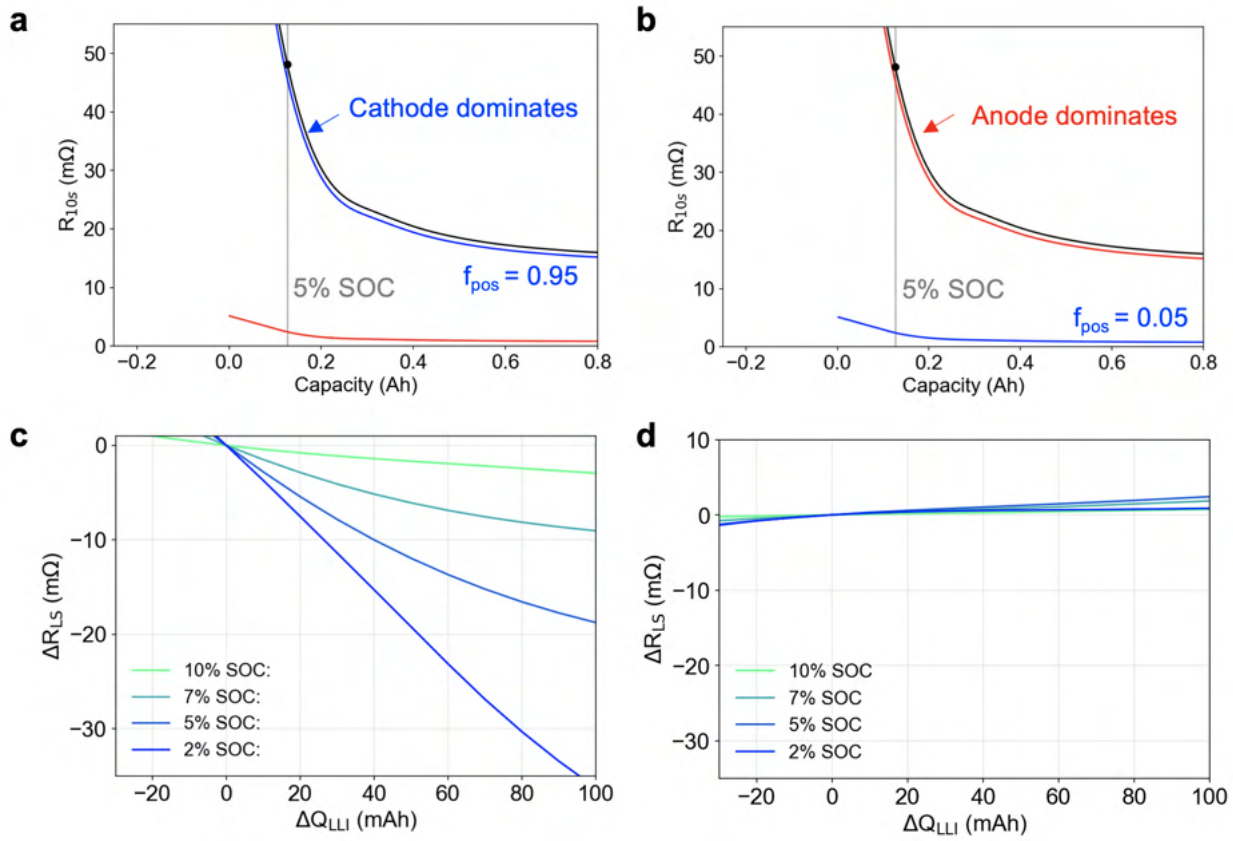

Figure 6.9: Sensitivity of low-SOC resistance to ΔQ_{SEI} depends on fractional contribution of the positive electrode to the total cell resistance: Example 1. Sensitivity of the low-SOC resistance metric to ΔQ_{SEI} when (a,c) positive electrode dominates the cell resistance and when (b,d) negative electrode dominates the cell resistance. f_{pos} is the fractional contribution of the positive electrode to the total cell resistance.

6.5.2.3 When Can R_{LS} Predict Cycle Life?

Our cycle life correlation study was presented in the context of the study of fast formation. To understand whether R_{LS} can predict cycle life for other use cases (i.e. chemistries and aging conditions), we start by reviewing why R_{LS} was predictive of cycle life for fast formation. Figure 6.10 outlines the connection between fast formation and cycle life. In brief, fast formation spent more time above 3.5V, creating a higher quantity of SEI that is more passivating [237]. The passivating SEI improved cycle life by protecting the negative electrode against side reactions over life. The low-SOC resistance, R_{LS}, provided an estimate of the amount of lithium consumption during formation, Q_{SEI}, and thus served as a proxy for both the amount of passivating SEI formed and the cycle life of the cell. This physical description rationalizes the predictive power of R_{LS} within the context of the degradation pathway (fast formation) and chemistry (NMC/graphite) explored in this study.

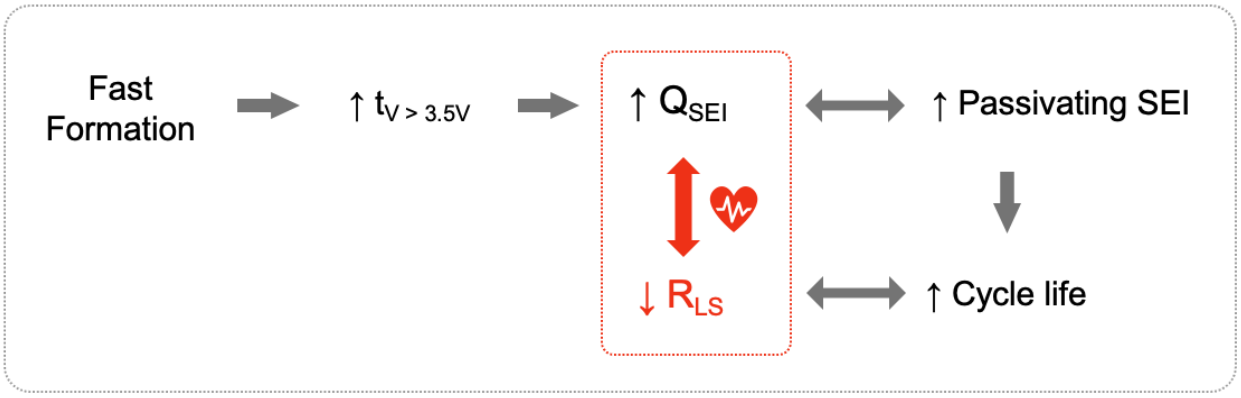

Figure 6.10: Connection Between the Fast Formation Degradation Pathway and the Low-SOC Resistance Early Life Diagnostic Signal. Inner box: the relationship between low-SOC resistance (R_{LS}) and lithium consumed during formation (Q_{SEI}) is general. Outer box: the relationship between low-SOC resistance (R_{LS}) and cycle life applies specifically to fast formation, where higher Q_{SEI} signaled the creation of a more passivating SEI [237] which improved cycle life. The relationship between R_{LS} and cycle life may differ for other use cases.

To gain confidence that R_{LS} can predict cycle life for other use cases, the relationship between lithium loss (Q_{SEI}) and cycle life must first be understood. For our study, the knowledge that increased Q_{SEI} signals a more passivating SEI was necessary for rationalizing why higher Q_{SEI} after formation could be beneficial to cycle life. For other use cases, the opposite may be true. For example, low first-cycle efficiencies for silicon-containing anodes [253] or lithium metal anodes [254] generally indicate poor negative electrode passivation which leads to poor cycle life. Under such use cases, R_{LS} may still be predictive of cycle life, but the relationship may become inverted.

6.5.3 Unique Properties of R_{LS}

Here, we highlight several unique properties of using the low-SOC resistance (R_{LS}) as an early-life diagnostic signal. First, since the positive electrode kinetics becomes poorer as the electrode becomes fully lithiated, the sensitivity of R_{LS} to lithium loss (Q_{SEI}) improves as the measurement SOC decreases (Figure 6.8d). The results from this study used R_{LS} measured at 5% SOC. For future work, the sensitivity to Q_{SEI} may be further improved by measuring at even lower SOCs. Second, R_{LS} can be used to extract information about Q_{SEI} within seconds and therefore can be deployed in manufacturing settings without decreasing production speed. By contrast, conventional measurements of Q_{SEI} relying on Coulomb counting require full charge-discharge cycles during formation which could take hours to days to com-

plete. Since measuring R_{LS} does not require full cycles, R_{LS} is also suitable for diagnosing differences in lithium consumption between formation protocols with different charge and discharge conditions. Finally, R_{LS} becomes stronger the earlier in life it is measured. As the cell ages, continual loss of lithium inventory will cause the highly sloped region of the positive electrode resistance curve to become inaccessible during the normal full cell voltage operating window. Typically, diagnostic features become less predictive of cycle life the earlier in life the feature is sampled [239]. R_{LS} is expected to have the opposite relationship: the earlier in life R_{LS} is sampled, the more sensitive it will be to changes in Q_{SEI}.

6.5.4 State of Health Beyond Cycle Life: Practical Considerations

Our discussion has so far focused on evaluating the merits of R_{LS} for diagnosing cycle life. However, in real manufacturing settings, cycle life is only one of many considerations for adopting new formation protocols. Here, we introduce two such considerations: (1) impact to gas buildup over life, and (2) impact to aging variability over life. In our analysis, R_{LS} could not be used to learn the impact of fast formation on gas buildup or aging variability. Here, we give an overview of these observations.

6.5.4.1 Gas Buildup Over Life

Swollen cells in a battery pack can compromise pack integrity and pose safety hazards to first-responders for electric vehicle fire accidents [255]. Understanding the impact of formation protocols on cell swelling is therefore just as important as understanding the impact on cycle life for practical purposes.

Fast formation caused a significant degree of swelling at the end of life for cells cycled at 45°C (Figures 6.11, B.26). At this temperature, 9 of 10 fast formation cells showed visible signs of swelling, compared to only 2 of 10 for baseline formation. None of the cells cycled at room temperature showed any appreciable degree of swelling. All swollen pouch cells were compliant and compressible, indicating that gas was occupying the space inside the pouch bags. Since the cells were de-gassed after formation, the gases present exclude the gas generated during formation and represent only the accumulation of gas during the cycle life test. The absence of gas during room temperature cycling indicates that the gas evolution is thermally activated. More experimental work is needed to determine the origin of gas evolution over cycle life due to fast formation. We provide speculation into the origin of gas evolution as part of Appendix B.

Our study found no correlations between R_{LS} and the gas amount as measured by pouch thickness. We attribute the lack of correlation primarily to the fact that the cell age was

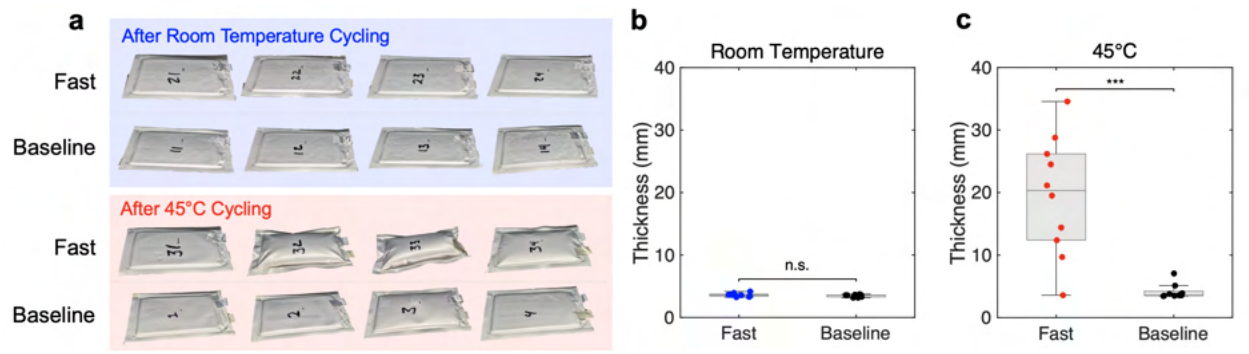

Figure 6.11: Pouch cell swelling at the end of the cycle life test. (a) Example images of pouch cells taken after aging showing varying degrees of swelling. (b-c) Comparison of pouch cell thicknesses measured at the end of the cycle life test. (b) Cells cycled at room temperature. (c) Cells cycled at 45°C. Cell thickness is measured using a manual caliper, which represents the point of maximum deflection. '***' - statistically significant with p-value < 0.001. 'n.s.' - not statistically significant.

not well-controlled at the time of the pouch thickness measurement: cells stopped cycling anywhere between 0% and 50% capacity retention. Future studies will be needed to confirm the relationship between R_{LS} and gas build-up.

6.5.4.2 Aging Variability

Adopting a new formation protocol in practice also requires a close understanding of the impact of new formation protocols on cell aging variability over life. Cells with non-uniform capacity fade could take longer to balance in a pack and cause a deterioration of energy available at the pack-level [256]. Pack imbalance issues could lead to consumer products being retired earlier, compounding existing battery recycling challenges [257]. Non-uniform cell degradation will also be more difficult to re-purpose into new modules [258, 259, 260], creating higher barriers for pack reuse.

The inter-quartile range (IQR) of cycle life for fast formation cells was higher than that of baseline formation cells (Figures 6.3b,d). The same result held under both room temperature and 45°C cycling, as well as across different end-of-life definitions (Figure 6.12), suggesting that fast formation increased aging variability. A key question is whether fast formation created more heterogeneous aging behavior which caused the higher variability in aging, or if the higher variability is due to the cells lasting longer. To answer this question, we employed the modified signed-likelihood ratio test [261] to check for equality of the coefficients of variation, defined as the ratio between the standard deviation and the mean cycle life. The resulting p-values were greater than 0.05 in all cases. Therefore, with the available data,

we cannot conclude that fast formation increased the variation in aging beyond the effect of improving cycle life. While a relationship between formation protocol and aging variability may still generally exist, this difference could not be determined with our sample sizes ($n = 10$ cells per group). This result motivates the continued usage of larger sample sizes for future studies on the impact of formation protocol on aging variability.

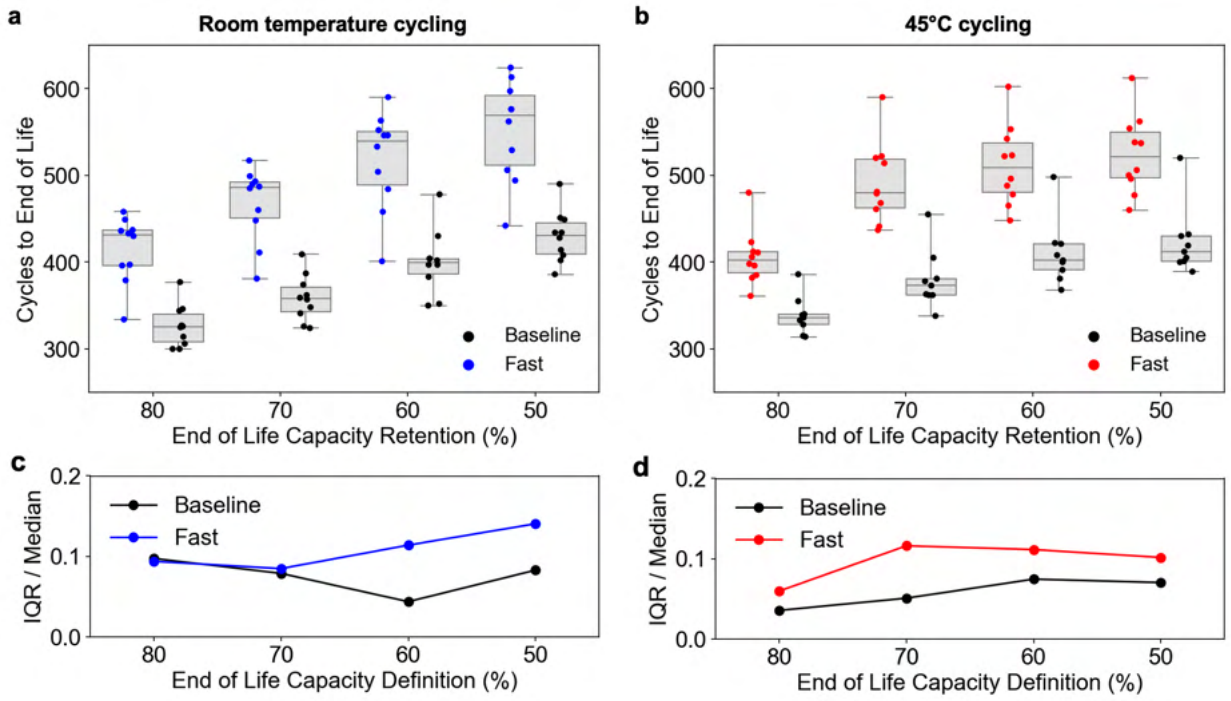

Figure 6.12: Aging variability as a function of end-of-life definition. (a,b) Cycles to end of life under (a) room temperature and (b) 45°C cycling. Boxes show inter-quartile range (IQR) and whiskers show the min and max values. (c,d) Inter-quartile range (IQR) divided by median plotted as a function of end of life capacity definition for (a) room temperature and (b) 45°C cycling.

6.5.5 Diagnostic Features Beyond R_{LS}

This section briefly revisits other diagnostic features introduced in Chapter 5 as candidate features for improving lifetime prediction models. These features are mostly collected via a slow-rate C/20 charge curve taken as part of the initial RPT before the cells begin cycling. The exceptions to this are the formation coulombic efficiency (CE_f) and the voltage decay ($\Delta V(V)$) which are collected directly from the formation data.

The results, shown in Figure 6.13, reveal that three additional features besides R_{LS} are correlated to cycles to 70%: the negative electrode capacity Q_n, the practical negative-to-positive ratio NPR, and the voltage decay metric ΔV measured during the high-SOC rest

period as part of the formation protocols themselves. Thus, R_{LS} is not the only feature that can potentially predict cycle life. There are many others. While the interpretation of these remaining metrics remain unclear, this result encourages the continued exploration of using DVA and signals measured directly from formation (ΔV) to improve battery lifetime prediction.

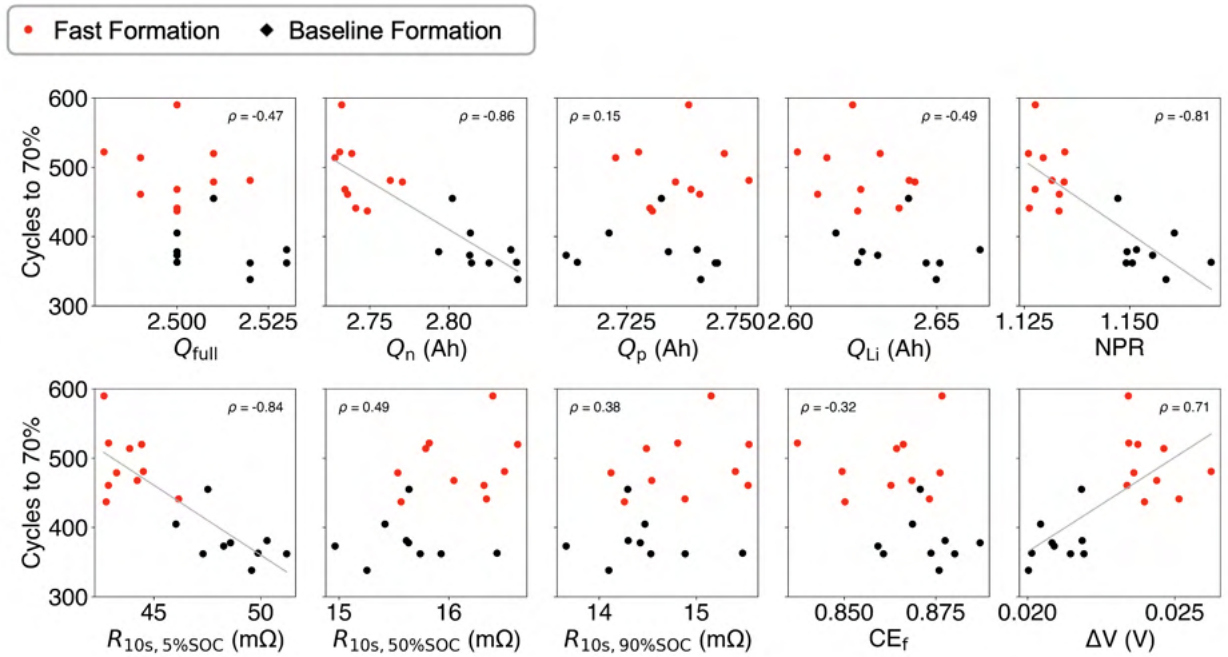

Figure 6.13: Diagnostic features beyond R_{LS}. Results are shown for the 45°C data only. Q_{full}: full cell capacity in Ah. Q_n: negative electrode capacity. Q_p: positive electrode capacity. Q_{Li}: capacity of lithium lost to SEI. NPR: Practical negative-to-positive ratio. $R_{10s,x\%SOC}$: 10-second resistance measured at x% SOC (when $x = 5$ then this metric is equivalent to R_{LS}). CE_f: formation coulombic efficiency. ΔV: 6-hour voltage decay. The last two metrics are measured during the formation protocols themselves.

We note that many of these trends disappear when inspecting the room-temperature cycle life tests (data not shown). The cause of this is unclear, though we speculate that the inadequate temperature control in the room-temperature test could be creating another source of cell aging variability that is masking the correlations.

Finally, we inspect how the correlations between the diagnostic signals and cycle life change as the diagnostic signals are measured later in life (see Figure 6.14). Whereas the diagnostic features we studied so far have been collected at the very beginning of the cycle life test, we now extract these features for aged RPTs (shown as asterisks in Figure 6.14), employing the same methods outlined in Chapter 5.

We now focus on two specific diagnostic features that are shown to correlate to cycle life:

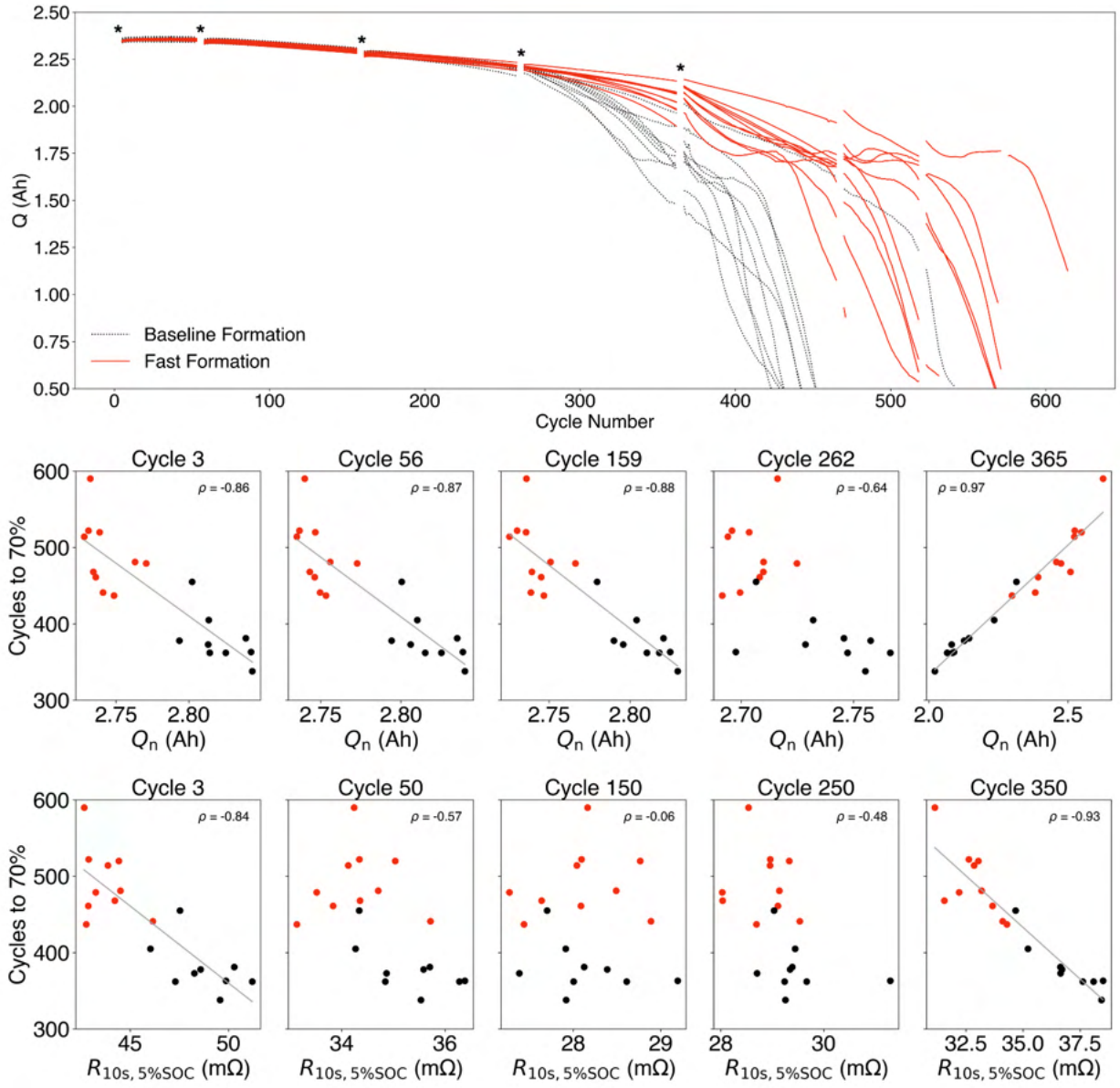

Figure 6.14: Trends in R_{LS} and Q_n correlations as the cells age.

Q_n and R_{LS}. For Q_n, the correlations remain present over intermediate cycle numbers below 200. However, once the knee occurs at cycle 262, the correlation disappears and inverts. At this time the reason for the inversion is unclear. For R_{LS}, we see that the correlation appears at cycle 3, consistent with the reports from the rest of this paper. However, after only 50 cycles, the correlation vanishes only to reappear at the end of life, after the cell has taken a knee. We attribute the disappearance of the signal over life to be due to the confounding effect of cell impedance growth (e.g. due to SEI growth at the anode or surface film growth at the cathode) which introduces another source of resistance variability. However, after the

knee has occurred, the resistance of all cells uniformly increases and the resistance becomes strongly correlated to the remaining capacity.

Overall, Figure 6.14 highlights the complicated dynamics of the correlations between diagnostic features and cycle life which warrant further study.

6.6 Conclusion

In this chapter, we demonstrated that low-SOC resistance (R_{LS}) correlates to cycle life across two different battery formation protocols. As a predictive feature, R_{LS} provided higher prediction accuracy compared to conventional measures of formation quality such as Coulombic efficiency as well as state-of-the art predictive features based on changes in discharge voltage curves. R_{LS} is measurable at the end of the manufacturing line using ordinary battery test equipment and can be measured within seconds. Changes in R_{LS} are attributed to differences in the amount of lithium consumed to the SEI during formation, where a decrease in R_{LS} indicates that more lithium is consumed. The sensitivity of R_{LS} to lithium consumption is due to the presence of kinetic limitations in the positive electrode causing the total cell resistance to increase at low SOCs. For this reason, R_{LS} provides a particularly strong signature in nickel-rich positive electrode systems where kinetic hindrance plays a strong role in limiting lithium transport towards high states of lithiation. Since the physical interpretation of R_{LS} is general, R_{LS} can be broadly applicable for screening any manufacturing process that impact the amount of lithium consumed during battery formation. As a whole, our results hold promise for decreasing lithium-ion battery formation time and cost while improving lifetime, as well as identifying rapid diagnostic signals for screening new manufacturing processes and cell designs based on cycle life.

CHAPTER 7

Variability Propagation in Parallel-Connected Systems

7.1 Abstract

This chapter proposes an analytical framework describing how initial capacity and resistance variability in parallel-connected battery cells may inflict additional variability or reduce variability while the cells age. We derive closed-form equations for current and SOC imbalance dynamics within a charge or discharge cycle. These dynamics are represented by a first-order equivalent circuit model and validated against experimental data. To demonstrate how current and SOC imbalance leads to cell degradation, we developed a successive update scheme in which the inter-cycle imbalance dynamics update the intra-cycle degradation dynamics, and vice versa. Using this framework, we demonstrate that current imbalance can cause convergent degradation trajectories, consistent with previous reports. However, we also demonstrate that different degradation assumptions, such as those associated with SOC imbalance, may cause divergent degradation. We finally highlight the role of different cell chemistries, including different OCV function nonlinearities, on system behavior, and derive analytical bounds on the SOC imbalance using Lyapunov analysis.

7.2 Introduction

The transition to sustainable energy and transportation will require building and operating battery manufacturing factories at a gigawatt-hour scale. Among the many challenges with rapidly opening new battery factories, the question of "how much manufacturing variability is too much?" remains pertinent. The presence of variability in battery cell capacities and resistances is widely known [262, 263, 264], the origins of which can be traced to manufacturing process variations affecting electrode-level thicknesses and loadings [265, 266, 6]. Beyond

the manufacturing of new battery packs, efforts to remanufacture second-life battery packs from aged batteries will introduce even higher variability in cell capacities and resistances [267, 268, 269]. Studying the effects of cell variability is thus a central question concerning both the manufacturing of new battery cells and the remanufacturing of aged battery packs.

When non-identical battery cells are connected in series and parallel to create a pack (see Fig. 7.1), the system dynamics can no longer be fully understood by studying an individual cell. In series-connected systems, for example, individual cells may be at different SOCs, but the cell having the lowest capacity is generally understood to limit the overall system capacity [270, 271, 272, 273, 274]. In parallel-connected systems, the currents passing through individual cells could additionally differ due to mismatches in cell internal resistances and current collection pathways. These current differences introduce another source of variability in degradation pathways, with unclear consequences over the lifetime of a battery pack. To further complicate matters, the current and SOC imbalance dynamics within parallel-connected cells are less observable in practical battery systems where individual branch currents may not be measured [275]. Finally, mathematical analysis of parallel systems has also historically been hindered by the appearance of differential-algebraic equations, complicating efforts to find closed-form solutions.

This work thus focuses on exploring the less-understood phenomena of current imbalance dynamics and variability propagation within parallel-connected battery systems.

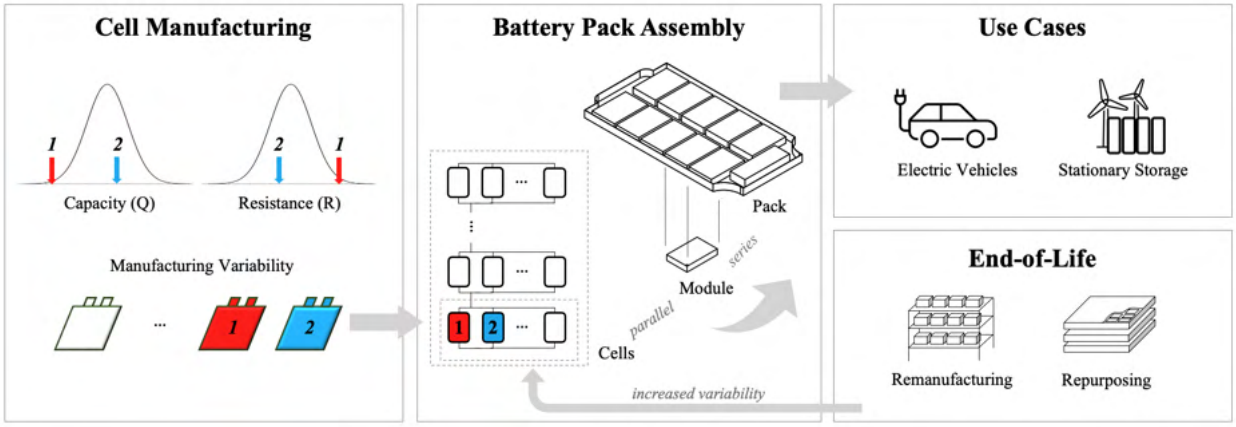

Figure 7.1: Battery manufacturing efforts spur the need to understand the coupled dynamics of non-identical battery cells connected in parallel.

7.2.1 Literature Review

Existing literature on parallel-connected systems can be grouped into three approaches: experimental, simulation-based, and model-based. Experimental approaches have focused on accurately measuring the current-sharing behavior of parallel-connected battery systems using sensors including current shunts and Hall effect sensors [276, 277, 278]. These experiments have shown that large current imbalances can persist during parallel-connected system operation [278]. The current-sharing behavior of parallel-connected cells has since been reproduced in simulation using a variety of battery models ranging from equivalent circuit models [279, 277, 280, 281] to physics-based models [110]. These experimental and simulation-based approaches have enabled accurate quantification of the imbalance dynamics, especially in the context of evaluating the impact of temperature gradients [282, 280, 283]. Model-based approaches have focused on developing state-space formulations enabling state estimation [284, 285, 286, 287], stability analysis [60] and steady-state analysis [277, 288, 289].

Despite these recent advances in measuring and modeling current imbalance in parallel-connected systems, a major gap in understanding remains: how does current imbalance affect long-term degradation behavior in parallel-connected systems? Reniers et al. [110] tackled this question by simulating the degradation of an entire energy storage system, initializing each cell with different initial capacities. The authors found that initial cell-to-cell variability barely affected long-term degradation. However, the degree to which this conclusion can generalize to additional use cases and cell systems remains under-explored. Song et al. [280] analytically demonstrated that capacity variation can decrease over time for convex or linear degradation curves and under certain degradation model assumptions. This analysis, however, was restricted to a battery model with a linearized open-circuit voltage (OCV) function.

7.2.2 Main Contributions

This work seeks to expand the analytical understanding of parallel-connected battery systems toward answering the question "how does current and SOC imbalance within each cycle affect long-term degradation trajectories?" (see Fig. 7.2). Towards this goal, Section 7.3 first develops a model of the intra-cycle (i.e. within a cycle) battery dynamics, starting with an affine model based on equivalent circuits. We derive closed-form solutions to the system dynamics, enabling a rigorous analysis of the intra-cycle dynamics and subsequent degradation convergence behavior. We then run numerical simulations with nonlinear OCV functions for two cathode chemistries. In doing so, we assess the error introduced by the affine OCV assumption. We also analyze the stability and bounds of the SOC imbalance

dynamics using Lyapunov analysis for the general case with a nonlinear OCV function and time-varying current inputs. Sec. 7.4 then introduces a reduced-order degradation modeling framework enabling cycle-by-cycle updates to cell capacities and resistances as a function of SOC and current imbalance within each cycle. The work from Secs. 7.3 and 7.4 are combined in Sec. 7.5 to realize the simulation framework outlined in Fig. 7.2, where the intra-cycle dynamics are used to update the inter-cycle degradation, and vice versa. Here, we highlight the importance of the underlying degradation model assumptions which ultimately determine whether degradation trajectories converge or diverge over time. Sec. 7.6 compares the modeled results to experiments, verifying the accuracy of the model-predicted intra-cycle dynamics as well as giving clues to degradation convergence/divergence for a real-world example. Sec. 8.2.4 finally suggests future research directions.

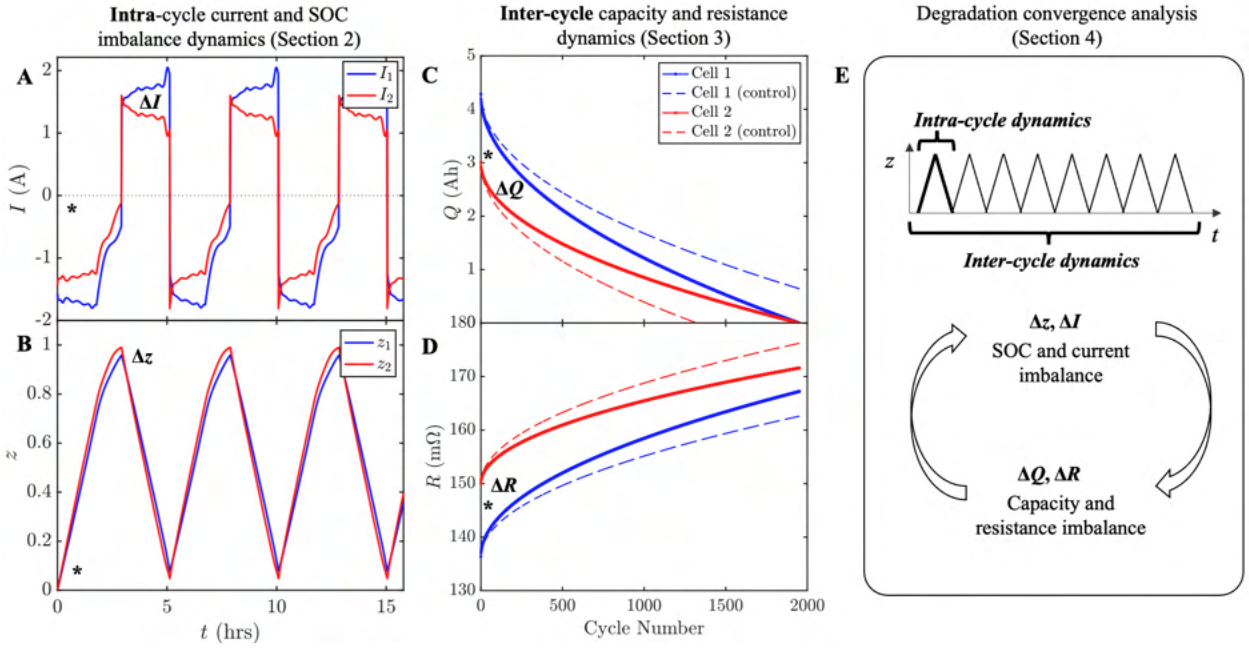

Figure 7.2: Main contributions of this work. (A,B) Intra-cycle current and SOC imbalance dynamics are first explored in detail (Section 7.3). (C,D) A framework for successively updating cell capacities and resistances as a function of the intra-cycle dynamics is next proposed (Section 7.4). (E) Convergence properties of degradation trajectories are explored by combining the intra-cycle dynamics with the inter-cycle dynamics from the previous sections (Section 7.5). Finally, comparisons of model predictions versus experimental results (Section 7.6) as well as recommended future work (Section 8.2.4) are provided.

7.3 Intra-Cycle Dynamics: Closed-Form Solutions

We start by deriving equations describing the intra-cycle dynamics of parallel-connected systems. Section 7.3.3 first develops closed-form solutions assuming an affine OCV function. Section 7.3.4 next discusses the system behavior with nonlinear OCV functions.

7.3.1 Model Selection

We chose an OCV-R model for this work (see Fig. 7.3). This model provides the simplest representation of cell-to-cell variability in capacity and resistance. We have omitted model components that would add complexity without improving the understanding of the effect of cell-to-cell variability and degradation. Specifically, the circuit representation of the parallel-connected system omits RC pairs and interconnect resistances. Cell resistances are also assumed to be constant parameters, though it is known that cell resistance is generally a nonlinear function of both SOC and temperature [290, 7]. A thermal model is also omitted to first focus on studying the effect of cell capacity and resistance variability on the electrical dynamics. The analysis is finally restricted to two parallel-connected cells. The analytical framework presented here can be extended in the future to support more cells [280], higher degrees of nonlinearities (e.g. temperature-dependent resistances) [281], and more physics-based cell models such as the single-particle model (SPM) [137, 138, 110].

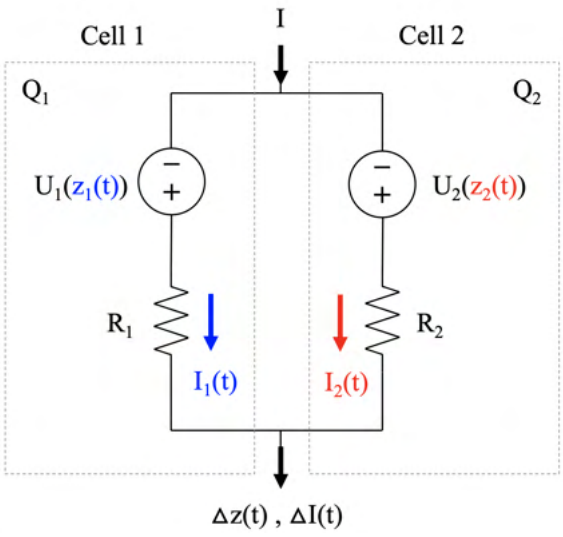

Figure 7.3: System representation

7.3.2 Model Description

Fig. 7.3 shows the parallel system under consideration. R_i and Q_i describe the resistances and capacities of cells $i \in 1, 2$, respectively. Since modern lithium-ion have coulombic efficiencies exceeding 99%, we assume that R_i and Q_i remain constant over the course of a single cycle. U_i is the OCV function and is generally a nonlinear, monotonically increasing function with respect to the cell SOC z_i. The system input is the applied current I which is defined to be positive on discharge. The system output is the terminal voltage, V_t, which is identical for all batteries due to voltage conservation, and is given by:

$$V_t(t) = U_i(z_i(t)) - I_i(t)R_i. \tag{7.1}$$

Current conservation further requires that:

$$I(t) = \sum_i I_i(t). \tag{7.2}$$

Applying (7.1) and (7.2) for two parallel-connected cells yields the following expressions for the terminal voltage and the two branch currents:

$$V_t(t) = \frac{R_1U_2(z_2(t)) + R_2U_1(z_1(t)) - R_1R_2I(t)}{R_{\text{tot}}} \tag{7.3}$$

$$I_1(t) = \frac{-\Delta U(t) + R_2I(t)}{R_{\text{tot}}} \tag{7.4}$$

$$I_2(t) = \frac{+\Delta U(t) + R_1I(t)}{R_{\text{tot}}}, \tag{7.5}$$

where $R_{\text{tot}} \triangleq R_1 + R_2$ and $\Delta U(t) \triangleq U_2(z_2(t)) - U_1(z_1(t))$. The SOC dynamics for each battery are given by the integrator state:

$$\dot{z}_i(t) = -\frac{1}{Q_i}I_i(t). \tag{7.6}$$

7.3.3 The Affine OCV-R System

The general behavior of the affine OCV-R system is previewed in Fig. 7.4 which serves as a reference throughout this section. This figure shows the analytical solutions throughout an entire charge and discharge cycle, including constant (CC) phases and a constant voltage (CV) phase at the top of charge. Panel A shows solutions to the branch current and cell SOC equations from Eqs. (7.9), (7.17), (7.18). Panel B shows solutions to the current and

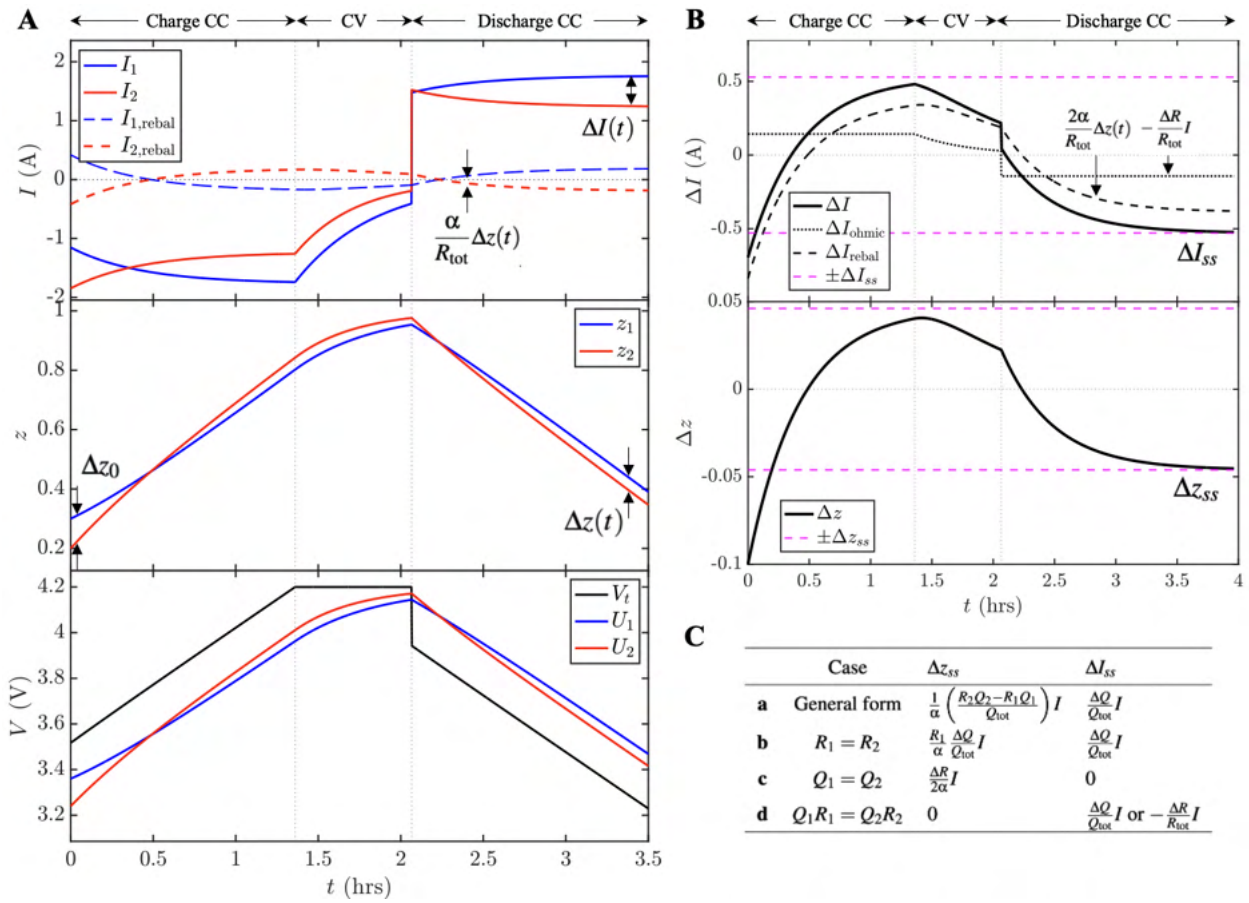

Figure 7.4: Demonstration of the affine OCV-R system. (A) Current: I, SOC: z, and voltage: V, over a complete charge-discharge cycle. (B) Current and SOC imbalance. The affine OCV function parameters used are $(\alpha, \beta) = (1.2, 3.0)$. The cell parameters used are $(Q_1, Q_2) = (4.3, 3.0)$Ah, $(R_1, R_2) = (136, 150)$mΩ. This cell pairing represents an aged cell (Cell 2), with lower capacity and higher resistance, connected with a less aged cell (Cell 1). The initial condition was set to $(z_{1,0}, z_{2,0}) = (0.3, 0.2)$ to highlight the effect of initial SOC imbalances on rebalancing currents. $|I| = 3$A during the constant current phases, and the CV termination condition was set to $Q_2/5$A. The green markers indicate that this same set of parameters will be referenced in later figures. (C) Steady-state solutions to SOC and current imbalance.

SOC imbalance equations from Eqs. (7.14), (7.21). During the CV phase, Eqs. (7.23) and (7.26) were used. Panel C shows steady-state solutions to current and SOC imbalance.

We start by considering the case of an affine OCV function:

$$U_i(z_i(t)) = \alpha z_i(t) + \beta, \tag{7.7}$$

where $\alpha, \beta > 0$. α is the characteristic slope of the OCV function and β defines the minimum voltage. We note that this is the same starting point as previous works [279, 289, 288,

280]. Section 7.3.4 later lifts this restriction and studies the model error introduced by this assumption. Here, we will also assume constant-current input unless stated otherwise.

7.3.3.1 SOC Imbalance

Combining equations (7.4-7.7) yields the following system of equations:

$$\begin{bmatrix}\dot{z}_1\\ \dot{z}_2\end{bmatrix} = \frac{\alpha}{R_{\text{tot}}}\begin{bmatrix}\frac{+1}{Q_1} & \frac{-1}{Q_1}\\ \frac{-1}{Q_2} & \frac{+1}{Q_2}\end{bmatrix}\begin{bmatrix}z_1\\ z_2\end{bmatrix} - \frac{1}{R_{\text{tot}}}\begin{bmatrix}\frac{R_2}{Q_1}\\ \frac{R_1}{Q_2}\end{bmatrix} I. \tag{7.8}$$

The solution to (7.8) reads:

$$\begin{bmatrix}z_1\\ z_2\end{bmatrix} = \frac{1}{Q_{\text{tot}}}\begin{bmatrix}Q_2(1-e^{-t/\tau}) & Q_1+Q_2e^{-t/\tau}\\ Q_1+Q_2e^{-t/\tau} & Q_1(1-e^{-t/\tau})\end{bmatrix}\begin{bmatrix}z_{1,0}\\ z_{2,0}\end{bmatrix} \tag{7.9}$$

$$+\frac{\kappa}{Q_{\text{tot}}}\begin{bmatrix}-Q_2(1-e^{-t/\tau})-t\\ +Q_1(1-e^{-t/\tau})-t\end{bmatrix} I, \tag{7.10}$$

where $Q_{\text{tot}} \triangleq Q_1 + Q_2$, and:

$$\tau \triangleq \frac{R_{\text{tot}}}{\alpha}\left(\frac{Q_1Q_2}{Q_{\text{tot}}}\right) \qquad \text{(Time constant)} \tag{7.11}$$

$$\kappa \triangleq \frac{1}{\alpha}\left(\frac{R_2Q_2 - R_1Q_1}{Q_{\text{tot}}}\right) \qquad \text{(Input sensitivity).} \tag{7.12}$$

Remark 1. *The parameters τ and κ can be physically interpreted: τ is the time constant of the system and κ describes the input sensitivity.*

The SOC imbalance is defined by $\Delta z(t) \triangleq z_2(t) - z_1(t)$ and can be written by inspection from (7.8) to yield:

$$\Delta\dot{z}(t) = -\underbrace{\frac{\alpha}{R_{\text{tot}}}\left(\frac{1}{Q_1}+\frac{1}{Q_2}\right)}_{1/\tau}\Delta z(t) + \underbrace{\frac{1}{R_{\text{tot}}}\left(\frac{R_2}{Q_1}-\frac{R_1}{Q_2}\right)}_{\kappa/\tau} I. \tag{7.13}$$

This is a standard linear time-invariant (LTI) system with the solution:

$$\Delta z(t) = \Delta z_0 e^{-t/\tau} + \kappa(1-e^{-t/\tau})I, \tag{7.14}$$

where $\Delta z_0 \triangleq z_{2,0} - z_{1,0}$ is the initial SOC imbalance.

7.3.3.2 Branch Current Imbalance

The branch currents for the affine OCV-R system can be written as a function of the SOC imbalance dynamics by substituting (7.7) directly into (7.4) and (7.5) to yield:

$$I_1(t) = -\frac{\alpha}{R_{\text{tot}}}\Delta z(t) + \frac{R_2}{R_{\text{tot}}}I(t) \tag{7.15}$$

$$I_2(t) = \underbrace{+\frac{\alpha}{R_{\text{tot}}}\Delta z(t)}_{I_{\text{rebalance}}(t)} + \underbrace{\frac{R_1}{R_{\text{tot}}}I(t)}_{I_{\text{ohmic}}(t)}. \tag{7.16}$$

The first terms in each equation represent the SOC rebalancing current and the second terms are due to the resistance (i.e. 'Ohmic') mismatch between the two cells. Direct substitution of (7.14) into (7.15-7.16) yields an explicit form of the branch current imbalance:

$$I_1(t) = -\frac{\alpha}{R_{\text{tot}}}\left[\Delta z_0 e^{-t/\tau} - \kappa(1-e^{-t/\tau})I\right] + \frac{R_2}{R_{\text{tot}}}I \tag{7.17}$$

$$I_2(t) = \underbrace{+\frac{\alpha}{R_{\text{tot}}}\left[\Delta z_0 e^{-t/\tau} + \kappa(1-e^{-t/\tau})I\right]}_{I_{\text{rebalance}}(t)} + \underbrace{\frac{R_1}{R_{\text{tot}}}I}_{I_{\text{ohmic}}(t)}. \tag{7.18}$$

The branch current imbalance $\Delta I \triangleq I_2 - I_1$ is then:

$$\Delta I(t) = \frac{2}{R_{\text{tot}}}\Delta U(t) - \frac{\Delta R}{R_{\text{tot}}}I \tag{7.19}$$

$$= \frac{2\alpha}{R_{\text{tot}}}\Delta z(t) - \frac{\Delta R}{R_{\text{tot}}}I \tag{7.20}$$

$$= \underbrace{\frac{2\alpha}{R_{\text{tot}}}\left[\Delta z_0 e^{-t/\tau} + \kappa(1-e^{-t/\tau})I\right]}_{\Delta I_{\text{rebalance}}(t)} - \underbrace{\frac{\Delta R}{R_{\text{tot}}}I}_{\Delta I_{\text{ohmic}}(t)}, \tag{7.21}$$

where $\Delta R \triangleq R_2 - R_1$.

A key insight from this derivation is that the input current term appears twice in Eq. (7.21): once as part of the SOC rebalancing term, and again as part of the Ohmic term. The applied current thus plays a dual role. First, the applied current directly contributes to the 'Ohmic' current as part of the resistor network. Second, and less intuitively, the applied current also creates an internal SOC imbalance which induces its own internal SOC rebalancing current driven by the voltage difference between the two cells. These two currents may flow in the same direction or in opposite directions depending on the sign of κ.

Table 7.1: Special cases for SOC and current imbalance in the affine OCV-R system. $\Delta Q \triangleq Q_2 - Q_1$.

	Case	$\Delta z(t)$	$\Delta I(t)$
a	General form	$\Delta z_0 e^{-t/\tau} + \kappa(1 - e^{-t/\tau})I$	$\frac{2\alpha}{R_{\text{tot}}}\Delta z(t) - \frac{\Delta R}{R_{\text{tot}}}I$
b	Zero input ($I = 0$)	$\Delta z_0 e^{-t/\tau}$	$\frac{2\alpha}{R_{\text{tot}}}\Delta z_0 e^{-t/\tau}$
c	R-matching ($R_1 = R_2$)	$\Delta z_0 e^{-t/\tau} - \frac{R_1 \Delta Q}{\alpha Q_{\text{tot}}}(1 - e^{-t/\tau})I$	$\frac{2\alpha}{R_{\text{tot}}}\Delta z(t)$
d	Q-matching ($Q_1 = Q_2$)	$\Delta z_0 e^{-t/\tau} - \frac{\Delta R}{2\alpha}(1 - e^{-t/\tau})I$	$\frac{2\alpha}{R_{\text{tot}}}\Delta z(t) - \frac{\Delta R}{R_{\text{tot}}}I$
e	QR-matching ($Q_1 R_1 = Q_2 R_2$)	$\Delta z_0 e^{-t/\tau}$	$\frac{2\alpha}{R_{\text{tot}}}\Delta z_0 e^{-t/\tau} - \frac{\Delta R}{R_{\text{tot}}}I$
f	Initial ($t = 0$)	Δz_0	$\frac{2\alpha}{R_{\text{tot}}}\Delta z_0$
g	Steady-state ($t \to \infty$)	$\frac{1}{\alpha}\left(\frac{R_2 Q_2 - R_1 Q_1}{Q_{\text{tot}}}\right) I \quad (= \kappa I)$	$\frac{\Delta Q}{Q_{\text{tot}}}I$
h	Max imbalance ($\max_t$)	$\max\left(\lvert\Delta z_0\rvert, \lvert\kappa I\rvert\right)$	$\max\left(\lvert\frac{2\alpha}{R_{\text{tot}}}\Delta z_0\rvert, \lvert\frac{\Delta Q}{Q_{\text{tot}}}I\rvert\right)$

7.3.3.3 Potentiostatic Mode

Since most battery charging protocols include a potentiostatic (i.e. constant voltage) hold, a complete description of a battery's charge-discharge cycle would need to consider this step. Closed-form state equations under potentiostatic mode can be derived by inverting the input and output from (7.3) to express the total current, $I_{cv}(t)$, as a function of a fixed voltage set-point $V_t = U(z = 1) = \alpha + \beta$, which yields:

$$I_{cv}(t) = \frac{\alpha}{R_1}(z_1(t) - 1) + \frac{\alpha}{R_2}(z_2(t) - 1). \tag{7.22}$$

The two terms in this equation correspond exactly to the two branch currents:

$$I_{i,cv}(t) = \frac{\alpha}{R_i}(z_i(t) - 1). \tag{7.23}$$

This result can be verified by substituting (7.22) into (7.4) and (7.5). The SOC dynamics can then be obtained by substituting (7.23) into (7.6) yielding:

$$\dot{z}_{i,cv} = -\frac{1}{\tau_{i,cv}} z_{i,cv} + \frac{1}{\tau_{i,cv}}, \tag{7.24}$$

where

$$\tau_{i,cv} \triangleq \frac{Q_i R_i}{\alpha} \tag{7.25}$$

is the characteristic time constant for SOC decay for each cell. Eq. (7.24) is readily solved to obtain:

$$z_i(t) = z_{i,cv,0}e^{-t/\tau_{i,cv}} - (e^{-t/\tau_{i,cv}} - 1). \tag{7.26}$$

Remark 2. *The states and time constants during the CV mode of operation are no longer coupled as was the case of CC operation: the SOC of each cell decays with its own characteristic time constant.*

Finally, the SOC and current imbalance dynamics during potentiostatic mode of operation can be trivially calculated from Eqs. (7.23) and (7.26).

7.3.3.4 Affine OCV-R System Properties

The closed-form solutions presented here are consistent with the derivations from Refs [277, 288, 60]. However, whereas previous works mostly focused on presenting special cases (e.g. steady-state solutions), our equations are more general. Table 7.1 summarizes how the system equations can be reduced to special cases. Useful system properties are additionally discussed below. These properties will be referenced in later sections.

a. Stability. The SOC imbalance system (Eq. 7.14), with a single negative eigenvalue with the value $\lambda = -1/\tau$, is globally exponentially stable. The current imbalance system (Eq. 7.21) is also globally exponentially stable.

b. Convergence Rate. Steady-state imbalance values can be realized to within 5% during a full charge or discharge cycle for C-rates lower than $1/3\tau$. The time constant τ depends on the cell capacities and resistances (see Eq. 7.11).

c. Steady-State SOC Imbalance. At steady-state, the SOC imbalance is:

$$\Delta z_{ss} = \kappa I \tag{7.27}$$

$$= \frac{1}{\alpha}\left(\frac{R_2Q_2 - R_1Q_1}{Q_{\text{tot}}}\right) I. \tag{7.28}$$

For the SOCs of the two cells to converge, it is thus sufficient that $Q_1R_1 = Q_2R_2$. When this condition is satisfied, zero SOC imbalance is achieved at steady-state under any applied current. To understand this effect, consider the case where $Q_2 < Q_1$, $R_2 > R_1$, and $Q_1R_1 = Q_2R_2$. In this case, Cell 2 experiences less current due to the higher resistance. However, since Cell 2 has a lower capacity, Cell 2 experiences the same effective C-rate. Both cells thus charge at the same rate on the basis of C-Rate or SOC.

d. Steady-State Current Imbalance. At steady-state, the current imbalance is

$$\Delta I_{ss} = \frac{\Delta Q}{Q_{\text{tot}}} I, \tag{7.29}$$

where $\Delta I_{ss} \triangleq I_{ss,2} - I_{ss,1}$ and $\Delta Q \triangleq Q_2 - Q_1$. The steady-state current imbalance is thus driven by capacity mismatches, not resistance mismatches. This result can be directly recovered from Eq. (7.21) by taking the limit of infinite time and realizing that all of the resistance terms cancel. Note, however, that under the special case of QR-matching (i.e. $Q_1 R_1 = Q_2 R_2$), the steady-state current imbalance can be equivalently expressed as $\Delta I_{ss} = -(\Delta R / R_{\text{tot}}) I$. Hence, capacity mismatch is equivalent to resistance mismatch but only under QR-matching.

e. Maximum Imbalance. If the initial SOC imbalance is zero, then the maximum SOC and current imbalances are equivalent to their steady-state values.

7.3.4 The Nonlinear OCV-R System

The affine OCV-R model derived in Section 7.3.3 provided an analytically tractable description of imbalance dynamics. But how accurate is this model? This section explores this question by revisiting the OCV-R model, this time relaxing the affine OCV assumption. Section 7.3.4.1 takes a numerical approach to explore the model behavior under nonlinear OCV functions for two popular battery chemistries. Section 7.3.4.6 then takes an analytical approach to bound the maximum SOC imbalance under arbitrary, nonlinear current inputs.

7.3.4.1 Numerical Simulations

Here, we revert to the general case of the OCV function $U(z)$ being a nonlinear, monotonically increasing function (Section 7.3.2). Fig. 7.5 summarizes the OCV functions used in this section. We focus on studying two OCV functions that are characteristic of two common battery cathode materials: NMC [171] and LFP [291]. Both cathodes were paired with conventional graphite (Gr) anodes. Affine OCV functions were also defined for comparison purposes. The nonlinear system was numerically solved by discretizing the state equations from Section 7.3.2 using a forward difference scheme with a 1-second timestep. CV mode of operation was simulated by inverting the input and output from Eq. (7.3). The code used to generate the simulation is available at https://github.com/wengandrew/current-imbalance.

Fig. 7.6 compares example simulation results using the NMC/Gr and LFP/Gr OCV curves. Each simulation consisted of five back-to-back charge-discharge cycles. A CV phase with a termination condition of $Q_2/5$ was included at the end of each charge, but not at the

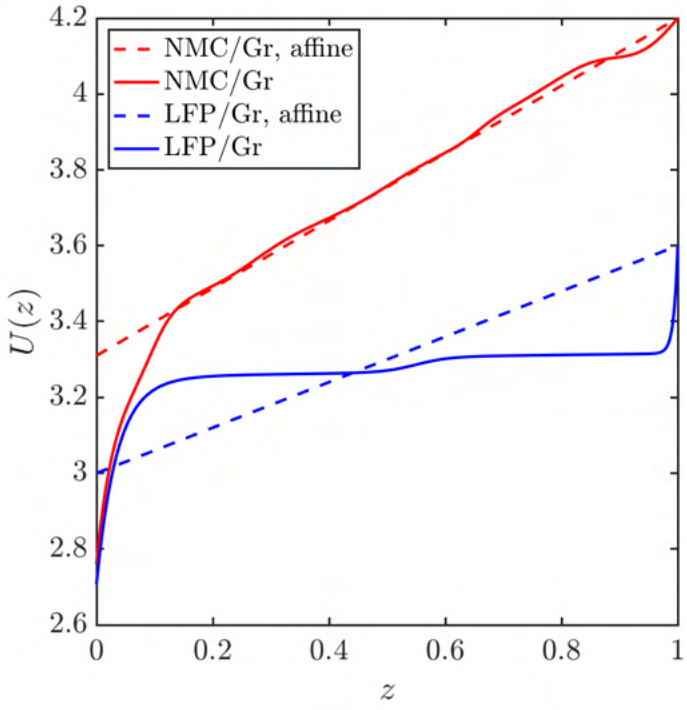

Figure 7.5: Nonlinear OCV functions used for this work. The LFP/Gr curve was adapted from Prada et al [291]. The NMC/Gr curve was adapted from Chen et al [171]. The affine approximation to the LFP/Gr curve used $(\alpha, \beta) = (0.6, 3.0)$. The affine approximation to the NMC/Gr curve used $(\alpha, \beta) = (0.89, 3.31)$.

end of each discharge. Analytical solutions for the affine OCV case were included for the first cycle only for comparison purposes. Since the duration of the CC charge phase was generally non-identical between the affine and nonlinear cases, the time vectors were realigned using the start and end of the CV phase as reference points.

7.3.4.2 Nonlinear System Behavior

The nonlinear OCV functions drive nonlinear oscillations in current and SOC imbalance. Meanwhile, the affine OCV system only predicts exponentially-decaying behavior (Section 7.3.3). The higher SOC imbalance in the LFP/Gr system can be attributed to the flatness of the LFP/Gr OCV function which suppresses the SOC re-balancing current (Eq. 7.21). SOC imbalance therefore accumulates in LFP/Gr systems until one of the cells reaches an inflection point in the OCV function. The majority of SOC re-balancing in LFP/Gr systems thus occurs as one of the cells approaches 100% SOC.

7.3.4.3 Nonlinear vs Affine Model Accuracy

NMC/Gr. The nonlinear NMC/Gr solution deviates from the affine solution the most at low and high SOCs, corresponding to regions where the slope of the OCV function dU/dz deviates the most from the affine approximation α. Overall, the affine solution provides only an approximation to the nonlinear behavior and fails to capture the localized perturbations to current imbalance due to dU/dz. The appropriateness of using affine dynamics to model the nonlinear system will depend on the accuracy requirements of the specific use case.

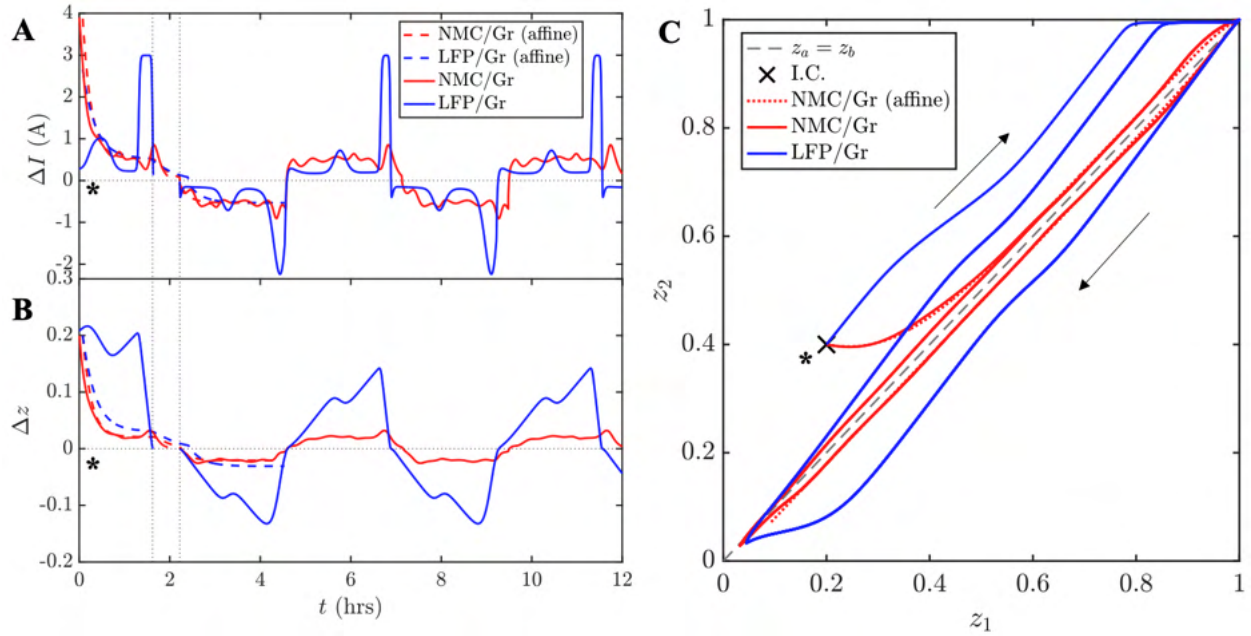

Figure 7.6: Intra-cycle current (A) and SOC (B) imbalance dynamics of the OCV-R system with nonlinear OCV functions. Vertical dotted lines denote the start and end of the charge CV phase. (C) Corresponding phase orbits in the (z_1, z_2) plane over a period of five complete charge-discharge cycles. Parameters used were $(Q_1, Q_2) = (4.28, 3.00)$Ah, $(R_1, R_2) = (45.5, 50.0)m\Omega$, $(z_{1,0}, z_{2,0}) = (0.2, 0.4)$, $|I| = 3$A during the constant current phases, and with a CV termination of $Q_2/5$ A.

LFP/Gr. The current and SOC imbalance observed in the nonlinear LFP/Gr system is greater than those in the NMC/Gr system. Affine approximations to the LFP/Gr curves fail to capture the dynamics of the LFP/Gr system whose behavior is dominated by transitions between low and high-sloping regions in the OCV function. For this system, it may be more appropriate to use piecewise-linear OCV functions to approximate the nonlinear OCV function, which we leave for future work.

Remark 3. *The results highlighted in Fig. 7.6 depend on the input assumptions, particularly the values of* (Q_2, R_2) *and the input magnitude* I*. The accuracy of the affine model and the*

behavior of the nonlinear OCV systems should thus be considered on a case-by-case basis.

7.3.4.4 Nonlinear System Stability

Fig. 7.6C shows a phase portrait of the SOC dynamics over five consecutive charge-discharge cycles. In both the affine and the nonlinear cases, the system converges to a stable orbit after just one complete charge-discharge cycle. This result holds for both NMC/Gr and LFP/Gr curves, although the hysteresis gap between charge and discharge is higher for LFP/Gr. This result highlights the stability of the system under nonlinear OCV functions and that convergence to a stable orbit can be realized within a few cycles.

7.3.4.5 QR-Matching Nullifies Nonlinearities

Here, we highlight a peculiar property of the nonlinear system: when $Q_1R_1 = Q_2R_2$, the nonlinear oscillations in the SOC and currents are nullified. We will refer to this condition as 'QR-matching'. Fig. 7.7 shows this effect by comparing the nonlinear dynamics for the NMC/Gr system under two specific cases. Case A (circle, Panel A) simulates two cells with capacities and resistance values identical to those from Fig. 7.4. Case B (square, Panel B) chooses resistance and capacities satisfying $Q_1R_1 = Q_2R_2$. Case A does not satisfy the QR-matching condition, while Case B does. (See Fig. 7.8 for the same plot but with LFP/Gr chemistry. The following discussion holds for both NMC/Gr and LFP/Gr chemistries.)

Panel B shows that, under QR-matching, the current oscillations disappear after one cycle, and the affine solution begins to overlap with the nonlinear solution. Thus, after one cycle, considerations for the nonlinear OCV dynamics appear to be no longer needed. To explain this phenomenon, consider the fact that, under QR-matching, $\kappa = 0$ in Eq. 7.14, so the SOC imbalance decays to zero under any input current. With zero SOC imbalance, the SOC re-balancing current in Eq. (7.21) also disappears. Current imbalance thus becomes purely driven by the resistance difference between the two cells, which does not depend on the SOC or OCV dynamics.

Overall, under QR-matching, the system appears to be analyzable without considering the nonlinear effects introduced by the OCV function. This result has practical implications since QR-balancing can describe certain scenarios in which aged cells are mixed with fresh cells. QR-balancing can also describe a scenario in which two cells having different electrode areas that are otherwise identical are connected in parallel.

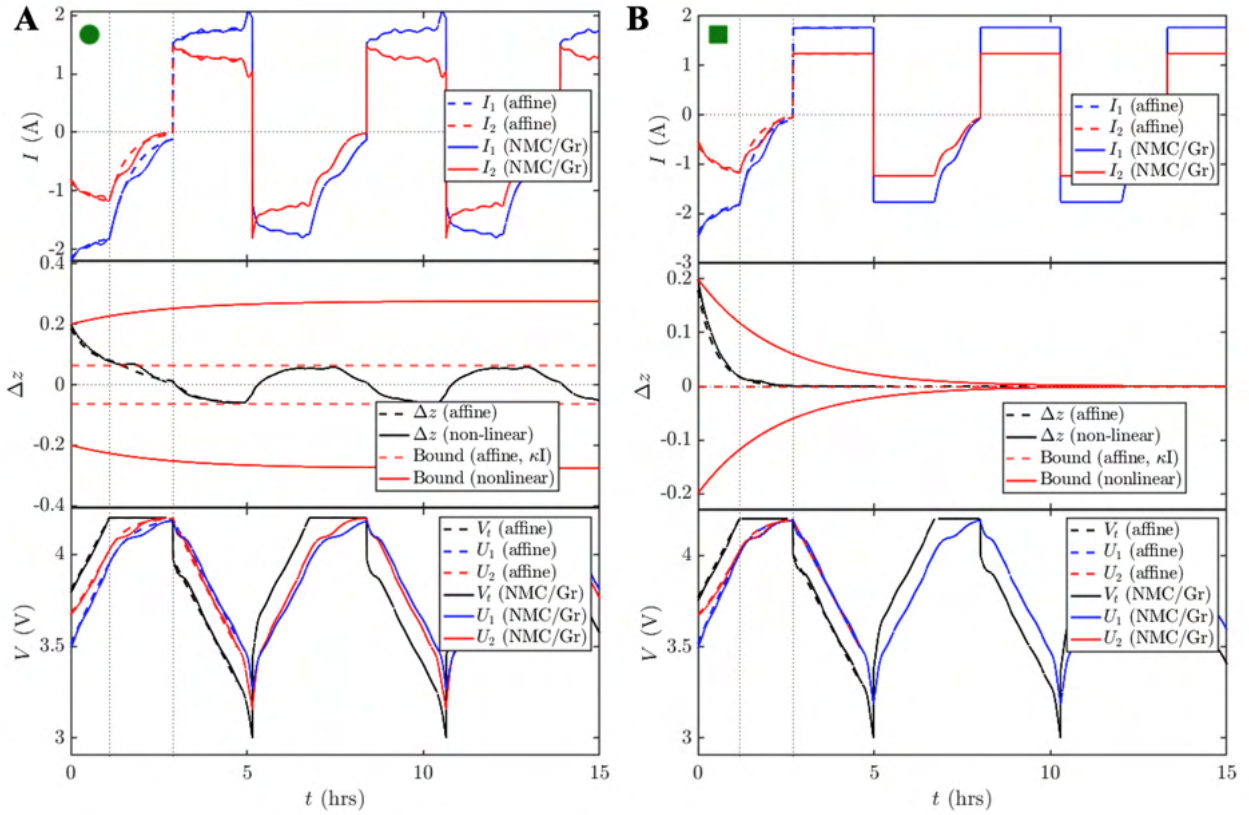

Figure 7.7: OCV-R model system dynamics with nonlinear OCV functions representing an NMC/Gr system. In both (A) and (B), $(Q_2, R_2) = (3\text{Ah}, 150\text{m}\Omega)$, $(z_{1,0}, z_{2,0}) = (0.4, 0.2)$, $|I| = 3\text{A}$ during the constant current phases, and with a CV termination of $Q_2/5$ A. (A) uses $(Q_2/Q_1, R_2/R_1) = (0.7, 1.1)$. This pairing represents a typical scenario in which an aged cell (Cell 2), with lower capacity and higher resistance, is paired with a less aged cell (Cell 1). (B) uses $(Q_2/Q_1, R_2/R_1) = (0.7, 1.43)$. This pairing also represents a typical scenario with an aged cell paired with a less aged cell, but this pairing additionally satisfies the 'QR-matching' condition, i.e. $Q_1R_1 = Q_2R_2$. Under this condition, the SOC imbalance dynamics become insensitive to the input current and exponentially decay to zero. The corresponding imbalance dynamics also become driven purely by resistance differences in the absence of SOC re-balancing currents. After the initial SOC imbalance fades, this system begins to behave identically to the affine OCV system, despite the presence of the nonlinear OCV function. See Section 7.3.4.5 for a complete discussion.

7.3.4.6 Stability and Analytic Bounds for SOC Imbalance

The previous sections showed that, with the exception of the QR-matching condition, the affine OCV-R model may fail to capture transient behavior in SOC and current imbalance, especially for systems having OCV functions with widely-varying slopes such as LFP/Gr. OCV function nonlinearities should thus be generally taken into account for accurate estimates of SOC and current imbalance. However, a nonlinear OCV function makes it difficult

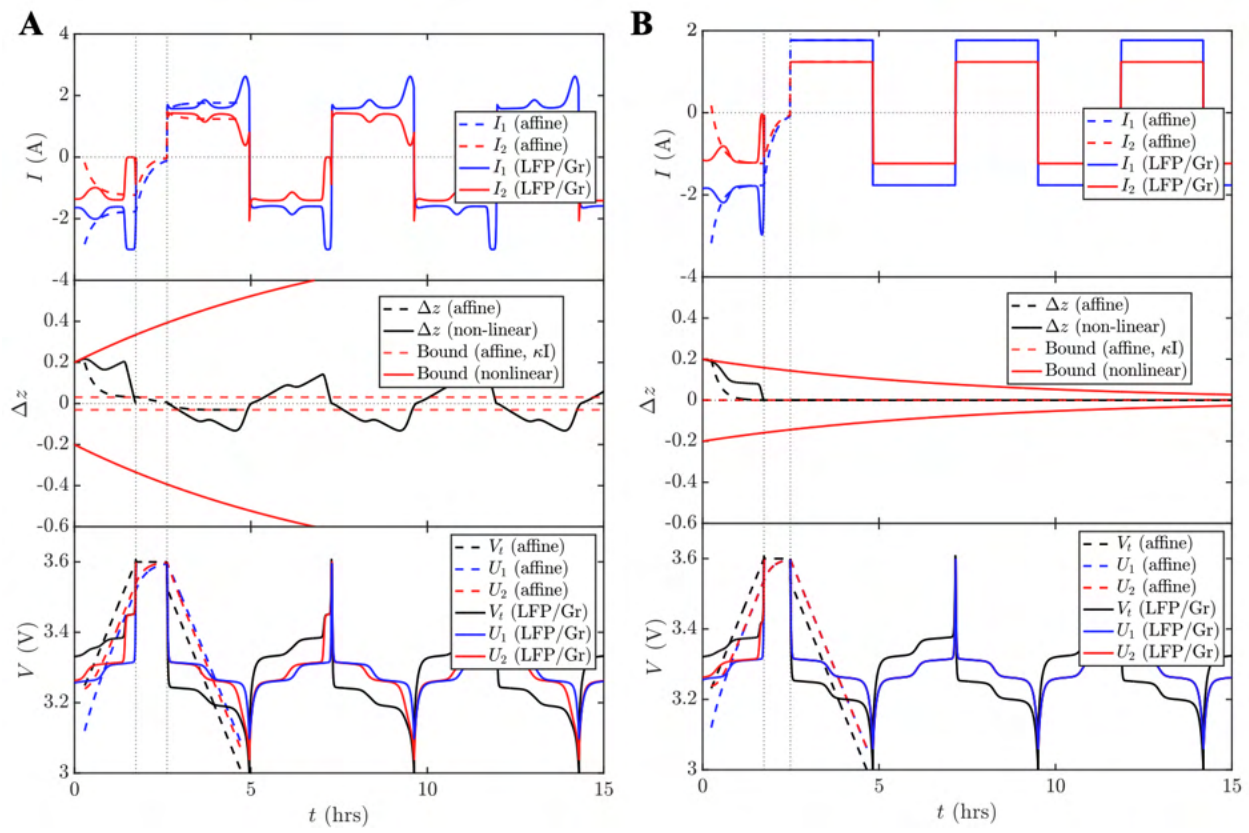

Figure 7.8: OCV-R model system dynamics with nonlinear OCV functions representing an LFP/Gr system. In both (A) and (B), $(Q_2, R_2) = (3\text{Ah}, 50\text{m}\Omega)$, $(z_{1,0}, z_{2,0}) = (0.4, 0.2)$, $|I| = 3\text{A}$ during the constant current phases, and with a CV termination of $Q_2/5$ A. (A) uses $(Q_2/Q_1, R_2/R_1) = (0.7, 1.1)$. This pairing represents a typical scenario in which an aged cell (Cell 2), with lower capacity and higher resistance, is paired with a less aged cell (Cell 1). (B) uses $(Q_2/Q_1, R_2/R_1) = (0.7, 1.43)$. This pairing also represents a typical scenario with an aged cell paired with a less aged cell, but this pairing additionally satisfies the 'QR-matching' condition, i.e. $Q_1R_1 = Q_2R_2$. Under this condition, the SOC imbalance dynamics become insensitive to the input current and exponentially decay to zero. The corresponding imbalance dynamics also become driven purely by resistance differences in the absence of SOC re-balancing currents. After the initial SOC imbalance fades, this system begins to behave identically to the affine OCV system, despite the presence of the nonlinear OCV function. See Section 7.3.4.5 for a complete discussion.

to find closed-form solutions. Yet, despite the absence of closed-form solutions, we may still attempt to use analytical methods to derive bounds on the maximum imbalance.

To derive imbalance bounds, we leverage concepts of input-output and $\mathcal{L}$-stability from Khalil [292]. Note that the imbalance system is not strictly asymptotically stable, but only partially asymptotically stable, since the SOCs can asymptotically approach any value between 0 and 1. We thus also leverage definitions from Haddad et al. [293] which apply to partially asymptotically stable systems. The main result is summarized below.

Theorem 1. *If the following condition is satisfied:*

$$\max(|I(t)|) \leq |\frac{\mathcal{A}k_1}{\mathcal{B}}|, \tag{7.30}$$

then $\Delta z(t)$ satisfies the following bounds:

$$\max(||\Delta z||) \leq |\Delta z(0)|e^{k_1 \mathcal{A}t} + |\frac{\mathcal{B}}{\mathcal{A}k_1}| \max(|I(t)|)(1 - e^{k_1 \mathcal{A}t}) \tag{7.31}$$

where:

$$k_1 = \min\left(\frac{\partial U(z)}{\partial z}\right) \tag{7.32}$$

$$\mathcal{A} = -\frac{1}{R_{\text{tot}}}\left(\frac{1}{Q_1} + \frac{1}{Q_2}\right) \tag{7.33}$$

$$\mathcal{B} = \frac{1}{R_{\text{tot}}}\left(\frac{R_1}{Q_2} - \frac{R_2}{Q_1}\right) \tag{7.34}$$

Remark 4. *Eq. (7.31) provides an l_2-vector norm bound. A signal-norm bound can similarly be calculated.*

A full derivation of the imbalance bounds is provided as follows. From Eqs. (7.4-7.6), the system can be represented as

$$\dot{z}_1(t) = -\frac{I_1(t)}{Q_1} = \frac{+\Delta U(t) - I(t)R_2}{Q_1 R_{\text{tot}}} \tag{7.35}$$

$$\dot{z}_2(t) = -\frac{I_2(t)}{Q_2} = \frac{-\Delta U(t) - I(t)R_1}{Q_2 R_{\text{tot}}} \tag{7.36}$$

where $\Delta U(t) \triangleq U(z_2(t)) - U(z_1(t))$. We can redefine the state as

$$x = \begin{bmatrix} x_1 \\ x_2 \end{bmatrix} = \begin{bmatrix} \Delta z \\ Q_1 z_1 + Q_2 z_2 \end{bmatrix}. \tag{7.37}$$

The dynamic system can then be presented as:

$$\dot{x}_1 = \Delta\dot{z} = \mathcal{A}\Delta U(x_1, x_2) + \mathcal{B}I(t) \tag{7.38}$$

$$\dot{x}_2 = -I(t) \tag{7.39}$$

where

$$\mathcal{A} = -\frac{1}{R_{\text{tot}}}\left(\frac{1}{Q_1} + \frac{1}{Q_2}\right) \tag{7.40}$$

$$\mathcal{B} = \frac{1}{R_{\text{tot}}}\left(\frac{R_1}{Q_2} - \frac{R_2}{Q_1}\right) \tag{7.41}$$

Since OCV functions monotonically increase, the bounds on the slope of the OCV function can be defined as:

$$0 < k_1 \leq \frac{\partial U(z)}{\partial z} \leq k_2 \tag{7.42}$$

Using the differential mean theorem from [294], we have

$$k_1\Delta z \leq \Delta U \leq k_2\Delta z. \tag{7.43}$$

Note that x_2 in (7.39) is neutrally stable. We therefore present the following definition for partial asymptotic stability.

Definition 7.3.1 (Partial asymptotic stability [293])**.** *The general system*

$$\begin{aligned}\dot{x}_1 &= f_1(x_1, x_2)\\ \dot{x}_2 &= f_2(x_1, x_2)\end{aligned} \tag{7.44}$$

is said to be asymptotically stable with respect to x_1 uniformly in initial value $x_2(0)$ if, for every value of $x_2(0)$, x_1 is stable and for every value of $||x_1(0)|| < \delta \Rightarrow \lim_{t\to\infty} x_1(t) = 0$.

Proposition 1. The unforced system ($I \equiv 0$) presented in (7.38) is asymptotically stable with respect to x_1 uniformly in $x_2(0)$.

Proof. Take the Lyapunov function candidate:

$$V = P\Delta z^2 \tag{7.45}$$

where $P > 0$. Taking the derivative, we have

$$\begin{aligned}\dot{V} &= 2\mathcal{A}P\Delta z\Delta U \\ &= \begin{bmatrix}\Delta z \\ \Delta U\end{bmatrix}^T \begin{bmatrix}0 & \mathcal{A}P \\ \mathcal{A}P & 0\end{bmatrix} \begin{bmatrix}\Delta z \\ \Delta U\end{bmatrix}\end{aligned} \tag{7.46}$$

The following sector condition can be easily derived from (7.42) [294]:

$$V_1 = \begin{bmatrix}\Delta z \\ \Delta U\end{bmatrix}^T \begin{bmatrix}k_1k_2 & -\frac{k_1+k_2}{2} \\ -\frac{k_1+k_2}{2} & 1\end{bmatrix} \begin{bmatrix}\Delta z \\ \Delta U\end{bmatrix} \leq 0. \tag{7.47}$$

Using the S-procedure lemma [295] for (7.46) and (7.47), if the following matrix inequality is satisfied, then x_1 is asymptotically stable [293]:

$$\begin{bmatrix}-k_1k_1 & \mathcal{A}P + \frac{k_1+k_2}{2} \\ \mathcal{A}P + \frac{k_1+k_2}{2} & -1\end{bmatrix} \preceq 0. \tag{7.48}$$

Since $k_1, k_2 > 0$ and $\mathcal{A} < 0$, this inequality is always satisfied. □

Remark 5. *The same logic can be applied for multiple cells in parallel by taking Δz for every two consecutive cells.*

Since, the system presented in (7.38) is input-x_1 stable, Theorem 1 holds, with the proof given below.

Proof. Here, we follow the procedure for input-state stability similar to [292]. Since the unforced system is asymptotically stable with respect to x_1, we can write:

$$\begin{aligned}\frac{d||\Delta z||}{dt} &= \frac{\Delta z\Delta \dot{z}}{||\Delta z||} \\ &= \frac{\mathcal{A}\Delta U\Delta z + \mathcal{B}I\Delta z}{||\Delta z||}.\end{aligned} \tag{7.49}$$

Using the left hand side of the inequality from (7.43), we can have the upper bound of (7.49) as:

$$\frac{d||\Delta z||}{dt} \leq k_1\mathcal{A}||\Delta z|| + |\mathcal{B}|||I(t)||. \tag{7.50}$$

By using the comparison lemma [292], we have:

$$||\Delta z|| \leq |\Delta z(0)|e^{k_1\mathcal{A}t} + |\mathcal{B}| \int_0^t e^{-(t-\tau)k_1\mathcal{A}}||I(t)||d\tau. \tag{7.51}$$

which can be simplified as:

$$||\Delta z|| \leq |\Delta z(0)|e^{k_1 \mathcal{A} t} + |\mathcal{B}| \max(|I(t)|) \int_0^t e^{-(t-\tau)k_1 \mathcal{A}} d\tau. \tag{7.52}$$

Taking the integral from 0 to t results in (7.31). It is apparent that condition (7.30) guarantees that $||\Delta z|| \leq 1$. □

7.3.4.7 Application of SOC Imbalance Bounds

To understand the utility of the nonlinear imbalance bounds, we applied the bounds to the cases shown in Fig. 7.7. Red solid lines drawn in the second rows show infinity-norm bounds (7.31) on the SOC imbalance. These bounds were computed for the cases shown in Panels A and B which both satisfy condition (7.30). These bounds were compared against the affine solution to the steady-state SOC imbalance ($\pm\kappa I$), shown in red dashed lines, which we interpret as 'affine bounds.' Panel A shows that these affine bounds were exceeded initially since they fail to capture the effect of initial SOC imbalance. However, after the initial transient response decays, the affine bounds successfully bounded the current imbalance for the remainder of the simulation. By comparison, the nonlinear bounds gave correct, albeit conservative, bounds on the maximum SOC imbalance. In Panel B, the affine bound again could not capture the initial SOC imbalance but trivially predicted the SOC imbalance at steady-state which decays to zero. Meanwhile, the nonlinear bound was able to bound both the initial SOC imbalance and capture the decay of the SOC imbalance towards zero at steady state.

This demonstration shows that the nonlinear bounds (7.31) correctly but weakly bound the SOC imbalance. The weakness of the bounds can be attributed to the fact that k_1, the minimum slope of the OCV function (7.32), must be large in order for the bound to be tight. Yet, for most practical lithium-ion battery chemistries, OCV functions often have regions with shallow slopes, so k_1 is generally small. Thus, battery chemistries having very flat OCV curves such as LFP may not be able to derive utility from these bounds (see Fig. 7.8). By comparison, the affine bound was surprisingly effective at providing bounds on the SOC imbalance after the initial transient response decays, at least for the NMC/Gr system. However, for the LFP/Gr system, the affine bounds also failed to bound the SOC imbalance since the rapid change in the OCV slope at the top of charge takes this system out of steady-state (see Fig. 7.8).

7.4 Inter-Cycle Degradation: Successive Update Scheme

Updating cell capacities and resistances based on the intra-cycle current and SOC dynamics derived in Section 7.3 requires a degradation model. This model specifically needs to allow for updates to the degradation states (i.e. capacity and resistance) as a function of time-varying parameters such as currents and SOCs which could change cycle-by-cycle. Empirical models, which rely on experimental curve fits to degradation data, cannot be used for this work since these models assume that the intra-cycle dynamics (e.g. C-rates, depths of discharges) remain fixed [91]. More physics-based approaches are thus needed. Such approaches may provide electrode-level state variables, such as solid-phase lithium concentrations and reaction current densities, which can be more directly tied to relevant degradation modes such as loss of lithium inventory and loss of active material [83, 296]. Reniers et al. [110], for example, used the SPM to represent the intra-cycle battery dynamics for each cell in a system of series and parallel-connected cells, and successfully coupled these dynamics to an 'inter-cycle' degradation model based on SEI growth and electrode particle cracking.

Here, we develop a simplified, semi-empirical representation of battery degradation enabling cycle-by-cycle cell capacity and resistance updates as a function of current and SOC imbalance. The model is semi-empirical in that degradation variables are restricted to full cell-level quantities (i.e. full cell capacities and resistances). Since this work focuses on making an elementary connection between the intra-cycle dynamics of parallel-connected systems to battery degradation, we have chosen the simplest representation of degradation. Provisions for electrode-level state variables (e.g. solid-phase lithium concentrations and interfacial potentials) have thus been omitted. The methodologies presented here, however, can be applied to more realistic degradation models and higher-fidelity models of battery dynamics, which is left for future work.

7.4.1 Incremental Capacity Loss Model Formulation

We start by considering discrete updates to cell capacity by writing down the incremental capacity loss at each cycle. The capacity of cell i at any given cycle number is:

$$Q_{i,n} = Q_{i,0} - L_{i,n}, \tag{7.53}$$

where $n \in 1, 2, ...$ is the cycle number, $Q_{i,0}$ is the initial cell capacity, and $L_{i,n}$ is the total capacity lost at the end of the nth cycle. $L_{i,n}$ is, in general, determined by multiple physical degradation phenomena including loss of lithium inventory and loss of active material [296].

Here, we adopt a generic form of the loss equation presented in Smith et al. [91] for solid-electrolyte interphase (SEI) growth [27]:

$$\frac{dL_i(t)}{dt} = r_i(t) \cdot p \cdot \left(\frac{r_i(t)}{L_i(t)}\right)^{\frac{1-p}{p}}, \tag{7.54}$$

where L_i is the total capacity lost at time t, $r_i(t)$ is a time-dependent reaction rate constant and p is an exponential factor. p is allowed to vary between 0.5 in the case of pure diffusion-limited SEI growth, and 1.0 in the case of pure reaction-limited SEI growth. By taking a constant reaction rate, Eq. (7.54) evaluates to the familiar form of $L_i(t) = r_i t^p$. However, this equation cannot be directly used if r changes cycle-by-cycle, which would lead to discontinuities in the degradation curve.

We therefore develop an integral form of Eq. (7.54) to describe the incremental capacity lost over a single cycle n, using Fig. 7.9 as a guide. In this formulation, r_i is allowed to vary cycle-to-cycle and within each cycle. The integration is performed through separation of variables, taking the initial condition to be $(t_0, L_{i,n-1})$, where t_0 is the time at the start of the nth cycle and $L_{i,n-1}$ is the total capacity lost immediately before the start of the nth cycle. Performing this integration yields:

$$L_{i,n}(t) = \left(\int_{t_{0,n}}^{t} r_{i,n}(\tau)^{1/p} d\tau + L_{i,n-1}^{1/p}\right)^p, \tag{7.55}$$

where $r_{i,n}$ now denotes the reaction rate, valid over cycle n. $L_{i,n}(t)$ is valid over the domain $t_{0,n} < t < t_{f,n}$, where $t_{0,n}$ and $t_{f,n}$ denote the start and the end time of the nth cycle. The total capacity lost at the end of the nth cycle is then $L_{i,n} \triangleq L_{i,n}(t_{f,n})$. The incremental capacity loss during cycle n is:

$$\delta L_{i,n} \triangleq L_{i,n} - L_{i,n-1} \tag{7.56}$$

$$= \left(\int_{t_{0,n}}^{t_{f,n}} r_{i,n}(\tau)^{1/p} d\tau + L_{i,n-1}^{1/p}\right)^p - L_{i,n-1}. \tag{7.57}$$

If $r_{i,n}$ is further assumed to be constant over the cycle, then the expression simplifies to:

$$\delta L_{i,n} = \left(r_{i,n}^{1/p} \Delta t_n + L_{i,n-1}^{1/p}\right)^p - L_{i,n-1}, \tag{7.58}$$

where $\Delta t_n \triangleq t_{f,n} - t_{0,n}$.

Eqs. (7.57) and (7.58) clarify the fact that the capacity lost at each cycle depends on how much capacity was lost previously. This result can be physically interpreted for $p < 1$ which

corresponds to a self-limiting SEI growth mechanism in which more capacity lost implies slower reaction rates, and hence lower capacity loss rates [27]. A similar interpretation of capacity loss is discussed in the context of path-dependent aging in Karger et al. [297].

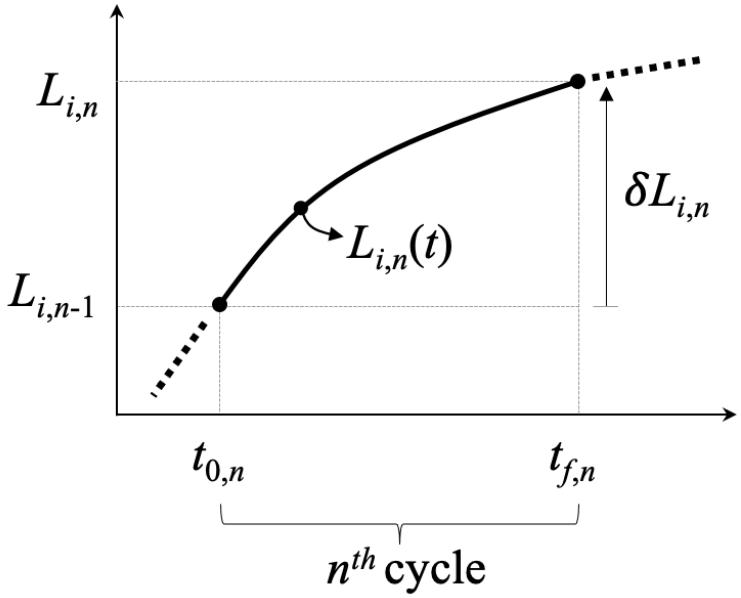

Figure 7.9: Methodology for calculating the incremental capacity loss at cycle n. $L_{i,n}$ represents the capacity lost at cycle n and is a discrete quantity. $L_{i,n}(t)$ is a continuous variable describing the instantaneous capacity loss value during cycle n and at time t, and is valid over the domain $t_{0,n} < t < t_{f,n}$.

To model resistance growth, we adopt a simple approach by considering the cell resistance at each cycle to be:

$$R_{i,n} = R_{i,0} + G_{i,n}, \tag{7.59}$$

where $R_{i,0}$ is the initial cell resistance and $G_{i,n}$ is the total resistance growth at the end of the nth cycle. We assume that $G_{i,n}$ is related to $L_{i,n}$ according to

$$G_{i,n} = \lambda_1 L_{i,n} + \lambda_2, \tag{7.60}$$

where $\lambda_1 > 0$ is a proportionality factor that describes the lithium-consuming SEI film growth process which leads to resistance growth [56] and $\lambda_2 > 0$ describes resistance growth contributions occurring independently from lithium-consuming processes such as SEI growth (i.e. film growth in layered oxide cathodes [298]).

Fig. 7.10 demonstrates how this model formulation can be used to simulate dynamic capacity fade trajectories on a single cell. In this simulation, δL_i is calculated at each cycle for an arbitrary cell i via successive updates according to Eq. (7.58). The cell capacity is

then updated according to Eq. (7.53). For demonstration purposes, r_i is set to 2 between 300 and 600 cycles and is otherwise set to 1 (Panel A). This trajectory is compared to two control trajectories in which r_i remain invariant throughout the simulation. The control trajectories bounded the dynamic capacity fade trajectory but neither correctly predicted the final cell capacity (Panel B). A similar observation follows for the resistance growth trend (Panel C), which was updated according to Eq. (7.59).

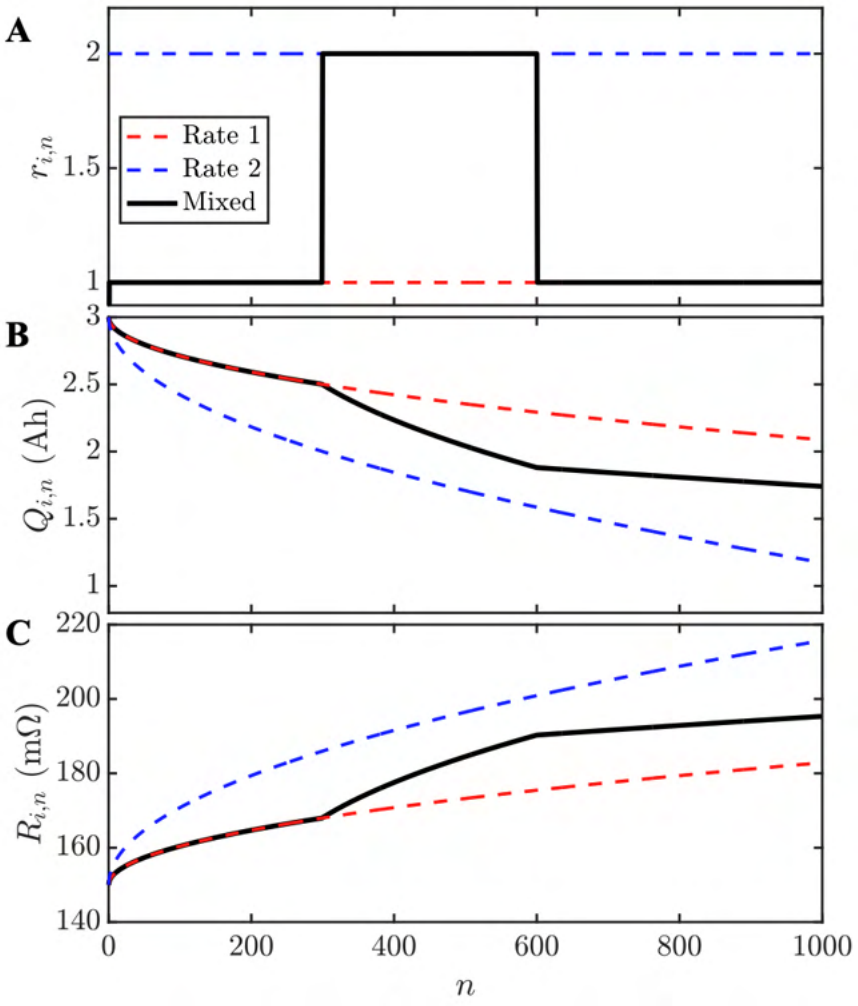

Figure 7.10: Demonstration of the incremental capacity loss update model which supports cycle-by-cycle updates to the reaction rate r. (A) Cycle-dependent reaction rate assumptions for each degradation trajectory. (B) Capacity fade over cycles. (C) Resistance growth over cycles.

7.4.2 Coupling Reaction Rates to Imbalance Dynamics

The incremental capacity loss model derived here can be used to study the effect of changing use conditions, irrespective of whether the change is due to external factors (e.g. customer use patterns) or internal factors (e.g. parallel-connected battery dynamics). In both cases, the effect of changing use conditions can be represented by treating the current and SOC dynamics as modifications to $r_i(t)$:

$$r_{i,n}(t) = g(z_{i,n}(t), I_{i,n}(t)), \tag{7.61}$$

where $z_{i,n}(t)$ and $I_{i,n}(t)$ are the SOC and current for cell i and cycle n. Since the imbalance values will generally change over life, $r_{i,n}(t)$ will take on different values over each cycle. In this manner, the incremental degradation in each cell at each cycle, $\delta L_{i,n}$, becomes coupled with the intra-cycle dynamics of that cell.

To resolve $r_{i,n}(t)$, expressions for $z_{i,n}(t)$ and $I_{i,n}(t)$ are needed. Fortunately, we have already developed analytical expressions for $z_{i,n}(t)$ and $I_{i,n}(t)$ in Section 7.3. We next explore model simplifications to $g(z_{i,n}(t), I_{i,n}(t))$ and what these simplifications imply about degradation convergence.

7.5 Degradation Convergence Analysis

This section highlights how the intra-cycle dynamics developed in Section 7.3 can be combined with the inter-cycle capacity loss formulation developed in Section 7.4 to analyze and simulate whether capacity degradation converges or diverges over the course of many cycles.

We will focus specifically on the case of a fresh cell connected in parallel with an aged cell. Taking Cell 1 to be the fresh cell and Cell 2 to be the aged cell, we thus impose the constraints that $Q_2 < Q_1$ (the aged cell has lost capacity) and $R_2 > R_1$ (the aged cell has increased resistance). Fig. 7.4 showed an example of one such system.

7.5.1 Current Imbalance Can Lead to Degradation Convergence

We now describe a set of assumptions under which current imbalance can lead to degradation convergence. Suppose that, for each cell i, the incremental capacity lost over a single cycle is proportional to the maximum current experienced during that cycle. This assumption approximates the lithium consumption process during SEI growth or lithium plating, both of which are accelerated at higher current densities due to Butler-Volmer kinetics [76, 56, 27].

Using the incremental capacity loss model developed in Section 7.4.1, we can represent

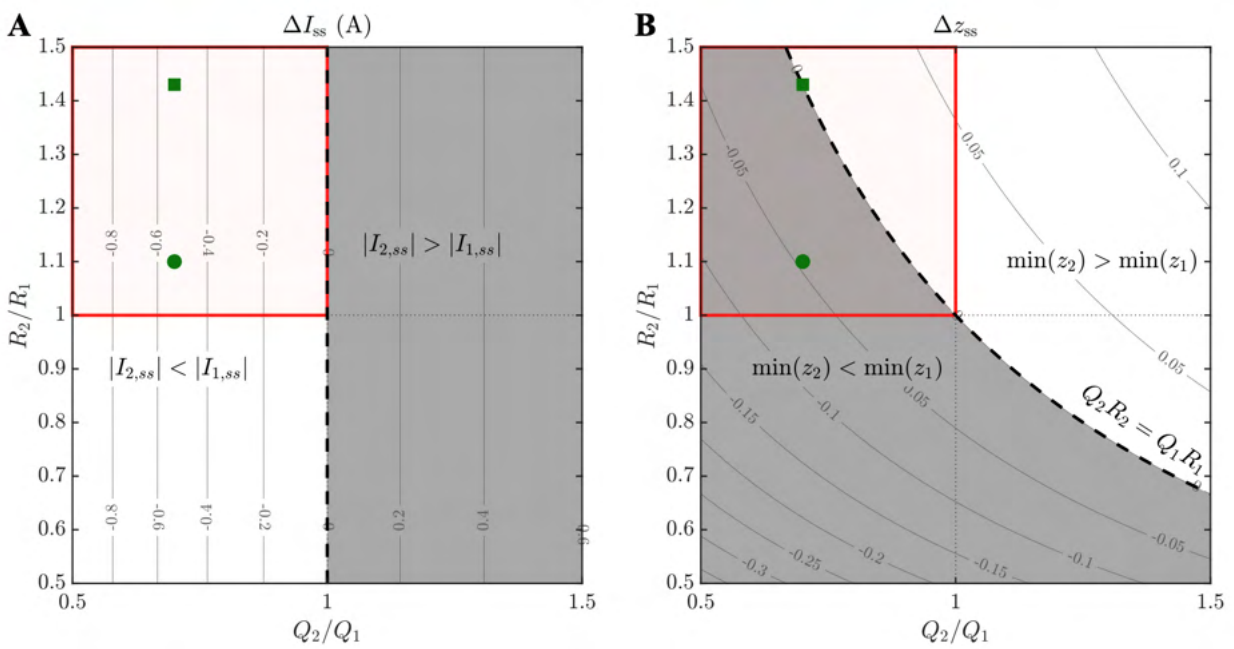

Figure 7.11: Maps of current and SOC imbalances at steady-state as a function of capacity and resistance variability. (A) Steady-state current imbalance ΔI_{ss} during CC charge or discharge. (B) Steady-state SOC imbalance Δz_{ss} during discharge. Red boxes show an aged cell (Cell 2) connected with a fresh cell (Cell 1), i.e. $Q_2 < Q_1$ and $R_2 > R_1$. Green markers correspond to the conditions shown in Figs. 7.4 and 7.6. White regions indicate scenarios in which degradation is expected to converge (see Section 7.5). Gray regions indicate scenarios in which degradation is expected to diverge. In Panel A, the convergence behavior is assumed to be driven by current magnitude differences (see Sections 7.5.1, 7.5.2). In Panel B, the convergence/divergence behavior is assumed to be driven by differences in depths of discharge or cell utilization (see Section 7.5.3).

the effect of current on the degradation rate as a modification to the reaction rate parameter:

$$r_{i,n} = \gamma_1 \cdot I_{ss,i,n}, \tag{7.62}$$

where γ_1 is a proportionality constant and $I_{ss,i,n}$ is the steady-state current for cell i and at cycle n. Here, the steady-state current provides a measure of the maximum current imbalance over the course of a cycle, assuming affine OCV-R model dynamics (Section 7.3.3.4). Also note that (7.62) represents a simplification of the function g from (7.61) in which the only factor that influences the reaction rate is the steady-state current.

Degradation convergence requires that the aged cell (Cell 2) degrade more slowly than the fresh cell (Cell 1), or:

$$r_{2,n} < r_{1,n}. \tag{7.63}$$

Expanding this inequality using (7.62) yields:

$$\Delta I_{ss,n} < 0, \tag{7.64}$$

where $\Delta I_{ss,n}$ is the steady-state current imbalance at cycle n as previously defined in (7.29). Substituting (7.29) into this expression yields simply $Q_2 < Q_1$ which is satisfied by definition. The capacity degradation rate for the aged cell will therefore always be lower than that of the fresh cell. The capacity difference between the aged cell and the fresh cell will thus converge over the course of repeated cycles.

Fig. 7.11A further visualizes why, in the affine OCV-R system, current imbalance 'favors' the aged cell while 'penalizing' the fresh cell. The red box highlights the region corresponding to when Cell 1 is a fresh cell and Cell 2 is an aged cell. The plot shows that the aged cell always experiences less current compared to the fresh cell at steady-state. This result is consistent with the condition simulated in Fig. 7.4, highlighted as a green circle.

We note that Song et al. [280] provided a similar analytical proof which also assumed affine OCV-R dynamics and a similar capacity loss model. This work showed that, with non-concave capacity degradation trajectories ($p < 1$), cell-to-cell variability in capacity decreases over age, i.e. degradation trajectories converge.

7.5.2 Simulating Degradation Convergence Due to Current Imbalance

Degradation convergence induced by current imbalance can also be numerically demonstrated by simulating both the inter and intra-cycle dynamics according to the framework originally proposed in Fig. 7.2. The simulation was initialized using the same cell parameters presented in Fig. 7.4. For each cycle, the steady-state current value was calculated based on Eqs. (7.15) and (7.16). The reaction rate constant for each cell was then updated according to (7.62). The incremental capacity loss was finally updated according to (7.58). The process was repeated until the lowest cell capacity reached zero. The procedure used in the simulation is summarized in Algorithm 1. Control cells were additionally simulated. For these cells, the current used to update the reaction rate was set to $I/2$ for all cycles.

Fig. 7.12 shows the simulation results under three values of p, representing three distinct degradation trajectories: self-limiting (A), linear (B), and accelerating (C). In all three cases, the aged cell (Cell 2), with lower initial capacity and higher initial resistance, lost capacity more slowly than the fresh cell (Cell 1). In fact, both cells reached zero capacity at exactly the same cycle number, irrespective of the value of p. The steady-state current values for both cells remained constant since the ratios Q_1/Q_{tot} and Q_2/Q_{tot} remained invariant even as

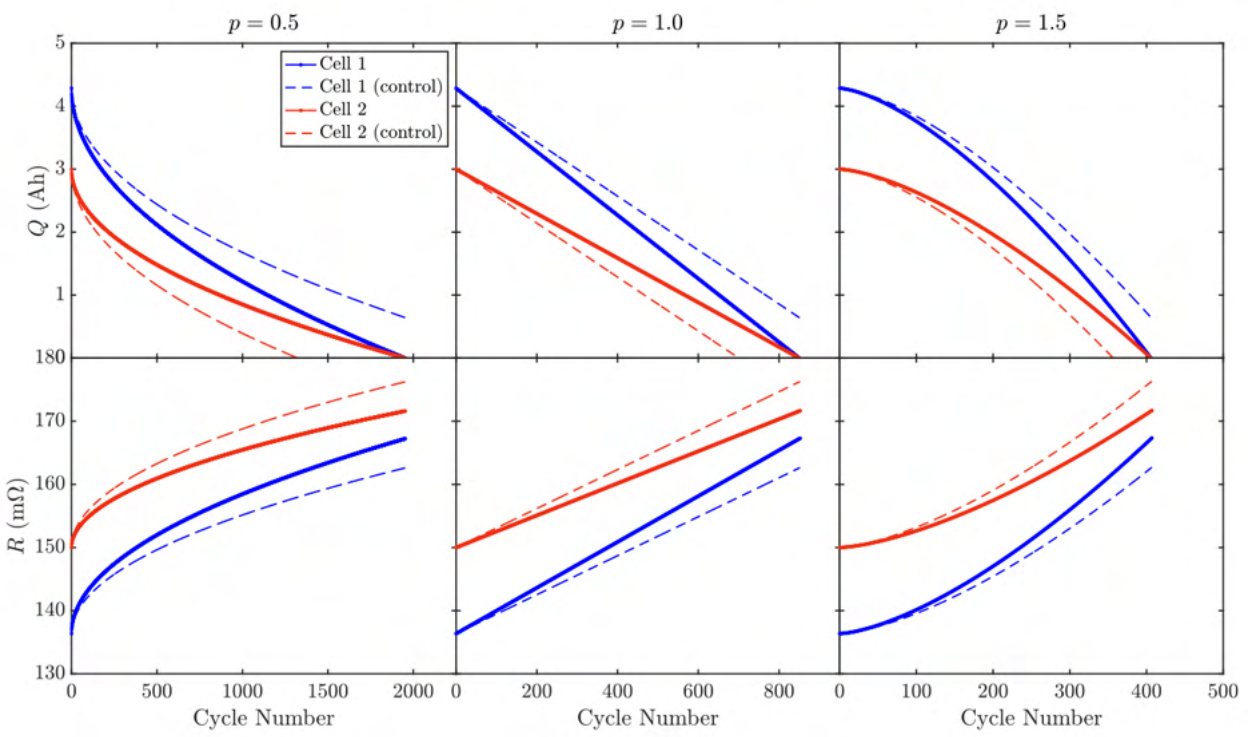

Figure 7.12: Simulation of degradation convergence due to current imbalance. This result uses the incremental capacity degradation model to represent inter-cycle dynamics (Section 7.4) and the affine OCV-R model to represent the intra-cycle dynamics (Section 7.3.3). In these simulations, steady-state current values (Eq. 7.62) are assumed to drive cell capacity fade and resistance growth. Subpanels show simulations of capacity fade performed using different values of the SEI exponential growth factor p. A: self-limiting, B: linear, C: accelerating. (D-F) show the corresponding resistance growth simulations.

Q_1 and Q_2 individually decreased. The current imbalance dynamics thus remained invariant over all cycles, with Cell 2 always seeing less current at steady-state than Cell 1.

Panels (D-F) show the corresponding resistance growth predictions. Resistance growth was calculated according to (7.60) with (λ_1, λ_2) set to $(2 \times 10^{-6}, 0)$ for demonstration purposes. The results show that resistance growth trajectories also converge for all tested values of p.

7.5.3 Degradation Convergence is not Guaranteed

While the previous section showed that current imbalance can lead to degradation convergence, we now highlight another set of degradation assumptions that do not guarantee degradation convergence.

Here, we assume that the cell degradation rate increases as the minimum SOC experienced

Algorithm 1 Successive update scheme for two cells

Require: $Q_{1,0}, Q_{2,0}, R_{1,0}, R_{2,0}$ ▷ Initial Conditions
  $L_{1,0} \leftarrow 0$
  $L_{2,0} \leftarrow 0$
  $n \leftarrow 1$
  while $(Q_{i,0} > Q_{\min}) \forall i \in \{1, 2\}$ **do**
    for each $i \in \{1, 2\}$ **do** ▷ Intra-Cycle Updates
      $I_{i,n}(t) \leftarrow f_1(t, Q_{1,n-1}, Q_{2,n-1}, R_{1,n-1}, R_{2,n-1})$
      $z_{i,n}(t) \leftarrow f_2(t, Q_{1,n-1}, Q_{2,n-1}, R_{1,n-1}, R_{2,n-1})$
    end for
    for each $i \in \{1, 2\}$ **do** ▷ Inter-Cycle Updates
      $r_{i,n}(t) \leftarrow g(I_{i,n}(t), z_{i,n}(t))$
      $\delta L_{i,n} \leftarrow \left(\int_{t_{0,n}}^{t_{f,n}} r_{i,n}(\tau)^{1/p} d\tau + L_{i,n-1}^{1/p} \right)^p - L_{i,n-1}$
      $Q_{i,n} \leftarrow Q_{i,n-1} - \delta L_{i,n}$
      $R_{i,n} \leftarrow R_{i,n-1} + \lambda_1 \delta L_{i,n} + \lambda_2$
    end for
    $n \leftarrow n + 1$
  end while

by the cell at the end of each discharge is decreased. This assumption could be justified considering that a lower minimum SOC is equivalent to a higher depth of discharge (DOD). Higher DODs may amplify cathode particle cracking mechanisms, leading to higher capacity fade, higher resistance growth, or both [299, 300, 178]. Note that, at the end of discharge, SOC re-balancing does not typically occur under practical applications which generally lack CV holds at the end of discharge cycles. It is thus possible that some cells in a parallel-connected group end discharge at lower SOCs compared to their neighbors. Under these assumptions, the reaction rate from Eq. 7.62 could take the following form:

$$r_{i,n} = \frac{\gamma_2}{\min(z_{i,n}) + 1}, \tag{7.65}$$

where $\gamma_2 > 0$ is another proportionality constant and $\min(z_{i,n})$ is the minimum SOC experienced by cell i at the end of discharge and for the nth cycle. The reaction rate here reaches a maximum value when $z_{i,n}$ approaches zero.

Figure 7.11B shows how the steady-state SOC imbalance $\Delta z_{ss} \triangleq z_2 - z_1$ (Eq. 7.27) can be used to predict which cell will end at a lower SOC. When $\Delta z_{ss} > 0$, Cell 2 (the aged cell) will end discharge with a higher SOC (i.e. lower DOD) and be degraded more slowly, leading to convergent degradation. We can thus interpret $\Delta z_{ss} > 0$ as the necessary condition for degradation convergence. However, according to Eq. (7.27), $\Delta z_{ss} > 0$ is only guaranteed if $Q_2 R_2 > Q_1 R_1$. Graphically, this condition corresponds to the white region in Figure 7.11B.

Recalling that the red box represents scenarios in which an aged cell (Cell 2) is connected with a fresh cell (Cell 1), we realize that degradation convergence is no longer guaranteed for all of these cases of interest. The green circle highlights one such case, wherein the aged cell ends discharge at a lower SOC (see Fig. 7.4), suggesting a higher DOD utilization and thus divergent degradation.

This simple example highlights that different degradation assumptions lead to different conclusions about the convergence and divergence of degradation trajectories. While the result from Sections 7.5.1 and 7.5.2 suggested degradation convergence, these results were obtained assuming that current imbalance was the sole driver for cell degradation. When other factors such as SOC imbalance are added to the mix, results may differ.

7.6 Experimental Verification

The utility of the modeling and analysis framework we propose in this work ultimately depends on its ability to predict real-world data. This section thus focuses on comparing model-based predictions to measured lab data. Section 7.6.1 outlines the experimental methods used to generate the lab data. Section 7.6.2 compares modeled versus measured intra-cycle dynamics. Section 7.6.3 discusses measured degradation convergence outcomes.

7.6.1 Methods

Two 2.5Ah lithium-ion pouch cells were built on a prototype battery manufacturing line. The cells both used graphite as the anode and NMC as the cathode. Each cell was individually pre-conditioned to different capacities and resistances by aging them via a 1C charge, 1C discharge cycling test protocol. Voltage limits during the cycling test were set to 3.0V to 4.2V. See Weng et al. [7, 6] for more details on the cell build process and experimental setup for the cycling tests.

Cell capacities and resistances were measured after pre-conditioning. Capacities were measured using a C/20 discharge from 4.2V to 3.0V. Resistances were calculated by taking the voltage difference between a C/20 charge curve and C/20 discharge curve, dividing this voltage difference by two times the input current, and averaging across all SOCs. The cell properties were measured to be $(Q_1, R_1) = (2.11\text{Ah}, 201\text{m}\Omega)$, $(Q_2, R_2) = (1.83\text{Ah}, 250\text{m}\Omega)$.

After pre-conditioning, cells were connected in a parallel arrangement and cycled using a commercial cycler (Arbin BT2000), according to Fig. 7.13. The cycling profile consisted of 1C CCCV charge and 1C CC discharge between 3.0V and 4.2V. The branch current for Cell 2 was measured using a commercial Hall effect sensor (Allegro ACS70331) and logged

using LabVIEW. The branch current for Cell 1 was calculated from the difference between the total input current and the branch current for Cell 2. Resistances of the wires and the Hall effect sensor were estimated to be less than 5mΩ in each branch and were thus ignored.

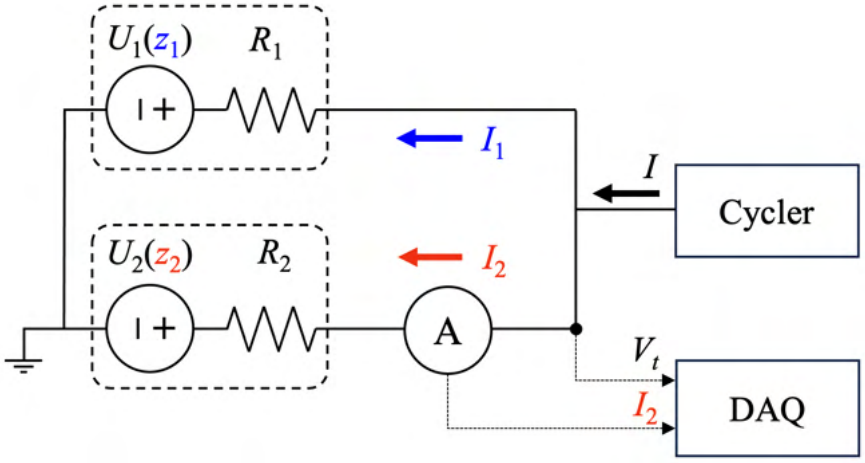

Figure 7.13: Experimental setup for measuring branch currents in two parallel-connected cells.

The parallel-connected system was cycled for 240 equivalent full cycles, then stopped. The system was then charged and discharged at different rates, including C/4 and C/10, to characterize the intra-cycle dynamics for different input currents. Finally, the cells were disconnected from the parallel connection to re-measure individual cell capacities and resistances using the same process described above.

7.6.2 Intra-Cycle Dynamics

To compare the model-predicted intra-cycle dynamics against experiment, the model was initialized using measured values for (Q_1, R_1, Q_2, R_2). The nonlinear OCV functions U_1 and U_2 were parameterized by taking the average of the C/20 charge and C/20 discharge voltage curves. The SOC for each cell was initialized to match the measured terminal voltage preceding the charge cycle (ca. 0.3%). The model was simulated using the method described in Section 7.3.4.1.

Fig. 7.14 compares the modeled versus measured intra-cycle dynamics at two different C-rates: C/4 (Panels A,C) and C/10 (Panels B,D). At C/4, the model-predicted current imbalances and terminal voltages show good agreement with the data. The model captured inflections in the current imbalance and correctly predicted the durations of both the CC and CV phases. This result is surprising considering the simplicity of the model which omits RC circuit elements and assumes a constant value for resistance. At C/10, the model-

predicted current imbalances qualitatively match the experimental results, though some model mismatches are evident. Specifically, during the CC charge, the model under-predicted the magnitude of the current imbalance, and during the CC discharge, the model over-predicted the current imbalance at mid-SOCs. The model also under-predicted the measured terminal voltage on both charge and discharge. The cause of the model mismatches at low currents is unclear and suggests the need for future investigations.

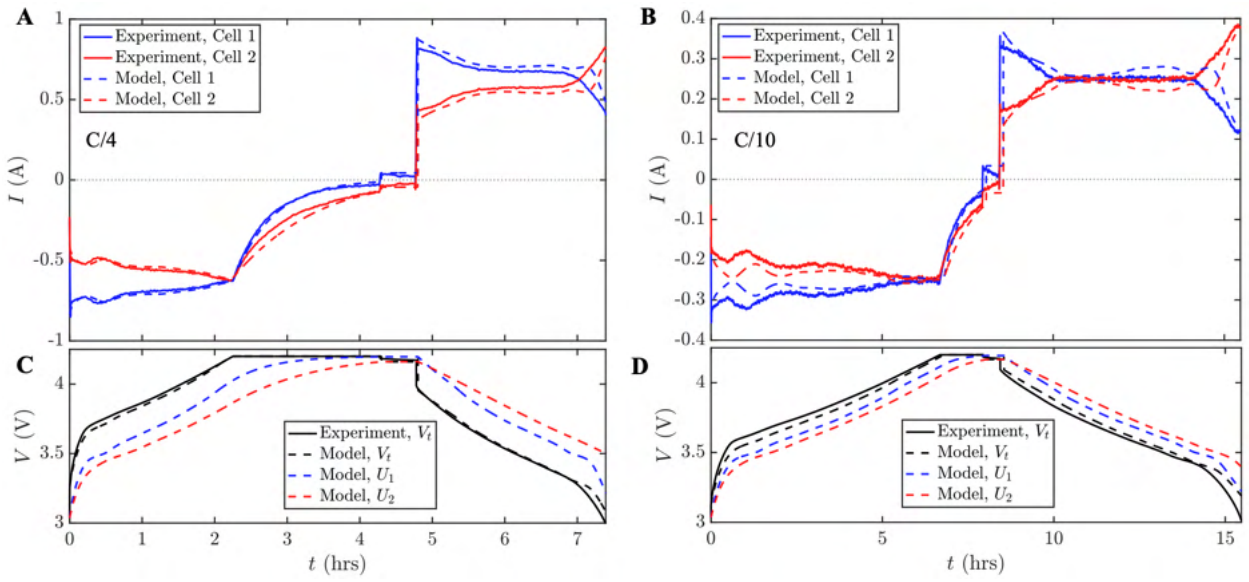

Figure 7.14: Model versus experimental comparison of intra-cycle dynamics for two cells with mismatched capacities and resistances. (Q_1, R_1) = (1.83Ah, 549mΩ) and (Q_2, R_2) = (1.93Ah, 277mΩ). The experimental profile consists of CCCV charging, resting for 30 minutes, followed by CC discharging. (A) C/4 charge and discharge. (B) C/10 charge and discharge. (C,D) The corresponding voltage profiles. The CV hold cut-off condition is set to C/30 for all cases.

7.6.3 Inter-Cycle Dynamics

Table 7.2 compares the measured cell capacities and resistances before and after the parallel cycling test. The measured results suggest that the capacities are converging, with Q_2/Q_1 increasing from 0.938 before cycling to 0.948 after cycling. However, the resistances are not converging but diverging: R_2/R_1 has increased from 1.59 to 1.99. This result thus highlights a scenario in which initial variability in cell properties has led to a convergence in the individual cell capacities but divergence in the individual cell resistances. Degradation convergence is thus not a universal guarantee and depends on the degradation metric (capacity or resistance). Degradation convergence is also likely strongly influenced by the

underlying degradation assumptions. For example, Section 7.5.3 explored how a degradation assumption based solely on current imbalance led to convergent degradation, but a degradation assumption based solely on SOC imbalance could lead to either convergent or divergent degradation depending on the values of the cell capacities and resistances.

Table 7.2: Comparison of experimentally-measured cell capacities and resistances before and after parallel cycling.

	Before Cycling	After Cycling
Q_2	1.98 Ah	1.83 Ah
Q_1	2.11 Ah	1.93 Ah
Q_2/Q_1	0.938	0.948
R_2	321 mΩ	550 mΩ
R_1	201 mΩ	277 mΩ
R_2/R_1	1.59	1.99

7.7 Conclusion

This chapter proposed a framework to model coupled degradation phenomena in parallel-connected battery systems. We first developed an incremental capacity loss scheme based on SEI growth dynamics which was used to compute the cycle-to-cycle (i.e. inter-cycle) evolution of the capacity loss and resistance growth of individual cells connected in parallel. We then developed a set of closed-form, analytical solutions to the affine OCV-R model which described the dynamics of current and SOC imbalance within a single cycle (i.e. intra-cycle). The two components were coupled by an SEI reaction rate term which was made a function of the intra-cycle dynamical variables such as the current and SOC for each individual cell.

The degradation analysis demonstrated in this work assumed a single degradation mode, SEI growth. With this assumption, we demonstrated that current imbalance can lead to convergent degradation trajectories. However, we further presented experimental evidence that degradation convergence may not be guaranteed, and that convergent capacity fade trajectories does not imply convergent resistance growth trajectories. Understanding this phenomenon will require the inclusion of additional degradation mechanisms.

The modeling and analysis framework developed here can be extended to further study general degradation phenomena in parallel-connected battery systems. Such developments remain necessary to fully answer the unavoidable yet essential questions in battery cell manu-

facturing ("how much manufacturing variability is too much?") and pack re-purposing ("how much dissimilarity can be tolerated when repairing old packs using fresher counterparts?").

CHAPTER 8

Conclusions and Future Work

8.1 Summary

This thesis stemmed from three core beliefs:

1. that the world needs to transition to sustainable energy quickly,
2. that battery manufacturing is at the core of this transition, and that
3. battery manufacturing processes, especially the battery formation process, play an outsize role in the cost, performance, and lifetime of batteries, but are far from being optimized.

This thesis clarifies how battery manufacturing, specifically the formation process, can be improved using better models and diagnostic techniques.

Part I: "Models" presented and explored a model-based framework for understanding and controlling the industrial battery formation process. Whereas existing models from literature focused exclusively on the SEI film growth process, our model puts the SEI growth process in the context of a full cell, mirroring the reality of the industrial battery formation process.

Chapter 3 introduced a dynamical model of formation that predicted key performance metrics including first cycle efficiency, cell thickness expansion, and features in the $\mathrm{d}Q/\mathrm{d}V$ curve. The model led to several crucial insights about the dynamics of SEI formation. First, the SEI growth process transitions from being reaction-limited to being diffusion-limited during the very first charge cycle and stays diffusion-limited throughout the remainder of the cell's life. Therefore, SEI diffusivity, rather than kinetic parameters such as reaction potentials and reaction rate constants, is a better indicator for SEI passivation. Second, SEI formation does not begin until an external current is applied to the cell, implying that

lithium loss accounting only needs to begin at the start of the first charge cycle as opposed to when the electrolyte is inserted into the cell. Third, a boosted SEI growth mechanism, i.e. due to SEI cracking, is necessary to reconcile the experimentally observed trends in cell thickness expansion during and after formation. SEI boosting is thus a fundamental process of formation that cannot be ignored.

Chapter 4 highlighted the potential for the formation model to advance five distinct applications relating to formation protocol design, manufacturing process control, and lifetime prediction. First, the formation model was used to predict the emergent behavior of a faster formation protocol including the first cycle charge dynamics, the cell thickness expansion, and the resulting SEI passivation. Second, we used the formation model as a lifetime simulator and showed that faster formation protocols are possible without compromising battery lifetime. The model provided a mechanistic explanation for why this is the case: the faster formation protocol was predicted to form a more passivating SEI which decreased the rate of further side reactions. The model also provided a novel insight into how a faster formation protocol can play a role in delaying a "knee" in the capacity fade trajectory due to electrolyte additive consumption. Third, the formation model was reformulated from a control-oriented perspective, including the introduction of block diagram and state-space representations of the system dynamics. These model reformulations will aid in the development of control-oriented approaches for formation protocol optimization. Fourth, we discussed how the formation model can help improve the identifiability of degradation model parameters. Finally, we showed how the formation model can be used to clarify the physical connection between constructed diagnostic features such as the lithium consumed during formation and the low-SOC resistance.

Part II: "Data" turned to a data-driven exploration of current-voltage signals collected during formation or immediately after formation. We developed techniques to analyze this data to yield features with electrochemical significance. We then explored applications of these features toward battery lifetime prediction and manufacturing process control.

Chapter 5 explored applications of the differential voltage analysis (DVA) and the hybrid pulse power characterization (HPPC) techniques for quantifying differences in initial cell state variables, including electrode capacities and SOC-dependent cell resistances. As part of this work, we expanded the DVA method by defining additional features relevant to manufacturing diagnostics including the capacity of lithium consumed during formation and the practical N:P ratio. We also highlighted the challenges with reproducible data collection hindering the broader adoption of the presented methods in a manufacturing setting. Finally, we showed that, if the challenges with data reproducibility can be overcome, then the DVA method can be a cost-effective, non-destructive, and scalable method for quantifying

electrode-level parameters without the need for cell dissections.

Chapter 6 showed that features measured at the beginning of life immediately after formation can be used to predict cell lifetime without requiring cycle life testing, thus demonstrating the promise of using manufacturing data to accelerate battery lifetime evaluation. Our work improves upon prior results in the field which require data from cycle life tests, usually 100 cycles to achieve a similar level of prediction accuracy. Leveraging the formation model, we proposed a mechanistic reason for why our feature selected for lifetime prediction, the low-SOC resistance, can act as a proxy for the lithium consumed during formation.

Part III: "Variability" started by asking an essential question: "how much manufacturing variability is too much?" We explored an answer to this question in **Chapter 7** which focused on modeling the collective dynamics of parallel-connected battery cells. We first built analytical tools to understand the intra-cycle dynamics of dissimilar cells connected in parallel. We combined the understanding of intra-cycle dynamics with a simple model of inter-cycle degradation based on SEI growth to demonstrate that the degradation trajectories of individual cells connected in parallel can converge. However, we also emphasized that the degradation trajectories may not converge under a different set of degradation assumptions. The work from this chapter highlights that not all variability is bad news, but a lot more work is needed to ultimately find the answer to the original question of how much variability is too much.

8.2 Future Work

8.2.1 Formation Modeling

Chapter 4 serves as a skeleton for eventual applications of the formation model we developed in this thesis. Each of these applications warrants further exploration. We call out a few focus areas for future work.

The usage of cell thickness expansion appeared to be a critical step in the development and parameterization of the formation model. However, how critical was this dataset, really? A rigorous answer to this question can be obtained through an *observability analyis*. Through this analysis technique, we can quantify the extent to which the expansion data helped to improve parameterization of certain model parameters such as D_{sei}.

Next, the usage of the formation model as a lifetime simulator is only beginning. A logical next step is to revisit the model parameterization approach to include cycle life data. While our work showed that there exists a single set of parameters that fit both formation cycling and formation aging, we did not demonstrate that these parameters could additionally fit

the cycle life test data that comes after. As a result, we could not directly compare our simulated cycle life results against experimental data.

Temperature-dependent factors can also be introduced into the model to understand the role of temperature in SEI film growth passivation. Temperature is another major control lever for formation protocol design so including this model consideration will help to improve the applicability of the model towards real-world use cases.

The formation process extends beyond formation cycling and aging. It also includes a pre-charge step, a de-gassing step, and electrolyte wetting. Both the pre-charge and de-gassing steps can be easily incorporated into the formation model. For pre-charging, the relevant electrochemistry we seek to capture is copper dissolution. For de-gassing the relevant electrochemistry is gas generation. Finally, to capture the electrolyte wetting step, we require a mechanical model of the wetting process. While modeling the wetting process will be challenging, it may ultimately be necessary to develop a full "digital twin" of the battery formation process.

8.2.2 Lifetime Prediction

Chapter 6 demonstrated the possibility of battery lifetime prediction without cycle life data. Yet, a major shortcoming of the work was that the dataset was limited to a single chemistry system (NMC/graphite) and only two formation protocols were tested. A natural next step is thus to repeat the experiment on a new set of cells and even more formation protocols.

Another confounding factor of the lifetime prediction study was that the diagnostic features seemed to predict cycle life at 45°C better than cycle life at room temperature. We speculated that the 45°C provided stronger correlations because of the improved temperature control. In general, more studies on the temperature effect on lifetime prediction will be needed.

Next, while we also demonstrated that some diagnostic features calculated from DVA and the formation protocol itself also correlated to cycle life, we could not come up with physical explanations for why this is. Lacking a physical understanding, these results were not included as part of the publication tied to this work. However, with the development of the formation model, it may be time to revisit this dataset through the lens of the formation model to see if additional insights can be gleaned.

8.2.3 Differential Voltage Analysis

A major obstacle preventing more widespread adoption of the DVA method presented in Chapter 5 is the difficulties with reproducible implementation and interpretation of model

outputs. These difficulties stem from a lack of literature guidance on a standard, rigorous method to implement the fitting model and an absence of understanding of how sensitive the model outputs are to small differences in input datasets, including both full cell and half cell data. While Chapter 5 set out to provide this guidance is ultimately needed.

Several avenues may be taken to further improve the reproducibility of the electrochemical features derived from the differential voltage analysis method. First, model input sensitivities need to be better understood. This work introduced several input sensitivity considerations including C-rate and current direction (charge versus discharge). However, a discussion on sensitivity to temperature was not covered by this work. Moreover, a quantitative assessment of the input-output sensitivities has not yet been completed. A logical next step is thus to quantify model output differences due to these differences in model inputs.

Another important consideration involves understanding the optimizer's ability to find the optimal solution θ_{opt}. Reproducibility requires that there exists a global minimum value of the error function defined by Equation 5.12 and that the optimizer can converge to this value. However, in general, neither condition is guaranteed since the objective function is, in general, non-convex. The solution uniqueness for the positive electrode parameters $\tilde{Q}_p$ and y_0 may be especially challenging for NMC systems which are relatively featureless (Figure 5.2). Some past efforts have been made to understand how model output parameter uncertainty increased as the data collection voltage window decreased [301]. These studies should be expanded. A better understanding here will enable practitioners to quantify how much of the variability in model-predicted outputs, such as those shown in Figure 5.9, are due to true manufacturing variability versus model uncertainty.

8.2.4 Variability Propagation

The modeling framework derived in Chapter 7 lends itself to mathematical analysis, enabling more rigorous treatments of degradation convergence or divergence for future studies. We envision that this framework can be expanded in the future to support analyzing parallel-connected systems in a more generalized context. This section highlights several areas for future exploration:

a. Arbitrary number of parallel-connected cells. This work presented only two cells connected parallel to highlight the effect of initial cell variability on an elementary system. Since only two cells were considered, the presented results may not generalize to the case of $n > 2$ cells connected in parallel. However, our analysis can be extended to the general case of n-cells by leveraging ideas presented by Song et al. [280, 281] and Drummond et al. [287] to resolve the algebraic constraint for the branch currents and describing the solutions

in state-space form.

b. Thermal analysis. Considerations for thermal imbalances (i.e. due to battery pack design or differences in individual cell heating rates) were also omitted in this work but will be important to consider for future work. To understand thermal effects, our proposed modeling approach can be combined with a cell thermal model such as those presented by Zhang et al., [286], Song et al. [280, 281], Reniers et al. [110] and Hosseinzadeh et al. [302]. Thermal model predictions should also be compared against recent experimental work including those from Fill et al. [288] and Paarmann et al. [283].

b. Interconnect resistances. Interconnect resistances also play an important role in determining current imbalances in real battery packs. This work ignored interconnect resistances to simplify the analysis. Other authors such as Reniers et al. [110] and Hosseinzadeh et al. [302] did consider interconnect resistances in their work. Ideas presented in these works can be incorporated in the future to understand the relative contribution of cell versus non-cell components on the overall system current imbalance.

c. Degradation mechanisms. Our experimental work showed that degradation convergence is not guaranteed in parallel-connected systems. Specifically, while capacity fade trajectories appeared to be converging, resistance growth trajectories appeared to be diverging. The divergent resistance growth trajectory was not predicted by our modeling framework which assumed a single degradation mechanism: SEI growth. In reality, degradation pathways in real lithium-ion devices are multi-faceted [296, 303, 304, 305, 306, 307], requiring more sophisticated degradation models [83, 81, 308] and parameterization methods [171, 82] to fully capture. Future work should thus explore how additional degradation assumptions could influence the convergence behavior in parallel-connected systems using a combination of simulation-based and analytical approaches.

APPENDIX A

Battery Passports for Promoting Electric Vehicle Resale and Repurposing

This chapter is based on the following published works:

- Andrew Weng, Eric Dufek, and Anna Stefanopoulou. *Battery passports for promoting electric vehicle resale and repurposing.* Joule, 7(5):837–842, May 2023

A.1 Introduction

Starting in 2026, most batteries sold in the European Union will require a battery passport. This initiative is part of a broader legislative framework, led by the European Commission, to improve sustainable battery materials sourcing practices and enable a circular economy. All batteries having a capacity of greater than 2 kilowatt-hours will be covered under the legislation, effectively encompassing all electric vehicle (EV) batteries and stationary grid storage batteries [309, 310].

At its core, a battery passport defines a minimum, standard set of information that must be reported for every battery made and sold (see Figure A.1). Legislative actions have so far focused on labeling standards enabling raw material traceability and recycling, which has received ongoing support from the European Council and Parliament [311]. However, work remains to finalize the electrochemical performance and durability minimum reporting requirements by 2024, which has been challenging since performance and durability are subject to many different interpretations.

This chapter advocates for including a key electrochemical performance indicator as part of the battery passport minimum data reporting requirements: the remaining useful life (RUL). The RUL can be broadly defined as the years, miles, or energy throughput (in kWh) until the battery state of health (SOH) falls below some target minimum:

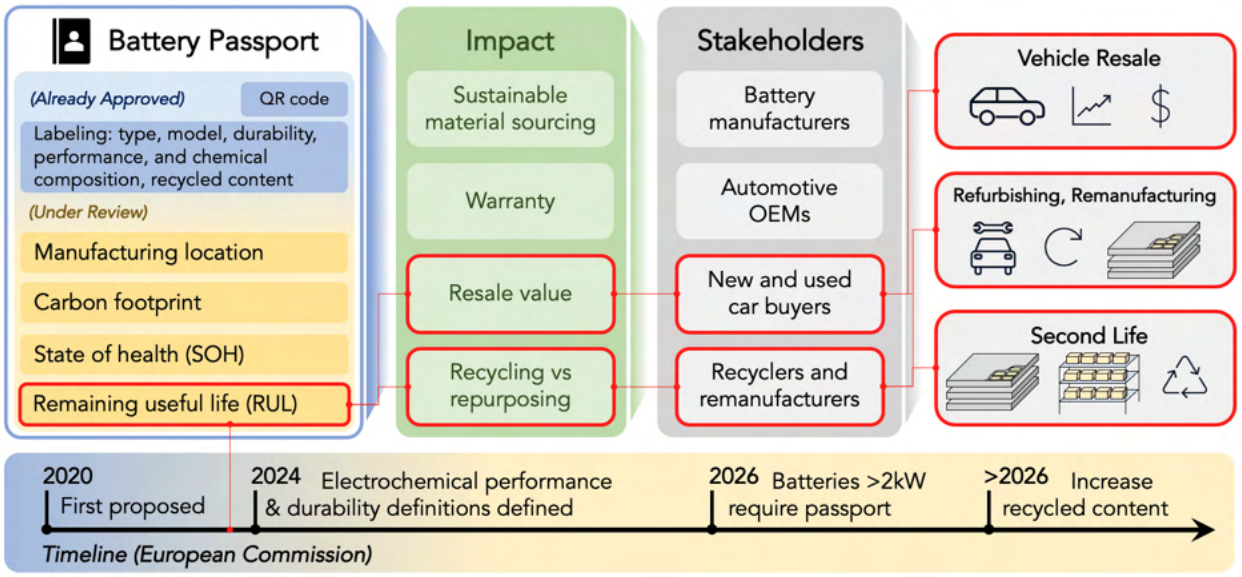

Figure A.1: Overview of the digital battery passport concept focusing on applications of the (remaining useful life (RUL)) metric for electric vehicle resale, recycling, and repurposing.

$$\text{RUL} = (\text{years, miles, or kWh}) \text{ until SOH} < \text{SOH}_{\text{min}}. \tag{A.1}$$

Unlike SOH which captures the present state of a battery, the RUL is a prediction of the future state of the battery. The RUL may rely on measurements of SOH to provide a forecast of future battery performance. The RUL enables used car buyers, who also earn the least income on average [312], to make informed purchasing decisions at the point of resale. The RUL also enables repurposers to decide whether it is more economical to recycle a battery or to repurpose it for second-life applications. The RUL is thus a metric at the core of the battery passport's mission to promote battery materials sustainability and equity.

Existing policy discussions concerning battery durability mainly focus on primary use, not secondary use. For example, both the United Nations Global Technical Regulation (GTR) [313] and the California Air Resources Board (CARB) [314] have framed EV durability from the perspective of an 8-year warranty, with no specific provisions for quantifying RUL beyond the first 8 years. Yet, since EVs are expected to be driven for 15 to 20 years and for over 300,000 kilometers [315], they will likely be resold to used car buyers at least once. Under the existing policy language, a battery that fails immediately after 8 years will still technically satisfy the 8-year warranty requirement and still be considered "durable." The battery passport directive has an opportunity to address the longevity of batteries beyond 8 years by carefully considering how RUL can be defined and reported as part of the electrochemical and performance indicators to be finalized by 2024.

The importance of RUL has been recognized by the European Commission. A key element of the European legislation is to establish requirements for longevity and performance management. Article 14 specifically mentions that a battery management system (BMS) must contain "data needed to determine the state of health and expected lifetime of batteries." Furthermore, access to the data must be provided to "evaluat[e] the residual value of the battery and capability for further use" and "facilitate[e] the reuse, repurposing or remanufacturing of the battery" [316]. In a parallel effort, CARB has also recently implemented state-level legislation requiring the battery SOH to be reported and accurate to within 5 percentage points by 2026 [317]. This SOH accuracy requirement, while not directly addressing RUL, acknowledges that SOH monitoring accuracy is necessary for quantifying battery durability.

This chapter highlights the reality that a battery's SOH is not the same as its RUL, and that more discussion around RUL is needed to enable battery reuse and repurposing. We discuss three pitfalls of obtaining a reliable RUL estimate, and, in doing so, highlight the reality that RUL accuracy needs to be carefully considered for RUL reporting to be useful. First, we argue that a single-point verification test to obtain SOH cannot, by itself, be used to predict the RUL. Second, we show that 5% SOH accuracy is not enough to make confident RUL predictions. Lastly, we highlight the need for more physics-based approaches to estimating RUL, especially for repurposing applications where the use case changes.

A.2 On Single-Point SOH Measurements

Here we argue that **single-point SOH measurements cannot be used to predict RUL.** Let us start with a thought exercise. Suppose that on-board SOH estimates are unavailable, inaccurate, or both. Then, to determine SOH, a battery pack owner is forced to conduct an external capacity check test, i.e. at a hypothetical battery testing station. The measured SOH can then be defined as:

$$\mathrm{SOH}_{\mathrm{measured}} = \frac{\mathrm{UBE}_{\mathrm{measured}}}{\mathrm{UBE}_{\mathrm{certified}}} \times 100\%, \tag{A.2}$$

where $\mathrm{UBE}_{\mathrm{measured}}$ and $\mathrm{UBE}_{\mathrm{certified}}$ are the measured and certified Useful Battery Energy values as proposed by the United Nations Global Technical Regulation [313].

In this example, the single SOH measurement was taken after 8 years of primary use and was measured to be 70%. This measurement suffices for evaluating whether an EV meets warranty requirements according to recent UN GTR [313] and CARB [314] legislation. However, this metric reveals no information about how long the battery will last beyond the

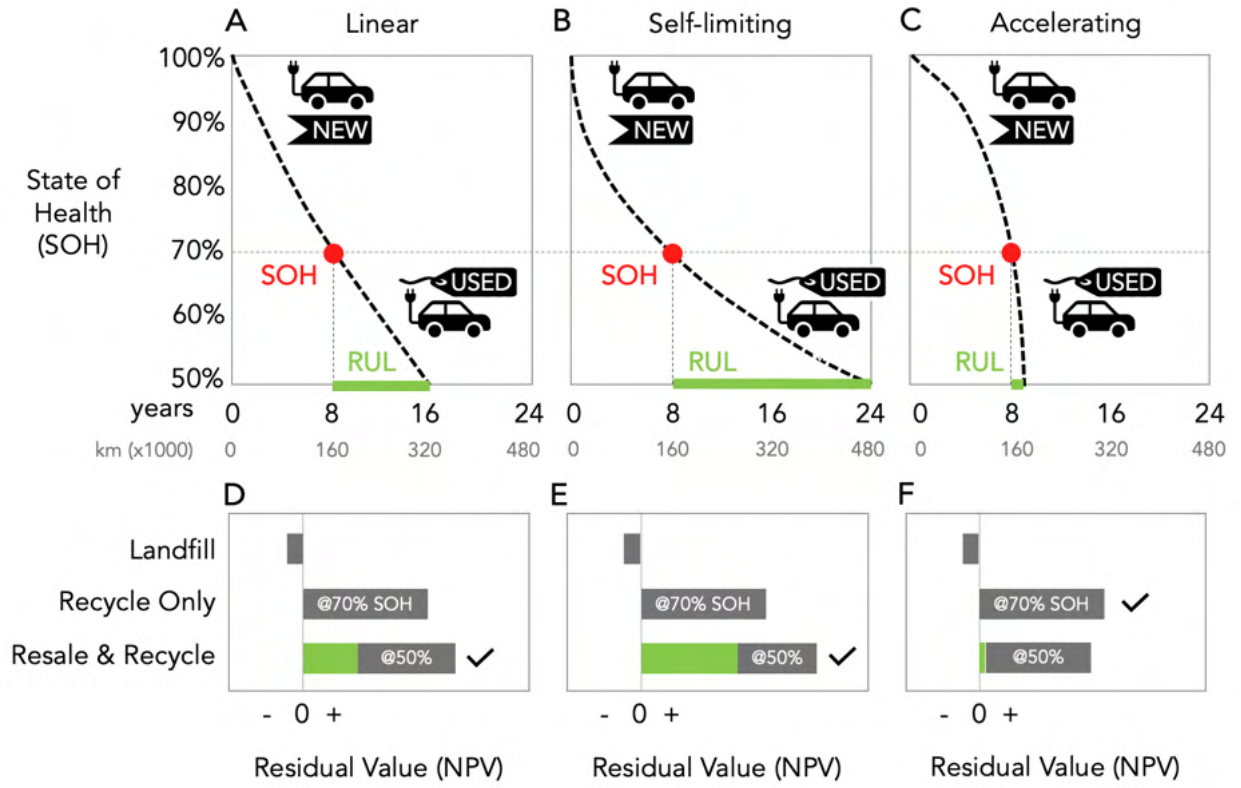

Figure A.2: RUL cannot be determined using a single-point SOH measurement. Three different aging trajectories are shown: (A) linear, (B) self-limiting, (C) and accelerating. In all three cases, the battery satisfies the warranty of 8 years, 160 kilometers, and 70% SOH (red markers). However, the aging trajectories beyond 8 years differ drastically, affecting the residual value during resale as shown in Panels (D-F). The residual value is quantified by the Net Present Value (NPV) which discounts the future value of recycling.

8 years of primary usage. Ultimately, the RUL depends on the underlying aging trajectory which can differ between battery packs due to differences in cell chemistries, manufacturing processes, and usage conditions.

Figure A.2 (A-C) illustrates three such possible aging trajectories: "linear" (A), "self-limiting" (B), and "accelerating" (C) [129]. Defining RUL here as the years from 70% SOH to 50% SOH, we find that the self-limiting trajectory yields an RUL of 16 years, while the accelerating trajectory yields only 1. The self-limiting scenario would thus add the most value in a second-hand electric vehicle market, or possibly even be fit for repurposing or second-life applications.

Critically, for all three aging trajectories, the SOH measured after 8 years yields an identical value of 70% SOH, revealing no difference in battery "durability." This example demonstrates that a single-point measurement of SOH, no matter how accurate, is insufficient

for predicting RUL. It follows that battery passports having only a single SOH measurement will have a limited ability to assess RUL. To enable modeling of the aging trajectory, a minimum of three SOH points should be measured and recorded over the life of a battery pack. These SOH points must either be obtained through external testing, i.e., at a battery inspection station, or from the onboard BMS.

Figure 2 (D-F) shows how knowledge of RUL can help bolster consumer confidence when deciding between recycling versus reselling an electric vehicle (EV) battery at the end of its 8-year warranty period. In calculating the residual value of EV resale, we consider both (1) the value from continued usage as an EV throughout its RUL and (2) the value from recycling the spent battery at the end of its RUL. The largest source of uncertainty in this calculation is the RUL. Accurate RUL is thus necessary for facilitating decisions around recycling versus reuse. Similarly, accurate RUL is also necessary for assessing the value of repurposing.

A.3 On SOH Accuracy Requirements

How accurate do SOH estimates need to be to enable accurate RUL predictions? In theory, accurate SOH estimates are obtainable by carefully controlled measurements which can, in theory, be administered by service centers. Yet, relying on capacity measurements at a service center to establish battery aging trajectories is undesirable since this will require a customer to bring in their pack multiple times throughout the service life, a potentially expensive and time-consuming process. A more economical way to establish an aging trajectory is thus to obtain continuously streaming SOH data from the onboard BMS. However, onboard SOH estimation inaccuracies are unavoidable due to numerous factors including sensor inaccuracy and limited measurement voltage windows.

Intuitively, SOH estimation inaccuracies should also lead to poor RUL prediction inaccuracies. Here, we explore this question more quantitatively using a simple probabilistic model of battery aging trajectories, shown in Figure A.3. Since our focus is to study the effect of measurement uncertainty, we employ the simplest possible empirical aging model of the form:

$$\mathrm{SOH}_{\mathrm{modeled}}(t) = a - bt^c, \tag{A.3}$$

where a, b, and c are model coefficients, and t is the age of the battery in years. Each SOH measurement is sampled from independent normal distributions, each with a standard deviation of 1 percentage point to represent "1% SOH measurement inaccuracy." The model is then fit to the sampled points, which can then be used to extrapolate to 50% SOH. The

process is repeated 100 times to generate a distribution of RUL outcomes (gray lines).

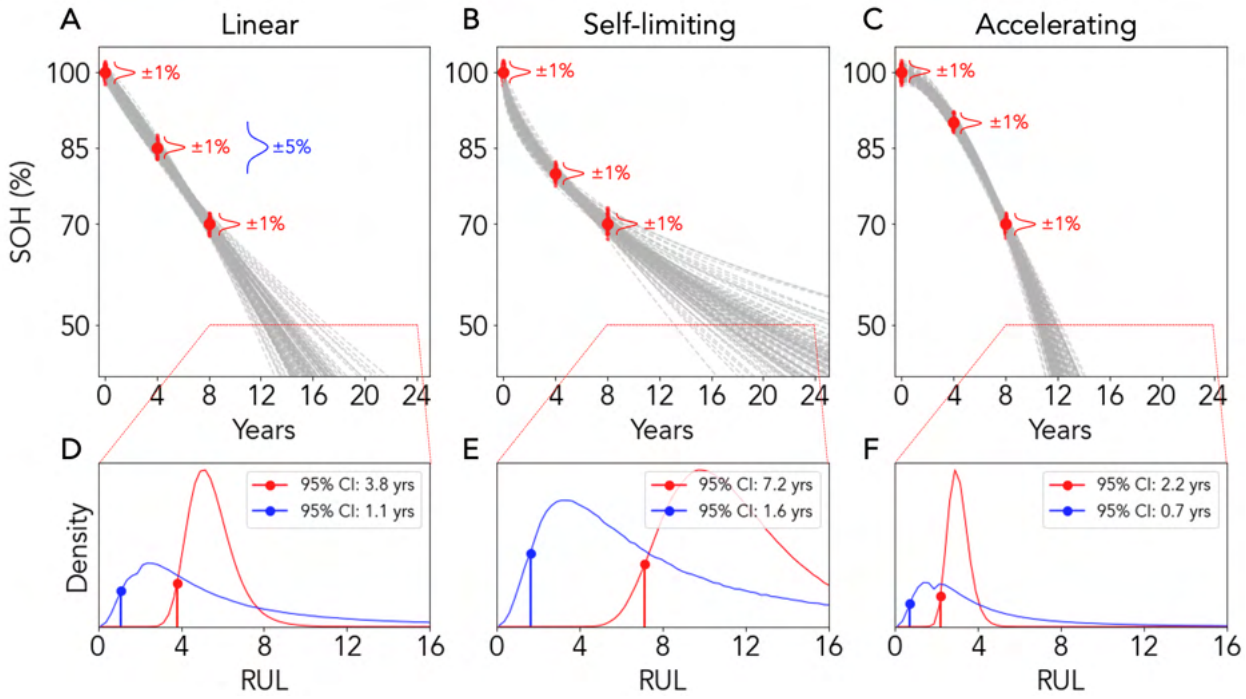

Figure A.3: Effect of SOH estimation inaccuracy on RUL estimation confidence. Panels (A-C) each show 100 aging trajectories (gray lines) modeled using noisy SOH estimates (red markers). Each subpanel represents different ground truth aging trajectories: (A): linear, (B): self-limiting, and (C): accelerating. Panels (D-F) show the corresponding empirical probability density functions for RUL. The red (blue) curve corresponds to 1% (5%) SOH estimation inaccuracy. The solid vertical lines represent 95% confidence interval (CI) RUL values.

The results shown in Panels (A-C) reveal that the distribution of RUL outcomes depends on the aging trajectory, with the self-limiting aging trajectory having the highest variability RUL variability, and the accelerating aging trajectory having the least. This numerical example shows how SOH estimation inaccuracies manifest as RUL prediction uncertainties.

To further understand how RUL distributions change with SOH inaccuracies, we study the empirical probability density function of RUL for two different SOH estimation inaccuracy scenarios: 1% inaccuracy (red) and 5% inaccuracy (blue), as shown in Panel (D-F). We define the 95% confidence interval (CI) RUL values to correspond to the years at which there is a 95% probability that the true RUL will exceed the given value. With 5% SOH inaccuracy, the 95% CI RUL for all three aging trajectories decreases significantly. For example, for the self-limiting aging trajectory, the 95% CI RUL decreases from 7.2 years to 1.6 years. A 5% SOH inaccuracy thus severely degrades the confidence of RUL predictions.

This example highlights an important fact about consumer confidence: even if a battery

pack is technically suitable for resale or repurposing, a consumer will not choose to do so unless they have confidence in the RUL. To achieve this confidence, SOH estimation uncertainty must be sufficiently low.

A.4 On Changing Use Cases for Repurposing

We finally highlight an inconvenient reality with RUL prediction for battery repurposing: simple, extrapolation-based methods for predicting RUL may fail to yield accurate RUL predictions for repurposing applications. This issue is unique to repurposing where the battery use case can differ drastically from the primary use case as a traction battery. Figure A.4 illustrates this by comparing the battery degradation trajectory in the context of EV resale (Panel A) and repurposing (Panel B). In the case of EV resale, the battery pack continues to be used as a traction battery, and while metrics such as daily mileage may change after resale, the overall battery limits of operation, being bounded by the same BMS, remain the same. The battery aging trajectory is thus expected to be similar during the secondary usage period beyond 8 years.

Comparatively, batteries that are repurposed may be used in completely different contexts compared to the primary usage in EVs, including for home backup power, grid frequency regulation, and low-power electric mobility [318]. For these use cases, the battery degradation rate will tend to be milder than compared to the traction battery use case. Extrapolating aging trajectories based on SOH measured during the primary use case may thus underestimate the RUL, leading to a mischaracterization of the battery's longevity in the second life application.

An accurate assessment of RUL for repurposing therefore requires models that parameterize the degradation rate based on the use case. Simple, extrapolation-based approaches based on past usage history alone cannot achieve this. Rather, more physics-based models [83] may be more appropriate for capturing the dynamics of changing use cases and their impacts to battery degradation. Such models typically parameterize battery degradation at the electrode level, whereby environmental factors, such as depth of discharge, temperature, and C-rate, are translated into electrode-level stressors, such as lithium concentration gradients and reaction overpotentials. These physical models can more readily evaluate the impact of repurposing on RUL by dynamically updating the degradation rate as the use case changes. A BMS that implements a physics-based model could, in principle, compute the RUL associated with multiple use cases, enabling consumers evaluate the suitability of a given battery system for different repurposing applications.

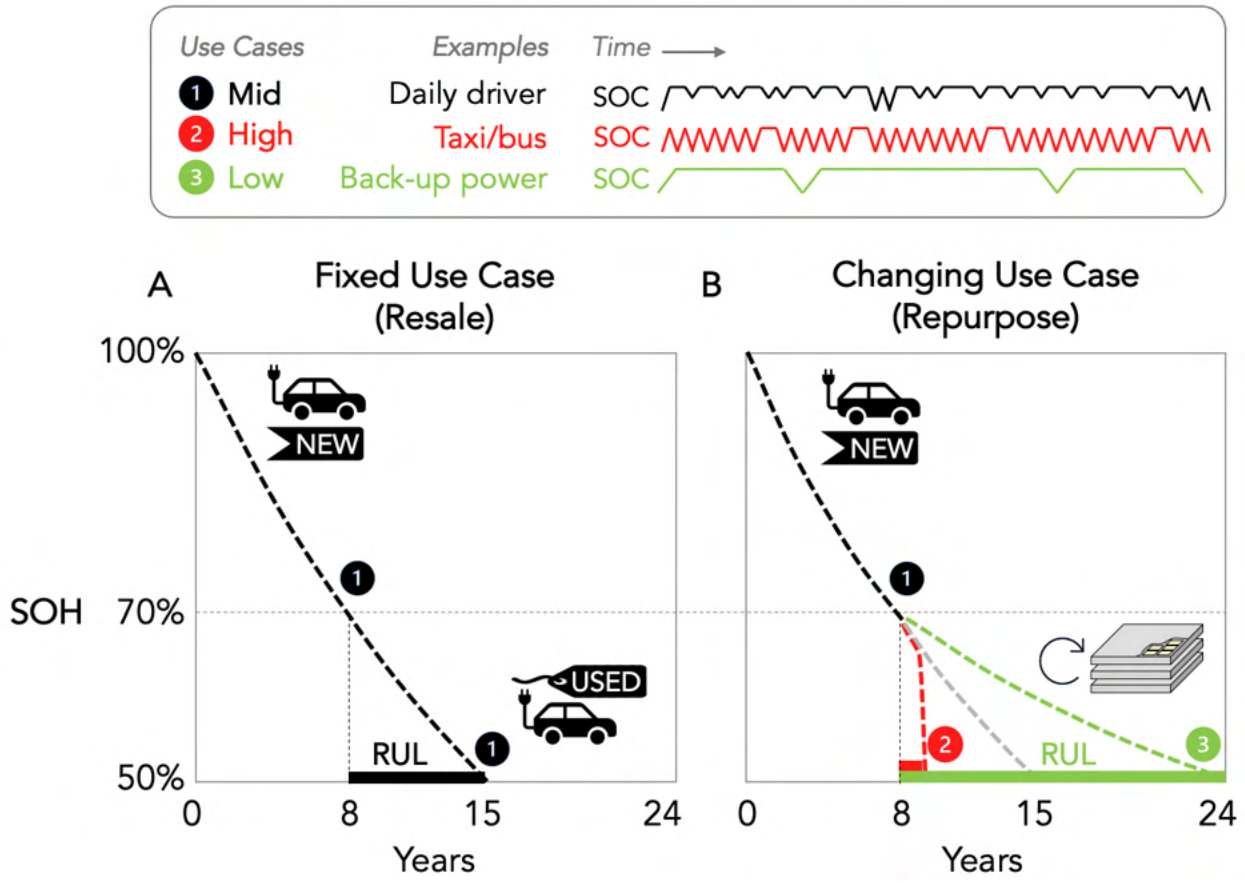

Figure A.4: Impact of changing use cases on battery long-term aging trajectory. Panel A shows the SOH trajectory before and after EV resale, where the use case remains relatively unchanged. Panel B shows how, in the case of battery repurposing, the SOH trajectory may deviate from the original trajectory due to changing use cases.

A.5 On Battery Management Systems

The BMS plays a central role in measuring and reporting battery SOH and RUL for each electric vehicle. Existing policy language from the EU and CARB are not prescriptive in how SOH or RUL estimation should be implemented but makes it clear that the BMS is responsible for computing and reporting this information. Here, we briefly discuss some additional considerations relevant to enacting battery passport policies promoting BMS development and RUL estimation.

First, since RUL can be defined at the cell-level, module-level, or pack-level, battery passport data requirements should carefully weigh the pros and cons of each level of representation. Repurposing applications will generally benefit from module or even cell-level information since individual units within a single battery pack can exhibit different aging behavior [319]. A remanufacturer with accurate RUL information on individual modules, for

example, can then choose which modules to remanufacture and which modules to recycle. On the other hand, for EV resale applications, pack-level RUL information is sufficient since the pack will not be disassembled. Enabling cell-level RUL will increase BMS sensor and development costs, which must be weighed against the benefit of improving re-manufacturability.

Second, given OEMs' general reluctance to publicly share BMS data, policy language around BMS development should focus on RUL accuracy targets and verification methods rather than prescribing implementation details. In this manner, legislators can focus on assuring sustainability end goals while remaining agnostic to technology implementation, thereby respecting the OEMs' needs to protect their technology.

Finally, although the BMS typically only adds 4-5% to total battery pack costs [320], this cost does not adequately capture the extra time and engineering effort needed to develop and validate advanced RUL estimation methods. The more complicated the RUL reporting requirements are, the more difficult it will be for OEMs to implement such requirements while remaining competitive in the global EV market. Thus, to encourage widespread adoption of standardized RUL reporting requirements, the requirements themselves should be kept as simple as possible.

A.6 Conclusions and Recommendations

Battery passport data requirements should be kept as simple as possible. Adopting complex requirements can increase battery costs, slow implementation, and become difficult to enforce. Yet, while existing battery passport data requirements may help maintain minimum performance guarantees for EVs within their first 8 years of use, these same requirements may not enable accurate prediction of remaining useful life (RUL) beyond 8 years. Without accurate RUL predictions, battery passports can only give limited guidance concerning EV resale and repurposing.

We outlined several key considerations to ensure battery passports can inform EV resale and repurposing decisions. At a minimum, three state of health (SOH) measurements should be made over different time points to establish an aging trajectory. Each SOH measurement must be sufficiently accurate: a 5% SOH inaccuracy cannot provide confident RUL predictions. Finally, the battery management system (BMS) must enable the accurate prediction of RUL under changing use cases, which may require the adoption of physics-based state estimation algorithms in the BMS. These additional considerations emphasize the need to develop and deploy high-performance BMS in electric vehicles.

Overall, this chapter raises awareness of the central role that the BMS plays in enabling battery passports to predict RUL. With an accurate BMS, battery passports can help boost

consumer confidence in the used EV market. With an accurate, physics-based BMS, repurposers can evaluate second-life application feasibility and fulfill the promise of a circular battery economy.

APPENDIX B

Formation Data Analysis

The contents in this appendix accompany the material from Chapter 6.

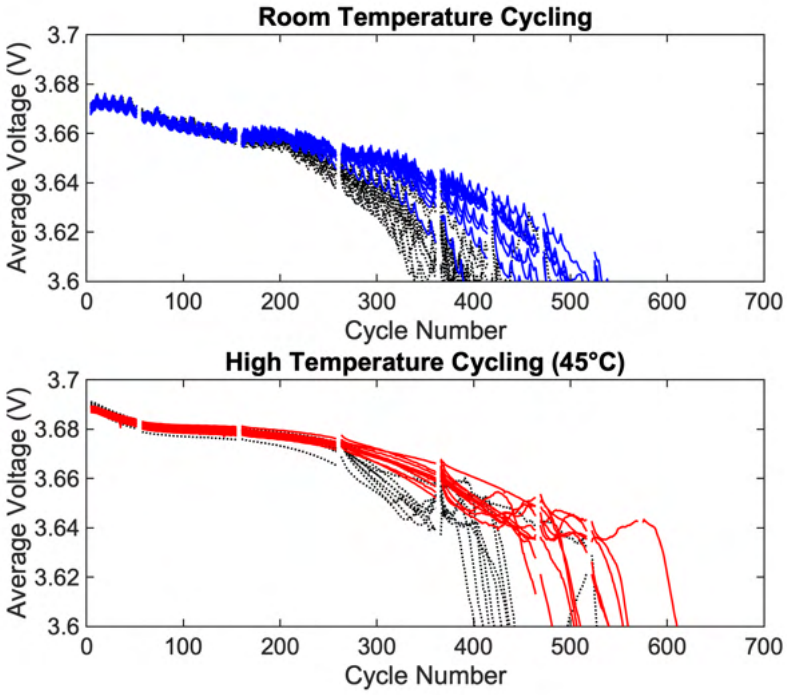

Figure B.1: Mean discharge voltage over cycle number

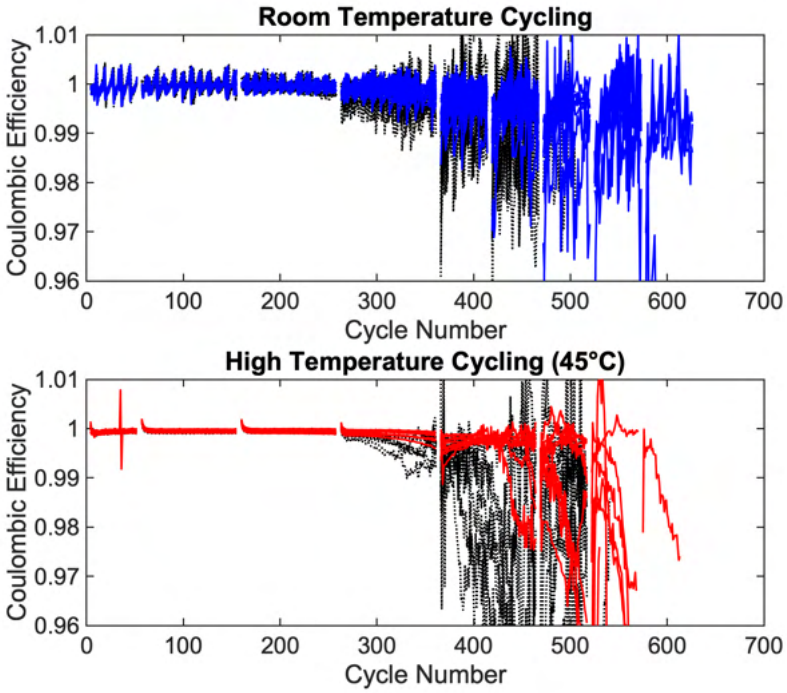

Figure B.2: Coulombic efficiency over cycle number

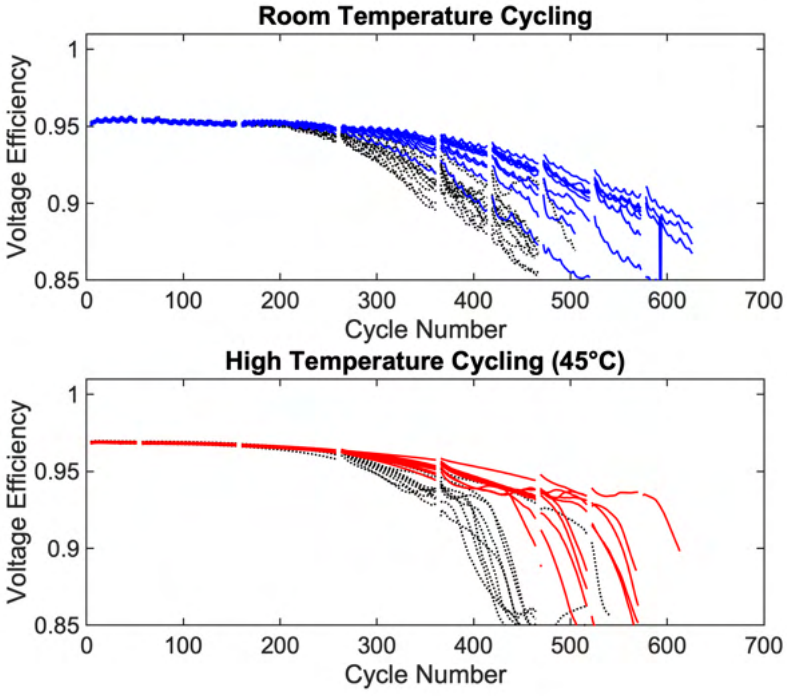

Figure B.3: Voltage efficiency over cycle number

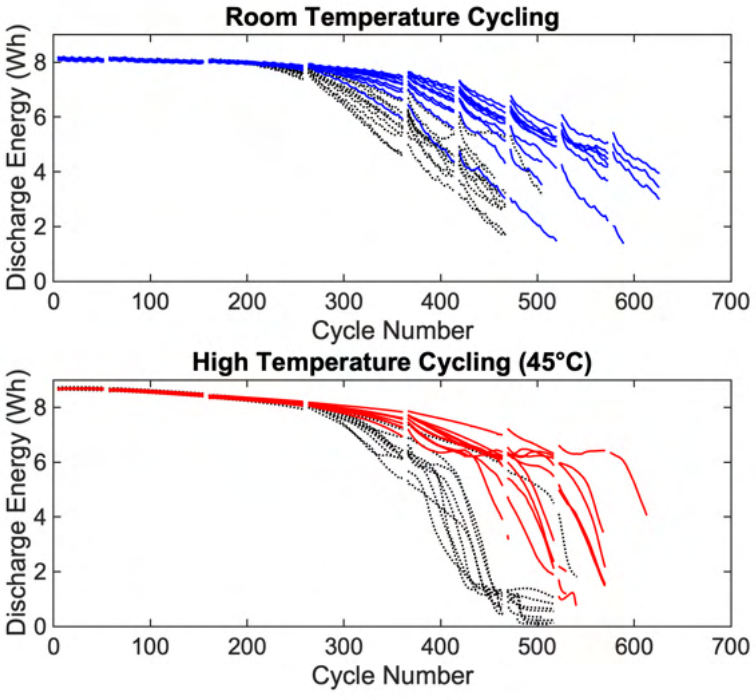

Figure B.4: Discharge energy over cycle number

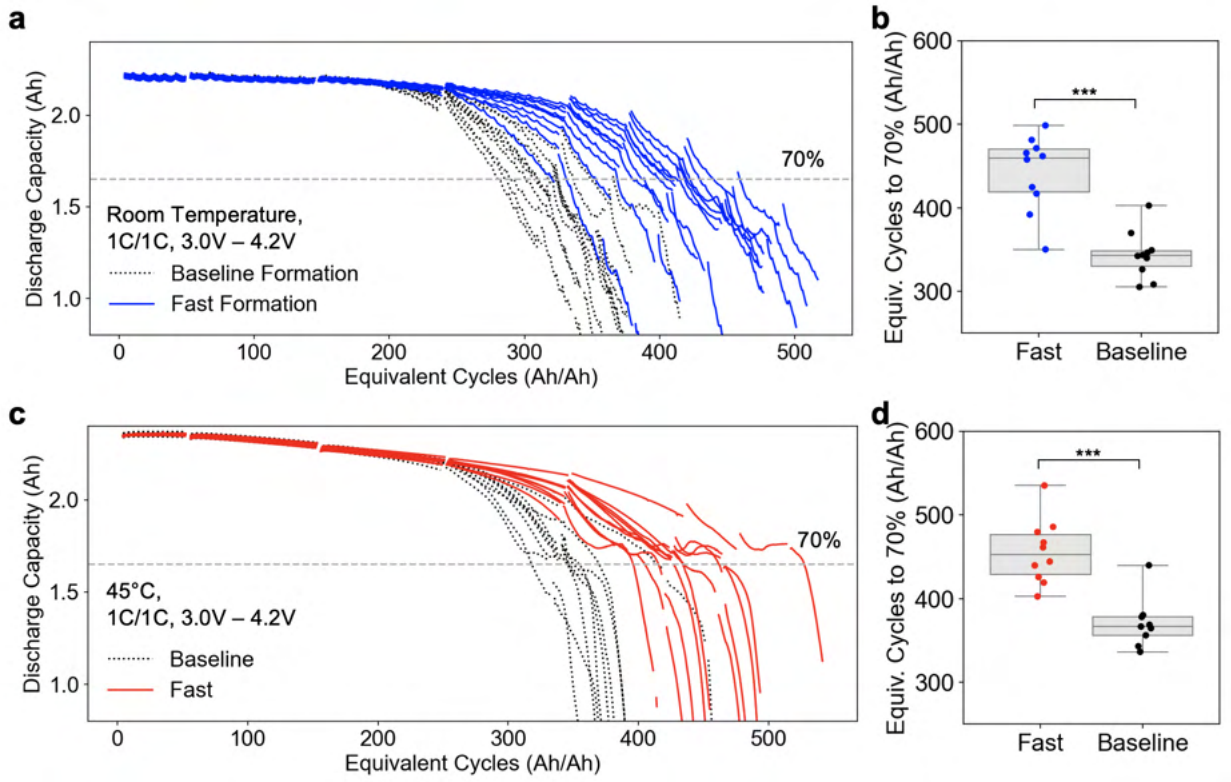

Figure B.5: Cycle life test results plotted with equivalent cycles (Ah/Ah) as the throughput basis. The total throughput is calculated by taking the cumulative discharge capacity and dividing by the cell nominal capacity (2.36 Ah). (a,c) Discharge capacity for the room temperature (a) and 45°C (c) tests. (b,d) Distribution of outcomes at the end of life for the room temperature (b) and 45°C (d) tests. End of life is defined as equivalent cycles to reach 70% of initial capacity.

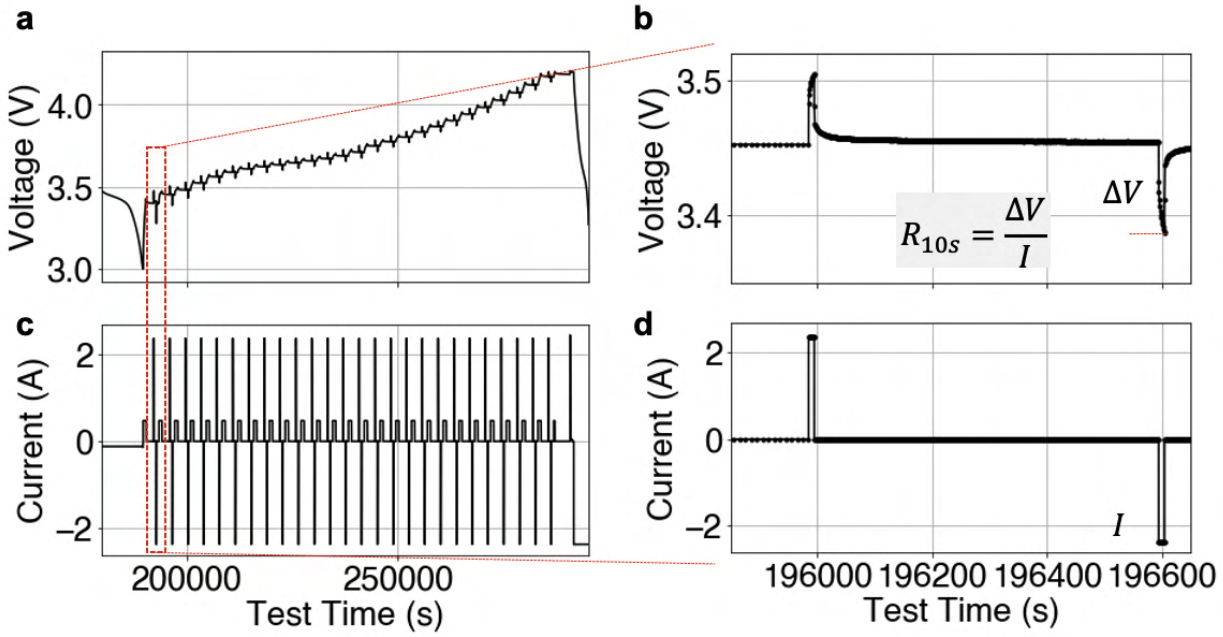

Figure B.6: Example HPPC sequence. HPPC is used to extract the 1C, 10-second charge and discharge resistances across different SOCs. (a,c) current and voltage traces from the HPPC protocol. (b,d) magnified view of the first charge and discharge pulse from the pulse sequence, which occurs at ∼4% SOC. The HPPC pulses are included as part of every reference performance test (RPT).

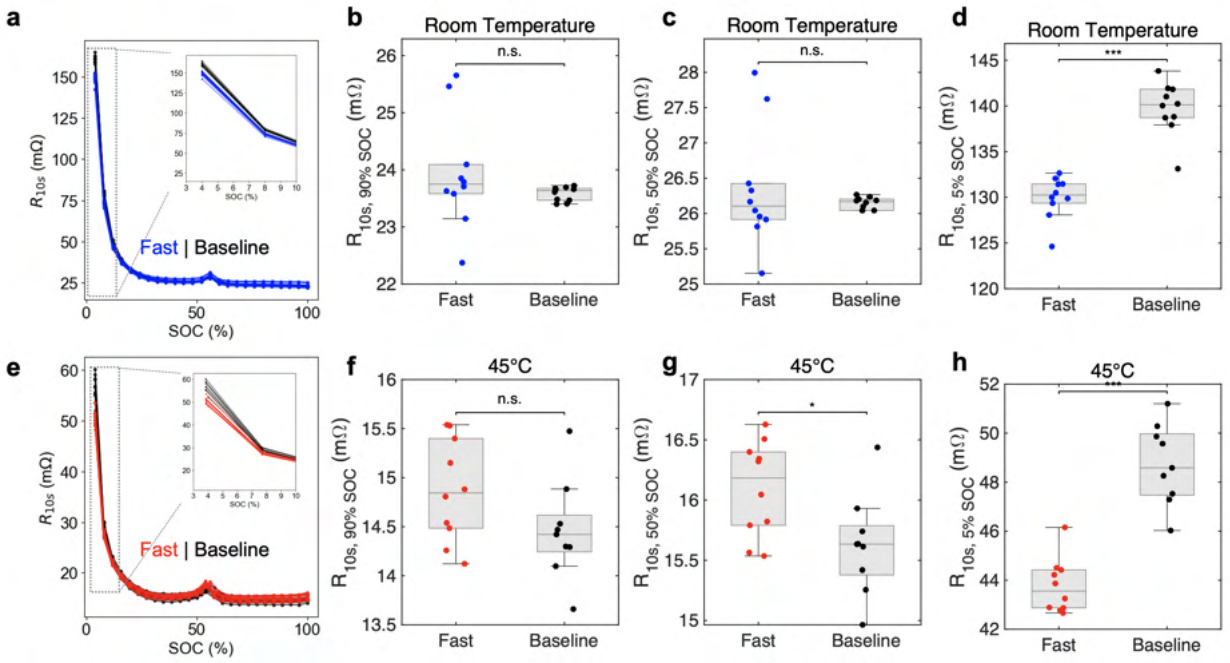

Figure B.7: Initial cell resistance comparison. Distribution of resistance measured at (a-c) room temperature and (d-f) 45°C. Resistance is calculated from the Hybrid Power Pulse Characterization (HPPC) test from the first RPT. 'n.s.': not statistically significant. '***': statistically significant with p-value < 0.001.

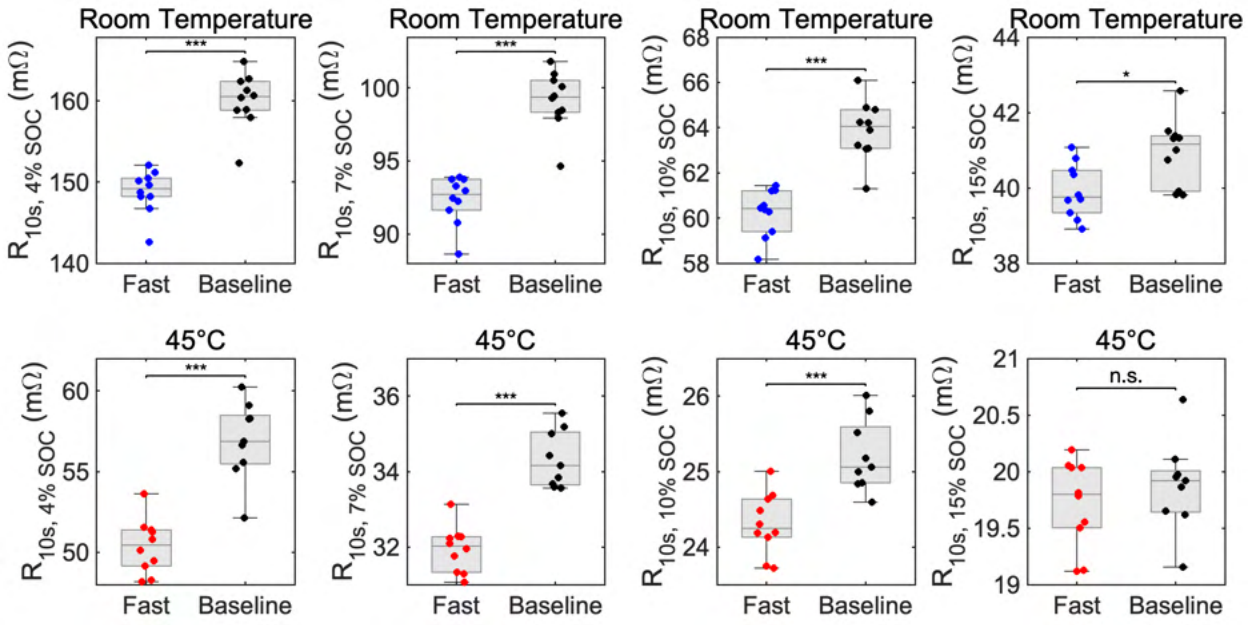

Figure B.8: Effect of measurement SOC on the cell resistance measured from HPPC. Top row: room temperature. Bottom row: 45°C. Values are obtained from the initial Reference Performance Test (RPT) run prior to the start of cycling. 'n.s.': not statistically significant. '***': statistically significant with p-value < 0.001. '*': statistically significant with p-value < 0.05.

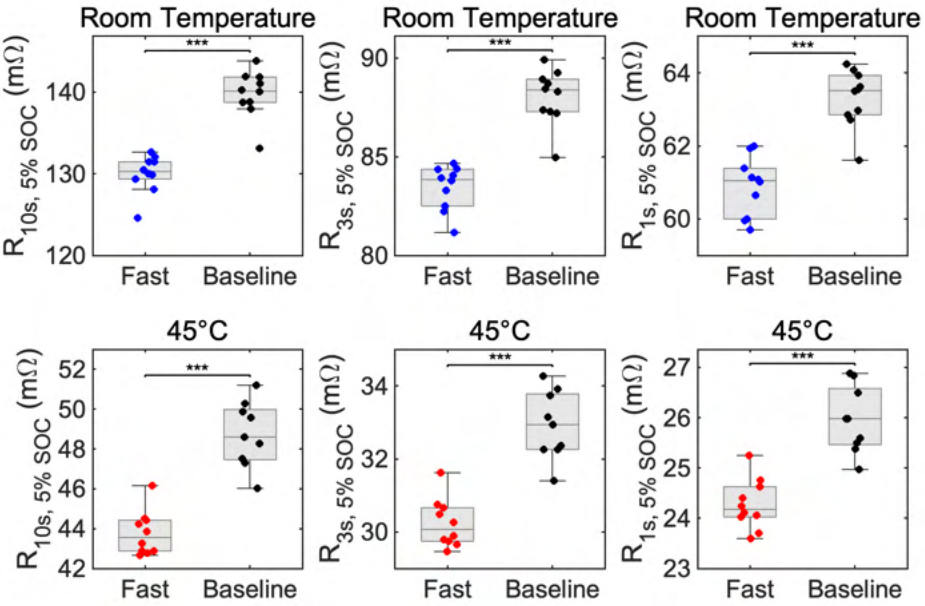

Figure B.9: Effect of pulse duration on the cell resistance measured from HPPC. Top row: room temperature. Bottom row: 45°C. Values are obtained from the initial RPT run prior to the start of cycling. '***': statistically significant with p-value < 0.001.

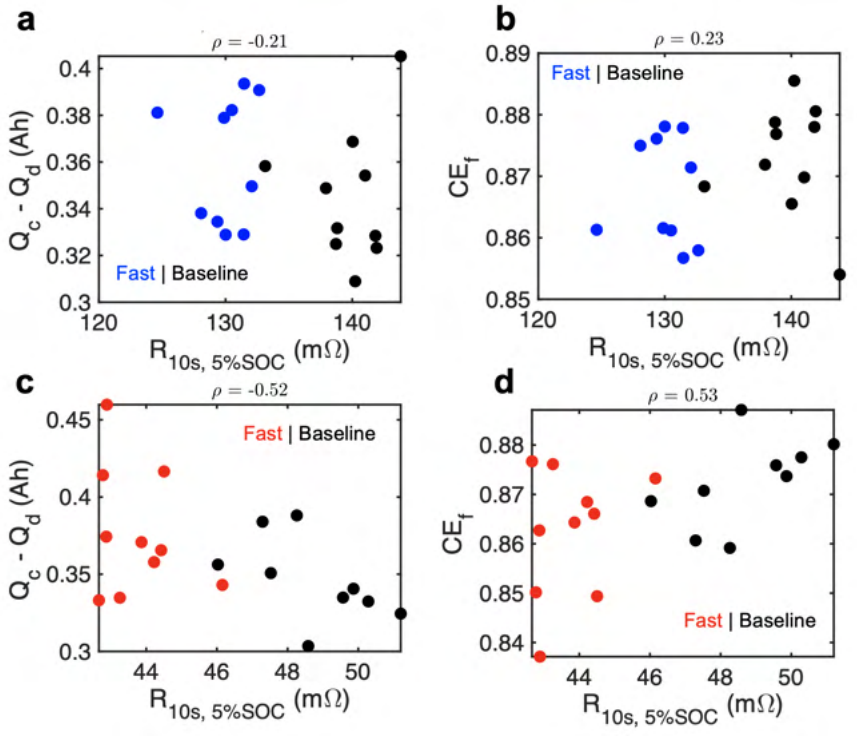

Figure B.10: Correlation between R_{LS} and conventional metrics of lithium consumption during formation. Conventional metrics include lithium consumed during formation ($Q_{SEI} = Q_c - Q_d$) and Coulombic efficiency (CE_f). (a,b) Correlation with R_{LS} measured at room temperature. (c,d) Correlation with R_{LS} measured at 45°C. $Q_{SEI} = Q_c - Q_d$ and CE_f are always measured at room temperature since these signals are derived directly from the formation protocol which ran at room temperature. R_{LS} was measured at the temperature of the cycling test.

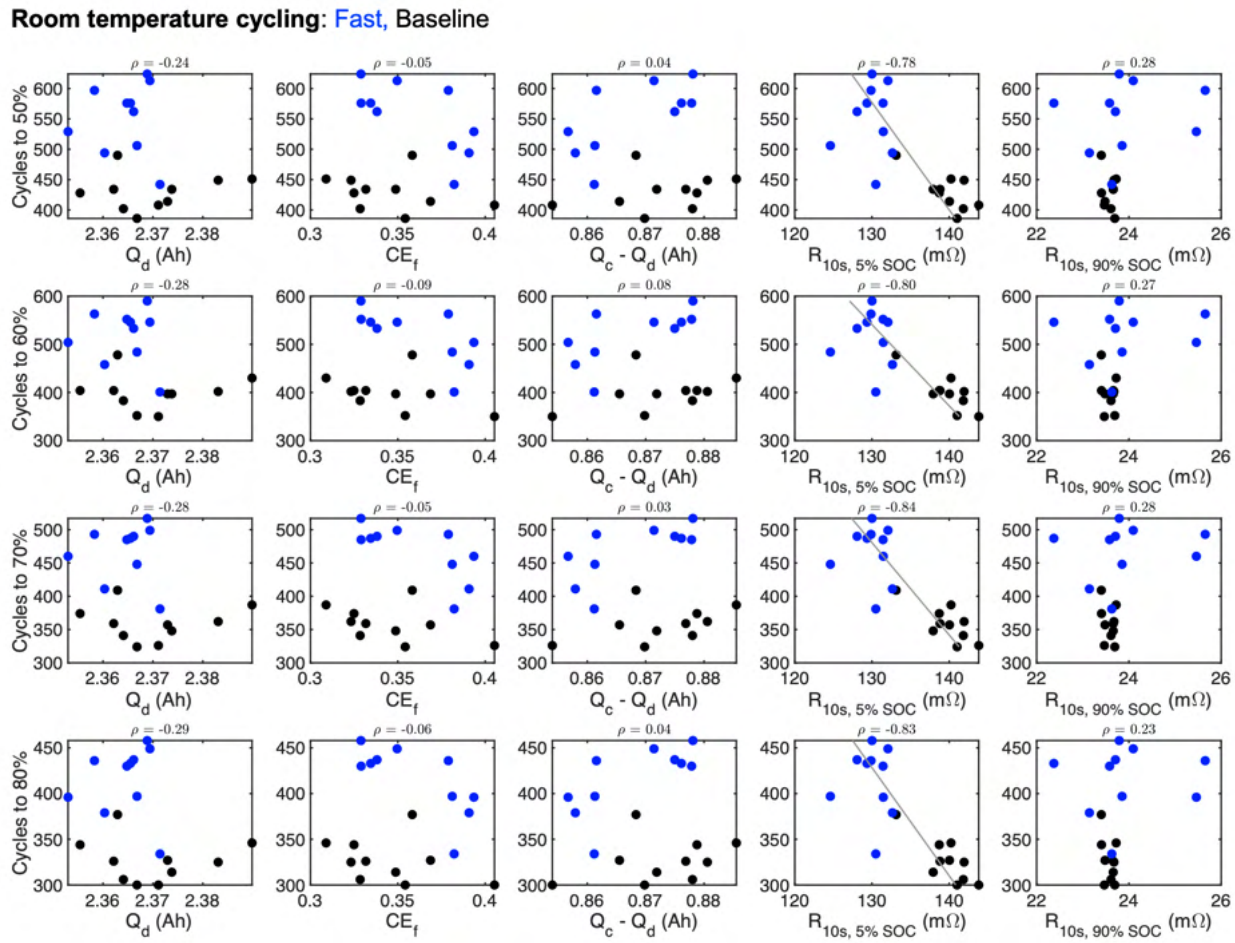

Figure B.11: Correlation between initial cell signals and cycle life for room temperature cycling. End of life is defined as cycles to x% of initial capacity, where $x = \{50, 60, 70, 80\}$. Formation signals ($Q_{\mathrm{SEI}} = Q_{\mathrm{c}} - Q_{\mathrm{d}}$ and $\mathrm{CE_f}$) are always measured at room temperature. $\mathrm{R_{10s,5\%SOC}}$ and $\mathrm{R_{10s,90\%SOC}}$ are measured at the same temperature as the cycle life test.

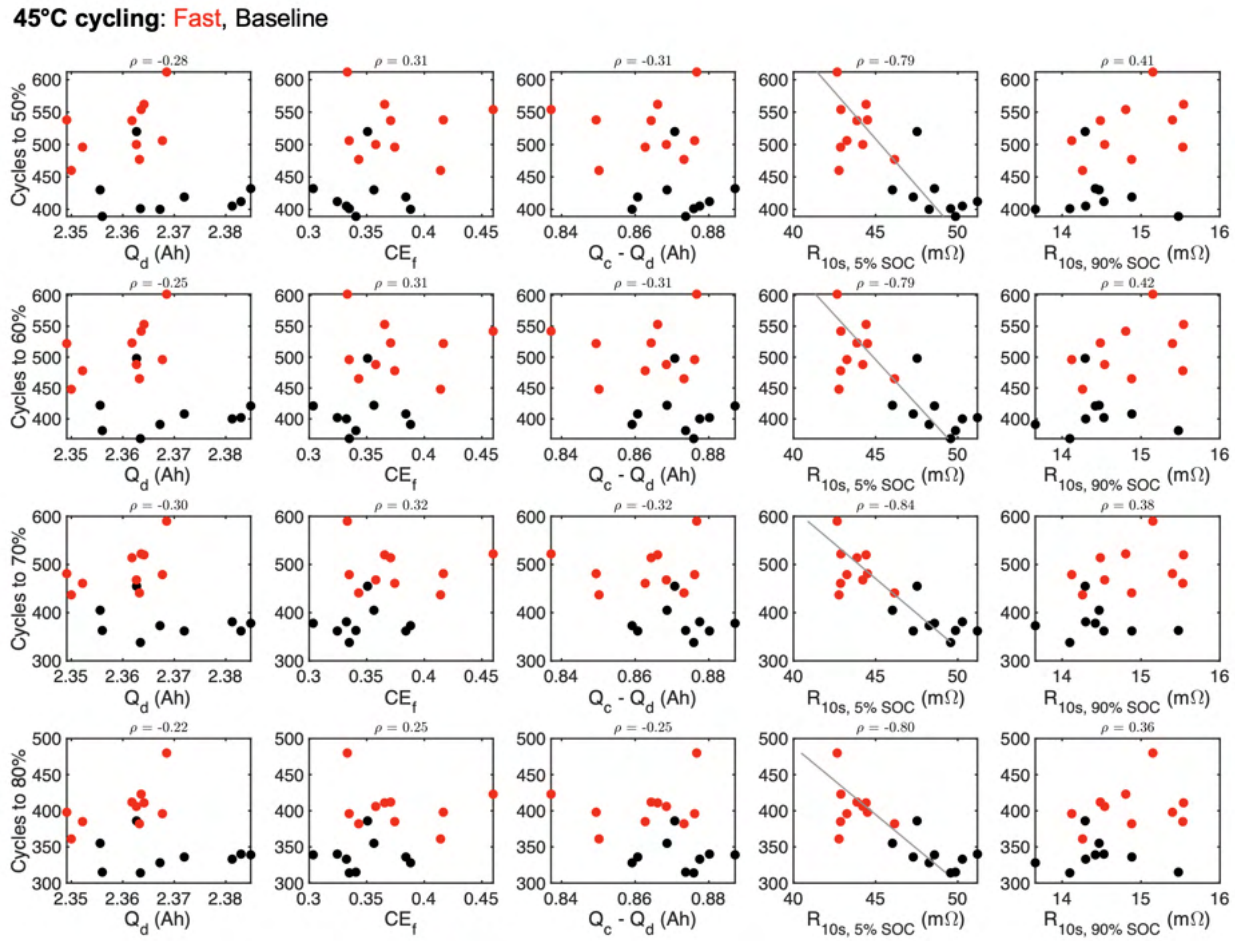

Figure B.12: Correlation between initial cell state signals and cycle life for 45°C cycling. End of life is defined as cycles to x% of initial capacity, where $x = \{50, 60, 70, 80\}$. Formation signals ($Q_{\mathrm{SEI}} = Q_{\mathrm{c}} - Q_{\mathrm{d}}$ and $\mathrm{CE_f}$) are always measured at room temperature. $\mathrm{R_{10s,5\%SOC}}$ and $\mathrm{R_{10s,90\%SOC}}$ are measured at the same temperature as the cycle life test.

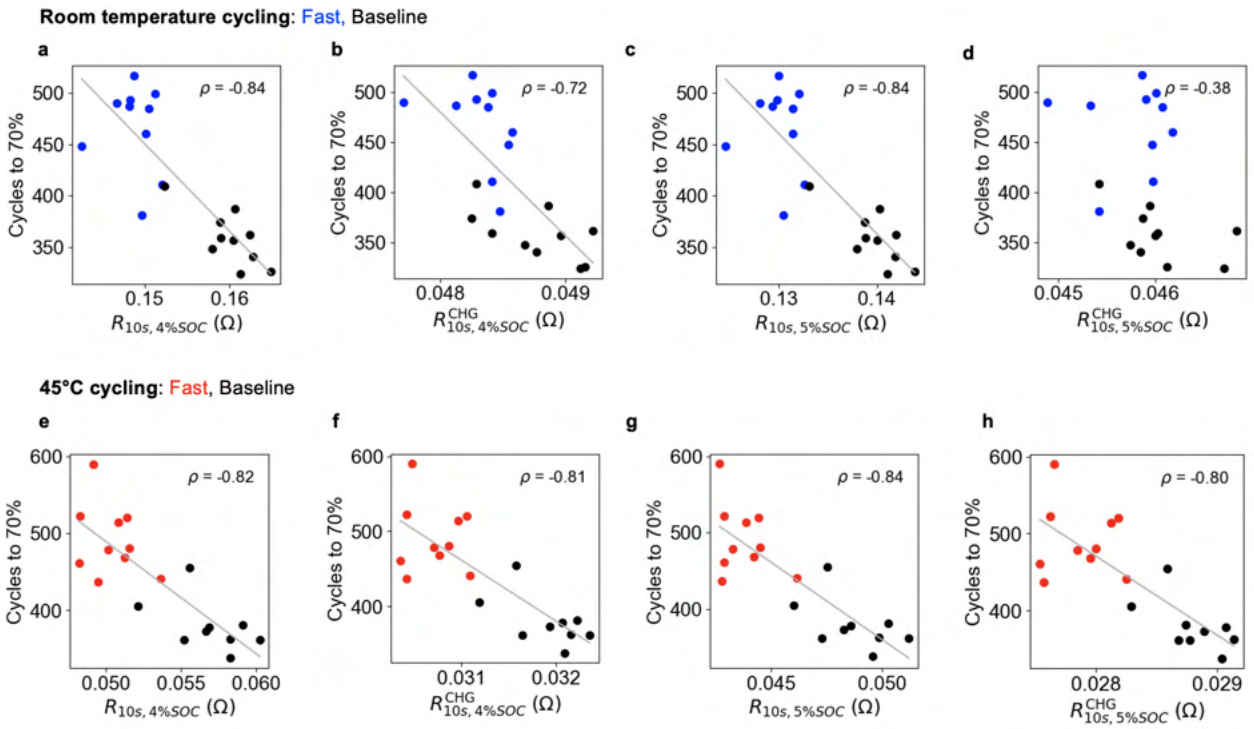

Figure B.13: Correlation between low-SOC resistance and cycle life: charge versus discharge pulses. Resistances are calculated from either discharge (a,c,e,g) or charge (b,d,f,h) pulses from the Hybrid Pulse Power Characterization (HPPC) sequence. The comparison is provided for resistances evaluated at both 4% SOC (a,b,e,f) and 5% SOC (c,d,g,h).

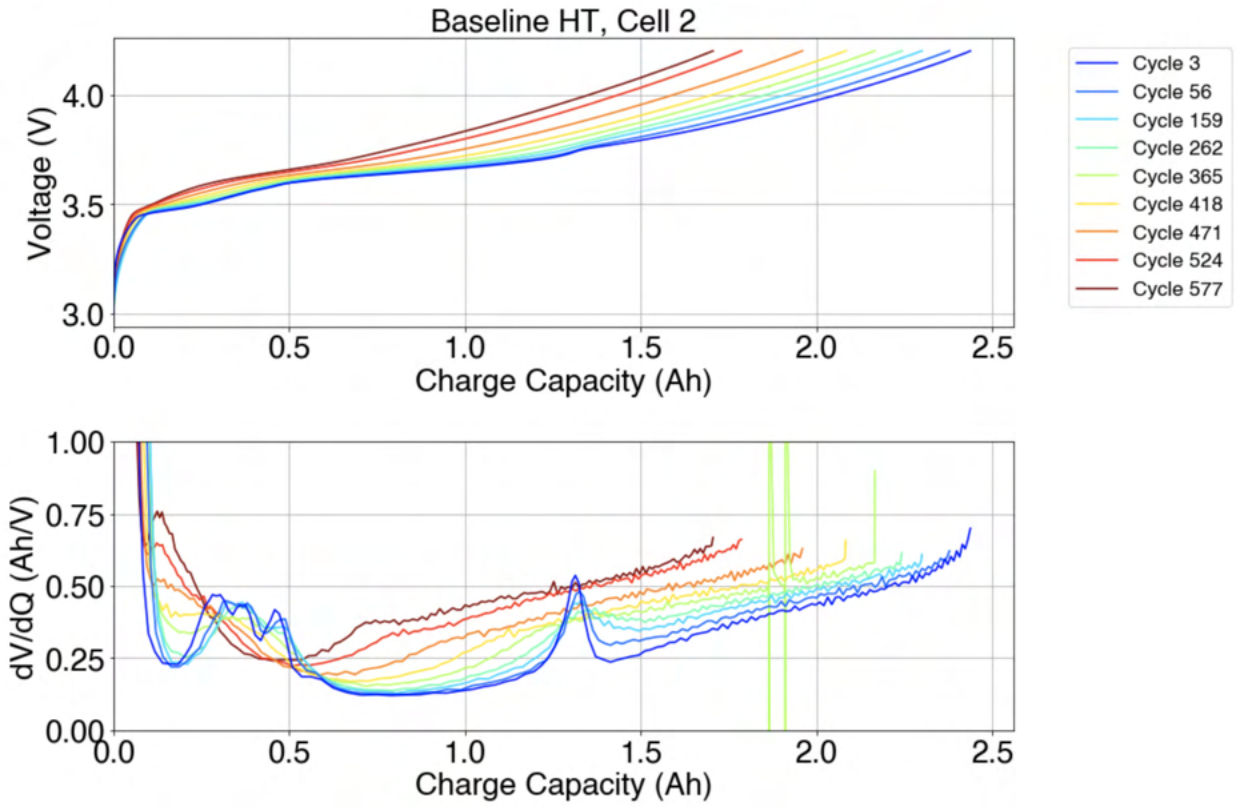

Figure B.14: Example set of C/20 charge curves used for voltage fitting analysis. The C/20 charge curves are embedded as part of the reference performance tests (RPTs).

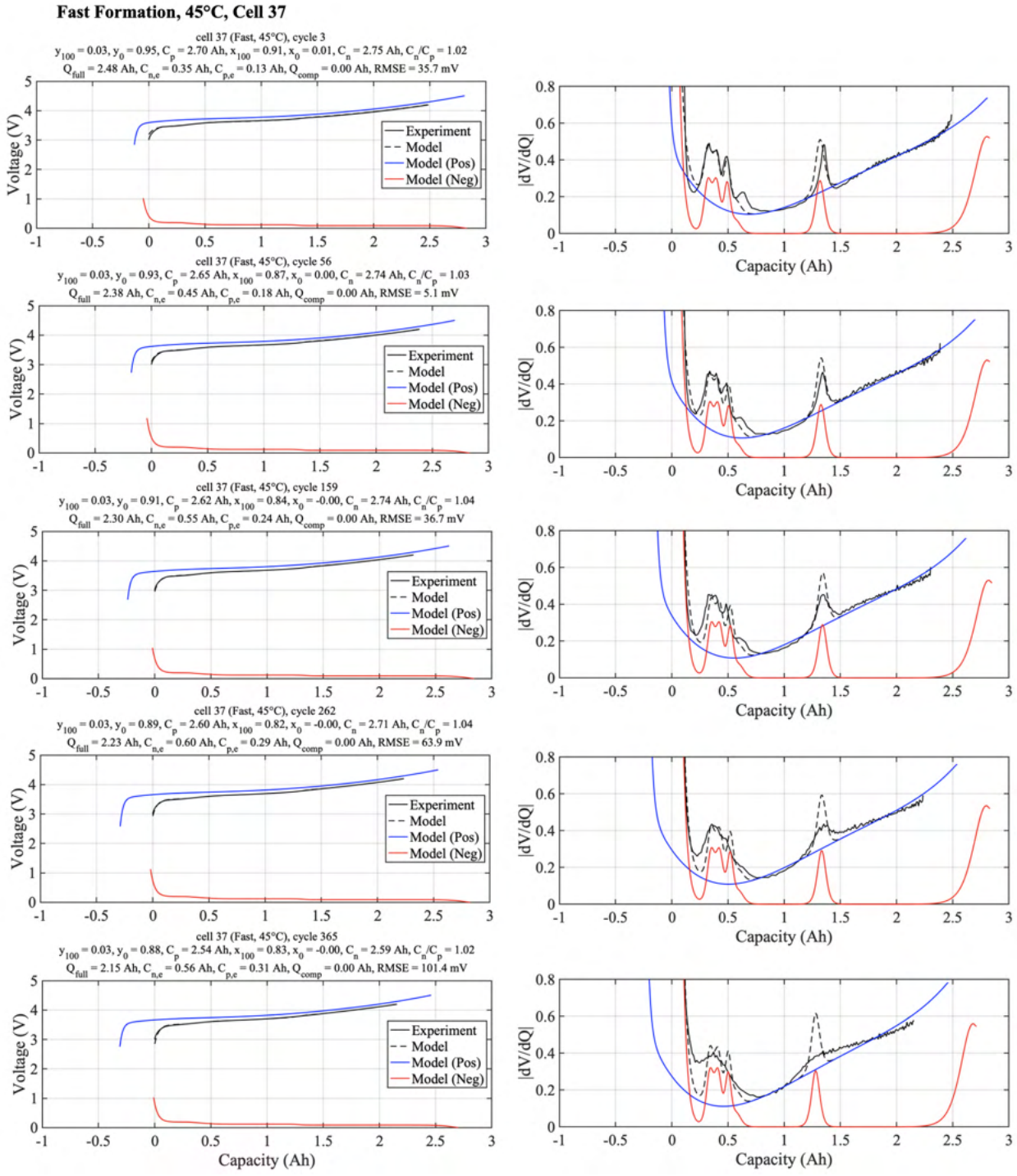

Figure B.15: Example of voltage fitting results obtained on a single cell over aging. Left column: voltage feature alignment. Right: differential voltage feature alignment. Top row: fresh cell. Bottom row: after 365 cycles have elapsed. Note that the voltage fitting algorithm only consumes voltage data.

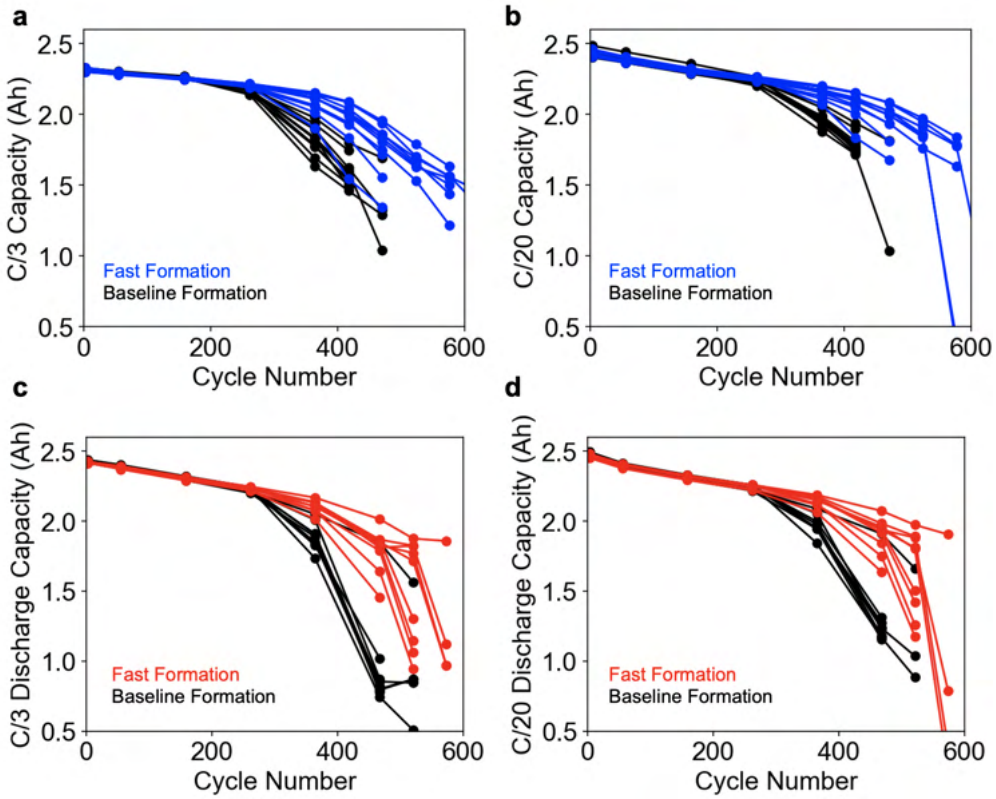

Figure B.16: Comparison of discharge capacity versus cycle number at different C-rates. (a,b) Cycle life tests run at room temperature. (c,d) Cycle life tests run at 45°C. (a,c) C/3 discharge capacity. (b,d) C/20 discharge capacity. All discharge capacities here are measured from the Reference Performance Tests (RPTs).

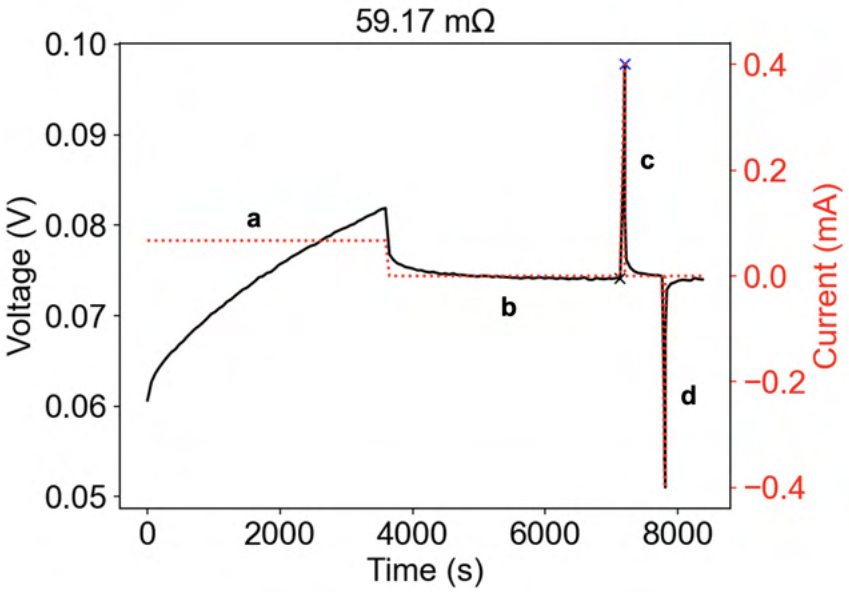

Figure B.17: Example pulse profile for a graphite/Li coin cell half cell. The pulses are obtained as part of the coin cell HPPC test. The coin cell HPPC profile consists of the following repeated sequence: (a) background charge, (b) rest, (c) 10-second charge pulse, and (d) 10-second discharge pulse. The markers (x) indicate the potential difference taken to compute the 10-second resistance using Ohm's law. The potential measured at the end of the rest period (b) is assumed to be in near-equilibrium. The current used during the pulses is 0.4mA for all cells.

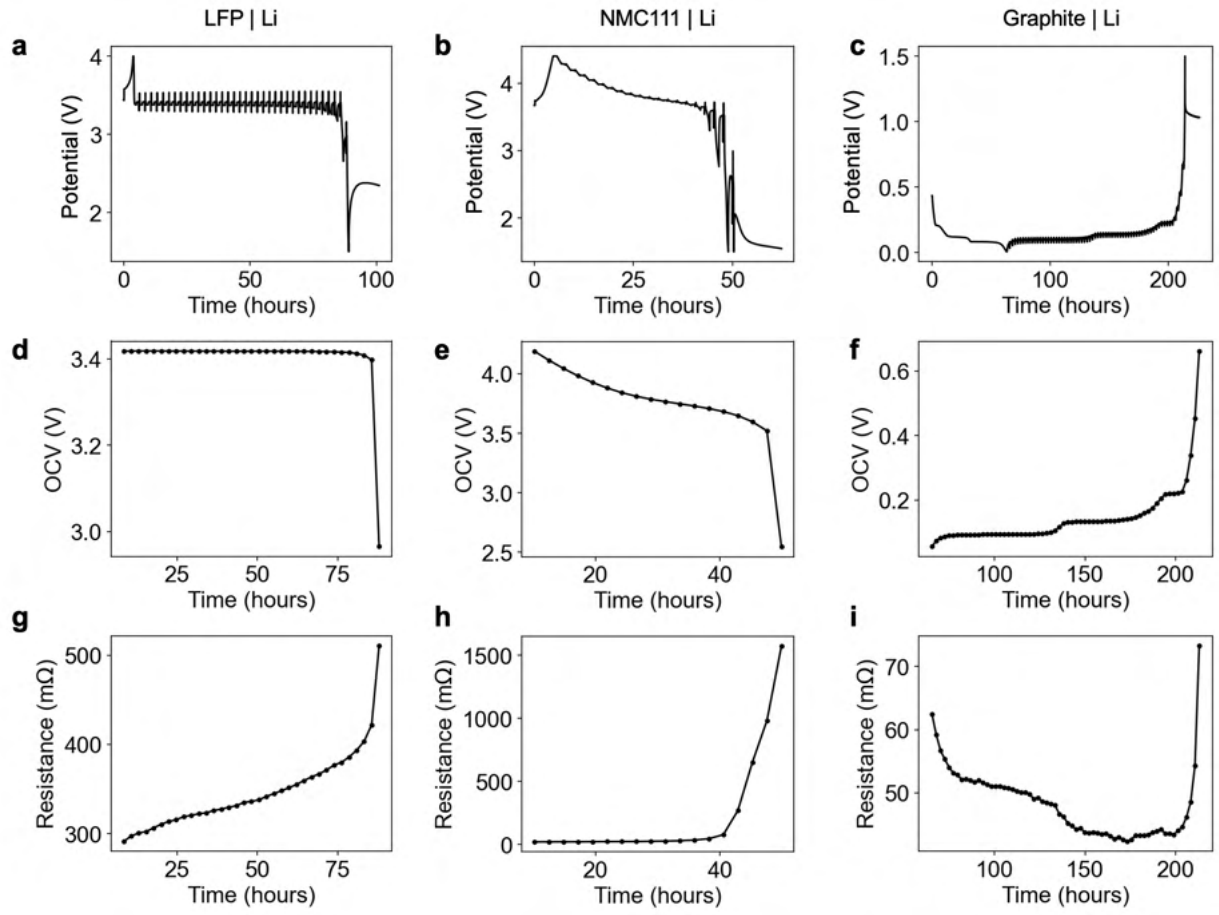

Figure B.18: HPPC tests performed on coin cell half cells. Potential vs time for (a) LFP/Li, (b) NMC/Li, and (c) Graphite/Li. (d-f) Corresponding pseudo-equilibrium potential curves, where the potential is measured immediately preceding each pulse. (g-h) Calculated 10-second resistances. For the positive electrodes, the resistances are calculated on discharge (i.e. during delithiation). For the graphite negative electrode, the resistances are calculated on charge (i.e. during lithiation).

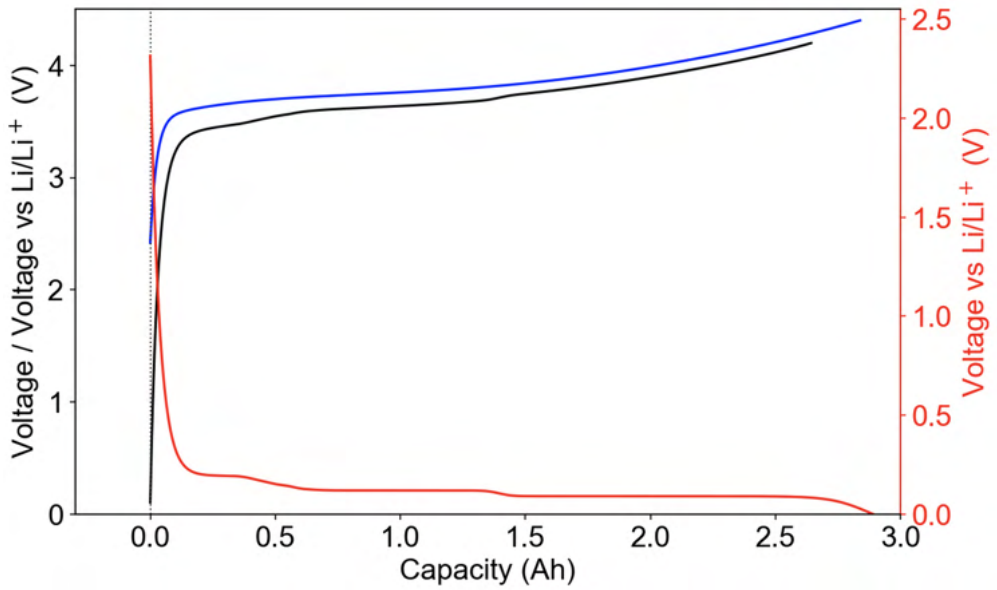

Figure B.19: Initial cell equilibrium potential curves before formation. The curves are generated using the electrode stoichiometry model by aligning the point of minimum negative electrode stoichiometry (maximum potential) with the point of maximum positive electrode stoichiometry (minimum potential). Blue: positive electrode. Red: negative electrode. Black: full cell.

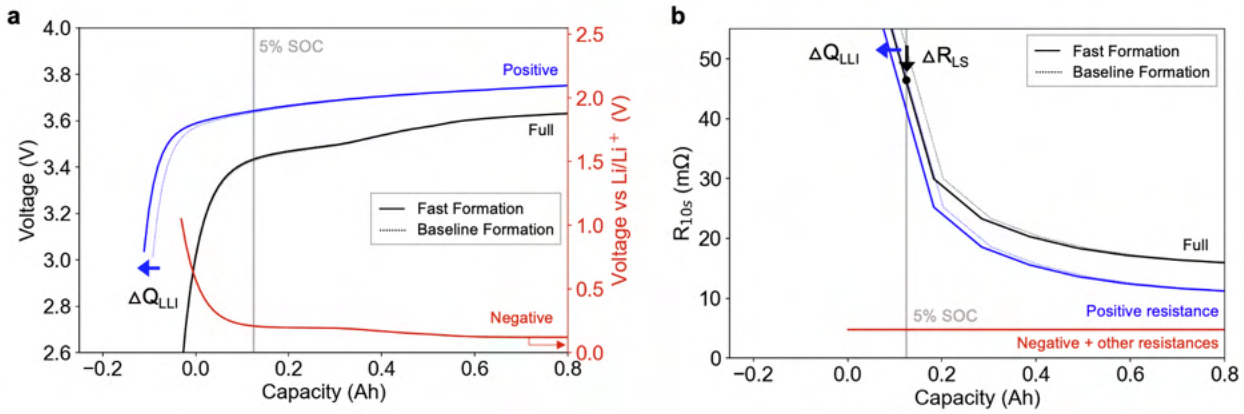

Figure B.20: Electrode stoichiometry model illustration. The model shows the impact of fast formation on the alignment of initial cell equilibrium potential curves (a) and resistance curves (b). In this plot, ΔQ_{SEI} has been set to ~23 mAh.

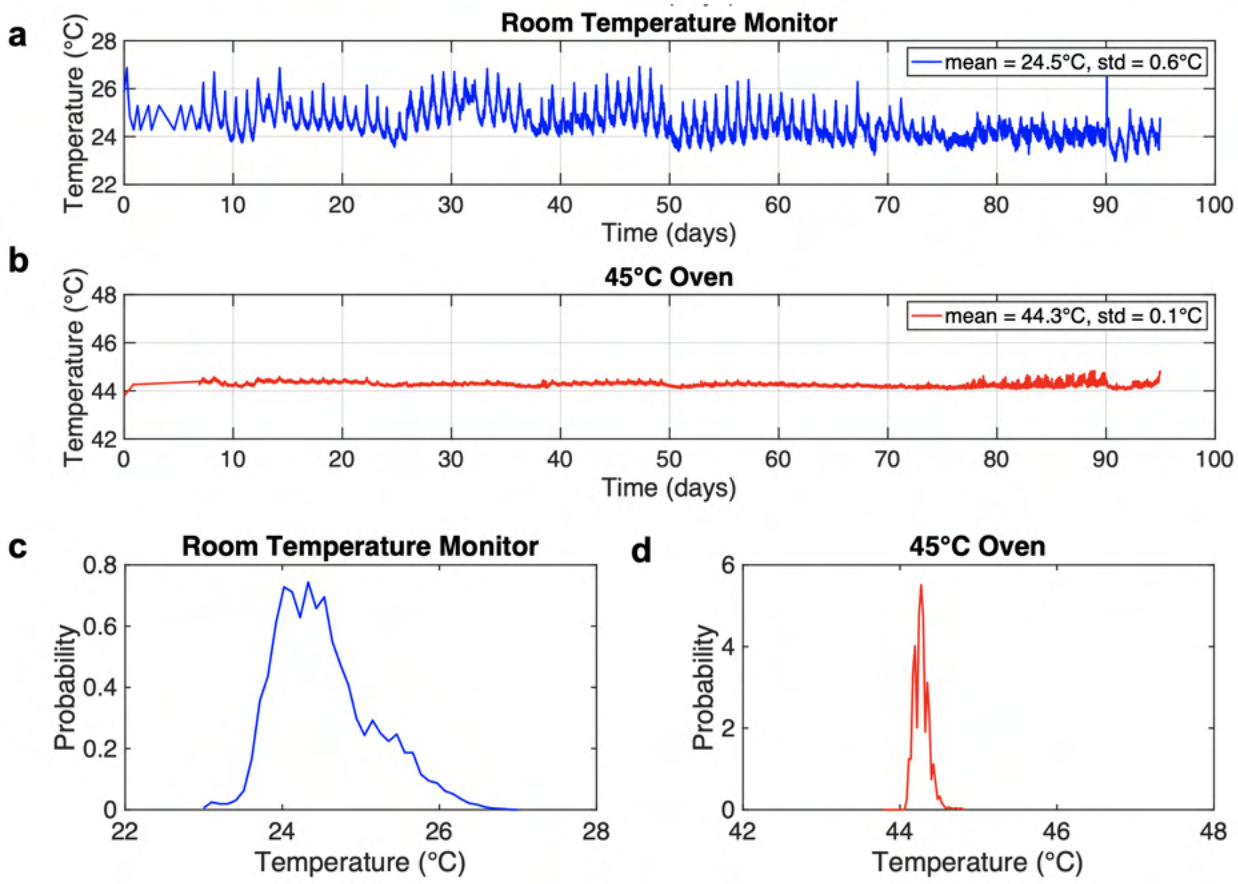

Figure B.21: Temperature measurement during cycle life testing. (a,b) Time-series data for the room temperature (a) and 45°C (b) tests. (c,d) Temperature histograms for the room temperature (a) and 45°C (d) tests.

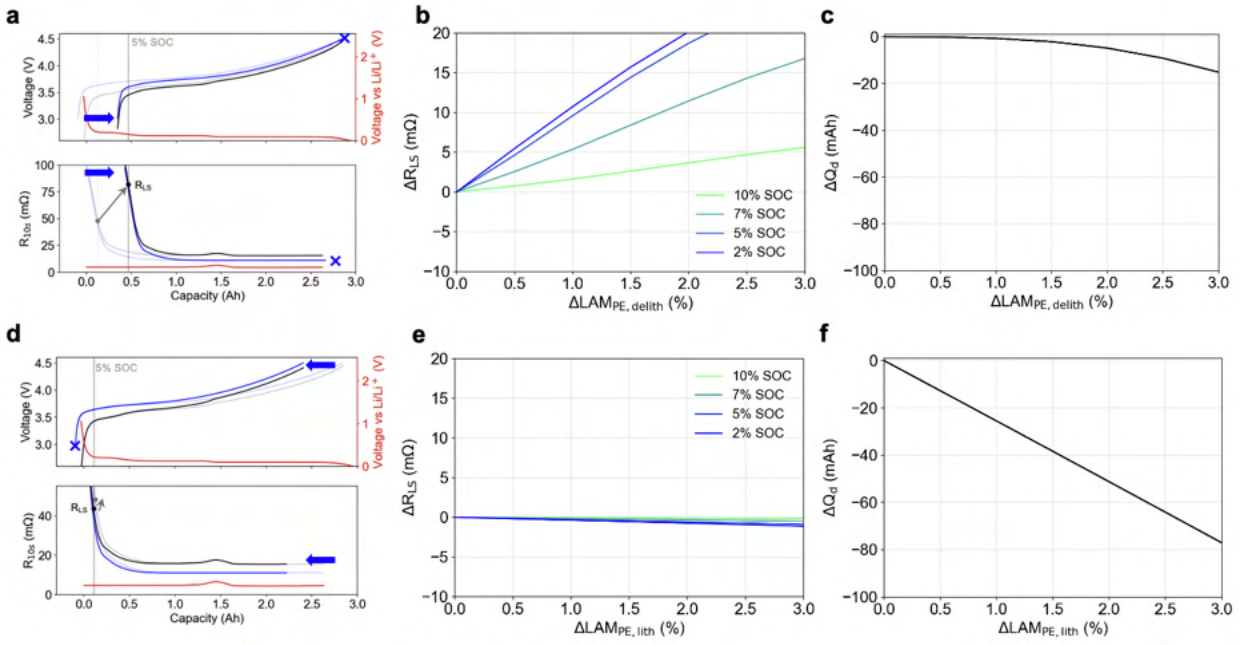

Figure B.22: Sensitivity of low-SOC resistance to loss of active material in the positive electrode. (a-c) Impact of loss of positive active material in the delithiated state. (d-e) Impact of loss of positive active material in the lithiated state. (c,f) Sensitivity of discharge capacity to loss of active material in the positive electrode. In (a,d), LAM is set to 15% for graphical clarity.

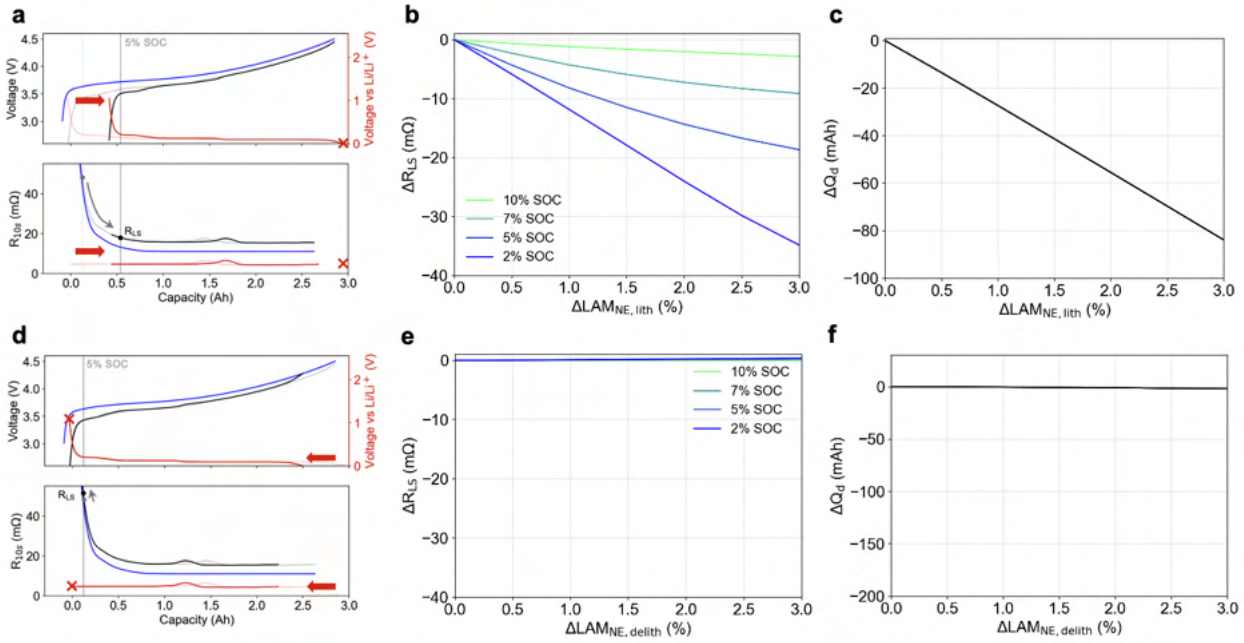

Figure B.23: Sensitivity of low-SOC resistance to loss of active material in the negative electrode. (a-c) Impact of loss of negative active material in the lithiated state. (d-e) Impact of loss of negative active material in the delithiated state. (c,f) Sensitivity of discharge capacity to loss of active material in the negative electrode. In (a,d), LAM is set to 15% for graphical clarity.

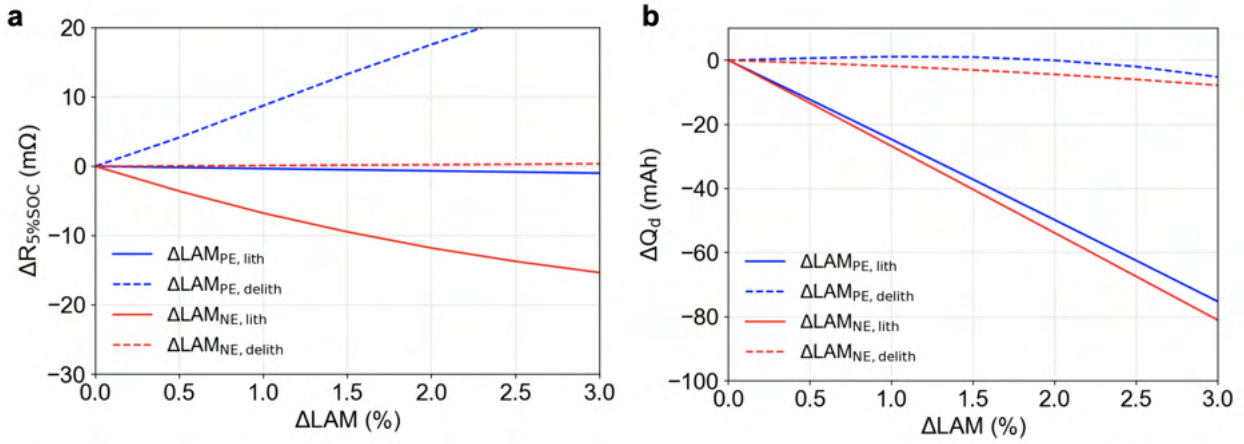

Figure B.24: Sensitivity of low-SOC resistance and discharge capacity to active material loss: summary. (a) Sensitivity of low-SOC resistance to different active material loss types. (b) Sensitivity of discharge capacity to different active material loss types. In general, active material can be lost at both the positive and negative electrodes, as well as in the lithiated and delithiated states.

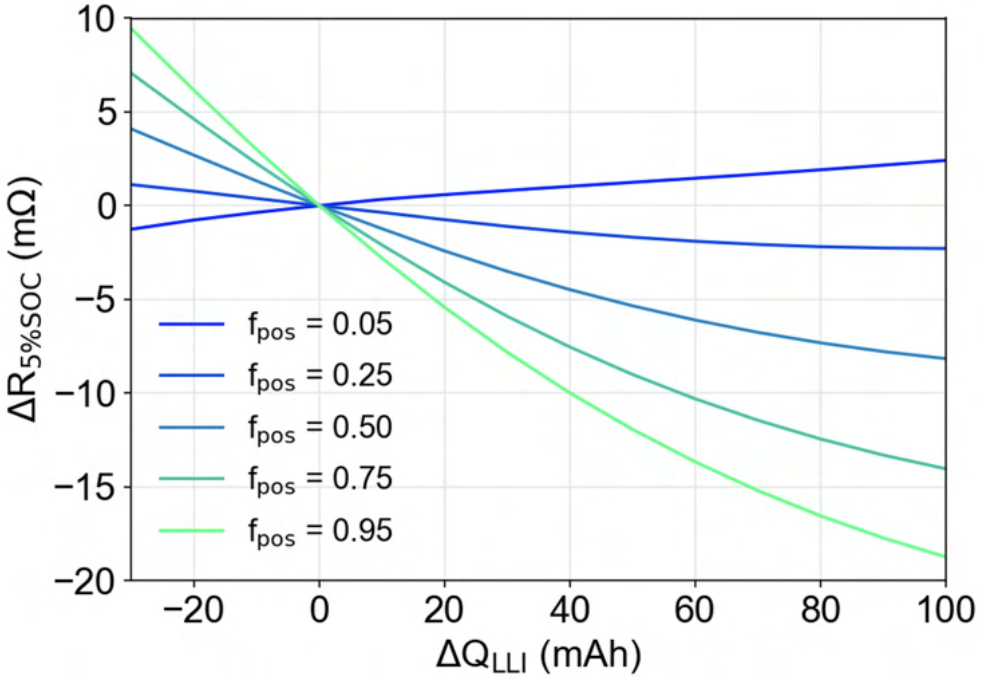

Figure B.25: Sensitivity of low-SOC resistance to ΔQ_{SEI} depends on fractional contribution of the positive electrode to the total cell resistance: example 2. Sensitivity of the resistance at 5% SOC to ΔQ_{SEI} for varying positive electrode resistance contributions to full cell resistance. f_{pos} is the fractional contribution of the positive electrode to the total cell resistance.

Figure B.26: Images of pouch cells taken after aging. Cell #9 has been excluded from the study due to tab weld issues.

B.1 Lithium Consumed During Formation: Signal-to-Noise

Here, we perform a simple set of calculations to determine the resolution limit of lithium consumed during formation (Q_{SEI}) as a function of the estimation method. We focus on comparing two estimation methods: the low-SOC resistance signal ($\mathrm{R_{LS}}$) and the cell discharge capacity (Q_{d}). Q_{d} represents a conventional signal measured using current integration. In this simplified analysis, we consider only the effect of lithium consumption and ignore possible effects from active material losses. For the analysis, we assume hardware specifications from the battery testing equipment used in our experiments (Maccor Series 4000). The hardware specifications and parameters used in the analysis are provided in Table B.1.

Parameter	**Symbol**	**Value**	**Unit**
Voltage Precision	V_{p}	0.02	% of FSR
Voltage Full-Scale Range	$\mathrm{V_{FSR}}$	5	V
Current Precision	$\mathrm{I_p}$	0.02	% of FSR
Current Full-Scale Range	$\mathrm{I_{FSR}}$	5	A
Current Setpoint for $\mathrm{R_{LS}}$ Calculations	$\mathrm{I_{set,1}}$	2.37 (= 1C)	A
Current Setpoint for Q_{d} Calculations	$\mathrm{I_{set,2}}$	0.237 (= C/10)	A

Table B.1: Parameters used for the signal-to-noise analysis

The current and voltage errors $\mathrm{I_{err}}$ and $\mathrm{V_{err}}$ can be calculated as

$$\begin{aligned} \mathrm{I_{err}} &= \mathrm{I_{FSR}} \cdot \mathrm{I_p}/100 \\ &= 0.001\mathrm{A} \end{aligned} \tag{B.1}$$

$$\begin{aligned} \mathrm{V_{err}} &= \mathrm{V_{FSR}} \cdot V_{\mathrm{p}}/100 \\ &= 0.001\mathrm{V}. \end{aligned} \tag{B.2}$$

The resolution limit for resistance, $\mathrm{R_{limit}}$, can be calculated as

$$\begin{aligned} \mathrm{R_{limit}} &= \mathrm{R_{high}} - \mathrm{R_{low}} \\ &= 0.88\mathrm{m}\Omega \end{aligned} \tag{B.3}$$

where

$$\mathrm{R_{high}} = \frac{\Delta V_{\mathrm{meas}} + \mathrm{V_{err}}}{\mathrm{I_{set,1}} - \mathrm{I_{err}}} \tag{B.4}$$

$$\mathrm{R_{low}} = \frac{\Delta V_{\mathrm{meas}} - \mathrm{V_{err}}}{\mathrm{I_{set,1}} + \mathrm{I_{err}}}. \tag{B.5}$$

In these equations, $\Delta \mathrm{V_{meas}}$ is the measured voltage drop during the discharge pulse. From Figure B.6, this value is less than 0.1V at low SOCs. For the remaining calculation, we assume $\Delta \mathrm{V_{meas}} = 0.1V$.

The resolution limit for a capacity measurement can be estimated as

$$\begin{aligned} \mathrm{Q_{limit}} &= \mathrm{Q_{high}} - \mathrm{Q_{low}} \\ &= 20\mathrm{mAh} \end{aligned} \tag{B.6}$$

where

$$\mathrm{Q_{high}} = (\mathrm{I_{set,2}} + \mathrm{I_{err}}) \cdot 10 \text{ hours} \tag{B.7}$$

$$\mathrm{Q_{low}} = (\mathrm{I_{set,2}} - \mathrm{I_{err}}) \cdot 10 \text{ hours}. \tag{B.8}$$

These capacities correspond to the C/10 constant current discharge steps during the final diagnostic cycle of the formation protocol (Figure 6.1b,c). Here, we neglect the effect of voltage inaccuracies which would add an additional error in the voltage termination condition for the discharge cycle. By ignoring this error, the estimate of the resolution limit for Q_{d} remains optimistic.

To calculate the sensitivity of ΔQ_{SEI} to $\Delta \mathrm{R_{LS}}$, we linearize the curve from Figure 4d at 5% SOC to find that

$$\begin{aligned} \frac{\Delta Q_{\mathrm{SEI}}}{\mathrm{R_{10s,5\%SOC}}} &= \frac{40\mathrm{mAh}}{10\mathrm{m}\Omega} \\ &= 5.00\mathrm{mAh/m}\Omega. \end{aligned} \tag{B.9}$$

A similar exercise is done for ΔQ_{d} which yields

$$\begin{aligned}\frac{\Delta Q_{\mathrm{SEI}}}{\Delta Q_{\mathrm{d}}} &= \frac{40\mathrm{mAh}}{37\mathrm{mAh}} \\ &= 1.08\mathrm{mAh/mAh}.\end{aligned} \tag{B.10}$$

Finally, the resolution of Q_{SEI} calculated using the two different methods are computed as

$$\begin{aligned}Q_{\mathrm{SEI}} \text{ calculated from } \mathrm{R}_{\mathrm{10s,5\%SOC}} &= \frac{\Delta Q_{\mathrm{SEI}}}{\Delta \mathrm{R}_{\mathrm{10s,5\%SOC}}} \cdot \mathrm{R}_{\mathrm{limit}} \\ &= 3.9\mathrm{mAh}\end{aligned} \tag{B.11}$$

$$\begin{aligned}Q_{\mathrm{SEI}} \text{ calculated from } Q_{\mathrm{d}} &= \frac{\Delta Q_{\mathrm{SEI}}}{\Delta Q_{\mathrm{d}}} \cdot \mathrm{Q}_{\mathrm{limit}} \\ &= 22.2\mathrm{mAh}.\end{aligned} \tag{B.12}$$

This simple calculation demonstrates that the low-SOC resistance metric improves the resolution limit of Q_{SEI} by five-fold compared to the same calculation made using Q_{d}.

We note that $\mathrm{Q}_{\mathrm{limit}} = 20$ mAh corresponds to the magnitude of the difference in lithium consumed between the fast formation and baseline formation protocols (23 mAh), which confirms that it would be difficult to detect such small changes in lithium consumption using ordinary cycler equipment.

The precision of the Q_{d} measurement can be improved in several ways. First, a higher C-rate discharge would lead to less current integration error and higher accuracy. However, a high-rate discharge would also include a kinetic contribution making it more difficult to correlate to lithium loss. Second, Q_{d} can also be improved by using higher precision cyclers. For example, if the voltage and current precision both increased by 100-fold, then the resolution limit of Q_{SEI} calculated from Q_{d} will have improved to 0.2 mAh. However, in this scenario, the resolution limit of Q_{SEI} calculated from $\mathrm{R}_{\mathrm{10s,5\%SOC}}$ would also have improved to 0.04 mAh.

B.2 Fast Formation and Gas Evolution over Cycle Life

At the negative electrode, some common gas-generating reaction pathways include the reduction of ethylene carbonate (EC) to form carbon monoxide (CO) and the reduction of water impurities (e.g. from manufacturing) which can form carbon dioxide (CO_2) and hydrogen gas [321]. Since every cell in the experiment was taken from the same manufacturing batch, their water content is expected to be similar. It is therefore unlikely that water reduction pathways is the major source of difference in the amount of gas formed between the two different formation protocols. Next, the reduction of EC is lithium-consuming and thus the amount of CO formed through this reaction pathway is expected to correlate to the loss of lithium inventory (LLI) over life. However, our voltage fitting analysis (Figures 6.6, 6.7) suggests that the rate of LLI for fast formation cells is equal to or lower than that of baseline formation. We therefore expect the formation rate of CO from the EC reduction pathway to be comparable between the two different formation protocols. From this brief survey, it is unlikely that a reaction pathway based on the negative electrode can account for differences in measured gas amount over life between the two different formation protocols.

We note that oxidation reactions at the positive electrode (e.g. at high potentials) can also contribute to gas evolution over aging. Common reaction pathways at the positive electrode include the decomposition of lithium carbonate at the surface of the NMC electrodes and the oxidation of EC. The reaction products include the generation of CO_2, CO, and oxygen gas [321]. These reactions are known to accelerate at higher positive electrode potentials vs Li/Li^+, a phenomenon studied in detail by Jung et al. [322].

To determine whether fast formation could have caused the positive electrode to experience higher potentials at the top of charge, we used the electrode stoichiometry model to measure the impact of increased lithium consumption during formation on the positive electrode potential vs Li/Li^+ at the top of charge (i.e. 4.2V in the full cell). The result, shown in Figure B.27, illustrates how an increase in the magnitude of ΔQ_{SEI} shifts the positive electrode stoichiometry window towards marginally lower values at both the bottom of discharge and the top of charge. From this graphical analysis, we see that the positive electrode stoichiometry at the top of charge (i.e. 4.2V in the full cell) has increased by 0.5 mV vs Li/Li^+. Thus, fast formation may have increased the positive electrode potential at the top of charge, creating a more oxidizing environment and promoting more gas generation. While the difference in the potential is marginal, a small change in oxidation rates could lead to a large difference in accumulated gas generated over the course of hundreds of cycles. We also note that a significant portion of the charge cycles are spent in the CV hold phase where the positive electrode would stay at this higher potential. A similar mechanism has been

identified as part of work by Dose et al. [323]. Note that Dose et al. observed that the positive electrode impedance increased due to these oxidation reactions, but in our work, this impedance rise was not observed (Figure 6.6a).

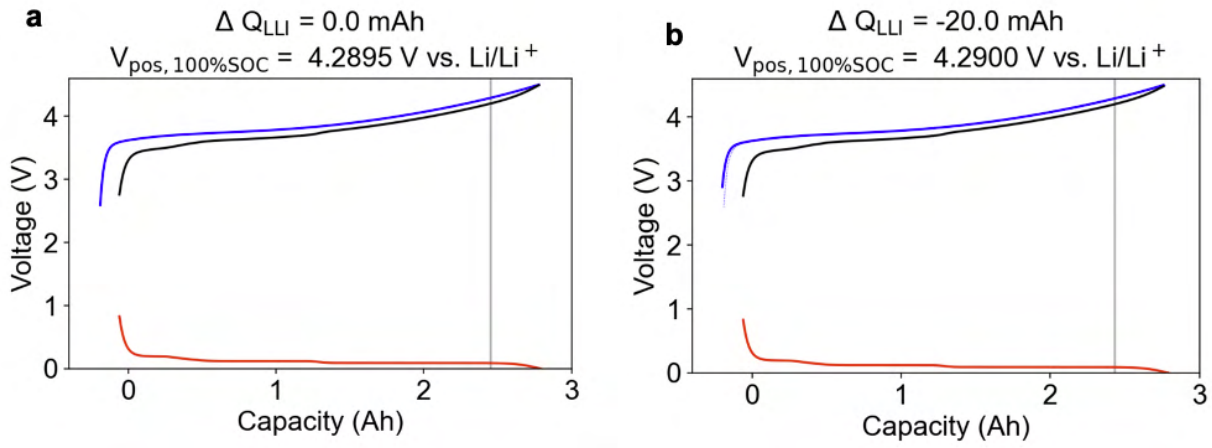

Figure B.27: Electrode stoichiometry model showing the impact of 20 mAh of additional lithium loss on the positive electrode potential at the top of charge. (a) Model for baseline formation. (b) Model for fast formation.

In general, gas build-up represents the combination of gas both generated and consumed. Xiong et al. [324] demonstrated that gas in NMC-graphite cells can be generated at the positive electrode and subsequently reduced at the negative electrode via a 'shuttle' mechanism [325]. At the positive electrode, gas species such as O_2, CO, and CO_2 can be generated through electrolyte oxidation pathways [321, 322], and at the negative electrode, gas species can be further reduced into solid products [321]. Fast formation may be exacerbating the gas generation rate, suppressing the gas consumption rate, or both.

We further hypothesize that the gas build-up over life may have a secondary benefit to cycle life. Krause et al. [326] and Chevrier et al. [327] have reported that the reduction of CO_2 at the negative electrode contributes to the SEI growth process and have a stabilizing effect. Since fast formation had increased cycle life, it is possible that more CO_2 is being generated at the positive electrode and reduced at the negative electrode, further improving SEI passivation and delaying the knee-point. More experimental work will be needed to confirm this theory.

B.3 Effect of Lithium Consumption during Formation on Maximum Positive Electrode Stoichiometry

A careful study of the electrode-specific equilibrium potential curves suggests another possible contributor to the improved cycle life seen in fast formation cells. Returning to Figure 4a, we observe that the capacity corresponding to the extra lithium consumed from fast formation, ΔQ_{SEI}, is also associated with a decrease in the maximum positive electrode stoichiometry, y_{max}. Since fast formation consumed more lithium to create the SEI, the positive electrode becomes less fully lithiated when the cell is fully discharged. By comparison, the positive electrodes of baseline formation cells will be more lithiated at the end of discharge.

Access to higher positive electrode lithiation states is associated with higher levels of particle-level stress, leading to more likelihood for cracking of the ceramic oxide secondary particles [328, 246, 248]. Stress-induced cracking over life can lead to electrical isolation of particles, resulting in loss of active sites. The cracking may also expose additional surface area which could accelerate the rate of parasitic reactions leading to earlier knee-points [130]. We speculate that this difference in y_{max}, while small, could protect the fast formation cells against cracking over the course of many cycles, leading to an overall improvement in the overall cycle life. This degradation mechanism is particularly relevant in our testing where every cycle ends on the minimum voltage target of 3.0V. This 'hidden degradation mechanism' involving the positive electrode motivates the usage of the low-SOC resistance, $\Delta \mathrm{R}_{\mathrm{LS}}$, to quantify the small changes in Δy_{max} due to new formation protocols.

BIBLIOGRAPHY

[1] Volta Foundation. The battery report 2022. Technical report, Volta Foundation, January 2022.

[2] Consultancy Uk. Global demand for lithium-ion batteries to quadruple by 2030. https://www.consultancy.uk/news/31072/global-demand-for-lithium-ion-batteries-to-quadruple-by-2030, April 2022. Accessed: 2023-8-1.

[3] Conor Sen. US 'battery belt' will be a new kind of job magnet. *The Washington Post*, December 2022.

[4] Liz Allen, Alison O'Connell, and Veronique Kiermer. How can we ensure visibility and diversity in research contributions? how the contributor role taxonomy (CRediT) is helping the shift from authorship to contributorship. *Learn. Publ.*, 32(1):71–74, January 2019.

[5] Andrew Weng, Everardo Olide, Iaroslav Kovalchuk, Jason B Siegel, and Anna Stefanopoulou. Modeling battery formation: Boosted SEI growth, Multi-Species reactions, and irreversible expansion. *J. Electrochem. Soc.*, 170(9):090523, September 2023.

[6] Andrew Weng, Jason B. Siegel, and Anna Stefanopoulou. Differential voltage analysis for battery manufacturing process control. *Frontiers in Energy Research*, 11, 2023.

[7] Andrew Weng, Peyman Mohtat, Peter M. Attia, Valentin Sulzer, Suhak Lee, Greg Less, and Anna Stefanopoulou. Predicting the impact of formation protocols on battery lifetime immediately after manufacturing. *Joule*, 5(11):2971–2992, 2021.

[8] Andrew Weng, Hamidreza Movahedi, Clement Wong, Jason B Siegel, and Anna G Stefanopoulou. Current imbalance in dissimilar Parallel-Connected batteries and the fate of degradation convergence. *J. Dyn. Syst. Meas. Control*, pages 1–22, November 2023.

[9] Andrew Weng, Sravan Pannala, Jason B Siegel, and Anna G Stefanopoulou. Parallel-connected battery current imbalance dynamics. *IFAC-PapersOnLine*, 55(37):37–43, 2022.

[10] Andrew Weng, Eric Dufek, and Anna Stefanopoulou. Battery passports for promoting electric vehicle resale and repurposing. *Joule*, 7(5):837–842, May 2023.

[11] Sravan Pannala, Andrew Weng, Ian Fischer, Jason B Siegel, and Anna G Stefanopoulou. Low-Cost inductive sensor and fixture kit for measuring battery cell thickness under constant pressure. *IFAC-PapersOnLine*, 55(37):712–717, January 2022.

[12] Omar Y Ahmed, Robert J Middleton, Vivian Tran, Andrew Weng, Anna G Stefanopoulou, Kenneth S Kim, and Chol-Bum M Kweon. Model predictive control of combustion phasing in compression ignition engines by coordinating fuel injection timing and ignition assist. *IFAC-PapersOnLine*, 55(24):90–96, January 2022.

[13] Heiner Heimes, Achim Kampker, Christoph Lienemann, Marc Locke, Christian Offermanns, Sarah Michaelis, and Ehsan Rahimzei. Lithium-ion battery cell production process. Technical report, Aachen University, February 2019.

[14] Yangtao Liu, Ruihan Zhang, Jun Wang, and Yan Wang. Current and future lithium-ion battery manufacturing. *iScience*, 24(4):102332, April 2021.

[15] W Blake Hawley and Jianlin Li. Electrode manufacturing for lithium-ion batteries—analysis of current and next generation processing. *Journal of Energy Storage*, 25:100862, October 2019.

[16] Pradeep Kumar Dammala, Kamil Burak Dermenci, Anish Raj Kathribail, Poonam Yadav, Joeri Van Mierlo, and Maitane Berecibar. A critical review of future aspects of digitalization next generation li-ion batteries manufacturing process. *Journal of Energy Storage*, 74:109209, December 2023.

[17] Kristian Kuhlmann, Sebastian Wolf, Cornelius Pieper, Gang Xu, and Justin Ahmad. The Future of Battery Production for Electric Vehicles. Technical report, Boston Consulting Group, 2018.

[18] Yang Zhang, Song Lu, Zaisheng Wang, Vladislav Volkov, Fengliu Lou, and Zhixin Yu. Recent technology development in solvent-free electrode fabrication for lithium-ion batteries. *Renewable Sustainable Energy Rev.*, 183:113515, September 2023.

[19] Mozaffar Abdollahifar, Heather Cavers, Sören Scheffler, Alexander Diener, Mark Lippke, and Arno Kwade. Insights into influencing electrode calendering on the battery performance. *Adv. Energy Mater.*, 13(40), October 2023.

[20] Chris Meyer, Henrike Bockholt, Wolfgang Haselrieder, and Arno Kwade. Characterization of the calendering process for compaction of electrodes for lithium-ion batteries. *J. Mater. Process. Technol.*, 249:172–178, November 2017.

[21] Hitesh Yadav. The heart of Lithium-Ion battery production: Winding machines. https://www.linkedin.com/pulse/heart-lithium-ion-battery-production-winding-machines-hitesh-yadav, April 2023. Accessed: 2024-1-3.

[22] Vic Sistos, Jung Park, Kevin Pope, Michael Tomcsi, Joao Yanez, and Michael Escobar. Establishment of a pilot manufacturing line for lithium ion modules for use as building

blocks for battery systems in electric vehicle applications. Technical Report CEC-600-2020-053, California Energy Commission, December 2020.

[23] Martin J Brand, Philipp A Schmidt, Michael F Zaeh, and Andreas Jossen. Welding techniques for battery cells and resulting electrical contact resistances. *Journal of Energy Storage*, 1:7–14, June 2015.

[24] Hao Cui, Youzhi Song, Dongsheng Ren, Li Wang, and Xiangming He. Electrocapillary boosting electrode wetting for high-energy lithium-ion batteries. *Joule*, December 2023.

[25] Hao He, Yadong Liu, Qi Liu, Zhefei Li, Fan Xu, Clif Dun, Yang Ren, Mei-Xian Wang, and Jian Xie. Failure investigation of LiFePO4 cells in Over-Discharge conditions. *J. Electrochem. Soc.*, 160(6):A793, March 2013.

[26] Perla B Balbuena and Yixuan Wang, editors. *Lithium-Ion Batteries: Solid-Electrolyte Interphase*. Imperial College Press, May 2004.

[27] M B Pinson and M Z Bazant. Theory of SEI formation in rechargeable batteries: Capacity fade, accelerated aging and lifetime prediction. *Pinson, M. B., and M. Z. Bazant. "Theory of SEI Formation in Rechargeable Batteries: Capacity Fade, Accelerated Aging and Lifetime Prediction." Journal of the Electrochemical Society*, 16:0.2, December 2012.

[28] E Peled and S Menkin. Review—SEI: Past, present and future. *J. Electrochem. Soc.*, 164(7):A1703–A1719, 2017.

[29] Satu Kristiina Heiskanen, Jongjung Kim, and Brett L Lucht. Generation and evolution of the solid electrolyte interphase of Lithium-Ion batteries. *Joule*, 3(10):2322–2333, 2019.

[30] Seong Jin An, Jianlin Li, Zhijia Du, Claus Daniel, and David L. Wood. Fast formation cycling for lithium ion batteries. *Journal of Power Sources*, 342(February 2018):846–852, 2017.

[31] David L Wood, Jianlin Li, and Seong Jin An. Formation challenges of Lithium-Ion battery manufacturing. *Joule*, 3(12):2884–2888, 2019.

[32] Paul A Nelson, Shabbir Ahmed, Kevin G Gallagher, and Dennis W Dees. Modeling the performance and cost of Lithium-Ion batteries for Electric-Drive vehicles, third edition. Technical report, Argonne National Laboratory, 2019.

[33] F Degen, M Winter, D Bendig, and J Tübke. Energy consumption of current and future production of lithium-ion and post lithium-ion battery cells. *Nature Energy*, 8(11):1284–1295, September 2023.

[34] Hsiang Hwan Lee, Yung Yun Wang, Chi Chao Wan, Mo Hua Yang, Hung Chun Wu, and Deng Tswen Shieh. A fast formation process for lithium batteries. *Journal of Power Sources*, 134(1):118–123, 2004.

[35] Peter M Attia, Stephen J Harris, and William C Chueh. Benefits of fast battery formation in a model system. *J. Electrochem. Soc.*, 168(5):050543, 2021.

[36] Nancy Dietz Rago, John K Basco, Anh Vu, Jianlin Li, Kevin Hays, Yangping Sheng, David L Wood, and Ira Bloom. Effect of formation protocol: Cells containing Si-Graphite composite electrodes. *J. Power Sources*, 435(February):126548, 2019.

[37] Michael Ryan, Patrick Münster, Marcel Diehl, Joop Enno, B Markus, Martin Winter, and Philip Niehoff. Effect of li plating during formation of lithium ion batteries on their cycling performance and thermal safety. *J. Power Sources*, 484:0–7, 2021.

[38] E Peled. The electrochemical behavior of alkali and alkaline earth metals in nonaqueous battery Systems—The solid electrolyte interphase model. *J. Electrochem. Soc.*, 126(12):2047, December 1979.

[39] Fridolin Röder, Richard D Braatz, and Ulrike Krewer. Multi-scale simulation of heterogeneous surface film growth mechanisms in lithium-ion batteries. *J. Electrochem. Soc.*, 164(11):E3335, June 2017.

[40] Seong Jin An, Jianlin Li, Claus Daniel, Debasish Mohanty, Shrikant Nagpure, and David L Wood. The state of understanding of the lithium-ion-battery graphite solid electrolyte interphase (SEI) and its relationship to formation cycling. *Carbon N. Y.*, 105:52–76, 2016.

[41] Remi Petibon. *Study of the Reactivity of Electrolyte Solvents and Additives in Li-Ion Cells and Design of New Electrolyte Blends*. PhD thesis, Dalhousie University, 2016.

[42] L D Ellis, J P Allen, I G Hill, and J R Dahn. High-Precision coulometry studies of the impact of temperature and time on SEI formation in Li-Ion cells. *J. Electrochem. Soc.*, 165(7):A1529, May 2018.

[43] A J Louli, L D Ellis, and J R Dahn. Operando pressure measurements reveal solid electrolyte interphase growth to rank Li-Ion cell performance. *Joule*, 3(3):745–761, March 2019.

[44] William Huang, Peter M Attia, Hansen Wang, Sara E Renfrew, Norman Jin, Supratim Das, Zewen Zhang, David T Boyle, Yuzhang Li, Martin Z Bazant, Bryan D McCloskey, William C Chueh, and Yi Cui. Evolution of the Solid-Electrolyte interphase on carbonaceous anodes visualized by Atomic-Resolution cryogenic electron microscopy. *Nano Lett.*, 19(8):5140–5148, August 2019.

[45] Junxiong Wu, Muhammad Ihsan-Ul-Haq, Yuming Chen, and Jang-Kyo Kim. Understanding solid electrolyte interphases: Advanced characterization techniques and theoretical simulations. *Nano Energy*, 89:106489, November 2021.

[46] Moon Young Yang, Sergey V Zybin, Tridip Das, Boris V Merinov, William A Goddard, Eun Kyung Mok, Hoe Jin Hah, Hyea Eun Han, Young Cheol Choi, and Seung Ha Kim. Characterization of the solid electrolyte interphase at the li metal–ionic liquid interface. *Adv. Energy Mater.*, 13(3):2202949, January 2023.

[47] Yaolin Xu, Kang Dong, Yulin Jie, Philipp Adelhelm, Yawei Chen, Liang Xu, Peiping Yu, Junghwa Kim, Zdravko Kochovski, Zhilong Yu, Wanxia Li, James LeBeau, Yang Shao-Horn, Ruiguo Cao, Shuhong Jiao, Tao Cheng, Ingo Manke, and Yan Lu. Promoting mechanistic understanding of lithium deposition and solid-electrolyte interphase (SEI) formation using advanced characterization and simulation methods: Recent progress, limitations, and future perspectives. *Adv. Energy Mater.*, 12(19):2200398, May 2022.

[48] Aiping Wang, Sanket Kadam, Hong Li, Siqi Shi, and Yue Qi. Review on modeling of the anode solid electrolyte interphase (SEI) for lithium-ion batteries. *npj Computational Materials*, 4(1), 2018.

[49] John Christensen and John Newman. A mathematical model for the Lithium-Ion negative electrode solid electrolyte interphase. *J. Electrochem. Soc.*, 151(11):A1977, October 2004.

[50] Harry J Ploehn, Premanand Ramadass, and Ralph E White. Solvent diffusion model for aging of Lithium-Ion battery cells. *J. Electrochem. Soc.*, 151(3):A456, February 2004.

[51] Lars von Kolzenberg, Arnulf Latz, and Birger Horstmann. Solid–Electrolyte interphase during battery cycling: Theory of growth regimes. *ChemSusChem*, 13(15):3901–3910, 2020.

[52] Lars von Kolzenberg, Jochen Stadler, Johannes Fath, Madeleine Ecker, Birger Horstmann, and Arnulf Latz. A four parameter model for the solid-electrolyte interphase to predict battery aging during operation. *J. Power Sources*, 539:231560, August 2022.

[53] Lars von Kolzenberg, Arnulf Latz, and Birger Horstmann. Chemo-mechanical model of SEI growth on silicon electrode particles. *Batter. Supercaps*, 5(2), February 2022.

[54] Supratim Das, Peter M Attia, William C Chueh, and Martin Z Bazant. Electrochemical kinetics of SEI growth on carbon black: Part II. modeling. *J. Electrochem. Soc.*, 166(4):E107, February 2019.

[55] E Peled, D Golodnitsky, and G Ardel. Advanced model for solid electrolyte interphase electrodes in liquid and polymer electrolytes. *J. Electrochem. Soc.*, 144(8):L208, August 1997.

[56] Xiao Guang Yang, Yongjun Leng, Guangsheng Zhang, Shanhai Ge, and Chao Yang Wang. Modeling of lithium plating induced aging of lithium-ion batteries: Transition from linear to nonlinear aging. *J. Power Sources*, 360:28–40, 2017.

[57] M Safari, M Morcrette, A Teyssot, and C Delacourt. Multimodal physics-based aging model for life prediction of Li-Ion batteries. *J. Electrochem. Soc.*, 156(3):A145, December 2008.

[58] Niloofar Kamyab, John Weidner, and R E White. Mixed mode growth model for the solid electrolyte interphase (sei). *Journal of the Electrochemical Society*, 166(2):A334–A341, January 2019.

[59] Alfred V Randall, Roger D Perkins, Xiangchun Zhang, and Gregory L Plett. Controls oriented reduced order modeling of solid-electrolyte interphase layer growth. *J. Power Sources*, 209:282–288, July 2012.

[60] Zhe Li, Anhao Zuo, Zhaobin Mo, Mu Lin, Chengyu Wang, Jianbo Zhang, Markus H Hofmann, and Andreas Jossen. Demonstrating stability within parallel connection as a basis for building large-scale battery systems. *Cell Reports Physical Science*, page 101154, November 2022.

[61] Shiv Krishna Madi Reddy, Wei Shang, and Ralph E White. Mathematical model for SEI growth under Open-Circuit conditions. *J. Electrochem. Soc.*, 169(9):090505, September 2022.

[62] A Jana, A S Mitra, S Das, W C Chueh, M Z Bazant, and others. Physics-based, reduced order degradation model of lithium-ion batteries. *J. Power Sources*, 2022.

[63] Joseph W Abbott and Felix Hanke. Kinetically corrected monte Carlo-Molecular dynamics simulations of solid electrolyte interphase growth. *J. Chem. Theory Comput.*, 18(2):925–934, February 2022.

[64] P Ramadass, Bala Haran, Parthasarathy M Gomadam, Ralph White, and Branko N Popov. Development of first principles capacity fade model for Li-Ion cells. *J. Electrochem. Soc.*, 151(2):A196, January 2004.

[65] Shan Yang, Binggong Yan, Jiaxiong Wu, Li Lu, and Kaiyang Zeng. Temperature-Dependent Lithium-Ion diffusion and activation energy of Li1.2Co0.13Ni0.13Mn0.54O2 Thin-Film cathode at nanoscale by using electrochemical strain microscopy. *ACS Appl. Mater. Interfaces*, 9(16):13999–14005, April 2017.

[66] Tao Gao, Yu Han, Dimitrios Fraggedakis, Supratim Das, Tingtao Zhou, Che-Ning Yeh, Shengming Xu, William C Chueh, Ju Li, and Martin Z Bazant. Interplay of lithium intercalation and plating on a single graphite particle. *Joule*, 5(2):393–414, February 2021.

[67] M Dubarry and D Anseán. Best practices for incremental capacity analysis. *Frontiers in Energy Research*, 2022.

[68] Hannah M Dahn, A J Smith, J C Burns, D A Stevens, and J R Dahn. User-Friendly differential voltage analysis freeware for the analysis of degradation mechanisms in Li-Ion batteries. *J. Electrochem. Soc.*, 159(9):A1405, August 2012.

[69] Suhak Lee, Jason B. Siegel, Anna G. Stefanopoulou, Jang-Woo Lee, and Tae-Kyung Lee. Electrode State of Health Estimation for Lithium Ion Batteries Considering Half-cell Potential Change Due to Aging. *Journal of The Electrochemical Society*, 167(9):090531, 2020.

[70] Lingxi Kong, Ryan Aalund, Mohammad Alipour, Stanislav I Stoliarov, and Michael Pecht. Evaluating the manufacturing quality of lithium ion pouch batteries. *J. Electrochem. Soc.*, 169:040541, April 2022.

[71] Guannan Qian, Federico Monaco, Dechao Meng, Sang-Jun Lee, Guibin Zan, Jizhou Li, Dmitry Karpov, Sheraz Gul, David Vine, Benjamin Stripe, Jin Zhang, Jun-Sik Lee, Zi-Feng Ma, Wenbin Yun, Piero Pianetta, Xiqian Yu, Linsen Li, Peter Cloeten, and Yijin Liu. The role of structural defects in commercial lithium-ion batteries. *Cell Reports Physical Science*, 2(9):100554, September 2021.

[72] Clement Bommier, Wesley Chang, Jianlin Li, Shaurjo Biswas, Greg Davies, Jagjit Nanda, and Daniel Steingart. Operando acoustic monitoring of SEI formation and Long-Term cycling in NMC/SiGr composite pouch cells. *J. Electrochem. Soc.*, 167(2):020517, 2020.

[73] Zhe Deng, Zhenyu Huang, Yue Shen, Yunhui Huang, Han Ding, Aidan Luscombe, Michel Johnson, Jessie E Harlow, Roby Gauthier, and Jeff R Dahn. Ultrasonic scanning to observe wetting and "unwetting" in Li-Ion pouch cells. *Joule*, 4(9):2017–2029, 2020.

[74] Peyman Mohtat, Suhak Lee, Valentin Sulzer, Jason B Siegel, and Anna G Stefanopoulou. Differential expansion and voltage model for li-ion batteries at practical charging rates. *J. Electrochem. Soc.*, 167(11):110561, 2020.

[75] Peyman Mohtat, Suhak Lee, Jason B Siegel, and Anna G Stefanopoulou. Reversible and irreversible expansion of Lithium-Ion batteries under a wide range of stress factors. *J. Electrochem. Soc.*, 168(10):100520, October 2021.

[76] Gang Ning, Ralph E White, and Branko N Popov. A generalized cycle life model of rechargeable li-ion batteries. *Electrochim. Acta*, 51(10):2012–2022, 2006.

[77] Henrik Ekström and Göran Lindbergh. A model for predicting capacity fade due to SEI formation in a commercial Graphite/LiFePO4 cell. *J. Electrochem. Soc.*, 162(6):A1003, March 2015.

[78] Jorn M Reniers, Grietus Mulder, and David A Howey. Review and performance comparison of Mechanical-Chemical degradation models for Lithium-Ion batteries. *J. Electrochem. Soc.*, 166(14):A3189–A3200, 2019.

[79] Christian Kupper, Björn Weißhar, Sascha Rißmann, and Wolfgang G Bessler. End-of-Life prediction of a Lithium-Ion battery cell based on mechanistic aging models of the graphite electrode. *J. Electrochem. Soc.*, 165(14):A3468–A3480, 2018.

[80] Izaro Laresgoiti, Stefan Käbitz, Madeleine Ecker, and Dirk Uwe Sauer. Modeling mechanical degradation in lithium ion batteries during cycling: Solid electrolyte interphase fracture. *J. Power Sources*, 300:112–122, December 2015.

[81] F Brosa Planella, W Ai, A M Boyce, A Ghosh, I Korotkin, S Sahu, V Sulzer, R Timms, T G Tranter, M Zyskin, S J Cooper, J S Edge, J M Foster, M Marinescu, B Wu, and

G Richardson. A continuum of physics-based lithium-ion battery models reviewed. *Prog. Energy Combust. Sci.*, 4(4):042003, July 2022.

[82] A A Wang, S E J O'Kane, F Brosa Planella, J Le Houx, K O'Regan, M Zyskin, J Edge, C W Monroe, S J Cooper, D A Howey, E Kendrick, and J M Foster. Review of parameterisation and a novel database (LiionDB) for continuum li-ion battery models. *Prog. Energy Combust. Sci.*, 4(3):032004, May 2022.

[83] Simon E J O'Kane, Weilong Ai, Ganesh Madabattula, Diego Alonso-Alvarez, Robert Timms, Valentin Sulzer, Jacqueline Sophie Edge, Billy Wu, Gregory J Offer, and Monica Marinescu. Lithium-ion battery degradation: how to model it. *Phys. Chem. Chem. Phys.*, 24(13):7909–7922, March 2022.

[84] Fabian Single, Birger Horstmann, and Arnulf Latz. Dynamics and morphology of solid electrolyte interphase (SEI). *Phys. Chem. Chem. Phys.*, 18(27):17810–17814, July 2016.

[85] Fabian Single, Birger Horstmann, and Arnulf Latz. Revealing SEI morphology: In-Depth analysis of a modeling approach. *J. Electrochem. Soc.*, 164(11):E3132–E3145, 2017.

[86] Lars von Kolzenberg, Martin Werres, Jonas Tetzloff, and Birger Horstmann. Transition between growth of dense and porous films: theory of dual-layer SEI. *Phys. Chem. Chem. Phys.*, 24(31):18469–18476, August 2022.

[87] Liya Guo, Daisy B Thornton, Mohamed A Koronfel, Ifan E L Stephens, and Mary P Ryan. Degradation in lithium ion battery current collectors. *J. Phys. Energy*, 3(3):032015, July 2021.

[88] Peter M Attia, William C Chueh, and Stephen J Harris. Revisiting the t 0.5 dependence of SEI growth. *J. Electrochem. Soc.*, 167(9):090535, 2020.

[89] Ben Rowden and Nuria Garcia-Araez. A review of gas evolution in lithium ion batteries. *Energy Reports*, 6:10–18, 2020.

[90] Sun-Ho Kang, Won-Sub Yoon, Kyung-Wan Nam, Xiao-Qing Yang, and Daniel P Abraham. Investigating the first-cycle irreversibility of lithium metal oxide cathodes for li batteries. *J. Mater. Sci.*, 43(14):4701–4706, July 2008.

[91] Kandler Smith, Paul Gasper, Andrew M Colclasure, Yuta Shimonishi, and Shuhei Yoshida. Lithium-Ion battery life model with electrode cracking and Early-Life break-in processes. *J. Electrochem. Soc.*, 2021.

[92] Zhixin Xu, Jun Yang, Tao Zhang, Yanna Nuli, Jiulin Wang, and Shin-Ichi Hirano. Silicon microparticle anodes with Self-Healing multiple network binder. *Joule*, 2(5):950–961, May 2018.

[93] Jijian Xu. Critical review on cathode-electrolyte interphase toward High-Voltage cathodes for Li-Ion batteries. *Nanomicro Lett*, 14(1):166, August 2022.

[94] Sungjemmenla, Vineeth, Chhail Bihari Soni, Vipin Kumar, and Zhi Wei Seh. Understanding the cathode–electrolyte interphase in lithium-ion batteries. *Energy Technol.*, 10(9):2200421, September 2022.

[95] *State of Charge Estimation Error due to Parameter Mismatch in a Generalized Explicit Lithium Ion Battery Model*, volume ASME 2011 Dynamic Systems and Control Conference and Bath/ASME Symposium on Fluid Power and Motion Control, Volume 1 of *Dynamic Systems and Control Conference*, 10 2011.

[96] Gregory L Plett. *Battery Management Systems, Volume I: Battery Modeling*. Artech House, September 2015.

[97] D Aurbach, M L Daroux, P W Faguy, and E Yeager. Identification of surface films formed on lithium in propylene carbonate solutions. *J. Electrochem. Soc.*, 134(7):1611, July 1987.

[98] Bo Zhang, Michael Metzger, Sophie Solchenbach, Martin Payne, Stefano Meini, Hubert A Gasteiger, Arnd Garsuch, and Brett L Lucht. Role of 1,3-propane sultone and vinylene carbonate in solid electrolyte interface formation and gas generation. *J. Phys. Chem. C*, 119(21):11337–11348, May 2015.

[99] Guorong V Zhuang, Kang Xu, Hui Yang, T Richard Jow, and Philip N Ross, Jr. Lithium ethylene dicarbonate identified as the primary product of chemical and electrochemical reduction of EC in 1.2 M LiPF6/EC:EMC electrolyte. *J. Phys. Chem. B*, 109(37):17567–17573, September 2005.

[100] Thomas F Fuller, Marc Doyle, and John Newman. Simulation and optimization of the dual lithium ion insertion cell. *J. Electrochem. Soc.*, 141(1):1, January 1994.

[101] B E Deal and A S Grove. General relationship for the thermal oxidation of silicon. *J. Appl. Phys.*, 36(12):3770–3778, December 1965.

[102] Valentin Sulzer, Peyman Mohtat, Sravan Pannala, Jason B Siegel, and Anna G Stefanopoulou. Accelerated battery lifetime simulations using adaptive inter-cycle extrapolation algorithm. *J. Electrochem. Soc.*, 168(12):120531, December 2021.

[103] Simon Schweidler, Lea de Biasi, Alexander Schiele, Pascal Hartmann, Torsten Brezesinski, and Jürgen Janek. Volume changes of graphite anodes revisited: A combined operando x-ray diffraction and in situ pressure analysis study. *J. Phys. Chem. C*, 122(16):8829–8835, April 2018.

[104] Jingyi Li, Zhiwei Zhou, Ziyan Luo, Zhenjiang He, Junchao Zheng, Yunjiao Li, Jing Mao, and Kehua Dai. Microcrack generation and modification of ni-rich cathodes for li-ion batteries: A review. *Sustainable Materials and Technologies*, 29(June):e00305, 2021.

[105] Jonas Keil and Andreas Jossen. Electrochemical modeling of linear and nonlinear aging of Lithium-Ion cells. *J. Electrochem. Soc.*, 167(11):110535, 2020.

[106] Drew J Pereira, Ashton M Aleman, John W Weidner, and Taylor R Garrick. A Mechano-Electrochemical battery model that accounts for preferential lithiation inside blended silicon graphite (Si/C) anodes. *J. Electrochem. Soc.*, 169(2):020577, 2022.

[107] E E Petersen. Diffusion in a pore of varying cross section. *AIChE J.*, 4(3):343–345, September 1958.

[108] Ding-Wen Chung, Martin Ebner, David R Ely, Vanessa Wood, and R Edwin García. Validity of the bruggeman relation for porous electrodes. *Modell. Simul. Mater. Sci. Eng.*, 21(7):074009, October 2013.

[109] Valentin Sulzer, Scott G Marquis, Robert Timms, Martin Robinson, and S Jon Chapman. Python battery mathematical modelling (PyBaMM). *Journal of Open Research Software*, 9(1), June 2021.

[110] Jorn M Reniers and David A Howey. Digital twin of a MWh-scale grid battery system for efficiency and degradation analysis. *Appl. Energy*, 336:120774, April 2023.

[111] Soon-Ki Jeong, Minoru Inaba, Ryo Mogi, Yasutoshi Iriyama, Takeshi Abe, and Zempachi Ogumi. Surface film formation on a graphite negative electrode in Lithium-Ion batteries: Atomic force microscopy study on the effects of Film-Forming additives in propylene carbonate solutions. *Langmuir*, 17(26):8281–8286, December 2001.

[112] Peter M Attia, Supratim Das, Stephen J Harris, Martin Z Bazant, and William C Chueh. Electrochemical kinetics of SEI growth on carbon black: Part i. experiments. *J. Electrochem. Soc.*, 166(4):E97, February 2019.

[113] Daniel Pritzl, Sophie Solchenbach, Morten Wetjen, and Hubert A Gasteiger. Analysis of vinylene carbonate (VC) as additive in Graphite/LiNi0.5Mn1.5O4 cells. *J. Electrochem. Soc.*, 164(12):A2625, August 2017.

[114] D Aurbach, K Gamolsky, B Markovsky, Y Gofer, M Schmidt, and U Heider. On the use of vinylene carbonate (VC) as an additive to electrolyte solutions for li-ion batteries. *Electrochim. Acta*, 47(9):1423–1439, February 2002.

[115] Hiroshi Haruna, Shin Takahashi, and Yasutaka Tanaka. Accurate consumption analysis of vinylene carbonate as an electrolyte additive in an 18650 Lithium-Ion battery at the first Charge-Discharge cycle. *J. Electrochem. Soc.*, 164(1):A6278, December 2016.

[116] Yixuan Wang, Shinichiro Nakamura, Ken Tasaki, and Perla B Balbuena. Theoretical studies to understand surface chemistry on carbon anodes for lithium-ion batteries: how does vinylene carbonate play its role as an electrolyte additive? *J. Am. Chem. Soc.*, 124(16):4408–4421, April 2002.

[117] Hitoshi Ota, Yuuichi Sakata, Atsuyoshi Inoue, and Shoji Yamaguchi. Analysis of vinylene carbonate derived SEI layers on graphite anode. *J. Electrochem. Soc.*, 151(10):A1659, September 2004.

[118] C R Birkl, E McTurk, M R Roberts, P G Bruce, and D A Howey. A parametric open circuit voltage model for lithium ion batteries. *J. Electrochem. Soc.*, 162(12):A2271, September 2015.

[119] Wolfgang Dreyer, Janko Jamnik, Clemens Guhlke, Robert Huth, Jože Moškon, and Miran Gaberšček. The thermodynamic origin of hysteresis in insertion batteries. *Nat. Mater.*, 9(5):448–453, 2010.

[120] Srivatsan Hulikal and Allan Bower. On the role of heterogeneity in Phase-Transforming electrodes: Origin of Zero-Current hysteresis. *J. Electrochem. Soc.*, 164(7):A1401–A1411, 2017.

[121] Shunyi Yang, Xianyou Wang, Xiukang Yang, Yansong Bai, Ziling Liu, Hongbo Shu, and Qiliang Wei. Determination of the chemical diffusion coefficient of lithium ions in spherical Li[Ni 0.5mn 0.3co 0.2]o 2. *Electrochim. Acta*, 66:88–93, 2012.

[122] Hui Zhou, Fengxia Xin, Ben Pei, and M Stanley Whittingham. What limits the capacity of layered oxide cathodes in lithium batteries? *ACS Energy Letters*, 4(8):1902–1906, 2019.

[123] Aaron Liu, Nutthaphon Phattharasupakun, Marc M E Cormier, Eniko Zsoldos, Ning Zhang, Erin Lyle, Phillip Arab, Montree Sawangphruk, and J R Dahn. Factors that affect capacity in the low voltage kinetic hindrance region of Ni-Rich positive electrode materials and diffusion measurements from a reinvented approach. *J. Electrochem. Soc.*, 168(7):070503, 2021.

[124] Chengyu Mao, Seong Jin An, Harry M Meyer, Jianlin Li, Marissa Wood, Rose E Ruther, and David L Wood. Balancing formation time and electrochemical performance of high energy lithium-ion batteries. *J. Power Sources*, 402(July):107–115, 2018.

[125] Christopher E Hendricks, Azzam N Mansour, Daphne A Fuentevilla, H Waller, Jonathan K Ko, and Michael G Pecht. Copper dissolution in overdischarged lithium-ion cells: X-ray photoelectron spectroscopy and x-ray absorption fine structure analysis. *J. Electrochem. Soc.*, 2020.

[126] A Eldesoky, Michael Bauer, S Azam, E Zsoldos, Wentao Song, Rochelle Weber, Sunny Hy, M B Johnson, Michael Metzger, and J R Dahn. Impact of graphite materials on the lifetime of NMC811/Graphite pouch cells: Part i. material properties, ARC safety tests, gas generation, and room temperature cycling. *J. Electrochem. Soc.*, 168(11):110543, November 2021.

[127] Seong Jin An, Jianlin Li, Zhijia Du, Claus Daniel, and David L Wood. Fast formation cycling for lithium ion batteries. *J. Power Sources*, 342(February 2018):846–852, 2017.

[128] Yuliya Preger, Heather M Barkholtz, Armando Fresquez, Daniel L Campbell, Benjamin W Juba, Jessica Roman-Kustas, Summer R Ferreira, and Babu Chalamala. Degradation of commercial Lithium-Ion cells as a function of chemistry and cycling conditions. *J. Electrochem. Soc.*, 167(12):120532, 2020.

[129] Valentin Sulzer, Peyman Mohtat, Sravan Pannala, Jason B Siegel, and Anna G Stefanopoulou. Accelerated battery lifetime simulations using adaptive Inter-Cycle extrapolation algorithm. *J. Electrochem. Soc.*, 168(12):0–0, December 2021.

[130] Xiaowei Ma, Jessie E. Harlow, Jing Li, Lin Ma, David S. Hall, Samuel Buteau, Matthew Genovese, Marc Cormier, and J. R. Dahn. Editors' Choice—Hindering Rollover Failure of Li[Ni 0.5 Mn 0.3 Co 0.2]O 2 /Graphite Pouch Cells during Long-Term Cycling . *Journal of The Electrochemical Society*, 166(4):A711–A724, 2019.

[131] Jing Li, Andrew R Cameron, Hongyang Li, Stephen Glazier, Deijun Xiong, M Chatzidakis, Jenn Allen, G A Botton, and J R Dahn. Comparison of single crystal and polycrystalline LiNi0.5Mn0.3Co0.2O2 positive electrode materials for high voltage Li-Ion cells. *J. Electrochem. Soc.*, 164(7):A1534, May 2017.

[132] Roland Jung, Michael Metzger, Dominik Haering, Sophie Solchenbach, Cyril Marino, Nikolaos Tsiouvaras, Christoph Stinner, and Hubert A Gasteiger. Consumption of fluoroethylene carbonate (FEC) on Si-C composite electrodes for Li-Ion batteries. *J. Electrochem. Soc.*, 163(8):A1705, June 2016.

[133] R Petibon, V L Chevrier, C P Aiken, D S Hall, S R Hyatt, R Shunmugasundaram, and J R Dahn. Studies of the capacity fade mechanisms of LiCoO2/Si-Alloy: Graphite cells. *J. Electrochem. Soc.*, 163(7):A1146, April 2016.

[134] Morten Wetjen, Daniel Pritzl, Roland Jung, Sophie Solchenbach, Reza Ghadimi, and Hubert A Gasteiger. Differentiating the degradation phenomena in Silicon-Graphite electrodes for Lithium-Ion batteries. *J. Electrochem. Soc.*, 164(12):A2840, September 2017.

[135] Andrew Weng, Everardo Olide, Iaroslav Kovalchuk, Jason B. Siegel, and Anna Stefanopoulou. Modeling battery formation: Boosted sei growth, multi-species reactions, and irreversible expansion. *Journal of The Electrochemical Society*, 170(9):090523, sep 2023.

[136] M Safari and C Delacourt. Simulation-Based analysis of aging phenomena in a commercial Graphite/LiFePO4 cell. *J. Electrochem. Soc.*, 158(12):A1436, 2011.

[137] Meng Guo, Godfrey Sikha, and Ralph E White. Single-Particle model for a Lithium-Ion cell: Thermal behavior. *J. Electrochem. Soc.*, 158(2):A122, December 2010.

[138] Scott J Moura, Federico Bribiesca Argomedo, Reinhardt Klein, Anahita Mirtabatabaei, and Miroslav Krstic. Battery state estimation for a single particle model with electrolyte dynamics. *IEEE Trans. Control Syst. Technol.*, 25(2):453–468, March 2017.

[139] Zhiqiang Chen, Dmitri L Danilov, Rüdiger-A Eichel, and Peter H L Notten. Porous electrode modeling and its applications to li-ion batteries. *Adv. Energy Mater.*, 12(32):2201506, August 2022.

[140] Mark Kane. Tesla fremont factory produces more than 1 car per minute. https://insideevs.com/news/591782/tesla-fremont-factory-record-production/, June 2022. Accessed: 2022-10-29.

[141] Ira Bloom, Andrew N. Jansen, Daniel P. Abraham, Jamie Knuth, Scott A. Jones, Vincent S. Battaglia, and Gary L. Henriksen. Differential voltage analyses of high-power, lithium-ion cells 1. Technique and application. *Journal of Power Sources*, 139(1-2):295–303, 2005.

[142] Matthieu Dubarry, Cyril Truchot, and Bor Yann Liaw. Synthesize battery degradation modes via a diagnostic and prognostic model. *Journal of Power Sources*, 219:204–216, 2012.

[143] Christoph R. Birkl, Matthew R. Roberts, Euan McTurk, Peter G. Bruce, and David A. Howey. Degradation diagnostics for lithium ion cells. *Journal of Power Sources*, 341:373–386, feb 2017.

[144] Jarred Z Olson, Carmen M López, and Edmund J F Dickinson. Differential analysis of galvanostatic cycle data from Li-Ion batteries: Interpretative insights and graphical heuristics. *Chem. Mater.*, February 2023.

[145] A. J. Smith, J. C. Burns, D. Xiong, and J. R. Dahn. Interpreting High Precision Coulometry Results on Li-ion Cells. *Journal of The Electrochemical Society*, 158(10):A1136, 2011.

[146] Caihao Weng, Yujia Cui, Jing Sun, and Huei Peng. On-board state of health monitoring of lithium-ion batteries using incremental capacity analysis with support vector regression. *Journal of Power Sources*, 235:36–44, 2013.

[147] D. García Elvira, R. Machado, G. L. Plett, M. S. Trimboli, H. Valderrama Blavi, A. Cid Pastor, and L. Martínez Salamero. Simplified Li Ion Cell Model for BMS Coupling an Equivalent Circuit Dynamic Model with a Zero Dimensional Physics Based SEI Model. *Journal of The Electrochemical Society*, 168(11):110526, 2021.

[148] Julius Schmitt, Markus Schindler, Andreas Oberbauer, and Andreas Jossen. Determination of degradation modes of lithium-ion batteries considering aging-induced changes in the half-cell open-circuit potential curve of silicon–graphite. *J. Power Sources*, 532:231296, June 2022.

[149] P Mohtat, S Lee, J B Siegel, and A G Stefanopoulou. Comparison of expansion and voltage differential indicators for battery capacity fade. *J. Power Sources*, 2022.

[150] Wenxiao Huang, Yusheng Ye, Hao Chen, Rafael A Vilá, Andrew Xiang, Hongxia Wang, Fang Liu, Zhiao Yu, Jinwei Xu, Zewen Zhang, Rong Xu, Yecun Wu, Lien-Yang Chou, Hansen Wang, Junwei Xu, David Tomas Boyle, Yuzhang Li, and Yi Cui. Onboard early detection and mitigation of lithium plating in fast-charging batteries. *Nat. Commun.*, 13(1):7091, November 2022.

[151] Matthieu Dubarry and David Beck. Analysis of synthetic voltage vs. capacity datasets for big data li-ion diagnosis and prognosis. *Energies*, 14(9), 2021.

[152] Jessie E Harlow, Xiaowei Ma, Jing Li, Eric Logan, Yulong Liu, Ning Zhang, Lin Ma, Stephen L Glazier, Marc M E Cormier, Matthew Genovese, Samuel Buteau, Andrew Cameron, Jamie E Stark, and J R Dahn. A wide range of testing results on an excellent Lithium-Ion cell chemistry to be used as benchmarks for new battery technologies. *J. Electrochem. Soc.*, 166(13):A3031–A3044, 2019.

[153] Hannah M. Dahn, A. J. Smith, J. C. Burns, D. A. Stevens, and J. R. Dahn. User-Friendly Differential Voltage Analysis Freeware for the Analysis of Degradation Mechanisms in Li-Ion Batteries. *Journal of The Electrochemical Society*, 159(9):A1405–A1409, 2012.

[154] Cyril Truchot, Matthieu Dubarry, and Bor Yann Liaw. State-of-charge estimation and uncertainty for lithium-ion battery strings. *Appl. Energy*, 119:218–227, April 2014.

[155] Dongliang Lu, M. Scott Trimboli, Guodong Fan, Ruigang Zhang, and Gregory L. Plett. Implementation of a Physics-Based Model for Half-Cell Open-Circuit Potential and Full-Cell Open-Circuit Voltage Estimates: Part I. Processing Half-Cell Data. *Journal of The Electrochemical Society*, 168(7):070532, 2021.

[156] Nutthaphon Phattharasupakun, Marc M E Cormier, Chenxi Geng, Montree Sawangphruk, and J R Dahn. Voltage-Dependent li kinetics leads to Charge-Discharge asymmetry in Co-Free Li-Rich Li1.12Ni0.44Mn0.44O2 under conditions without transition metal migration. *J. Electrochem. Soc.*, 168(9):090564, September 2021.

[157] Peyman Mohtat, Suhak Lee, Jason B. Siegel, and Anna G. Stefanopoulou. Reversible and Irreversible Expansion of Lithium-Ion Batteries Under a Wide Range of Stress Factors. *Journal of The Electrochemical Society*, 168(10):100520, 2021.

[158] J Kasnatscheew, M Evertz, B Streipert, R Wagner, R Klöpsch, B Vortmann, H Hahn, S Nowak, M Amereller, A-C Gentschev, P Lamp, and M Winter. The truth about the 1st cycle coulombic efficiency of LiNi1/3Co1/3Mn1/3O2 (NCM) cathodes. *Phys. Chem. Chem. Phys.*, 18(5):3956–3965, January 2016.

[159] Florian Reuter, Anne Baasner, Jonas Pampel, Markus Piwko, Susanne Dörfler, Holger Althues, and Stefan Kaskel. Importance of capacity balancing on the electrochemical performance of Li[Ni0.8Co0.1Mn0.1]O2 (NCM811)/Silicon full cells. *J. Electrochem. Soc.*, 166(14):A3265, September 2019.

[160] Mei Luo, Marco-Tulio F. Rodrigues, Leon L Shaw, and Daniel P Abraham. Examining effects of negative to positive capacity ratio in Three-Electrode Lithium-Ion cells with layered oxide cathode and si anode. *ACS Appl. Energy Mater.*, 5(5):5513–5518, May 2022.

[161] Valentin Sulzer, Peyman Mohtat, Sravan Pannala, Jason B. Siegel, and Anna G. Stefanopoulou. Accelerated Battery Lifetime Simulations Using Adaptive Inter-Cycle

Extrapolation Algorithm. *Journal of The Electrochemical Society*, 168(12):120531, 2021.

[162] Shunyi Yang, Xianyou Wang, Xiukang Yang, Yansong Bai, Ziling Liu, Hongbo Shu, and Qiliang Wei. Determination of the chemical diffusion coefficient of lithium ions in spherical Li[Ni 0.5Mn 0.3Co 0.2]O 2. *Electrochimica Acta*, 66:88–93, 2012.

[163] Hui Zhou, Fengxia Xin, Ben Pei, and M. Stanley Whittingham. What Limits the Capacity of Layered Oxide Cathodes in Lithium Batteries? *ACS Energy Letters*, 4(8):1902–1906, 2019.

[164] Aaron Liu, Nutthaphon Phattharasupakun, Marc M. E. Cormier, Eniko Zsoldos, Ning Zhang, Erin Lyle, Phillip Arab, Montree Sawangphruk, and J. R. Dahn. Factors that Affect Capacity in the Low Voltage Kinetic Hindrance Region of Ni-Rich Positive Electrode Materials and Diffusion Measurements from a Reinvented Approach. *Journal of The Electrochemical Society*, 168(7):070503, 2021.

[165] Simon Müller, Patrick Pietsch, Ben-Elias Brandt, Paul Baade, Vincent De Andrade, Francesco De Carlo, and Vanessa Wood. Quantification and modeling of mechanical degradation in lithium-ion batteries based on nanoscale imaging. *Nat. Commun.*, 9(1):1–8, June 2018.

[166] Matthieu Dubarry and George Baure. Perspective on commercial li-ion battery testing, best practices for simple and effective protocols. *Electronics (Switzerland)*, 9(1), 2020.

[167] Peter Keil, Simon F. Schuster, Jörn Wilhelm, Julian Travi, Andreas Hauser, Ralph C. Karl, and Andreas Jossen. Calendar Aging of Lithium-Ion Batteries. *Journal of The Electrochemical Society*, 163(9):A1872–A1880, 2016.

[168] Jiangtao Hu, Bingbin Wu, Sujong Chae, Joshua Lochala, Yujing Bi, and Jie Xiao. Achieving highly reproducible results in graphite-based li-ion full coin cells. *Joule*, 5(5):1011–1015, May 2021.

[169] Vivian Murray, David S Hall, and J R Dahn. A guide to full coin cell making for academic researchers. *J. Electrochem. Soc.*, 166(2):A329, January 2019.

[170] A A Wang, S E J O'Kane, F Brosa Planella, J Le Houx, K O'Regan, M Zyskin, J Edge, C W Monroe, S J Cooper, D A Howey, E Kendrick, and J M Foster. Review of parameterisation and a novel database (LiionDB) for continuum li-ion battery models. *Prog. Energy Combust. Sci.*, 4(3):032004, 2022.

[171] Chang-Hui Chen, Ferran Brosa Planella, Kieran O'Regan, Dominika Gastol, W Dhammika Widanage, and Emma Kendrick. Development of experimental techniques for parameterization of multi-scale lithium-ion battery models. *J. Electrochem. Soc.*, 167(8):080534, May 2020.

[172] Michael Hess. *Kinetics and stage transitions of graphite for lithium-ion batteries*. PhD thesis, ETH Zurich, 2013.

[173] Abraham Savitzky and M J E Golay. Smoothing and differentiation of data by simplified least squares procedures. *Anal. Chem.*, 36(8):1627–1639, July 1964.

[174] Xuning Feng, Yu Merla, Caihao Weng, Minggao Ouyang, Xiangming He, Bor Yann Liaw, Shriram Santhanagopalan, Xuemin Li, Ping Liu, Languang Lu, Xuebing Han, Dongsheng Ren, Yu Wang, Ruihe Li, Changyong Jin, Peng Huang, Mengchao Yi, Li Wang, Yan Zhao, Yatish Patel, and Gregory Offer. A reliable approach of differentiating discrete sampled-data for battery diagnosis. *eTransportation*, 3:100051, February 2020.

[175] Michael Schmid, David Rath, and Ulrike Diebold. Why and how Savitzky-Golay filters should be replaced. *ACS Meas Sci Au*, 2(2):185–196, April 2022.

[176] Yi Wu, Saurabh Saxena, Yinjiao Xing, Youren Wang, Chuan Li, Winco K C Yung, and Michael Pecht. Analysis of Manufacturing-Induced defects and structural deformations in Lithium-Ion batteries using computed tomography. *Energies*, 11(4):925, April 2018.

[177] Toby Bond, Roby Gauthier, Sergey Gasilov, and J R Dahn. In-Situ computed tomography of particle microcracking and electrode damage in cycled NMC622/Graphite pouch cell batteries. *J. Electrochem. Soc.*, 169(8):080531, August 2022.

[178] Roby Gauthier, Aidan Luscombe, Toby Bond, Michael Bauer, Michel Johnson, Jessie Harlow, Alex Louli, and Jeff R Dahn. How do depth of discharge, c-rate and calendar age affect capacity retention, impedance growth, the electrodes, and the electrolyte in Li-Ion cells? *J. Electrochem. Soc.*, January 2022.

[179] Katharina Rumpf, Maik Naumann, and Andreas Jossen. Experimental investigation of parametric cell-to-cell variation and correlation based on 1100 commercial lithium-ion cells. *Journal of Energy Storage*, 14:224–243, December 2017.

[180] Florian J Günter, Jan Bernd Habedank, David Schreiner, Tobias Neuwirth, Ralph Gilles, and Gunther Reinhart. Introduction to electrochemical impedance spectroscopy as a measurement method for the wetting degree of Lithium-Ion cells. *J. Electrochem. Soc.*, 165(14):A3249–A3256, 2018.

[181] Xiangdong Kong, Gregory L Plett, M Scott Trimboli, Zhendong Zhang, Dongdong Qiao, Tongzheng Zhao, and Yuejiu Zheng. Pseudo-two-dimensional model and impedance diagnosis of micro internal short circuit in lithium-ion cells. *Journal of Energy Storage*, 27:101085, February 2020.

[182] Anup Barai, Kotub Uddin, W D Widanage, Andrew McGordon, and Paul Jennings. A study of the influence of measurement timescale on internal resistance characterisation methodologies for lithium-ion cells. *Sci. Rep.*, 8(1):21, January 2018.

[183] Jon P. Christopherson. Battery Test Manual for Plug-In Hybrid Electric Vehicles. Technical report, Idaho National Laboratory, Idaho Falls, Idaho, 2015.

[184] Nina Meddings, Marco Heinrich, Frédéric Overney, Jong Sook Lee, Vanesa Ruiz, Emilio Napolitano, Steffen Seitz, Gareth Hinds, Rinaldo Raccichini, Miran Gaberšček, and Juyeon Park. Application of electrochemical impedance spectroscopy to commercial li-ion cells: A review. *J. Power Sources*, 480(August), 2020.

[185] Sabine Ernst, Tom Patrick Heins, Nicolas Schlüter, and Uwe Schröder. Capturing the Current-Overpotential nonlinearity of Lithium-Ion batteries by nonlinear electrochemical impedance spectroscopy (NLEIS) in charge and discharge direction. *Frontiers in Energy Research*, 7, 2019.

[186] J. R. Dahn. Phase diagram of li_xc_6. *Phys. Rev. B*, 44:9170–9177, Nov 1991.

[187] Allen J. Bard and Larry R. Faulkner. *Electrochemical Methods: Fundamentals and Applications*. Wiley, 2nd edition, 2001.

[188] Ankit Verma, Kandler Smith, Shriram Santhanagopalan, Daniel Abraham, Koffi Pierre Yao, and Partha P Mukherjee. Galvanostatic intermittent titration and performance based analysis of LiNi 0.5 co 0.2 mn 0.3 O 2 cathode. *J. Electrochem. Soc.*, 164(13):A3380–A3392, 2017.

[189] Seonbaek Ha, Vijay K. Ramani, Wenquan Lu, and Jai Prakash. Optimization of inactive material content in lithium iron phosphate electrodes for high power applications. *Electrochimica Acta*, 191:173–182, 2016.

[190] Jun Huang, Jianbo Zhang, Zhe Li, Shaoling Song, and Ningning Wu. Exploring differences between charge and discharge of LiMn2O4/Li half-cell with dynamic electrochemical impedance spectroscopy. *Electrochim. Acta*, 131:228–235, June 2014.

[191] Naoto Tanibata, Riku Morimoto, Kei Nishikawa, Hayami Takeda, and Masanobu Nakayama. Asymmetry in the Solvation–Desolvation resistance for li metal batteries. *Anal. Chem.*, 92(5):3499–3502, March 2020.

[192] Antti Aitio and David A. Howey. Predicting battery end of life from solar off-grid system field data using machine learning. *Joule*, 5(12):3204–3220, 2021.

[193] Mohammad Alipour, Carlos Ziebert, Fiorentino Valerio Conte, and Riza Kizilel. A review on temperature-dependent electrochemical properties, aging, and performance of lithium-ion cells. *Batteries*, 6(3):1–32, 2020.

[194] Ryan A Adams, Arvind Varma, and Vilas G Pol. Temperature dependent electrochemical performance of graphite anodes for k-ion and li-ion batteries. *J. Power Sources*, 410-411:124–131, January 2019.

[195] A S Keefe, Samuel Buteau, I G Hill, and J R Dahn. Temperature dependent EIS studies separating charge transfer impedance from contact impedance in lithium-ion symmetric cells. *J. Electrochem. Soc.*, 166(14):A3272–A3279, 2019.

[196] Johannes Landesfeind and Hubert A Gasteiger. Temperature and concentration dependence of the ionic transport properties of Lithium-Ion battery electrolytes. *J. Electrochem. Soc.*, 166(14):A3079, September 2019.

[197] Australian Trade and Investment Commission. The Lithium-Ion Battery Value Chain: New Economy Opportunities for Australia. Technical report, Australian Government, 2018.

[198] Benchmark Minerals Intelligence. EV Battery arms race enters new gear with 115 megafactories, Europe sees most rapid growth, 2019.

[199] Wood Mackenzie. Global lithium-ion cell manufacturing capacity to quadruple to 1.3 TWh by 2030, 2020.

[200] Yangtao Liu, Ruihan Zhang, Jun Wang, and Yan Wang. Current and future lithium-ion battery manufacturing. *iScience*, 24(4):102332, 2021.

[201] Paul A Nelson, K G Bloom, and D W I Dees. Modeling the performance and cost of lithium-ion batteries for electric-drive vehicles. Technical report, USDOE Office of Energy Efficiency and Renewable Energy, Vehicle Technologies Office, Argonne National Lab, 2011.

[202] Fabian Duffner, Lukas Mauler, Marc Wentker, Jens Leker, and Martin Winter. Large-scale automotive battery cell manufacturing: Analyzing strategic and operational effects on manufacturing costs. *International Journal of Production Economics*, 232:107982, 2021.

[203] David L. Wood, Jianlin Li, and Claus Daniel. Prospects for reducing the processing cost of lithium ion batteries. *Journal of Power Sources*, 275:234–242, 2015.

[204] Martin Winter. The solid electrolyte interphase - The most important and the least understood solid electrolyte in rechargeable Li batteries. *Zeitschrift fur Physikalische Chemie*, 223(10-11):1395–1406, 2009.

[205] Seong Jin An, Jianlin Li, Claus Daniel, Debasish Mohanty, Shrikant Nagpure, and David L. Wood. The state of understanding of the lithium-ion-battery graphite solid electrolyte interphase (SEI) and its relationship to formation cycling. *Carbon*, 105:52–76, 2016.

[206] Aiping Wang, Sanket Kadam, Hong Li, Siqi Shi, and Yue Qi. Review on modeling of the anode solid electrolyte interphase (SEI) for lithium-ion batteries. *npj Computational Materials*, 4(1), 2018.

[207] E. Peled and S. Menkin. Review—SEI: Past, Present and Future. *Journal of The Electrochemical Society*, 164(7):A1703–A1719, 2017.

[208] Dietrich Goers, Michael E. Spahr, Antonio Leone, Wolfgang Märkle, and Petr Novák. The influence of the local current density on the electrochemical exfoliation of graphite in lithium-ion battery negative electrodes. *Electrochimica Acta*, 56(11):3799–3808, 2011.

[209] Peng Lu, Chen Li, Eric W. Schneider, and Stephen J. Harris. Chemistry, impedance, and morphology evolution in solid electrolyte interphase films during formation in lithium ion batteries. *Journal of Physical Chemistry C*, 118(2):896–903, 2014.

[210] David L. Wood, Jianlin Li, and Seong Jin An. Formation Challenges of Lithium-Ion Battery Manufacturing. *Joule*, 3(12):2884–2888, 2019.

[211] Chengyu Mao, Seong Jin An, Harry M. Meyer, Jianlin Li, Marissa Wood, Rose E. Ruther, and David L. Wood. Balancing formation time and electrochemical performance of high energy lithium-ion batteries. *Journal of Power Sources*, 402(July):107–115, 2018.

[212] Verena Müller, Rudi Kaiser, Silvan Poller, Daniel Sauerteig, Radu Schwarz, Martin Wenger, Vincent R.H. Lorentz, and Martin März. Introduction and application of formation methods based on serial-connected lithium-ion battery cells. *Journal of Energy Storage*, 14:56–61, 2017.

[213] Byron Konstantinos Antonopoulos, Christoph Stock, Filippo Maglia, and Harry Ernst Hoster. Solid electrolyte interphase: Can faster formation at lower potentials yield better performance? *Electrochimica Acta*, 269:331–339, 2018.

[214] S. S. Zhang, K. Xu, and T. R. Jow. Optimization of the forming conditions of the solid-state interface in the Li-ion batteries. *Journal of Power Sources*, 130(1-2):281–285, 2004.

[215] Heiner Hans Heimes, Christian Offermanns, Ahmad Mohsseni, Hendrik Laufen, Uwe Westerhoff, Louisa Hoffmann, Philip Niehoff, Michael Kurrat, Martin Winter, and Achim Kampker. The Effects of Mechanical and Thermal Loads during Lithium-Ion Pouch Cell Formation and Their Impacts on Process Time. *Energy Technology*, 8(2):1–12, 2020.

[216] Tanveerkhan S Pathan, Muhammad Rashid, Marc Walker, W D Widanage, and Emma Kendrick. Active formation of Li-ion batteries and its effect on cycle life. *Journal of Physics: Energy*, 1(4):044003, 2019.

[217] Verena Müller, Rudi Kaiser, Silvan Poller, and Daniel Sauerteig. Importance of the constant voltage charging step during lithium-ion cell formation. *Journal of Energy Storage*, 15:256–265, 2018.

[218] Nancy Dietz Rago, John K. Basco, Anh Vu, Jianlin Li, Kevin Hays, Yangping Sheng, David L. Wood, and Ira Bloom. Effect of formation protocol: Cells containing Si-Graphite composite electrodes. *Journal of Power Sources*, 435(February):126548, 2019.

[219] Xianming Wang, Yoshitsugu Sone, Go Segami, Hitoshi Naito, Chisa Yamada, and Koichi Kibe. Understanding Volume Change in Lithium-Ion Cells during Charging and Discharging Using In Situ Measurements. *Journal of The Electrochemical Society*, 154(1):A14, 2007.

[220] Marius Bauer, Mario Wachtler, Hendrik Stöwe, Jon V. Persson, and Michael A. Danzer. Understanding the dilation and dilation relaxation behavior of graphite-based lithium-ion cells. *Journal of Power Sources*, 317:93–102, 2016.

[221] Peyman Mohtat, Suhak Lee, Valentin Sulzer, Jason B. Siegel, and Anna G. Stefanopoulou. Differential Expansion and Voltage Model for Li-ion Batteries at Practical Charging Rates. *Journal of The Electrochemical Society*, 167(11):110561, 2020.

[222] Yao Yunwei Zhang, Qiaochu Tang, Yao Yunwei Zhang, Jiabin Wang, Ulrich Stimming, and Alpha A. Lee. Identifying degradation patterns of lithium ion batteries from impedance spectroscopy using machine learning. *Nature Communications*, 11(1):6–11, 2020.

[223] Clement Bommier, Wesley Chang, Yufang Lu, Justin Yeung, Greg Davies, Robert Mohr, Mateo Williams, and Daniel Steingart. In Operando Acoustic Detection of Lithium Metal Plating in Commercial LiCoO2/Graphite Pouch Cells. *Cell Reports Physical Science*, 1(4):100035, 2020.

[224] Greg Davies, Kevin W. Knehr, Barry Van Tassell, Thomas Hodson, Shaurjo Biswas, Andrew G. Hsieh, and Daniel A. Steingart. State of Charge and State of Health Estimation Using Electrochemical Acoustic Time of Flight Analysis. *Journal of The Electrochemical Society*, 164(12):A2746–A2755, 2017.

[225] Kevin W. Knehr, Thomas Hodson, Clement Bommier, Greg Davies, Andrew Kim, and Daniel A. Steingart. Understanding Full-Cell Evolution and Non-chemical Electrode Crosstalk of Li-Ion Batteries. *Joule*, 2(6):1146–1159, 2018.

[226] Patrick Pietsch and Vanessa Wood. X-Ray Tomography for Lithium Ion Battery Research: A Practical Guide. *Annual Review of Materials Research*, 47:451–479, 2017.

[227] Vanessa Wood. X-ray tomography for battery research and development. *Nature Reviews Materials*, 3(9):293–295, 2018.

[228] Seong Jin An, Ji Yong Park, Jaehee Song, Jaeyeon Lee, Gil Ho Kim, Jongmoon Yoon, and Bookeun Oh. A fast method for evaluating stability of lithium ion batteries at high C-rates. *Journal of Power Sources*, 480(August):228856, 2020.

[229] Matthieu Dubarry and George Baure. Perspective on commercial Li-ion battery testing, best practices for simple and effective protocols. *Electronics (Switzerland)*, 9(1), 2020.

[230] Peter M. Attia, Kristen A. Severson, and Jeremy D. Witmer. Statistical Learning for Accurate and Interpretable Battery Lifetime Prediction. *Journal of The Electrochemical Society*, 168(9):090547, 2021.

[231] Sang Pil Kim, Adri C.T.Van Duin, and Vivek B. Shenoy. Effect of electrolytes on the structure and evolution of the solid electrolyte interphase (SEI) in Li-ion batteries: A molecular dynamics study. *Journal of Power Sources*, 196(20):8590–8597, 2011.

[232] Shengshui Zhang, Michael S. Ding, Kang Xu, Jan Allen, and T. Richard Jow. Understanding solid electrolyte interface film formation on graphite electrodes. *Electrochemical and Solid-State Letters*, 4(12):206–209, 2001.

[233] Damjan Krstajic, Ljubomir J. Buturovic, David E. Leahy, and Simon Thomas. Cross-validation pitfalls when selecting and assessing regression and classification models. *Journal of Cheminformatics*, 6(1):1–15, 2014.

[234] Qunwei Wu, Wenquan Lu, and Jai Prakash. Characterization of a commercial size cylindrical Li-ion cell with a reference electrode. *Journal of Power Sources*, 88(2):237–242, 2000.

[235] Daniel P. Abraham. Diagnostic Examination of Generation 2 Lithium-Ion Cells and Assessment of Performance Degradation Mechanisms prepared by Chemical Engineering Division. Technical report, Argonne National Laboratory, 2005.

[236] Matthieu Dubarry, M. Berecibar, A. Devie, D. Anseán, N. Omar, and I. Villarreal. State of health battery estimator enabling degradation diagnosis: Model and algorithm description. *Journal of Power Sources*, 360:59–69, 2017.

[237] Peter M. Attia, Stephen J. Harris, and William C. Chueh. Benefits of Fast Battery Formation in a Model System. *Journal of The Electrochemical Society*, 168(5):050543, 2021.

[238] R. Fathi, J. C. Burns, D. A. Stevens, Hui Ye, Chao Hu, Gaurav Jain, Erik Scott, Craig Schmidt, and J. R. Dahn. Ultra High-Precision Studies of Degradation Mechanisms in Aged LiCoO 2 /Graphite Li-Ion Cells . *Journal of The Electrochemical Society*, 161(10):A1572–A1579, 2014.

[239] Kristen A. Severson, Peter M. Attia, Norman Jin, Nicholas Perkins, Benben Jiang, Zi Yang, Michael H. Chen, Muratahan Aykol, Patrick K. Herring, Dimitrios Fraggedakis, Martin Z. Bazant, Stephen J. Harris, William C. Chueh, and Richard D. Braatz. Data-driven prediction of battery cycle life before capacity degradation. *Nature Energy*, 4(5):383–391, 2019.

[240] Kristina Edström, Marie Herstedt, and Daniel P. Abraham. A new look at the solid electrolyte interphase on graphite anodes in Li-ion batteries. *Journal of Power Sources*, 153(2):380–384, 2006.

[241] Peng Lu and Stephen J. Harris. Lithium transport within the solid electrolyte interphase. *Electrochemistry Communications*, 13(10):1035–1037, 2011.

[242] J. C. Burns, Adil Kassam, N. N. Sinha, L. E. Downie, Lucie Solnickova, B. M. Way, and J. R. Dahn. Predicting and Extending the Lifetime of Li-Ion Batteries. *Journal of The Electrochemical Society*, 160(9):A1451–A1456, 2013.

[243] Jorn M. Reniers, Grietus Mulder, and David A. Howey. Review and Performance Comparison of Mechanical-Chemical Degradation Models for Lithium-Ion Batteries. *Journal of The Electrochemical Society*, 166(14):A3189–A3200, 2019.

[244] Seong Jin An, Jianlin Li, Claus Daniel, Sergiy Kalnaus, and David L. Wood. Design and Demonstration of Three-Electrode Pouch Cells for Lithium-Ion Batteries. *Journal of The Electrochemical Society*, 164(7):A1755–A1764, 2017.

[245] Gregory L. Plett. *Battery Management Systems Volume I: Battery Modeling*. Artech House, 2015.

[246] Shoichiro Watanabe, Masahiro Kinoshita, Takashi Hosokawa, Kenichi Morigaki, and Kensuke Nakura. Capacity fade of LiAlyNi1-x-yCoxO 2 cathode for lithium-ion batteries during accelerated calendar and cycle life tests (surface analysis of LiAlyNi1-x-yCo xO2 cathode after cycle tests in restricted depth of discharge ranges). *Journal of Power Sources*, 258:210–217, 2014.

[247] Pengfei Yan, Jianming Zheng, Meng Gu, Jie Xiao, Ji Guang Zhang, and Chong Min Wang. Intragranular cracking as a critical barrier for high-voltage usage of layer-structured cathode for lithium-ion batteries. *Nature Communications*, 8:1–9, 2017.

[248] Sheng S. Zhang. Problems and their origins of Ni-rich layered oxide cathode materials. *Energy Storage Materials*, 24(August 2019):247–254, 2020.

[249] Kenji Takahashi and Venkat Srinivasan. Examination of Graphite Particle Cracking as a Failure Mode in Lithium-Ion Batteries: A Model-Experimental Study. *Journal of The Electrochemical Society*, 162(4):A635–A645, 2015.

[250] Christian Kupper, Björn Weißhar, Sascha Rißmann, and Wolfgang G. Bessler. End-of-Life Prediction of a Lithium-Ion Battery Cell Based on Mechanistic Aging Models of the Graphite Electrode. *Journal of The Electrochemical Society*, 165(14):A3468–A3480, 2018.

[251] Sara Taslimi Taleghani, Bernard Marcos, Karim Zaghib, and Gaétan Lantagne. A Study on the Effect of Porosity and Particles Size Distribution on Li-Ion Battery Performance. *Journal of The Electrochemical Society*, 164(11):E3179–E3189, 2017.

[252] Debasish Mohanty, Kevin Dahlberg, David M. King, Lamuel A. David, Athena S. Sefat, David L. Wood, Claus Daniel, Subhash Dhar, Vishal Mahajan, Myongjai Lee, and Fabio Albano. Modification of Ni-Rich FCG NMC and NCA Cathodes by Atomic Layer Deposition: Preventing Surface Phase Transitions for High-Voltage Lithium-Ion Batteries. *Scientific Reports*, 6(May):1–16, 2016.

[253] Yan Jin, Bin Zhu, Zhenda Lu, Nian Liu, and Jia Zhu. Challenges and recent progress in the development of Si anodes for lithium-ion battery. *Advanced Energy Materials*, 7(23), 2017.

[254] Jie Xiao, Qiuyan Li, Yujing Bi, Mei Cai, Bruce Dunn, Tobias Glossmann, Jun Liu, Tetsuya Osaka, Ryuta Sugiura, Bingbin Wu, Jihui Yang, Ji Guang Zhang, and M. Stanley Whittingham. Understanding and applying coulombic efficiency in lithium metal batteries. *Nature Energy*, 5(8):561–568, 2020.

[255] Peiyi Sun, Roeland Bisschop, Huichang Niu, and Xinyan Huang. A Review of Battery Fires in Electric Vehicles. *Fire Technology*, pages 1–50, 01 2020.

[256] Xinhua Liu, Weilong Ai, Max Naylor Marlow, Yatish Patel, and Billy Wu. The effect of cell-to-cell variations and thermal gradients on the performance and degradation of lithium-ion battery packs. *Applied Energy*, 248(April):489–499, 2019.

[257] Gavin Harper, Roberto Sommerville, Emma Kendrick, Laura Driscoll, Peter Slater, Rustam Stolkin, Allan Walton, Paul Christensen, Oliver Heidrich, Simon Lambert, Andrew Abbott, Karl Ryder, Linda Gaines, and Paul Anderson. Recycling lithium-ion batteries from electric vehicles. *Nature*, 575(7781):75–86, 2019.

[258] Hauke Engel, Patrick Hertzke, and Giulia Siccardo. Second-life EV batteries: The newest value pool in energy storage. Technical Report April, McKinsey & Company, 2019.

[259] Katharina Rumpf, Alexander Rheinfeld, Markus Schindler, Jonas Keil, Tobias Schua, and Andreas Jossen. Influence of Cell-to-Cell Variations on the Inhomogeneity of Lithium-Ion Battery Modules. *Journal of The Electrochemical Society*, 165(11):A2587–A2607, 2018.

[260] Marium Rasheed, Mohamed Kamel, Hongjie Wang, Regan Zane, and Kandler Smith. Investigation of Active Life Balancing to Recondition Li-ion Battery Packs for 2ndLife. *2020 IEEE 21st Workshop on Control and Modeling for Power Electronics, COMPEL 2020*, 2020.

[261] K. Krishnamoorthy and Meesook Lee. Improved tests for the equality of normal coefficients of variation. *Computational Statistics*, 29(1-2):215–232, 2014.

[262] Thorsten Baumhöfer, Manuel Brühl, Susanne Rothgang, and Dirk Uwe Sauer. Production caused variation in capacity aging trend and correlation to initial cell performance. *J. Power Sources*, 247:332–338, 2014.

[263] M Schindler, J Sturm, S Ludwig, J Schmitt, and A Jossen. Evolution of initial cell-to-cell variations during a three-year production cycle. *eTransportation*, 8:100102, 2021.

[264] Leo Wildfeuer and Markus Lienkamp. Quantifiability of inherent cell-to-cell variations of commercial lithium-ion batteries. *eTransportation*, 9:100129, August 2021.

[265] Ben Kenney, Ken Darcovich, Dean D MacNeil, and Isobel J Davidson. Modelling the impact of variations in electrode manufacturing on lithium-ion battery modules. *J. Power Sources*, 213:391–401, 2012.

[266] Oke Schmidt, Matthias Thomitzek, Fridolin Röder, Sebastian Thiede, Christoph Herrmann, and Ulrike Krewer. Modeling the impact of manufacturing uncertainties on Lithium-Ion batteries. *J. Electrochem. Soc.*, 167(6):060501, 2020.

[267] Gavin Harper, Roberto Sommerville, Emma Kendrick, Laura Driscoll, Peter Slater, Rustam Stolkin, Allan Walton, Paul Christensen, Oliver Heidrich, Simon Lambert, Andrew Abbott, Karl Ryder, Linda Gaines, and Paul Anderson. Recycling lithium-ion batteries from electric vehicles. *Nature*, 575(7781):75–86, 2019.

[268] Mengyuan Chen, Xiaotu Ma, Bin Chen, Renata Arsenault, Peter Karlson, Nakia Simon, and Yan Wang. Recycling End-of-Life electric vehicle Lithium-Ion batteries. *Joule*, 3(11):2622–2646, 2019.

[269] Xin Lai, Yunfeng Huang, Cong Deng, Huanghui Gu, Xuebing Han, Yuejiu Zheng, and Minggao Ouyang. Sorting, regrouping, and echelon utilization of the large-scale retired lithium batteries: A critical review. *Renewable Sustainable Energy Rev.*, 146(April):111162, 2021.

[270] Xueyuan Wang, Qiaohua Fang, Haifeng Dai, Qijun Chen, and Xuezhe Wei. Investigation on cell performance and inconsistency evolution of series and parallel Lithium-Ion battery modules. *Energy Technology*, 9(7):1–10, 2021.

[271] I Zilberman, J Schmitt, S Ludwig, M Naumann, and A Jossen. Simulation of voltage imbalance in large lithium-ion battery packs influenced by cell-to-cell variations and balancing systems. *Journal of Energy Storage*, 32(April):101828, 2020.

[272] Marium Rasheed, Mohamed Kamel, Hongjie Wang, Regan Zane, and Kandler Smith. Investigation of active life balancing to recondition li-ion battery packs for 2ndlife. *2020 IEEE 21st Workshop on Control and Modeling for Power Electronics, COMPEL 2020*, 2020.

[273] Xuning Feng, Chengshan Xu, Xiangming He, Li Wang, Shang Gao, and Minggao Ouyang. A graphical model for evaluating the status of series-connected lithium-ion battery pack. *Int. J. Energy Res.*, 43(2):749–766, 2019.

[274] Jian Chen, Quan Ouyang, and Zhisheng Wang. Overview of cell equalization systems. In Jian Chen, Quan Ouyang, and Zhisheng Wang, editors, *Equalization Control for Lithium-ion Batteries*, pages 13–28. Springer Nature Singapore, Singapore, 2023.

[275] Xinfan Lin, Hector E Perez, Jason B Siegel, and Anna G Stefanopoulou. Robust estimation of battery system temperature distribution under sparse sensing and uncertainty. *IEEE Trans. Control Syst. Technol.*, 2020.

[276] Xianzhi Gong, Rui Xiong, and Chunting Chris Mi. Study of the characteristics of battery packs in electric vehicles with Parallel-Connected Lithium-Ion battery cells. *IEEE Trans. Ind. Appl.*, 51(2):1872–1879, March 2015.

[277] Martin J Brand, Markus H Hofmann, Marco Steinhardt, Simon F Schuster, and Andreas Jossen. Current distribution within parallel-connected battery cells. *J. Power Sources*, 334:202–212, December 2016.

[278] Robert Luca, Michael Whiteley, Toby Neville, Tom Tranter, Julia Weaving, James Marco, Paul R Shearing, and Dan J L Brett. Current imbalance in parallel battery strings measured using a Hall-Effect sensor array. *Energy Technology*, 9(4):1–11, 2021.

[279] Thomas Bruen and James Marco. Modelling and experimental evaluation of parallel connected lithium ion cells for an electric vehicle battery system. *J. Power Sources*, 310:91–101, 2016.

[280] Ziyou Song, Xiao-Guang Yang, Niankai Yang, Fanny Pinto Delgado, Heath Hofmann, and Jing Sun. A study of cell-to-cell variation of capacity in parallel-connected lithium-ion battery cells. *eTransportation*, 7:100091, February 2021.

[281] Z Song, N Yang, X Lin, F P Delgado, H Hofmann, and J Sun. Progression of cell-to-cell variation within battery modules under different cooling structures. *Appl. Energy*, 2022.

[282] Xinhua Liu, Weilong Ai, Max Naylor Marlow, Yatish Patel, and Billy Wu. The effect of cell-to-cell variations and thermal gradients on the performance and degradation of lithium-ion battery packs. *Appl. Energy*, 248(April):489–499, 2019.

[283] Sabine Paarmann, Lisa Cloos, Jakob Technau, and Thomas Wetzel. Measurement of the temperature influence on the current distribution in lithium-ion batteries. *Energy Technol.*, 9(6):2000862, June 2021.

[284] Markus H Hofmann, Kevin Czyrka, Martin J Brand, Marco Steinhardt, Andreas Noel, Franz B Spingler, and Andreas Jossen. Dynamics of current distribution within battery cells connected in parallel. *Journal of Energy Storage*, 20:120–133, December 2018.

[285] Dong Zhang, Luis D. Couto, Sebastien Benjamin, Wente Zeng, Daniel F. Coutinho, and Scott J. Moura. State of charge estimation of parallel connected battery cells via descriptor system theory. In *2020 American Control Conference (ACC)*, pages 2207–2212, 2020.

[286] Dong Zhang, Luis D Couto, Preet Gill, Sebastien Benjamin, Wente Zeng, and Scott J Moura. Interval observer for SOC estimation in Parallel-Connected lithium-ion batteries. *Proc. Am. Control Conf.*, 2020-July:1149–1154, 2020.

[287] Ross Drummond, Luis D Couto, and Dong Zhang. Resolving kirchhoff's laws for parallel Li-Ion battery pack State-Estimators. *IEEE Trans. Control Syst. Technol.*, 30(15):2220–2227, 2021.

[288] Alexander Fill and Kai Peter Birke. Influences of cell to cell variances and the battery design on thermal and electrical imbalances among parallel Lithium-Ion cells. In *Proceedings of the IEEE International Conference on Industrial Technology*, volume 2021-March, pages 391–396. Institute of Electrical and Electronics Engineers Inc., March 2021.

[289] Alexander Fill, Sascha Koch, Andres Pott, and Kai-Peter Birke. Current distribution of parallel-connected cells in dependence of cell resistance, capacity and number of parallel cells. *J. Power Sources*, 407:147–152, December 2018.

[290] Lin Chen, Mo Zhang, Yunhui Ding, Shuxiao Wu, Yijing Li, Gang Liang, Hao Li, and Haihong Pan. Estimation the internal resistance of lithium-ion-battery using a multi-factor dynamic internal resistance model with an error compensation strategy. *Energy Reports*, 7:3050–3059, November 2021.

[291] E Prada, D Di Domenico, Y Creff, J Bernard, V Sauvant-Moynot, and F Huet. A simplified electrochemical and thermal aging model of LiFePO 4 -graphite li-ion batteries: Power and capacity fade simulations. *J. Electrochem. Soc.*, 160(4):A616–A628, 2013.

[292] Hassan K. Khalil. *Nonlinear Systems, 3rd Edition*. Prentice Hall, 2002.

[293] Wassim M. Haddad and VijaySekhar Chellaboina. *Nonlinear Dynamical Systems and Control: A Lyapunov-Based Approach*. Princeton University Press, 2008.

[294] Rajesh Rajamani, Woongsun Jeon, Hamidreza Movahedi, and Ali Zemouche. On the need for switched-gain observers for non-monotonic nonlinear systems. *Automatica*, 114:108814, April 2020.

[295] Stephen P. Boyd. *Linear Matrix Inequalities in system and control theory*. Society for Industrial and Applied Mathematics, 1994.

[296] Christoph R Birkl, Matthew R Roberts, Euan McTurk, Peter G Bruce, and David A Howey. Degradation diagnostics for lithium ion cells. *J. Power Sources*, 341:373–386, February 2017.

[297] Alexander Karger, Leo Wildfeuer, Deniz Aygül, Arpit Maheshwari, Jan P Singer, and Andreas Jossen. Modeling capacity fade of lithium-ion batteries during dynamic cycling considering path dependence. *Journal of Energy Storage*, 52:104718, August 2022.

[298] Daniel P Abraham. Diagnostic examination of generation 2 Lithium-Ion cells and assessment of performance degradation mechanisms prepared by chemical engineering division. Technical report, Argonne National Laboratory, 2005.

[299] Shoichiro Watanabe, Masahiro Kinoshita, Takashi Hosokawa, Kenichi Morigaki, and Kensuke Nakura. Capacity fade of LiAlyNi1-x-yCoxO 2 cathode for lithium-ion batteries during accelerated calendar and cycle life tests (surface analysis of LiAlyNi1-x-yCo xo2 cathode after cycle tests in restricted depth of discharge ranges). *J. Power Sources*, 258:210–217, 2014.

[300] Jing Li, Jessie Harlow, Nikolai Stakheiko, Ning Zhang, Jens Paulsen, and Jeff Dahn. Dependence of cell failure on Cut-Off voltage ranges and observation of kinetic hindrance in LiNi 0.8 co 0.15 al 0.05 O 2. *J. Electrochem. Soc.*, 165(11):A2682–A2695, 2018.

[301] Suhak Lee, Peyman Mohtat, Jason B Siegel, Anna G Stefanopoulou, Jang Woo Lee, and Tae Kyung Lee. Estimation error bound of battery electrode parameters with limited data window. *IEEE Trans. Ind. Inf.*, 16(5):3376–3386, 2020.

[302] Elham Hosseinzadeh, Sebastian Arias, Muthu Krishna, Daniel Worwood, Anup Barai, Dhammika Widanalage, and James Marco. Quantifying cell-to-cell variations of a parallel battery module for different pack configurations. *Appl. Energy*, 282(PA):115859, 2021.

[303] Xuebing Han, Languang Lu, Yuejiu Zheng, Xuning Feng, Zhe Li, Jianqiu Li, and Minggao Ouyang. A review on the key issues of the lithium ion battery degradation among the whole life cycle. *eTransportation*, 1(August):100005, 2019.

[304] Maxwell Woody, Maryam Arbabzadeh, Geoffrey M Lewis, Gregory A Keoleian, and Anna Stefanopoulou. Strategies to limit degradation and maximize li-ion battery service lifetime - critical review and guidance for stakeholders. *Journal of Energy Storage*, 28:101231, April 2020.

[305] Jacqueline S Edge, Simon O'Kane, Ryan Prosser, Niall D Kirkaldy, Anisha N Patel, Alastair Hales, Abir Ghosh, Weilong Ai, Jingyi Chen, Jiang Yang, Shen Li, Mei-Chin Pang, Laura Bravo Diaz, Anna Tomaszewska, M Waseem Marzook, Karthik N Radhakrishnan, Huizhi Wang, Yatish Patel, Billy Wu, and Gregory J Offer. Lithium ion battery degradation: what you need to know. *Phys. Chem. Chem. Phys.*, 23(14):8200–8221, April 2021.

[306] Ming Jiang, Dmitri L Danilov, Rüdiger-A Eichel, and Peter H L Notten. A review of degradation mechanisms and recent achievements for ni-rich cathode-based li-ion batteries. *Adv. Energy Mater.*, 11(48):2103005, December 2021.

[307] Peter M Attia, Alexander Bills, Ferran Brosa Planella, Philipp Dechent, Gonçalo dos Reis, Matthieu Dubarry, Paul Gasper, Richard Gilchrist, Samuel Greenbank, David Howey, Ouyang Liu, Edwin Khoo, Yuliya Preger, Abhishek Soni, Shashank Sripad, Anna G Stefanopoulou, and Valentin Sulzer. Review—"Knees" in Lithium-Ion battery aging trajectories. *J. Electrochem. Soc.*, 169(6):060517, June 2022.

[308] Ferran Brosa Planella and W Dhammika Widanage. A single particle model with electrolyte and side reactions for degradation of lithium-ion batteries. *Appl. Math. Model.*, 121:586–610, September 2023.

[309] Vivian Loonela, Sonya Gospodinova, Daniela Stoycheva, and Celia Dejond. Green deal: Sustainable batteries for a circular and climate neutral economy. https://ec.europa.eu/commission/presscorner/detail/en/ip_20_2312, 2020.

[310] Hans Eric Melin, Mohammad Ali Rajaeifar, Anthony Y Ku, Alissa Kendall, Gavin Harper, and Oliver Heidrich. Global implications of the EU battery regulation. *Science*, 373(6553):384–387, July 2021.

[311] European Parliament. New batteries regulation, legislative train schedule. https://www.europarl.europa.eu/legislative-train/theme-a-european-green-deal/file-revision-of-the-eu-battery-directive-(refit), January 2023. Accessed: 2023-2-14.

[312] Laura Paszkiewicz. The cost and demographics of vehicle acquisition. *Consumer Expenditure Survey Anthology*, 61, 2003.

[313] Economic Commission for Europe. (GRPE) proposal for a new UN GTR on in-vehicle battery durability for electrified vehicles. https://unece.org/transport/documents/2021/12/working-documents/grpe-proposal-new-un-gtr-vehicle-battery-durability, January 2022. Accessed: 2022-12-11.

[314] California Air Resources Board. Final regulation order for section 1962.8 warranty requirements for Zero-Emission and batteries in plug-in hybrid electric 2026 and subsequent model year passenger cars and Light-Duty trucks. Technical report, California Air Resources Board, August 2022.

[315] Alexander Tankou, Nic Lutsey, and Dale Hall. Understanding and supporting the used zero-emission vehicle market. Technical report, The International Council on Clean Transportation, December 2021.

[316] European Commission. Proposal for a regulation of the european parliament and of the council concerning batteries and waste batteries, repealing directive 2006/66/EC and amending regulation (EU) no 2019/1020. Technical Report 2020/0353, European Commission, October 2020.

[317] California Air Resources Board. Final regulation order for section 1962.5 data standardization requirements for 2026 and subsequent model year Light-Duty zero emission vehicles and plug-in hybrid electric vehicles. Technical report, California Air Resources Board, August 2022.

[318] Linda Colarullo and Jagruti Thakur. Second-life EV batteries for stationary storage applications in local energy communities. *Renewable Sustainable Energy Rev.*, 169:112913, November 2022.

[319] Simon F Schuster, Martin J Brand, Philipp Berg, Markus Gleissenberger, and Andreas Jossen. Lithium-ion cell-to-cell variation during battery electric vehicle operation. *J. Power Sources*, 297:242–251, 2015.

[320] Argonne National Lab. BatPaC model software. https://www.anl.gov/cse/batpac-model-software, March 2022. Accessed: 2023-2-20.

[321] Ben Rowden and Nuria Garcia-Araez. A review of gas evolution in lithium ion batteries. *Energy Reports*, 6:10–18, 2020.

[322] Roland Jung, Michael Metzger, Filippo Maglia, Christoph Stinner, and Hubert A. Gasteiger. Oxygen Release and Its Effect on the Cycling Stability of LiNi x Mn y Co z O 2 (NMC) Cathode Materials for Li-Ion Batteries . *Journal of The Electrochemical Society*, 164(7):A1361–A1377, 2017.

[323] Wesley M. Dose, Chao Xu, Clare P. Grey, and Michael F.L. De Volder. Effect of Anode Slippage on Cathode Cutoff Potential and Degradation Mechanisms in Ni-Rich Li-Ion Batteries. *Cell Reports Physical Science*, 1(11):100253, 2020.

[324] D. J. Xiong, L. D. Ellis, Remi Petibon, Toren Hynes, Q. Q Liu, and J. R. Dahn. Studies of Gas Generation, Gas Consumption and Impedance Growth in Li-Ion Cells with Carbonate or Fluorinated Electrolytes Using the Pouch Bag Method. *Journal of The Electrochemical Society*, 164(2):A340–A347, 2017.

[325] L. D. Ellis, J. P. Allen, L. M. Thompson, J. E. Harlow, W. J. Stone, I. G. Hill, and J. R. Dahn. Quantifying, Understanding and Evaluating the Effects of Gas Consumption in Lithium-Ion Cells. *Journal of The Electrochemical Society*, 164(14):A3518–A3528, 2017.

[326] L. J. Krause, V. L. Chevrier, L. D. Jensen, and T. Brandt. The Effect of Carbon Dioxide on the Cycle Life and Electrolyte Stability of Li-Ion Full Cells Containing Silicon Alloy. *Journal of The Electrochemical Society*, 164(12):A2527–A2533, 2017.

[327] V. L. Chevrier, L. J. Krause, L. D. Jensen, Cuong Huynh, Matthew Triemert, Emily L. Bowen, and James Thorson. Design of Positive Electrodes for Li-Ion Full Cells with Silicon. *Journal of The Electrochemical Society*, 165(13):A2968–A2977, 2018.

[328] Matthew Li, Ming Feng, Dan Luo, and Zhongwei Chen. Fast Charging Li-Ion Batteries for a New Era of Electric Vehicles. *Cell Reports Physical Science*, 1(10):100212, 2020.